

Linear Iron-core Permanent Magnet Motor with High Force and Low Acoustic Noise

by

Jun Young Yoon

Submitted to the Department of Mechanical Engineering
in partial fulfillment of the requirements for the degree of

Doctor of Philosophy in Mechanical Engineering

at the

MASSACHUSETTS INSTITUTE OF TECHNOLOGY

February 2017

© Massachusetts Institute of Technology 2017. All rights reserved.

Signature redacted

Author

Department of Mechanical Engineering
Jan 15, 2017

Signature redacted

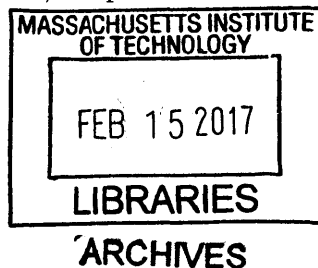
Certified by

David L. Trumper
Professor of Mechanical Engineering
Thesis Supervisor

Signature redacted

Accepted by

Rohan Abeyaratne
Chairman, Department Committee on Graduate Theses



Linear Iron-core Permanent Magnet Motor with High Force and Low Acoustic Noise

by

Jun Young Yoon

Submitted to the Department of Mechanical Engineering
on Jan 15, 2017, in partial fulfillment of the
requirements for the degree of
Doctor of Philosophy in Mechanical Engineering

Abstract

Acoustic noise and associated vibration are potentially troubling characteristics of electric machines including variable-reluctance motors, induction machines, and permanent magnet synchronous motors. The severity of this problem depends on the types of motors and their applications. One exemplary case where the vibro-acoustic noise becomes especially detrimental is iron-core linear motors operating at high acceleration and targeted for high accuracy applications.

In this doctoral research, we identify root causes of the vibro-acoustic noise of iron-core linear motors, and create magnetic designs paired with control algorithms to achieve high-acceleration with low noise and vibration. Vibro-acoustic noise issues of rotary machines have been researched over the years, but not as much work has been done for linear machines whose major causes of noise generation might be different from rotary motors due to the structural differences. This thesis focuses on the following aspects: 1) Investigate the causes and develop and verify theory for acoustic noise emitted from linear iron-core machines. 2) Design, construct, and test a new linear iron-core motor that can simultaneously provide high force and low noise. 3) Design and construct an experimental linear motor testbed to investigate the noise issue of conventional iron-core motors, and to demonstrate the new motor's desired performance of high force and low noise.

We hypothesize and experimentally validate that the acoustic noise and associated vibration of linear iron-core permanent magnet motors are caused by high frequency force harmonics vibrating the moving stage. Such stage vibration can be transmitted through the system structure and can also radiate as acoustic noise, thereby disturbing precision machines. In order to reduce high frequency force harmonic content, our new motor has fine teeth, narrow slots with high slot aspect ratio, five phases, and a moving Halbach magnet array. With our new *fine-tooth* motor, we significantly reduce the vibro-acoustic noise of linear iron-core motors while substantially enhancing the shear stress density, compared to conventional 3-4 combination iron-core motors. The overall acoustic noise level in Pascals is reduced by 93% during the acceleration period with non-skewed magnets. In terms of the sound pressure level (SPL), this is

a significant noise reduction from 83 dB to 60 dB. The cogging-driven and velocity-dependent noise, which is dominant in constant velocity regions, is also significantly reduced in our new motor design. Our fine-tooth motor design reduces the cogging force by a factor of 10-to-1 when using skewed magnets, thereby reducing cogging-driven acoustic noise by 90 % in Pascals. We also present in this thesis the force performance of our new fine-tooth motor both in simulations and experiments. Our new motor shows predicted shear stress improvements of 28 % (from 0.090 N/mm² to 0.115 N/mm²) at the prototype practical power level of 10 W/mm and 84 % (from 0.167 N/mm² to 0.308 N/mm²) at an anticipated ultimate RMS (root mean square) current density limit in the coil wires of 50 A/mm², relative to a conventional motor.

Understanding causes of the vibro-acoustic noise and how to mitigate it in both the design and post-design phases provides useful tools to achieve high-performance and quiet linear motion devices. This research will benefit many industrial applications which require both high throughput and high accuracy.

Thesis Supervisor: David L. Trumper
Title: Professor of Mechanical Engineering

Acknowledgments

I would first and foremost like to thank my thesis advisor Professor David Trumper for his guidance, encouragement, and patience throughout my graduate years. I have learned a great deal from him both academically and non-academically including how to define and construct research problems, how to effectively design a precision mechatronics system, how to see both the big picture and small details, and how to write and present effectively. His advice and support provided me with the invaluable opportunities to successfully complete the thesis work and develop my professional career. He has been a great mentor to me, and it has been an honor and privilege to work with him.

I would also like to thank my thesis committee for their invaluable advice, kind support, and encouragements. Professor Jeffrey Lang had a keen interest in my project, and helped me with great suggestions on essential experiments on the motor noise and force performance. It was in fact his early work on the noise issue of variable reluctance rotary motors that forms a foundation for my research work. Professor Steven Leeb encouraged me a great deal by showing his trust on my research work. He helped me to broaden my thinking by sharing his out-of-the-box ideas. All of my committee members were always willing to help on any aspects of the work, and I am sincerely grateful for their support.

Over my graduate years, I have worked with ASML and I would like to thank them for their collaboration and financial support. Mark Schuster helped me from the start of the project and always offered valuable feedback. I would like to thank him and his team for all the support. Steve Roux provided great ideas on every aspect of the research work. It was always helpful to have his inputs and suggestions. I would also like to thank Minkyu Kim, who helped me a great deal to make progress. We had a weekly meeting throughout the project period, which was always productive and helpful. I also thank Ruvinda Gunawardana for his support and all the fruitful discussions we had.

I also extend my sincere thanks to Fred Sommerhalter, who built the new linear

iron-core permanent magnet motors for my thesis. Working with him, I could learn a great deal about the motor fabrication process. His efforts were key to my project, and I deeply appreciate all his help. I would like to also thank Drew Devitt of New Way Air Bearings for his valuable ideas on the air bearing stage design and kind offerings on the guide bars, which became the base structure of our experimental setup. I also thank Steve Ludwick for being always accessible and responsive to any of my questions. The link-less hinge-less noise-free cable carrier he recommended was a tremendous help to our experimental stage testbed. Patrick McAtamney in the Edgerton center at MIT helped me with manufacturing the hardware components, and I thank him for his time and help. I also thank National Instruments for the controller hardware donation and their technical support.

My dear labmates created a friendly atmosphere in our lab and helped make my time at MIT gratifying. Ian MacKenzie was and still is a dearest friend of mine, who was always willing to take time to help me on any matters both academically and personally. He was my first go-to person for discussion of any kind and it was always fruitful and enjoyable. Darya Amin-Shahidi always had answers for my control and mechatronics design questions. I enjoyed the business trips we had to ASML in Wilton. Mohammad Imani Nejad was willing to offer his expertise in manufacturing and answered many machining questions I had. I also enjoyed spending time with Roberto Meléndez who helped me machine parts and introduced me to many activities and people at MIT. I also thank Aaron Gawlik who helped me settle in our lab when I first came to MIT. He supported a great deal on my Master's project on the robotic manipulator for single-cell pick-and-place. Minkyun Noh has been a great friend whom I can bounce ideas with. I really enjoyed frequent brainstorming sessions with him. Lei Zhou has always been willing to take time to help. All the discussions with her on the magnetic design and control issues were fruitful and enjoyable. I would also like to thank Tyler Hamer who brought a bright energy to our lab. The digital signal analyzer (DSA) he developed was of great help for my work too. I also thank Brij Bhushan, Luis Soenksen, Joseph Church, Phillip Daniel, and Jim Zhen Sun for being great friends and offering their support. I would also like to express my gratitude to

Laura Zaganjori for her valuable and friendly help on all the administrative matters. I also thank the mechanical department office staff, especially Leslie Regan for all the help and support.

From the day one of my MIT life, I have had a tremendous help from the Korean Graduate Student Association (KGSA) and I would like to express my thanks to all the members. I would especially like to thank my dearest friend, Changrak Choi. He has always been the most willing and respectful friend to offer help and support in any way I needed. I really enjoyed all the discussions and conversions we had, which was always amusing, stimulating, and productive. I also sincerely thank Dr. Sangok Seok, Dr. Youngsoo Joung, Prof. Hyunglae Lee, Prof. Kenneth Kyoochul Park, Dr. Sanha Kim, and Dr. Hyukmin Kwon for all the discussions we had on the research, career goals, and life. They made my graduate life at MIT more fruitful and enjoyable. I also thank Dong Hoon Yi and Byung Gu Cho for their valuable help on the acoustics side of my research work. I would also like to extend my thanks to the friends in my study group: Changrak Choi, Junghee Park, Minkyun Noh, Heejin Ahn, and Jongwoo Lee. We shared a number of interesting subjects together over many years, and every session was helpful, educational, and inspiring.

I cannot fully express my gratitude to my parents and parents-in-law, who have freely given their unconditional love and support throughout my life. I am forever indebted to their love and prayer, with which I can be where I am at this moment. I also thank my brother and his family for their support and sincere prayer. I am most grateful to my wife, Sun Hyang Kyung, and my daughter, Sarie Yoon for their tremendous sacrifice throughout many years of my graduate study. With their love, support, and prayer, I could successfully finish my Ph.D. I sincerely thank them for being amazingly supportive and understanding.

This work was sponsored by ASML and Samsung Scholarship, and performed at the Massachusetts Institute of Technology.

All the Glory To God

Contents

1	Introduction	33
1.1	Accomplishments and Contributions	34
1.2	Prior Art	35
1.2.1	Acoustic Noise Issue of Rotary Motors	36
1.2.2	High Acceleration Motors	39
1.3	Hypothesis on Noise Mechanism of Linear Motor	41
1.4	Thesis Overview	43
1.4.1	Conventional Linear Iron-core Motor	43
1.4.2	New Motor Design and Construction	45
1.4.3	Testbed Design and Construction	47
1.4.4	Experimental Results	49
2	Conventional Linear Iron-core Permanent Magnet Motor	53
2.1	Linear 3-4 Combination Motor	54
2.1.1	Conventional Design of 3-4 Combination Motor	55
2.1.2	Simplified Analysis	57
2.2	Motor Performance in Simulation	61
2.2.1	Finite Element Analysis Model	61
2.2.2	Cogging and Force Ripple	66
2.3	Summary	72
3	Fine-tooth Motor Modeling, Design, and Construction	75
3.1	Fine-tooth Motor	76

3.1.1	Simplified Analysis	77
3.1.2	Pros and Cons	80
3.2	Hybrid Layer Model	81
3.2.1	Maxwell Model for Magnet Track	82
3.2.2	Flux-tube Model for Stator Armature	90
3.2.3	Iteration of Hybrid Layer Model	98
3.2.4	Performance Compared to Finite Element Method	99
3.3	New Motor Design Process by Motor Performance Comparison	101
3.3.1	Design Parameters	102
3.3.2	Design Parameter Selection by HLM	103
3.3.3	Design Parameter Selection by FEM	105
3.4	Final Design of New Fine-tooth Motor	120
3.4.1	Practical Design Modification	121
3.4.2	Performance Expectation of Final New Motor Design	123
3.5	Construction of New Fine-tooth Motor	128
3.5.1	Stator Armature	128
3.5.2	Magnet Tracks	134
3.6	Summary	136
4	Experimental Testbed Design	139
4.1	Functional Requirements	140
4.2	Conceptual Designs	143
4.2.1	Moving Short Magnet and Stationary Long Coil	143
4.2.2	Stationary Long Magnet and Moving Short Coil	149
4.2.3	Moving Long Magnet and Stationary Short Coil	152
4.2.4	Stationary Short Magnet and Moving Long Coil	154
4.3	Design Selection	156
4.3.1	Base Structure and Bearing Selection	157
4.3.2	Selected Testbed Design and CAD models	165
4.4	Summary	173

5	Experimental Testbed Construction	175
5.1	Linear Stage Testbed with Conventional Motor	176
5.1.1	Steel Guide Bar	176
5.1.2	Dynamometer	179
5.1.3	Stage with Air Bearings	183
5.1.4	Position Sensors	188
5.1.5	Shock Absorbers and Cable Carrier	189
5.1.6	Power Electronics	192
5.2	Testbed Modification for New Fine-tooth Motor	194
5.2.1	Stator Mounting Plate Redesign and Reconstruction	195
5.2.2	Dynamometer Reconfiguration	196
5.2.3	Airbearings Adjustment	198
5.2.4	Power Electronics Reconnection	199
5.3	Noise Measurement Systems	199
5.3.1	Vibration Measurement System	200
5.3.2	Acoustic Noise Measurement System	201
5.4	Summary	202
6	Experiments with Conventional 3-4 Combination Motor	205
6.1	Control of Conventional Motor	206
6.1.1	Zero Electric Position	206
6.1.2	Commutation	210
6.1.3	Position Control	213
6.2	Experimental Results	220
6.2.1	Vibro-acoustic Noise in Stationary Position	220
6.2.2	Vibro-acoustic Noise during Cycle Operation	226
6.2.3	Brief Summary	233
7	Experiments with Fine-tooth Motor	235
7.1	Control of Fine-tooth Motor	236
7.1.1	Zero Electrical Position	236

7.1.2	Commutation	240
7.1.3	Position Control	243
7.2	Experimental Results and Comparisons	247
7.2.1	Vibro-acoustic Noise by Stage Dynamics	248
7.2.2	Vibro-acoustic Noise by Cogging Force	251
7.2.3	Force Performance of New Fine-tooth Motor	266
7.2.4	Thermal Performance of New Fine-tooth Motor	269
7.2.5	Brief Summary	273
8	Conclusions and Suggestions for Future Work	277
8.1	Conclusions	277
8.2	Suggestions for Future Work	284
8.2.1	Control Algorithms for Further Noise Reduction	285
8.2.2	Hybrid Layer Model Upgrade	285
8.2.3	Double-sided Stage Configurations	286
8.2.4	Liquid Cooling	289
A	Drawings of Testbed Components	291
B	List of Vendors and Manufacturers	319

List of Figures

1-1	Possible sources of the motor noise problems.	36
1-2	Hypothesis on the mechanism of the vibro-acoustic noise in linear iron-core permanent magnet motors.	42
1-3	The stator armature of the conventional linear iron-core motor, TL18 by Tecnotion. Photo courtesy of Tecnotion.	44
1-4	Pictures of the stator armature of our new fine-tooth motor. The right photo shows the top view and the left one the side view. A U.S. quarter coin is for the size reference.	46
1-5	Pictures of the experimental linear stage testbed with the conventional 3-4 combination motor (right) and our new fine-tooth motor (left). . .	48
1-6	Cumulative amplitude spectrum (CAS) of the measured acoustic noise from both the conventional 3-4 combination motor (black curve) and our new fine-tooth motor (green curve). Noise measured with non-skewed magnets during an acceleration period.	50
1-7	Spectrogram comparison of the measured acoustic noise of our new motor with the non-skewed (upper) and skewed (lower) magnets. The cogging-oriented noise during constant velocity regions (brighter portions) is significantly reduced by using the skewed magnets due to the fine-tooth motor design. The commanded velocity profiles are shown in white.	51

2-1	Pictures of a conventional 3-4 combination linear iron-core motor, TL18 model by Tecnotion. Moving magnet track (upper) and stator armature (lower). Stator photo courtesy of Tecnotion.	54
2-2	Pictures of magnet track of the conventional 3-4 combination linear iron-core motor. Non-skewed magnet track (left) and skewed magnet track (right).	55
2-3	Schematic magnetic design of the conventional 3-4 combination linear iron-core motor.	56
2-4	Magneto-motive force (MMF) vectors of the stator (\mathcal{F}_s) and magnet track (or rotor) (\mathcal{F}_r) in polar coordinates of the electrical angle, θ_e . .	57
2-5	Magneto-motive force (MMF) waveforms of the stator and magnet track (or rotor) of the conventional linear iron-core motor.	59
2-6	Finite element model of the conventional linear iron-core motor, with 4 pitches of magnets and coil currents of zero.	62
2-7	Schematic explanation of the magnet skewing effect in reducing the cogging force. Non-skewed magnet and related cogging harmonics (left) and skewed magnet and related cogging harmonics (right).	63
2-8	Segmented magnets in the 2D finite element model to approximately capture the magnet skewing effect of the conventional iron-core motor.	65
2-9	Simulated cogging force of the conventional iron-core motor with both non-skewed and skewed magnets. The cogging force is per basic motor unit. By unit, we mean the basic combination of 3 iron-core teeth and 4 magnets.	67
2-10	Simulated cogging force spectrum of the conventional iron-core motor with both non-skewed and skewed magnets.	67
2-11	Simulated force ripple of the conventional iron-core motor with both non-skewed and skewed magnets. The force ripple is per basic motor unit. By unit, we mean the basic combination of 3 iron-core teeth and 4 magnets.	70

2-12	Simulated force ripple spectrum of the conventional iron-core motor with both non-skewed and skewed magnets.	70
3-1	Schematic magnetic designs of a unit length of the conventional 3-4 combination motor (left) and our new fine-tooth motor (right).	76
3-2	Magneto-motive force (MMF) waveforms of the stator and magnet track (or rotor) of our new fine-tooth motor.	78
3-3	Hybrid layer model of a linear iron-core motor. Flux-tube model for the stator armature and Maxwell model for the magnet track (or rotor).	82
3-4	Example schematic of a 3-phase linear iron-core motor with Halbach magnet array in Cartesian coordinates.	83
3-5	Vertical and horizontal magnetization waveform of the Halbach magnet array with the magnetization amplitude M_0 . Both magnetizations are a function of y and periodic with the period of $\lambda_u = \lambda_{pp}$. The locations of $y = y_1, y_2, y_3$, and y_4 are the magnet boundaries as shown in Figure 3-4.	85
3-6	Network of nonlinear reluctances in the flux-tube model for the example 3-phase stator shown in Figure 3-3. The equivalent magnetic circuit is solved for the magnetic potential ψ 's when the magnetic flux ϕ 's are given as the input from the Maxwell model.	90
3-7	Schematic of assumed flux tube for the fringing fields in the slots. The magnified view of teeth and a slot is in the green box showing the characteristic length of $w_s\pi/8$ and the area of $(w_s/2)D_{motor}$, where D_{motor} is the depth of the motor into the page.	91
3-8	Iteration schematic of the hybrid layer model (HLM) between the flux-tube model in the armature core and the Maxwell model in the magnet track.	98

3-9	Simulated air-gap magnetic flux density by both the finite element method (blue solid line) and our hybrid layer model (red dotted line). Magnetic flux density in Tesla in both the normal (upper) and tangential (lower) directions.	100
3-10	Computed cogging force by both the finite element method (blue solid line) and our hybrid layer model (red dotted line). Cogging force in Newtons in both the normal (upper) and tangential (lower) directions.	100
3-11	Design parameters of our new fine-tooth motor.	102
3-12	Shear stress per power versus the number of motor phases. Shear stress per power is simulated by our hybrid layer model. Power is calculated over a motor unit, which is one pole-pair.	103
3-13	Normalized thrust versus Halbach array ratio, f_{magnet} . Thrust force is simulated by our hybrid layer model.	105
3-14	Simulated shear stress versus power dissipation per unit 1) to compare our hybrid layer model (HLM) to the finite element model (FEM) and 2) to observe the non-convergence issue of HLM at high currents. The shear stress and power are calculated with the motor design parameters of Case 1 in Figure 3-15 for both HLM (orange curve) and FEM (blue asterisk). The hybrid layer model begins to fail at around 900 W per unit in this case. The meaning of the ordinate and abscissa will be explained shortly in the text.	106
3-15	Table of various cases to determine design parameters. Four different groups are color-coded for the selection process of five design parameters, $w_t (= w_s)$, R_{slot} , PM_{thick} , N , and AWG	107
3-16	Simulated shear stress in (3.29) versus power dissipation per unit in (3.31). By unit, we mean the minimal motor magnetic configuration required to generate a thrust, which consists of 3 iron-core teeth and 4 magnets for the conventional motor and one pole pair for our new fine-tooth motor.	110

3-17	Simulated shear stress in (3.29) versus RMS current density in wire in (3.32). Shear stress performance of the conventional motor in light blue line serves as a design reference.	110
3-18	Simulated stage acceleration in (3.30) versus power dissipation per unit in (3.31). As before, by unit, we mean the minimal motor magnetic configuration required to generate a thrust. The stage acceleration is estimated for a double-sided motor configuration with a stage mass of 10 kg.	111
3-19	Simulated stage acceleration in (3.30) versus RMS current density in wire in (3.32). The stage acceleration is estimated for a double-sided motor configuration with a stage mass of 10 kg.	111
3-20	Simulated shear stress in (3.29) versus power dissipation per unit in (3.31). By unit, we mean the minimal motor magnetic configuration required to generate a thrust.	113
3-21	Simulated shear stress in (3.29) versus RMS current density in wire in (3.32). Shear stress performance of the conventional motor in light blue line serves as a design reference.	113
3-22	Simulated stage acceleration in (3.30) versus power dissipation per unit in (3.31). By unit, we mean the minimal motor magnetic configuration required to generate a thrust. The stage acceleration is estimated for a double-sided motor configuration with a stage mass of 10 kg.	114
3-23	Simulated stage acceleration in (3.30) versus RMS current density in wire in (3.32). The stage acceleration is estimated for a double-sided motor configuration with a stage mass of 10 kg.	114
3-24	Simulated shear stress in (3.29) versus power dissipation per unit in (3.31). By unit, we mean the minimal motor magnetic configuration required to generate a thrust.	116
3-25	Simulated shear stress in (3.29) versus RMS current density in wire in (3.32). Shear stress performance of the conventional motor in light blue line serves as a design reference.	116

3-26 Simulated shear stress in (3.29) versus power dissipation per unit in (3.31). By unit, we mean the minimal motor magnetic configuration required to generate a thrust.	118
3-27 Simulated shear stress in (3.29) versus RMS current density in wire in (3.32). Shear stress performance of the conventional motor in light blue line serves as a design reference.	118
3-28 Simulated stage acceleration in (3.30) versus power dissipation per unit in (3.31). By unit, we mean the minimal motor magnetic configuration required to generate a thrust. The stage acceleration is estimated for a double-sided motor configuration with a stage mass of 10 kg.	119
3-29 Simulated stage acceleration in (3.30) versus RMS current density in wire in (3.32). The stage acceleration is estimated for a double-sided motor configuration with a stage mass of 10 kg.	119
3-30 Final design parameters of a new fine-tooth motor using silicon-iron stator material to reduce prototype cost.	120
3-31 Simulated shear stress in (3.29) versus power dissipation per unit in (3.31). By unit, we mean the minimal motor magnetic configuration required to generate a thrust. Comparison between the conventional motor (light blue line) and our new fine-tooth motor with final design parameters (black line).	124
3-32 Simulated shear stress in (3.29) versus RMS current density in wire in (3.32). Comparison between the conventional motor (light blue line) and our new fine-tooth motor with final design parameters (black line).	124
3-33 Simulated stage acceleration in (3.30) versus power dissipation per unit in (3.31). By unit, we mean the minimal motor magnetic configuration required to generate a thrust. Comparison between the conventional motor (light blue line) and our new fine-tooth motor with final design parameters (black line).	125

3-34 Simulated stage acceleration in (3.30) versus RMS current density in wire in (3.32). Comparison between the conventional motor (light blue line) and our new fine-tooth motor with final design parameters (black line). 125

3-35 Simulated force ripple comparison between the conventional motor (light blue line) and our new fine-tooth motor with final design parameters (black line). 127

3-36 Simulated force ripple spectrum comparison between the conventional motor (light blue line) and our new fine-tooth motor with final design parameters (black line). 127

3-37 Pictures of stator laminations showing the total length of 728 mm and the tooth pitch of 4 mm. Quarter is for a size reference. 129

3-38 Winding scheme of 5-phase double-layered full-pitch concentrated windings for the newly-designed fine-tooth motor stator. 130

3-39 Wiring scheme of the phase-A coils in the first section. The total of 8 phase-A coils are connected in series to have alternating polarities. . . 131

3-40 Cabling scheme of our newly-designed fine-tooth motor. Total of 40 cables for 20 resultant phase winding coils (5-phase coils per section) with 10 cables brought out to each corner. 132

3-41 Completed stator armature with all the winding, wiring, and cabling. Quarter is for a size reference. 133

3-42 Assembly process of Halbach magnet array. Photos courtesy of Fred Sommerhalter. 134

3-43 Completed Halbach array magnet tracks with both non-skewed and skewed magnets. The short tracks are for the single-sided motor configuration and the long ones for the double-sided configuration. We thank Fred Sommerhalter for the fabrication of the magnet tracks. . . 135

4-1	Hand sketch of a possible stage design with moving short magnet and stationary long coil. Front view (upper), isometric view (lower left), and top view (lower right).	144
4-2	Hand sketch of a possible stage design with moving short magnet and stationary long coil. Essentially a 90°-rotated version of the previous concept.	146
4-3	Hand sketch of a possible stage design with moving short magnet and stationary long coil. Moving magnets are configured outside. Front view (upper), top view (lower left), and side view (lower right).	147
4-4	Hand sketch of a possible stage design with stationary long magnet and moving short coil. Front view of overall structure (upper) and side view of motor magnetic configuration (lower).	150
4-5	Hand sketch of another possible stage design with stationary long magnet and moving short coil. Essentially a 90°-rotated version of the previous concept.	151
4-6	Hand sketch of a possible stage design with moving (or stationary) long magnet and stationary (or moving) short coil.	153
4-7	Hand sketch of a possible stage design with stationary short magnet and moving long coil. Front view (upper) and isometric view (lower).	155
4-8	Picture of base guide bars with the same cross-section area, but with the different length of 1040 mm and 1295 mm.	158
4-9	Hand sketch of a possible design with air bearings symmetrically preloaded by other air bearings. Front view (upper) and isometric view (lower).	160
4-10	Hand sketch of a possible design with vacuum preloaded (VPL) air bearings.	162
4-11	Hand sketch of another possible design with air bearings preloaded by magnets. Front view (upper) and top view (lower).	164
4-12	CAD model of selected testbed design showing mounting details of air bearings and holding magnets. Side view (upper) and Top view (lower).	166

4-13	Front views of selected testbed design with the conventional Tecnotion Motors both for single-sided (upper) and double-sided (lower) configurations.	169
4-14	Isometric views of selected testbed design with the conventional Tecnotion Motors both for single-sided (upper) and double-sided (lower) configurations.	170
4-15	Front views of selected testbed design with our newly-designed fine-tooth Motors both for single-sided (upper) and double-sided (lower) configurations.	171
4-16	Isometric views of selected testbed design with our newly-designed fine-tooth Motors both for single-sided (upper) and double-sided (lower) configurations.	172
5-1	The completed assembly of the linear stage setup with a conventional 3-4 combination motor (TL18 by Tecnotion).	176
5-2	Mounting plate on a granite table for the guide bar to be firmly installed.	177
5-3	51-inch steel guide bar (donated by New Way Air Bearings) mounted on the granite table by an intermediate breadboard and L-brackets.	178
5-4	Heat treated 1045 steel mounting plate for the stator serves also as the dynamometer top plate, where the four corner pockets accommodate four Kistler 9250A4 triaxial load cells.	180
5-5	Formed dynamometer installed on the base guide bar to provide direct force measurements in all three directions.	181
5-6	Dynamometer Z-direction force measurement test with a force-meter exerting +Z force of 35 to 40 N.	182
5-7	Dynamometer Y-direction force measurement test with a force-meter exerting -Y force of -35 to -40 N.	182
5-8	Dynamometer X-direction force measurement test with a force-meter exerting -X force of -35 to -40 N.	183

5-9	Pre-assembled moving stage with four top air bearings, two side air bearings, air paths, and preloading holding magnets.	184
5-10	Detailed bottom views of the pre-assembled moving stage before being installed on the base guide bar. Patterned material protects face of air bearings, and is removed before operation.	184
5-11	Simulated preloading force versus gap curves of holding magnets (right) by finite element analysis with models of top holding magnet (upper left) and side holding magnet (lower left).	186
5-12	Moving stage installed on the base guide bar with air bearings preloaded by holding magnets against the well-ground guide surfaces. Pressure gauge shows our operation air pressure of 80 psi (lower left), and a magnified view shows how air bearings and a holding magnet are engaged against the guide surface (lower right).	186
5-13	Stage flying height measured at five different points by a dial gauge showing the average flying height of 6 μm at the air pressure of 80 psi.	187
5-14	Linear encoder system using a scale on the base and a read-head on the moving stage. Green LED on the read-head indicates correct clearance associated with a normal signal level of 70 % to 135 %.	188
5-15	Shock absorbers (SCS33-25 by ACE) installed on a spacer to provide enough damping to stop the stage in case of motor or control failure.	190
5-16	Schematic of low-noise and low-vibration link-less cable carrier provided by the manufacturer, Tsubaki KabelSchlepp. Link-free and hinge-free design with side-bands made of continuously extruded polymers.	191
5-17	Stage testbed with a link-less and hinge-less cable carrier (Quantum 040-28 by Tsubaki) carrying encoder cables and air inlet tubing. Cable stresses are isolated by strain reliefs.	191
5-18	Power electronics drive target of multiple individual coils on a Tecnotion motor armature: 18 coils exposed before potting (upper) and potted stator (lower). Upper photo courtesy of Tecnotion.	192

5-19	Schematic of power electronics configuration with 5 power supplies and 18 power amplifiers.	193
5-20	Customized rack for 5 power supplies and 18 power amplifiers: front view (left) and rear view (right).	194
5-21	The completed assembly of the linear stage setup with our new fine-tooth motor.	195
5-22	Mounting plate for the new fine-tooth motor, also serving as a top plate for the dynamometer formed by four load cells located as indicated. .	196
5-23	New mounting plate placed on top of four load cells forming the dynamometer.	197
5-24	New fine-tooth stator mounted on the dynamometer. Long dove-tail inserts are used to clamp the stator down on the mounting plate. . .	197
5-25	Top air bearing flying height measured at four corners on the stage by a dial indicator with the resolution of 1 μm , showing the average flying height of 6 μm at the air pressure of 80 psi.	198
5-26	Single-axis (353B15) and triaxial (356A26) accelerometers, by PCB Piezotronics, to measure vibration noise of our linear stage testbed. .	200
5-27	Microphone, 130E20 by PCB Piezotronics, to measure acoustic noise emitted from the experimental motor setup.	201
5-28	Microphone array to measure the motor acoustic noise both from side (left) and above (right).	201
6-1	Schematic of conventional 3-4 combination linear iron-core motor configuration indicating the desired zero reference position, y_{ref} . By 3-4 we mean the motor periodically includes 3 coils/poles for every 4 magnets.	206
6-2	Measured back EMF of coil #7 in the Tecnotion TL18 conventional iron-core stator showing the zero-crossings with the interval of pole pitch, $\lambda_p = 12$ mm.	208
6-3	Schematic explanation of the measured back EMF of coil #7, region-by-region.	208

6-4	Squarewave commutation algorithm for the conventional Tecnotion TL18 three-phase iron-core motor. Magnet track shown is located at the zero reference position. Phase difference is one third of pole-pair pitch, $\lambda_{pp}/3$ from one phase to another.	212
6-5	Schematic of position control loop with a plant of linear motor system, power amplifiers, commutation law, and a PID (lead-lag) controller. . .	214
6-6	Schematic for measuring the relevant frequency responses of control loop: plant (left) and loop transmission (right).	215
6-7	Measured and modeled frequency responses of plant and loop return ratio showing a crossover frequency of about 100 Hz and a phase margin of about 45°.	216
6-8	Measured time response of cogging resonance when perturbed about a stable equilibrium showing the frequency of about 4.5 Hz, consistent with the low frequency resonance observed in the measured frequency responses.	216
6-9	Measured step response of closed position control system to a step of 20 μm showing a rise time of about 1.7 msec and encoder quantization of 1 μm	218
6-10	Measured tracking performance of closed position control system following a smooth trajectory with maximum acceleration of 10 m/s^2 and maximum velocity of 0.3 m/s	219
6-11	Encoder quantization and corresponding control effort with an interpolated resolution of 1 μm (left), and associated cumulative amplitude spectrum (CAS) (right).	222
6-12	Cumulative amplitude spectrum (CAS) of accelerometer measurement data for four different conditions investigating motor stationary noise with the encoder resolution of 1 μm . Z-direction (left) and X-direction (right).	222
6-13	Schematic of major stage eigen-modes with a brief description, experimentally obtained by a ping test.	224

6-14	Encoder quantization and corresponding control effort with an interpolated resolution of $0.1 \mu\text{m}$ compared to the case with $1 \mu\text{m}$ resolution (left) and associated CAS (right).	224
6-15	CAS of accelerometer measurement. Comparison between the encoder resolutions, $\Delta=0.1 \mu\text{m}$ and $\Delta=1 \mu\text{m}$, showing significant reduction of motor stationary noise with finer resolution. Z-direction data (left) and X-direction data (right).	225
6-16	CAS of microphone measurement for four different conditions. Comparison between the encoder resolutions, $\Delta=0.1 \mu\text{m}$ (left) and $\Delta=1 \mu\text{m}$ (right), showing significant reduction of motor stationary noise.	225
6-17	CAS comparison between squarewave and sinewave commutation cases: Z-direction accelerometer (left) and microphone measurement (right) at $A_{max} = 25 \text{ m/s}^2$ and $V_{max} = 1 \text{ m/s}$ with non-skewed magnets.	228
6-18	CAS comparison between squarewave and sinewave commutation cases: X-direction accelerometer (left) and microphone measurement (right) at $A_{max} = 25 \text{ m/s}^2$ and $V_{max} = 1 \text{ m/s}$ with non-skewed magnets.	228
6-19	CAS of accelerometer measurements on stage side plate at $A_{max} = 25 \text{ m/s}^2$ and $V_{max} = 1 \text{ m/s}$ with skewed and non-skewed magnets both during acceleration (left) and constant velocity (right), showing stage eigen-modes excitation for both cases. Eigen-modes associated with area of rapid change in CAS.	229
6-20	CAS of microphone measurements from above stage at $A_{max} = 25 \text{ m/s}^2$ and $V_{max} = 1 \text{ m/s}$ with skewed and non-skewed magnets both during acceleration (left) and constant velocity (right) regions, showing stage eigen-modes excitation for both regions.	229
6-21	Spectrogram of microphone measurements during a half cycle of velocity profile with $A_{max} = 25 \text{ m/s}^2$ and $V_{max} = 0.4 \text{ m/s}$ with non-skewed magnets. Velocity profile commanded is overlapped in white to indicate acceleration/deceleration and constant velocity regions. The color-map shows sound pressure level (SPL) in dB re $P_{ref} = 20 \mu\text{Pa}$	231

6-22	Spectrogram of microphone measurements during a half cycle of velocity profile with $A_{max} = 25 \text{ m/s}^2$ and $V_{max} = 0.6 \text{ m/s}$ with non-skewed magnets. Color-map shows SPL in dB re $P_{ref} = 20 \mu\text{Pa}$	231
6-23	Spectrogram of microphone measurements during a half cycle of velocity profile with $A_{max} = 25 \text{ m/s}^2$ and $V_{max} = 1.0 \text{ m/s}$ with non-skewed magnets. Color-map shows SPL in dB re $P_{ref} = 20 \mu\text{Pa}$	232
7-1	Picture of fine-tooth motor installed on the stage testbed, showing four winding sections.	237
7-2	Schematic of fine-tooth linear motor lap winding configuration to measure the back EMF of the phase A coil in Section#3.	237
7-3	Measured back EMF of phase A coil in Section#3 of our new fine-tooth stator with non-skewed magnets, showing the zero-crossings with the interval of pole pitch, $\lambda_p = 20 \text{ mm}$. Numbers in circles are discussed in text.	238
7-4	Measured back EMF of phase A coil in Section#2 after defining the desired zero reference position, which is illustrated by a blue dot.	238
7-5	Measured back EMF of phase A coil in Section#2 with skewed magnets after defining the desired zero reference position, which is illustrated by a blue dot.	239
7-6	Squarewave commutation algorithm for a five-phase fine-tooth motor. Magnet track is shown at the desired zero reference position.	241
7-7	Schematic of position control loop with a plant of five-phase fine-tooth linear motor system and a PID (or lead-lag) controller.	244
7-8	Measured and simulated frequency responses of plant and loop return ratio with the fine-tooth motor, showing a crossover frequency of about 100 Hz and a phase margin of about 45°	245

7-9	Measured time response of cogging resonance when perturbed about a stable equilibrium showing the frequency of about 7.6 Hz, consistent with the low frequency resonance observed in the measured frequency responses.	245
7-10	Measured tracking performance of closed position control system following a smooth trajectory with maximum acceleration of 25 m/s ² and maximum velocity of 0.4 m/s.	246
7-11	CAS comparison of accelerometer measurements between Tecnotion motor and new fine-tooth motor, showing more than average of 90 % noise level reduction. Vibrational noises are measured for a stage cycle at $A_{max} = 25 \text{ m/s}^2$ and $V_{max} = 1 \text{ m/s}$ both during acceleration (left) and constant velocity (right) regions.	249
7-12	CAS comparison of microphone measurements between Tecnotion motor and new fine-tooth motor, showing more than average of 90 % noise level reduction. Acoustic noises are measured at $A_{max} = 25 \text{ m/s}^2$ and $V_{max} = 1 \text{ m/s}$ both during acceleration (left) and constant velocity (right) regions.	249
7-13	Overall noise level comparison for both vibrational and acoustic noises in all four motor cases experimented at $A_{max} = 25 \text{ m/s}^2$ and $V_{max} = 1 \text{ m/s}$. Ratio is presented for each noise with a reference level (1) of Tecnotion with non-skewed PM during an acceleration region.	250
7-14	Cogging force comparison between FEM simulation and experiment, both with non-skewed magnets. Cogging fundamental period of a tooth pitch, $\lambda_t = w_t + w_s = 4 \text{ mm}$	253
7-15	Spatial spectrum comparison of cogging force between FEM simulation and experiment, both with non-skewed magnets. Major component is the fundamental, as expected.	253

7-16 Spectrogram comparison of vibrational (left) and acoustic (right) noises of our new fine-tooth motor in Z-direction during a half cycle with $A_{max} = 45 \text{ m/s}^2$ and $V_{max} = 1.6 \text{ m/s}$, showing clear distinction between acceleration and constant velocity regions. Note cogging-driven noise at 400 Hz.	255
7-17 Spectrogram comparison of vibrational (left) and acoustic (right) noises of our new fine-tooth motor in X-direction during a half cycle with $A_{max} = 45 \text{ m/s}^2$ and $V_{max} = 1.6 \text{ m/s}$, showing clear distinction between acceleration and constant velocity regions. Note cogging-driven noise at 400 Hz.	255
7-18 Spectrogram comparison of vibrational (left) and acoustic (right) noises of our new fine-tooth motor in Z-direction during a half cycle with $A_{max} = 45 \text{ m/s}^2$ and $V_{max} = 2.0 \text{ m/s}$, showing clear distinction between acceleration and constant velocity regions. Note cogging-driven noise at 500 Hz.	256
7-19 Spectrogram comparison of vibrational (left) and acoustic (right) noises of our new fine-tooth motor in X-direction during a half cycle with $A_{max} = 45 \text{ m/s}^2$ and $V_{max} = 2.0 \text{ m/s}$, showing clear distinction between acceleration and constant velocity regions. Note cogging-driven noise at 500 Hz.	256
7-20 Spectrogram comparison of vibrational (left) and acoustic (right) noises of our new fine-tooth motor in Z-direction during a half cycle with $A_{max} = 45 \text{ m/s}^2$ and $V_{max} = 2.4 \text{ m/s}$, showing clear distinction between acceleration and constant velocity regions. Note cogging-driven noise at 600 Hz.	257
7-21 Spectrogram comparison of vibrational (left) and acoustic (right) noises of our new fine-tooth motor in X-direction during a half cycle with $A_{max} = 45 \text{ m/s}^2$ and $V_{max} = 2.4 \text{ m/s}$, showing clear distinction between acceleration and constant velocity regions. Note cogging-driven noise at 600 Hz.	257

7-22 Spectrogram of acoustic noise of new fine-tooth motor with non-skewed magnets during an increasing-velocity cycles with $A_{max} = 45 \text{ m/s}^2$ and $V_{max} = 1.6 \text{ m/s}$ to 2.2 m/s , showing cogging-oriented and velocity-dependent noise during constant velocity regions. Note varying frequency cogging-driven noise at 400, 450, 500, and 550 Hz. 259

7-23 Fine-tooth motor cogging force measurement comparison between non-skewed and skewed magnets, showing significant reduction in cogging with skewing. Cogging fundamental period equals a tooth pitch, $\lambda_t = w_t + w_s = 4 \text{ mm}$ 261

7-24 Spectrogram comparison of vibrational noises of our new fine-tooth motor between non-skewed (left) and skewed (right) magnets during a half cycle with $A_{max} = 45 \text{ m/s}^2$ and $V_{max} = 1.6 \text{ m/s}$, showing significant reduction of 400 Hz cogging-related noise during constant velocity region. 262

7-25 Spectrogram comparison of acoustic noises of our new fine-tooth motor between non-skewed (left) and skewed (right) magnets during a half cycle with $A_{max} = 45 \text{ m/s}^2$ and $V_{max} = 1.6 \text{ m/s}$, showing significant reduction of 400 Hz cogging-related noise during constant velocity region. 262

7-26 Spectrogram comparison of vibrational noises of our new fine-tooth motor between non-skewed (left) and skewed (right) magnets during a half cycle with $A_{max} = 45 \text{ m/s}^2$ and $V_{max} = 2.0 \text{ m/s}$, showing significant reduction of 500 Hz cogging-related noise during constant velocity region. 263

7-27 Spectrogram comparison of acoustic noises of our new fine-tooth motor between non-skewed (left) and skewed (right) magnets during a half cycle with $A_{max} = 45 \text{ m/s}^2$ and $V_{max} = 2.0 \text{ m/s}$, showing significant reduction of 500 Hz cogging-related noise during constant velocity region. 263

7-28	Spectrogram comparison of vibrational noises of our new fine-tooth motor between non-skewed (left) and skewed (right) magnets during a half cycle with $A_{max} = 45 \text{ m/s}^2$ and $V_{max} = 2.4 \text{ m/s}$, showing significant reduction of 600 Hz cogging-related noise during constant velocity region.	264
7-29	Spectrogram comparison of acoustic noises of our new fine-tooth motor between non-skewed (left) and skewed (right) magnets during a half cycle with $A_{max} = 45 \text{ m/s}^2$ and $V_{max} = 2.4 \text{ m/s}$, showing significant reduction of 600 Hz cogging-related noise during constant velocity region.	264
7-30	Spectrogram of acoustic noise of new fine-tooth motor with skewed magnets during an increasing-velocity cycles with $A_{max} = 45 \text{ m/s}^2$ and $V_{max} = 1.6 \text{ m/s}$ to 2.2 m/s , showing that cogging-oriented noises during constant velocity regions are significantly reduced.	265
7-31	Motor force performance comparison between conventional and new motors. Several experimental data are overlapped with simulation results, showing reasonable agreement.	267
7-32	Table of parameters required to obtain shear stress data points over unit power both for conventional and new motors.	268
7-33	Temperature response to a power input to show the thermal performance of our new fine-tooth motor. The orange curve with data points shows the temperature measurements and the black line is a fitted curve with a first order thermal model. Note that the ordinate shows the motor coil temperature increase relative to an initial temperature of 25°C	270
7-34	Simplified first order thermal model of RC circuit for the motor, where P , C_T , and R_T are the power source, thermal capacitance, and thermal resistance.	270
8-1	Network of nonlinear reluctances including the leakage paths between teeth to upgrade the hybrid layer model.	286

8-2 CAD design of the double-sided motor configuration (lower) augmented from the existing experimental testbed with the single-sided motor configuration (upper). 287

8-3 Proposed method of flipping the 1040-mm (41-in) base guide bar using two rotating wheels at the ends. 288

A-1 Drawing of the stage top plate. Page 1 of 2. 292

A-2 Drawing of the stage top plate. Page 2 of 2. 293

A-3 Drawing of the stage left-side plate. Page 1 of 2. 294

A-4 Drawing of the stage left-side plate. Page 2 of 2. 295

A-5 Drawing of the stage right-side plate. Page 1 of 2. 296

A-6 Drawing of the stage right-side plate. Page 2 of 2. 297

A-7 Drawing of the top holding magnet for preloading top air bearings. 298

A-8 Drawing of the side holding magnet for preloading side air bearings. 299

A-9 Drawing of the threaded stud for the top holding magnet to control the preloading force in the normal (Z) direction. 300

A-10 Drawing of the threaded stud for the side holding magnet to control the preloading force in the cross-scan (X) direction. 301

A-11 Drawing of the mounting plate for the conventional motor (TL18 by Tecnotion), also serving as the dynamometer upper plate. Page 1 of 3. 302

A-12 Drawing of the mounting plate for the conventional motor (TL18 by Tecnotion), also serving as the dynamometer upper plate. Page 2 of 3. 303

A-13 Drawing of the mounting plate for the conventional motor (TL18 by Tecnotion), also serving as the dynamometer upper plate. Page 3 of 3. 304

A-14 Drawing of the spacer, providing correct space for the double-sided stage configuration. The spacer also serves as the mounting plate for the shock absorbers. 305

A-15 Drawing of the stator laminations of our new fine-tooth motor. Page 1 of 2. 306

A-16 Drawing of the stator laminations of our new fine-tooth motor. Page 2 of 2.	307
A-17 Drawing of the dove-tail insert used to mount our new fine-tooth motor stator.	308
A-18 Drawing of the mounting plate for our new fine-tooth motor, also serving as the dynamometer upper plate. Page 1 of 4.	309
A-19 Drawing of the mounting plate for our new fine-tooth motor, also serving as the dynamometer upper plate. Page 2 of 4.	310
A-20 Drawing of the mounting plate for our new fine-tooth motor, also serving as the dynamometer upper plate. Page 3 of 4.	311
A-21 Drawing of the mounting plate for our new fine-tooth motor, also serving as the dynamometer upper plate. Page 4 of 4.	312
A-22 Drawing of the vertical (wide) and horizontal (narrow) magnets used in the magnet tracks of our new fine-tooth motor.	313
A-23 Drawing of the non-skewed magnet track of our new fine-tooth motor. Short version used in the single-sided motor configuration.	314
A-24 Drawing of the skewed magnet track of our new fine-tooth motor. Short version used in the single-sided motor configuration.	315
A-25 Drawing of the non-skewed magnet track of our new fine-tooth motor. Long version to be used in the double-sided motor configuration.	316
A-26 Drawing of the skewed magnet track of our new fine-tooth motor. Long version to be used in the double-sided motor configuration.	317

Chapter 1

Introduction

In the semiconductor industry, it is an essential process to print chips on silicon wafers using photo-lithography. Targeting to manufacture denser integrated circuits (ICs) at higher rates, lithography machine technology has been advancing rapidly, following the Moore's law of doubling the number of transistors per square inch on ICs every two years [1]. Together with the size shrinking, it has been demanded in the semiconductor industry to have higher speed of production. The linear motor stage in a state-of-the-art lithography scanner cycles to carry a wafer or photo-mask, also called a reticle, at tens of G's to achieve high throughput while keeping the position error within less than a nanometer at the same time.

There have been efforts to increase the reticle stage acceleration further by replacing iron-less Lorentz motors with iron-core permanent magnet motors since they produce higher shear stress (force divided by force-generating area in $[\text{N}/\text{mm}^2]$) and higher force density (force to moving mass ratio in $[\text{N}/\text{kg}]$). However, when conventional linear iron-core motors are used to cycle the reticle stage, it can be observed that such motors emit a significant amount of noise, which is transmitted in both structural- and air-borne pathways. Such vibrations disturb the lens and metro-frame, thereby deteriorating the system accuracy performance. Thus, the current lithography machines typically use iron-less Lorentz actuators for the reticle stage [2].

In the pursuit of smaller chip size and faster speed of production, the next-generation EUVL (Extreme Ultra-Violet Lithography) machines require higher ac-

celeration than the current DUVL (Deep Ultra-Violet Lithography) scanners with even tighter accuracy requirements. These industrial needs motivates the design of a new high force, but quiet motor. The main focus of this thesis is thus to design and test a new linear iron-core permanent magnet motor to simultaneously achieve high force and low noise. We have designed and constructed a new five-phase iron-core permanent magnet motor, called a fine-tooth motor, which has the magnetic design features of fine teeth, narrow slots with high aspect ratio, and Halbach magnet array. With our new fine-tooth motor, we have successfully demonstrated the potential to significantly reduce the vibro-acoustic noise of iron-core motors while substantially enhancing the shear stress density, compared to conventional 3-4 combination iron-core motors. By simultaneously providing high force and low noise, our new fine-tooth motor design can help enable higher throughput without compromising required system accuracy in the semiconductor industry.

In this chapter, we first present an overview of the contributions of the thesis. We then present prior art for the motor noise issues of rotary machines and also for high force/torque machines. In the following section, the vibro-acoustic noise of linear motors is discussed with our hypothesis on the noise mechanism. We then outline the overview of the thesis at the end of this chapter.

1.1 Accomplishments and Contributions

We summarize the accomplishments and contributions of this thesis in this section. The detailed results and explanations are discussed throughout many chapters of this thesis.

- Experimentally investigated the causes of vibro-acoustic noise emitted by a conventional linear iron-core permanent magnet motor.
- Designed a new linear iron-core motor to achieve lower noise while producing higher force than a conventional motor.

- Constructed a new linear motor, which consists of a five-phase fine-tooth deep-slot stator armature with double-layered full-pitch concentrated windings and non-skewed/skewed moving magnet tracks with the Halbach magnet array pattern.
- Experimentally demonstrated that our new motor outperforms the conventional 3-4 combination iron-core motor in terms of high force and low noise.
- Designed and constructed an experimental linear stage testbed to investigate the motor noise issue of both the conventional motor and our new motor in both the single- and double-sided configurations.
- Developed a modeling method, called a hybrid layer model, for the new linear iron-core permanent magnet motor. This modeling method is adapted from a rotary motor model invented by Dr. Angle at MIT [3].

1.2 Prior Art

Acoustic noise and the associated vibration are the potentially troubling characteristics of electrical machines. There have been a number of research works to consider this issue in rotary motors, including variable-reluctance motors (VRMs) [4, 5], switched reluctance motors (SRMs) [6–8], permanent-magnet synchronous motors [9, 10], and induction machines [11, 12]. However, not as much work has been done for linear machines, where the major causes of noise generation might be different from rotary motors due to structural differences. In this thesis, we explore the vibro-acoustic noise issue of linear motion iron-core permanent-magnet motors to design, build, and test a high force linear motor with low vibro-acoustic noise.

The severity of the vibro-acoustic noise problem depends on the types of motors and their applications. One exemplary case where the vibro-acoustic noise becomes detrimental is iron-core permanent-magnet linear motors operating at high acceleration and targeting for high accuracy and high throughput. Iron-core permanent-magnet linear motors have the potential for high force density. However, such motors

have the problem of managing the large normal and tangential forces acting between the permanent magnets and the iron. These forces can introduce vibrations and acoustic noise. In this thesis, we find root causes of the vibro-acoustic noise of linear iron-core permanent-magnet motors, and create magnetic designs to achieve high force with low noise.

Within these thesis objectives, we review in this section relevant prior art for the acoustic noise issue of rotary machines (Section 1.2.1) and for high torque/force motors (Section 1.2.2).

1.2.1 Acoustic Noise Issue of Rotary Motors

Acoustic noise and vibration of electric motors can be generated by many causes including magnetic, mechanical, electrical, and fluid dynamical sources [13,14]. A list of possible causes is organized into these four categories in Figure 1-1.

Cameron et al. [4] provide an experimental study of the acoustic noise of a doubly salient four-phase variable-reluctance motor (VRM). They show that the major noise source of such a machine is the radial deformation of the stator caused by the radial magnetic force. The emitted noise is observed particularly strongly when the radial force harmonics excite the stator natural resonances. They suggest to introduce a dither into the fire angle of the motor drive current waveforms to spread the spec-

Magnetic	Mechanical	Electronic	Fluid dynamic
- Force harmonics	- Bearings	- Switching harmonics	- Air/water cooling
- Cogging	- Unbalanced parts	- Encoder quantization	- Any windage
- Magnetostriction	- Vibration modes (stator or rotor)	- Interpolation error	
- Moments	- Cables		
- Lorentz force (on windings in slots)			

Figure 1-1: Possible sources of the motor noise problems.

trum of noise excitation so as not to excite the stator harmonics, thereby reducing the acoustic noise. The same type of four-phase 8/6 (8 stator poles and 6 rotor poles) switched reluctance motor (SRM) is studied for the emitted acoustic noise in [6, 7] where the control of phase current pulses is discussed as a method to reduce the acoustic noise and associated vibration. Since the stator's structural frequency is one of the main sources of the vibro-acoustic noise in rotary machines, there have been efforts to predict the natural modes of the motor stator. Colby et al. [8] present an approximate formula to predict the stator eigen-frequencies using the stator lamination dimensions and material properties. Girgis and Verma [15] give the general frequency equation of the motor stator using the energy method. The effect of varying stator lengths on the stator natural frequencies are considered in [16–18].

There are also relevant prior art for the noise issue of other types of rotary machines. Islam and Husain [9] argue that the normal component of the electromagnetic force field in the motor air gap causes the radial vibration of the stator structure in permanent magnet synchronous motors. They provide an analytical model to calculate the radial deformation of the stator so as to predict the noise and vibration. Asano et al. [10] discuss that permanent magnet synchronous motors with lumped windings produce higher vibration than those with distributed windings. They show that vibration and noise can be reduced by having a partially enlarged air gap to smooth the radial magnetic stress in the air gap. Cassoret et al. [11] discuss the noise of induction machines and propose a noise reduction method of injecting controlled current harmonics in the stator windings so as to generate opposing forces to cancel the force components contributing the noise.

While the strong radial forces together with the stator vibrational modes are considered the main culprit of the vibrational and acoustic noise of rotary electric machines, there have been research works to explore other possible noise sources. Zhu et al. [19] discuss a direct torque control approach to reduce the cogging and the associated motor vibration of permanent magnet brushless motors. Hwang et al. [20] provide a teeth paring method of stacking two armature teeth with different widths to reduce the cogging torque and related acoustic noise. They report an acoustic

noise drop of 3.1 dB by this method. Note that the cogging reduction methods for permanent magnet machines have been researched over many decades regardless of direct relation to the motor noise issue. Various classical techniques for cogging torque minimization are discussed in [21–23] including skewing armature lamination stacks or magnets, choice of magnet pole arc width, dummy teeth/slots, and control techniques. In [21] especially, Jahns and Soong provide clear definitions of the pulsating torque, which consists of the cogging torque and ripple torque. There is an interesting cogging reduction method, called the pole-shifting, where the magnets in permanent magnet machines are shifted non-symmetrically [24–26]. This technique can be considered as a mechanical dither (counterpart of electric dither method presented in [4]) to spread the slot harmonics, thereby reducing the torque/force fluctuation.

Magnetostriction, a property of ferromagnetic materials to deform the material itself when magnetized [27], can be also considered as a noise source. The transformer noise, also known as electric hum, is caused by magnetostriction [28–31], and such noise can also be present in electric motors. The effect of magnetostriction on the vibration of induction machines is discussed in [32,33] where the results indicate that the contribution of the magnetostriction effect to the induction motor noise is minor.

In the mechanical sources of the motor noise, there can be several auxiliary sources other than the vibrational modes of the motor stator [13,14]. The use of rolling-element bearings requires mechanical contact, thereby possibly causing vibrational and acoustic noise. Rotor unbalance can also be a source of noise in rotary machines by causing eccentricity and thus rotor vibration. In addition, electrical cable dynamics might also be a cause of motor noise, especially at high acceleration and high speed operations.

There are also various electronic noise sources. When PWM switching drives are used, the harmonics of high bus voltage switching might generate vibrational and acoustic noise. Techniques to reduce switching harmonics are introduced in [34,35] for the random pulse width modulation method and in [36] for spreading switching harmonics by pulse frequency modulation. In induction motors [37,38] and switched reluctance motors [6], the converter and commutation algorithm become a significant

electric noise source, especially when the rate of phase current change is high, the current amplitude is high, and the exciting phase current contains frequency components coinciding with the stator natural frequencies. Krishnan and Vijayraghavan [39] present various noise reduction methods for switched reluctance actuators including current waveform shaping, two-step commutation to lower the rate of current change, and introduction of dither in the firing turn-on/off angles, which is also discussed in [4, 5]. The encoder quantization and interpolation error can be also an electronic noise source. In fact, we found in this thesis work that relatively coarse encoder quantization can be a major noise source for a conventional linear iron-core motor even when the motor is stationary. The coarse quantization error together with a high-loop-gain position controller exerts impulsive forces on the moving stage, thereby causing vibrational and acoustic noise. We discuss this issue in detail in Chapter 6. When a cooling system is used in a motor either by air or liquid, it can create fluid dynamic noise. However, in the scope of this thesis, not much of consideration of this noise source is taken, since our prototype stage system does not include a cooling mechanism or any sorts of fluid dynamical noise sources.

As presented in this subsection, there have been a number of research works conducted on the noise issue of rotary motors over many decades. However, not as much work has been done for the noise issue of linear motors. In this thesis, we study the vibro-acoustic noise of linear iron-core permanent magnet motors, and provide a new promising motor design to resolve such issue. In Section 1.3, we discuss our hypothesis on the noise causes of linear iron-core motors. In Chapters 3 and 7, we present the magnetic design of our new linear iron-core motor and its experimental results on the noise reduction, respectively.

1.2.2 High Acceleration Motors

While achieving motor noise reduction, we also require for high force performance. We thus discuss in this subsection the prior art of high torque/force motors. Farve [40] presents design process and experimental results of a low-mass high-torque low-loss permanent magnet synchronous motor for the MIT Cheetah robot or for a quadruped

robot in general targeting high speed motion. The motor design is based on a simplified calculation of torque by fundamental electromagnetic principles. Since such motors are used for the shoulder and knee actuators of the MIT Cheetah, the total mass of both stator and rotor needs to be reduced while also increasing the torque. She reports a torque increase of 60% while reducing the motor mass by 23%, compared to a conventional permanent magnet motor of similar size, which the MIT Cheetah used at the time. Angle [3] takes this work further to design and test a higher-torque and lower-mass permanent magnet (PM) motor for the Cheetah. He develops a hybrid modeling method to optimize the rotary PM machine, which becomes the base work of our hybrid layer model for the linear iron-core PM motor discussed in Chapter 3 of this thesis. He reports an order of magnitude increase in torque density (37% mass reduction and 180% torque increase) compared to a commercial off-the-shelf motor of similar size. Banerjee et al. [41] show a design for a high torque density PM synchronous motor. They describe the theoretical limit of torque density in a surface-mounted PM motor within the given limitations of peak magnetic flux due to material saturation and exciting RMS (root mean square) currents due to losses. They suggest a fine grain commutation method of individually controlling currents to ideally utilize all harmonics of stator and rotor magneto-motive forces (MMFs) to maximize the torque performance.

As for linear high-force motors, various tubular linear motors have been studied over many decades. Iron-cored tubular permanent magnet (PM) linear motors are introduced in [42, 43], a surface wound tubular PM linear motor is discussed in [44] with the configuration of moving magnets and stationary coils, an iron-less tubular PM linear motor is studied in [45] with long moving coils and short stationary Halbach magnet array, and tubular linear induction motors are introduced in [46, 47]. Sato et al. [48] present the design and test of high-acceleration moving permanent magnet linear motor in a double-sided configuration. By reducing the mass of the moving magnet track without back iron, this motor design shows a high force density and acceleration. However, due to the magnetic configuration of 4 coils/poles and 2 magnets with 2-phase commutation, a significant force fluctuation is observed. This

high force ripple issue is partially resolved in [49, 50] by modifying the magnetic configuration to 4 coils/poles and 3 magnets with 4-phase current commutation, which is a counterpart of the conventional 3-4 combination (3-phase-4-magnet) motor as discussed in Chapter 2 of this thesis.

Although there have been a number works on high torque/force motors over many years, it is difficult to find a research work that tries to generate high force while achieving low motor noise. In this thesis, we present the magnetic design of a new linear iron-core permanent magnet motor which can simultaneously provide high force and low noise. The magnetic design approach and design parameter selection process of our new motor is discussed in detail in Chapter 3. The noise and force performance of our new motor is experimentally validated in Chapter 7.

1.3 Hypothesis on Noise Mechanism of Linear Motor

In this section, we discuss our hypothesis on the noise mechanism of linear iron-core permanent magnet motors. Figure 1-2 shows the schematic configuration of a conventional motor with moving magnets and stationary armature. When such a motor is operated, it experiences two major forces: one is the coil-driven force and the other is a force disturbance such as the cogging. Note that the cogging force is a force fluctuation caused by the magnetic interaction between the iron-core teeth (geometric saliency) and the magnets. Depending on the magnetic design of a motor, these forces can have high harmonics. The high force harmonics can vibrate the moving stage, which is especially severe when the stage dynamics are excited. This stage vibration can be transmitted through the system structure, and also can radiate as acoustic noise as illustrated in Figure 1-2.

Based on this speculation, we focus on the noise sources of strong magnetic force harmonics, cogging force, mechanical dynamics of rotor (or moving stage), and encoder quantization error among many possible causes listed in Figure 1-1. These sources are considered to be major culprits of the linear motor noise since they can cause significant vibrations on the moving stage. Our hypothesis is elaborated further

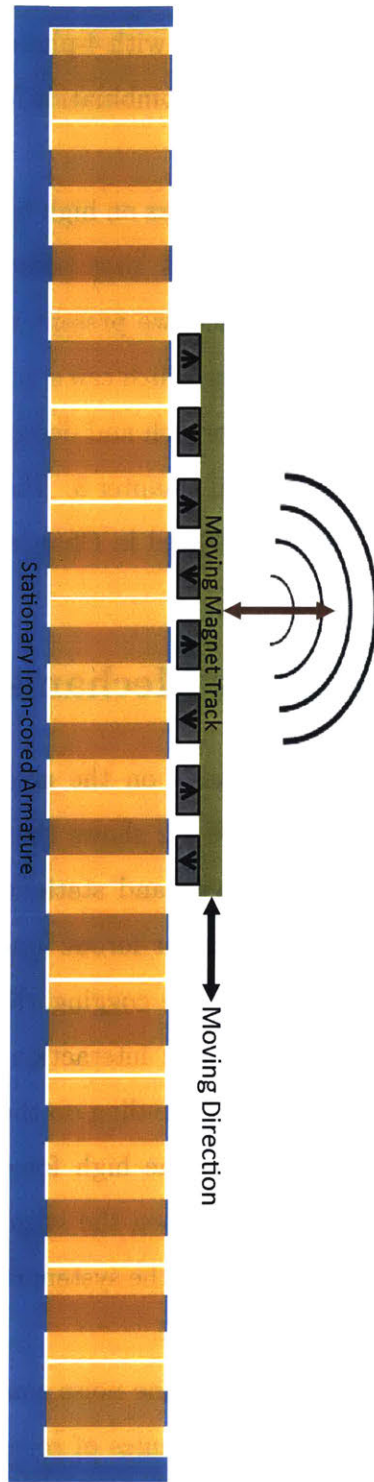


Figure 1-2: Hypothesis on the mechanism of the vibro-acoustic noise in linear iron-core permanent magnet motors.

in Chapters 2 and 3 for the conventional motor design and for our new motor design, respectively. Various experiments are conducted to investigate the noise causes using both the conventional linear iron-core motor and our newly-designed motor. Chapters 6 and 7 provide relevant experimental results and measured data to validate our hypothesis discussed in this section.

1.4 Thesis Overview

In this thesis, we mainly focus on the design, construction, and test of a new linear iron-core permanent magnet motor that simultaneously produces high force and low noise. We speculate that the major source of the linear motor noise is the high force harmonics vibrating the stage and thus radiating the acoustic noise. We first study the magnetic design of a conventional 3-4 combination linear iron-core permanent magnet motor to understand the force harmonic content of such a motor design. We then take a different design approach of having multiple fine teeth closely packed together with deep slots to reduce the force harmonics in both the generated force and the cogging force while enhancing the thrust performance. This new linear iron-core motor, which we call a fine-tooth motor, is built and tested to experimentally demonstrate the potential for the higher shear stress density and lower vibro-acoustic noise.

We briefly outline the overview of the thesis in this section with a few exemplary outcomes and results. More details are discussed in each corresponding chapter of the thesis.

1.4.1 Conventional Linear Iron-core Motor

We present studies of a conventional linear iron-core motor in Chapter 2 in order to understand its force harmonic content and expected motor noise. The magnetic design of a conventional motor has 3 coils/poles interacting periodically with 4 magnets to generate a force. This is why such a motor is often called a 3-4 combination motor. Figure 1-3 shows a picture of the stator armature of such a conventional three-phase

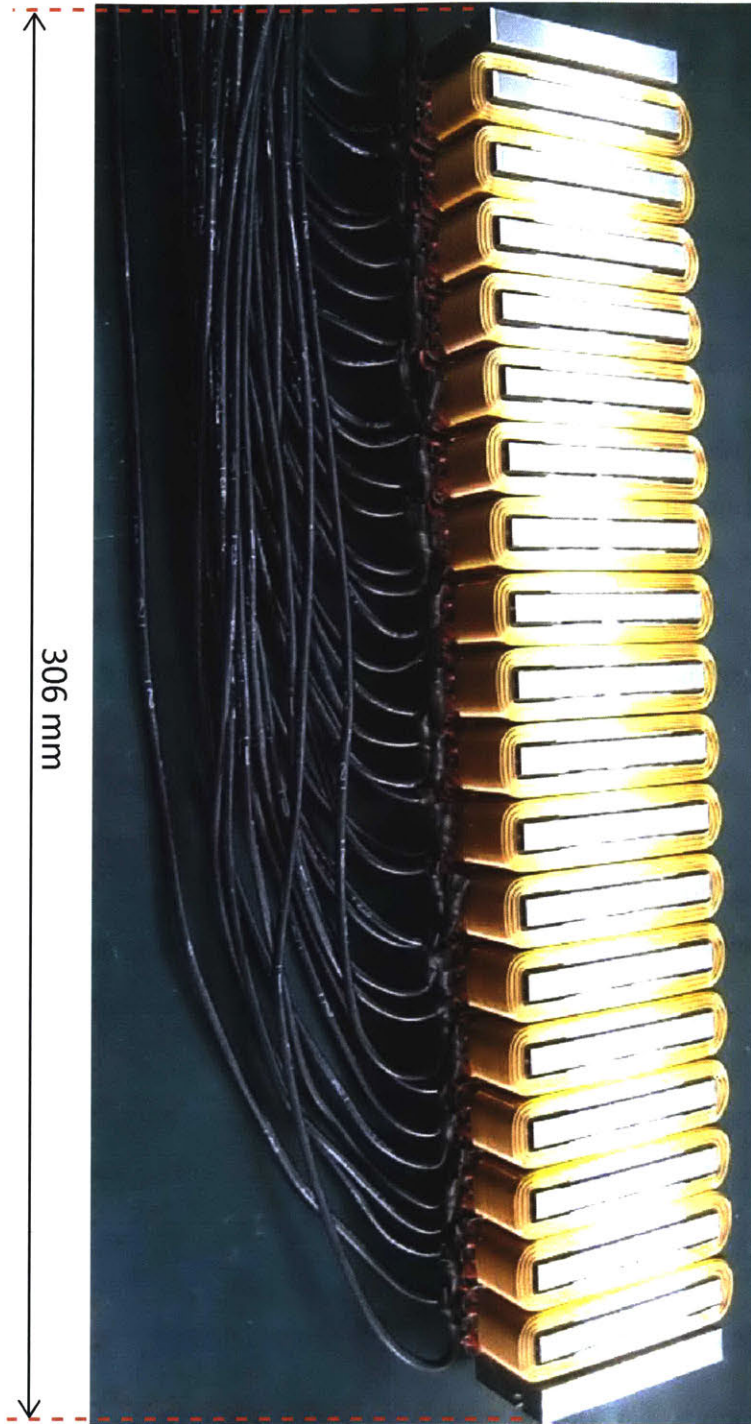


Figure 1-3: The stator armature of the conventional linear iron-core motor, TL18 by Tecnotion. Photo courtesy of Tecnotion.

iron-core motor we use, TL18 by Tecnotion. As can be seen in the figure, the iron-core teeth are widely separated from each other, creating a large slot space for the lumped phase windings. In Chapter 2, we discuss 1) the effect of these thick teeth on the stator magneto-motive force (MMF) waveform, 2) how the stator MMF contains high harmonics, and 3) how such a motor design generates high force harmonics together with the rotor (moving magnet track) MMF wave generated by the conventional magnet array. We also provide an analysis of the expected motor performance of the conventional linear iron-core motor. The motor force is predicted by the finite element method (FEM) in terms of cogging force, force ripple, and their spectral components so as to discuss the expected motor noise.

1.4.2 New Motor Design and Construction

In Chapter 3, we describe a new linear motor design approach of having fine teeth, narrow deep slots, multiple phases greater than the conventional three phases, and a moving Halbach magnet array. Such a magnetic design can produce smoother stator and rotor MMF waveforms with less harmonic content, thereby generating less force harmonics while enhancing the shear stress density. We call our new motor a fine-tooth motor. For the new motor design, we adapt and develop the hybrid layer model (HLM) for our new fine-tooth linear iron-core permanent magnet motor. We use this hybrid layer model together with the finite element method (FEM) to optimize the design parameters of our new motor. We provide the details on the hybrid layer model in Chapter 3, where the design process is also described in detail.

The finalized magnetic design of our new fine-tooth motor is provided together with the expected force performance in terms of shear stress density and acceleration. Our new fine-tooth motor shows significant potential to outperform the conventional 3-4 combination motor. We also discuss the construction of our new fine-tooth motor in Chapter 3 including the stator laminations, windings, wirings, cabling, and the Halbach magnet array assembly. Figure 1-4 shows photos of the stator armature of our new fine-tooth motor in both top and side views. More pictures of the constructed fine-tooth motor are presented in Chapter 3 along with its performance predictions.

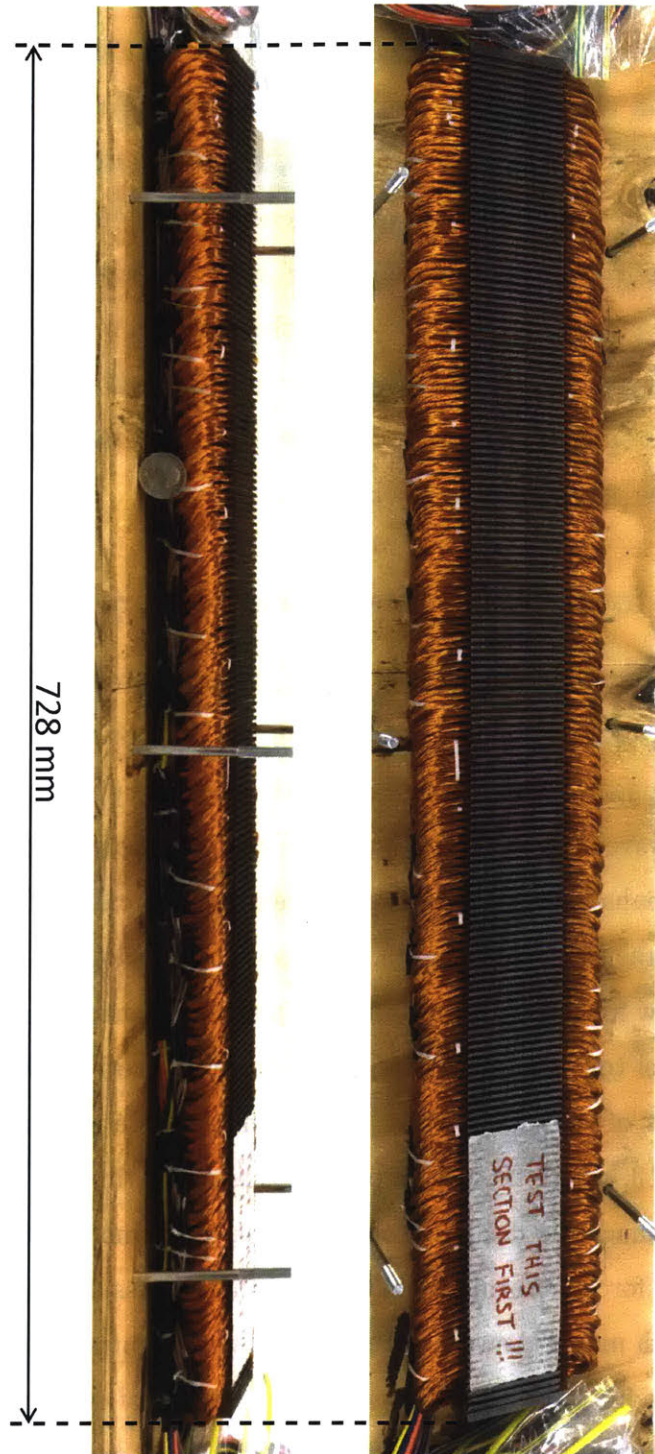


Figure 1-4: Pictures of the stator armature of our new fine-tooth motor. The right photo shows the top view and the left one the side view. A U.S. quarter coin is for the size reference.

Note that all the relevant part drawings of our new fine-tooth motor are given in Appendix A.

1.4.3 Testbed Design and Construction

In order to investigate the motor noise issue, an experimental linear stage testbed is designed and constructed. In Chapter 4, we discuss various testbed designs to fulfill necessary functionalities such as 1) hardware flexibility to accommodate both the conventional motor and our new fine-tooth motor in either a single- or double-sided stage configuration, 2) direct force measurement by a customized dynamometer, and 3) the usage of air bearings to eliminate the noise source caused by mechanical contact in the bearings and thus to isolate the magnetic noise sources. The testrig design variants are categorized into four groups depending on the motor's magnetic configuration of which part is moving or stationary and which is long or short. We choose to work with a moving short magnets with stationary long armature configuration mainly to achieve high acceleration and reduced cabling feeds to the stage. The details of the testbed design selection are provided in Chapter 4.

Based on the finalized design, the experimental linear stage testbed is built. We present the construction details in Chapter 5 to describe the essential functions of the testbed. We also discuss in that chapter the necessary hardware and assembly modifications to accommodate our new fine-tooth motor, whose dimensions are different from the conventional motor. Figure 1-5 shows photos of our experimental single-sided linear stage testbed with the conventional motor (right picture) and with our new fine-tooth motor (left picture). More relevant photos of the hardware components and the whole testbed setup are provided in Chapter 5. The drawings of the components used in the experimental testbed are given in Appendix A, and the vendors and manufactures we worked with are listed in Appendix B.

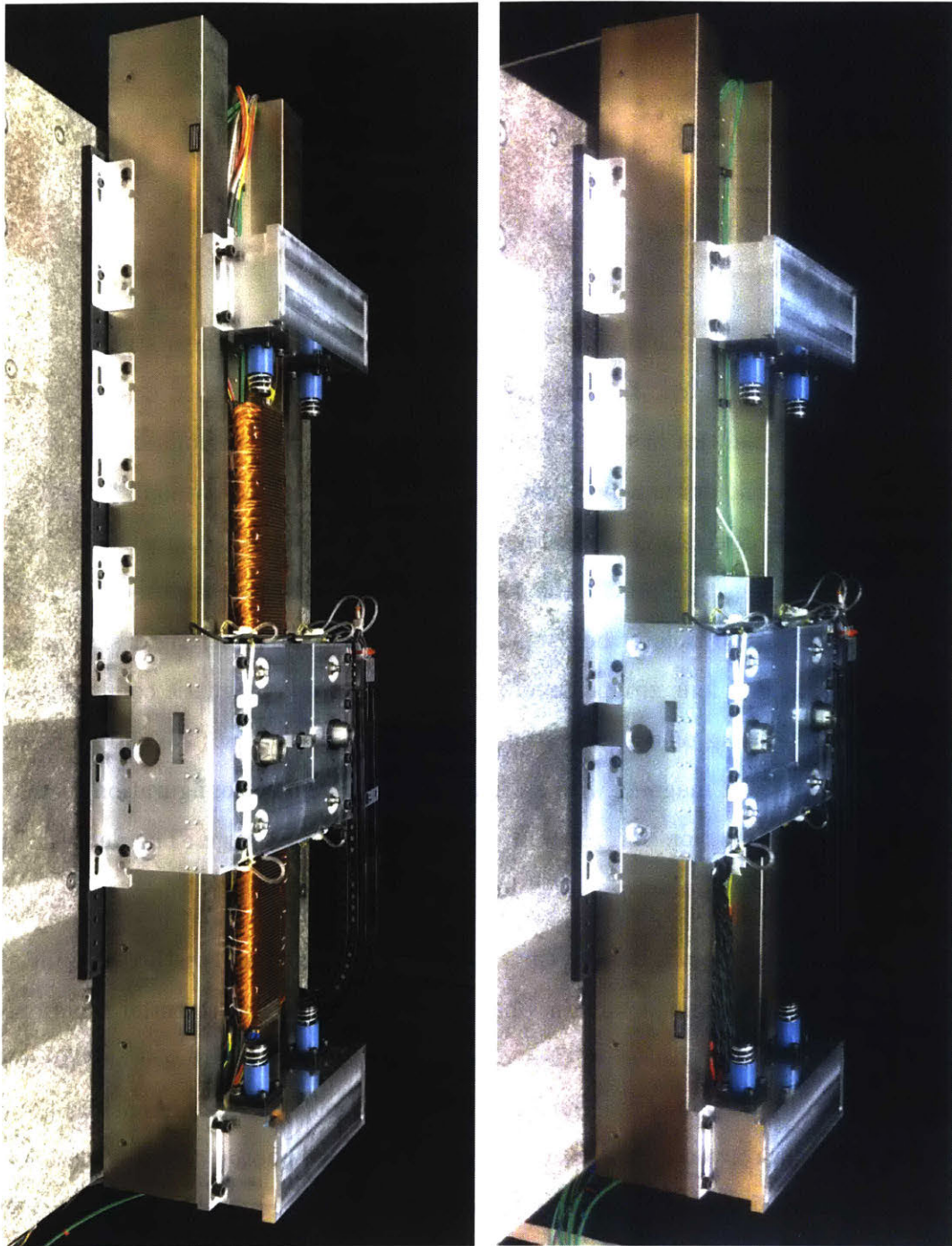


Figure 1-5: Pictures of the experimental linear stage testbed with the conventional 3-4 combination motor (right) and our new fine-tooth motor (left).

1.4.4 Experimental Results

We conduct various experiments on both the conventional motor and our new fine-tooth motor to 1) investigate the motor noise issue and 2) validate the performance of our new motor, as compared to the conventional motor. In Chapter 6, we describe the commutation algorithm and the position control of the conventional three-phase linear iron-core motor. We then present the experimental results on the motor noise of the conventional linear iron-core permanent magnet motor, TL18 by Tecnotion. The acoustic noise observed even when the stage is stationary is first investigated. This stationary noise is caused by relatively coarse encoder quantization error ($1 \mu\text{m}$), and is solved by upgrading the encoder to have a finer resolution ($0.1 \mu\text{m}$). We experimentally demonstrate significant reduction of this motor stationary noise and present relevant test data in Chapter 6. As described in Chapter 2, the conventional motor shows significant vibrational and acoustic noise during cyclic operation for both the acceleration and constant velocity regions due to high force harmonics. The measured data of both the vibrational and acoustic noise are shown in Chapter 6.

In Chapter 7, we present experimental results on the vibro-acoustic noise of our new fine-tooth motor. We first discuss in this chapter the five-phase commutation algorithm and the position controller design for our new fine-tooth motor. The same experiments as presented in Chapter 6 are conducted to compare the noise experimental data to the conventional motor. Figure 1-6 shows the comparison of the cumulative amplitude spectrum (CAS) of the measured acoustic noise between our new fine-tooth motor (green curve) and the conventional motor (black curve). Note that the cumulative amplitude spectrum (CAS) is the standard deviation integrated over frequencies [51, 52]. The value at the end of the CAS curve, therefore, shows the total standard deviation in the chosen bandwidth, which is up to 5 kHz for the measured acoustic noise in Figure 1-6. The CAS data shows that our new fine-tooth motor has an acoustic noise reduction of 93 % in Pascals as compared with the conventional motor in the acceleration region with both using non-skewed magnets. In terms of the sound pressure level (SPL), this significant noise reduction from 83 dB

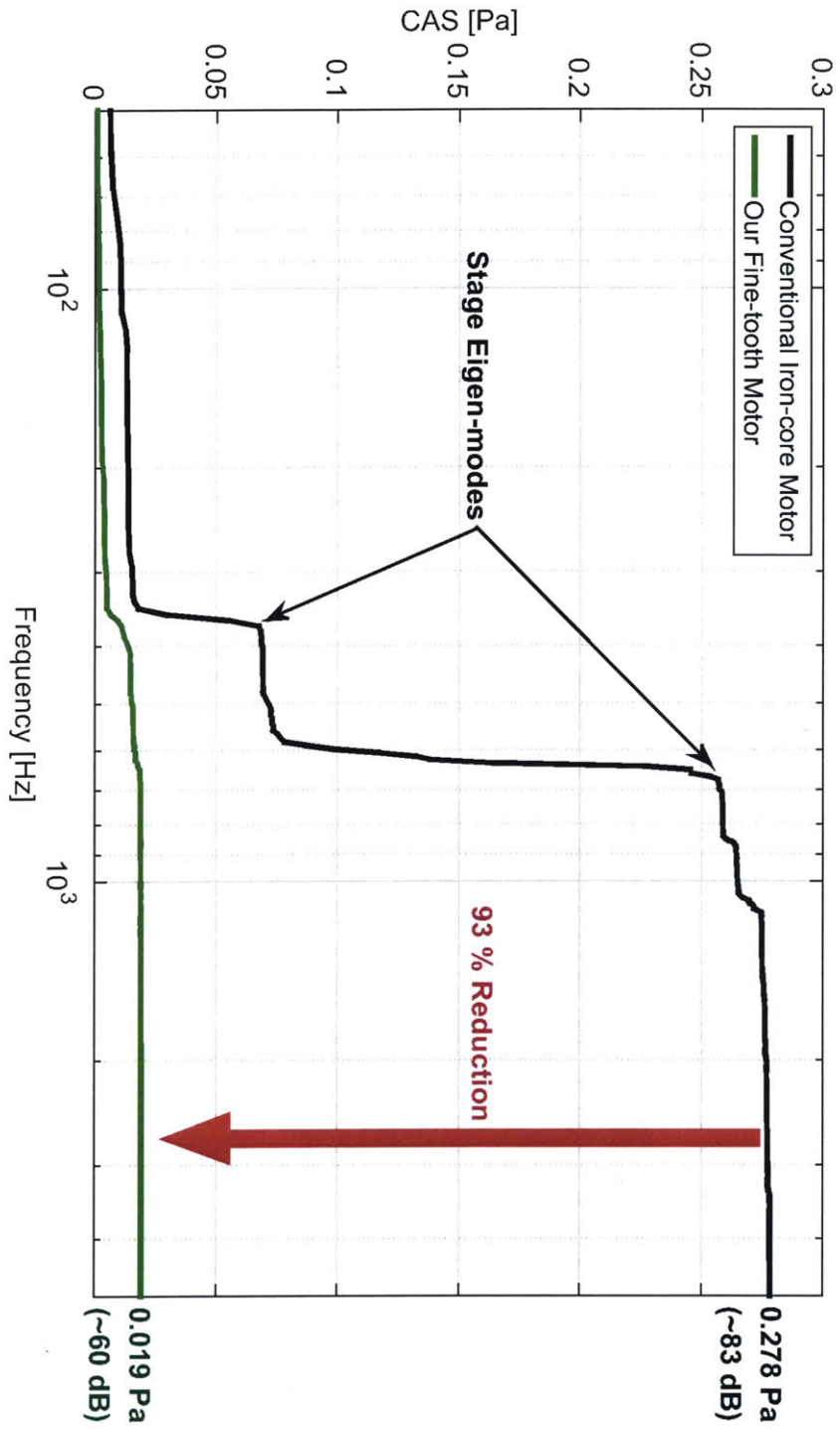


Figure 1-6: Cumulative amplitude spectrum (CAS) of the measured acoustic noise from both the conventional 3-4 combination motor (black curve) and our new fine-tooth motor (green curve). Noise measured with non-skewed magnets during an acceleration period.

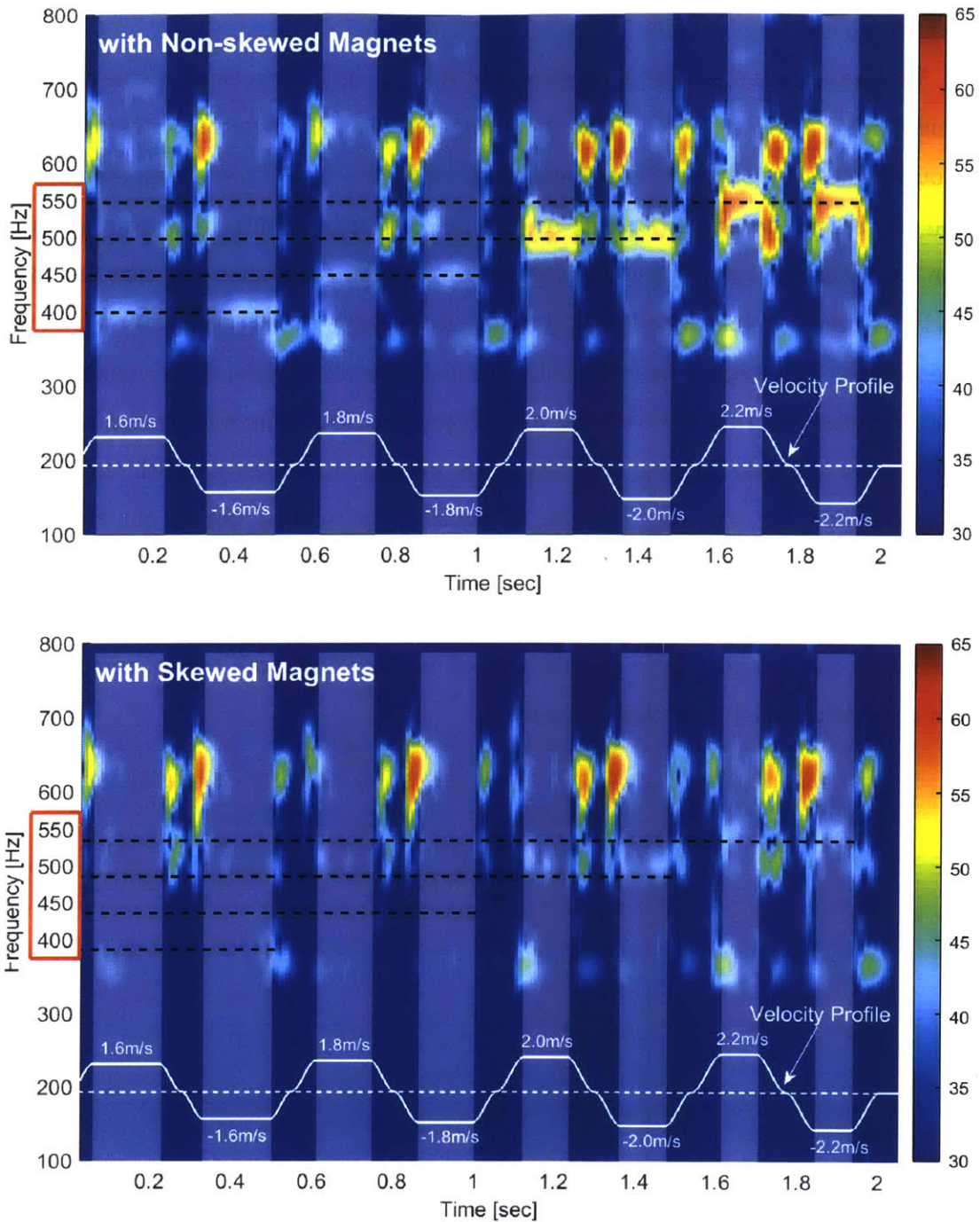


Figure 1-7: Spectrogram comparison of the measured acoustic noise of our new motor with the non-skewed (upper) and skewed (lower) magnets. The cogging-oriented noise during constant velocity regions (brighter portions) is significantly reduced by using the skewed magnets due to the fine-tooth motor design. The commanded velocity profiles are shown in white.

to 60 dB is qualitatively equivalent to the noise difference we feel between a big truck passing by and a quiet office.

We also discuss the cogging-oriented and velocity-dependent noise of our new fine-tooth motor in Chapter 7. Figure 1-7 compares the spectrograms of the measured acoustic noise by our new fine-tooth motor with the non-skewed magnets (upper) and the skewed magnets (lower). As can be seen in the figure, the noise behavior can be distinguished between the acceleration/deceleration regions (darker portions) and the constant velocity regions (brighter portions). In the acceleration periods, the noise by the stage dynamics excitations is dominant while it is the cogging noise that dominates during the constant velocity periods. With the non-skewed magnets, we observe the clear cogging noise with the velocity-dependency. With the skewed magnets, however, the cogging noise is significantly reduced due to our fine-tooth motor design. More relevant data is presented in Chapter 7 to demonstrate a low noise performance of our new motor. We also provide in Chapter 7 the experimental validation on the motor force performance of our new fine-tooth motor, compared to the conventional 3-4 combination motor.

Chapter 2

Conventional Linear Iron-core Permanent Magnet Motor

This chapter discusses studies of the conventional linear iron-core motor. We first present the magnetic design of the conventional 3-4 combination linear motor, and discuss how such a motor generates relatively high force harmonics which result in vibrations and acoustic noise as hypothesized in Chapter 1. We also introduce in the first section the commercial linear iron-core motor (TL18 by Tecnotion) we use.

In the next section, we present the motor performance prediction of the conventional motor using the finite element method (FEM). We use a 2D finite element (FE) tool, called FEMM [53]. We discuss the finite element model of the conventional linear iron-core motor, and present a method to capture the skewed magnet effects even with a 2D FE tool. The motor's cogging force and force ripple are calculated using the FEM model so as to predict the force harmonic contents of the conventional 3-4 combination motor. Note that the cogging is a force fluctuation caused by the magnetic interaction between the iron-core teeth and the magnets with no phase coils energized and is thus largely independent of excitation current. The force ripple, on the other hand, is a force variation observed when the phase coils are energized, and is thus approximately proportional to excitation current. Using the predicted motor performance, we discuss the expected vibro-acoustic noise characteristics of the conventional linear iron-core motor at the end of this chapter, followed by a summary.

2.1 Linear 3-4 Combination Motor

The conventional linear iron-core motor consists of two parts: 1) an armature with iron-core teeth and 2) a permanent magnet array with back iron. The magnetic configuration of such a motor can vary depending on which part is long or short and which is moving or stationary. We use the configuration of moving short magnet with stationary long armature. The details on these various magnetic configurations and how we choose one are discussed in Chapter 4.

Figure 2-1 shows pictures of the conventional 3-phase linear iron-core motor, TL18 by Tecnotion, with the magnetic configuration of moving short magnet and stationary long armature. As can be seen in the figure, the armature stator of TL18 contains a total of 18 lumped phase windings. Note that the stator armature is customized

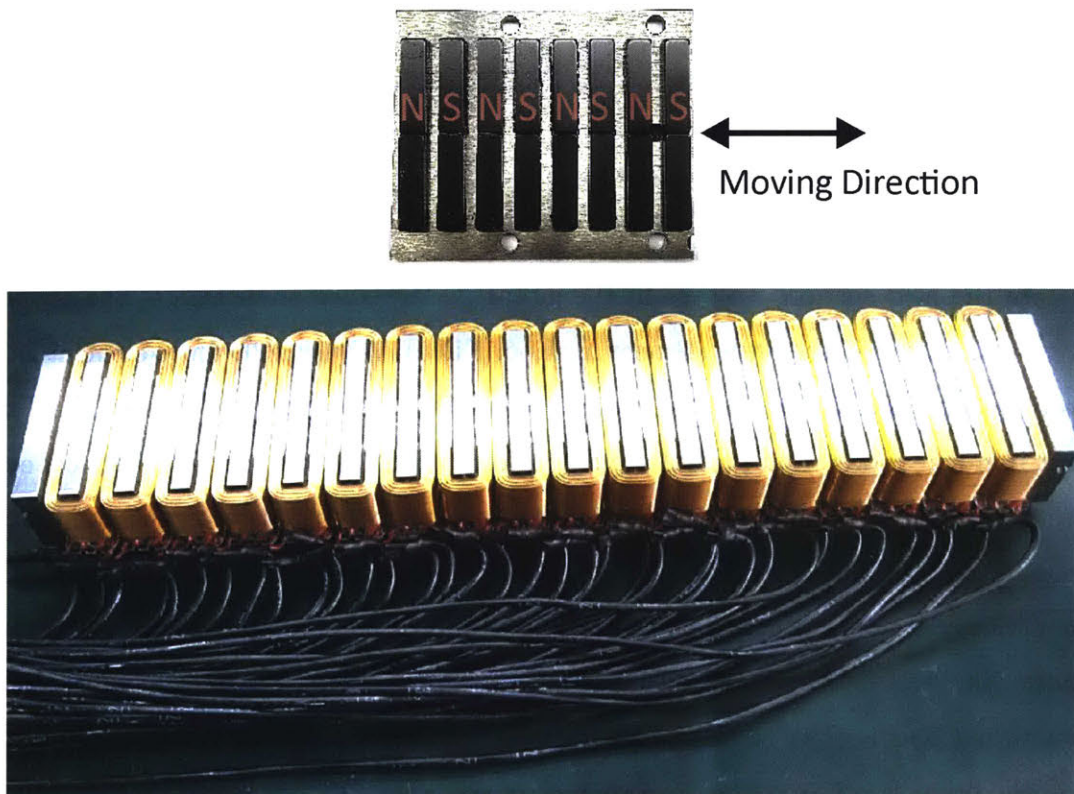


Figure 2-1: Pictures of a conventional 3-4 combination linear iron-core motor, TL18 model by Tecnotion. Moving magnet track (upper) and stator armature (lower). Stator photo courtesy of Tecnotion.

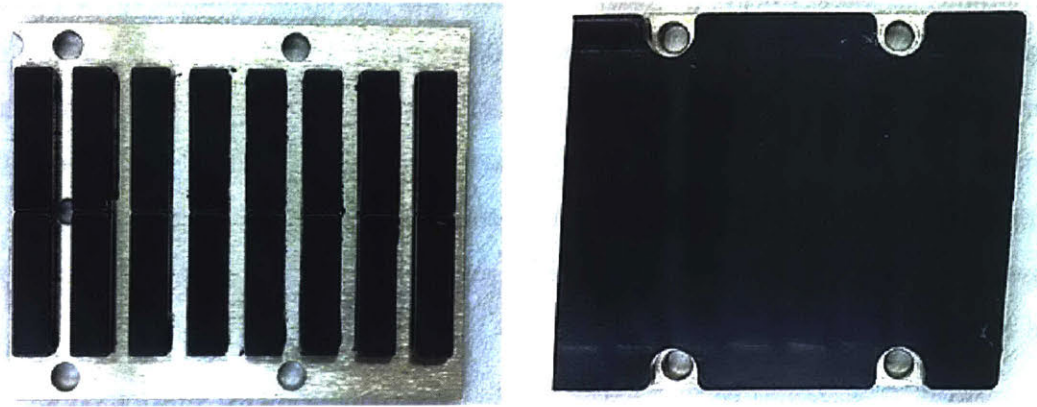


Figure 2-2: Pictures of magnet track of the conventional 3-4 combination linear iron-core motor. Non-skewed magnet track (left) and skewed magnet track (right).

for us by Tecnotion by bringing out leads for each motor coil. This allows the individual winding coils to be independently driven by multiple power amplifiers so as to distribute the driving power. We discuss the details of the power electronics and its connections in Chapter 5. The moving magnet track has a conventional array pattern of N-S-N-S. We use both non-skewed and skewed magnet tracks for the motor performance prediction in this chapter, and also for the hardware experiments discussed in Chapter 6. The pictures of both non-skewed and skewed magnet tracks (TL18 by Tecnotion) we use are shown in Figure 2-2. Note that the skewed magnet track is a commercial off-the-shelf product by Tecnotion so that it has the cover while the non-skewed one is customized and does not have the cover. The magnet type and size are, however, the same for both the non-skewed and skewed magnet tracks.

In this section, we discuss the magnetic design of the conventional linear iron-core motor. Specifically, the magneto-motive force (MMF) waveforms for both the stator armature and the magnet track are presented so as to discuss the harmonic contents of the MMFs and the resultant generated force.

2.1.1 Conventional Design of 3-4 Combination Motor

Figure 2-3 depicts the schematic magnetic design of the conventional linear iron-core motor shown in Figure 2-1. The stator armature has three phase windings A, B, and

C wound on three iron core teeth. Note that the prime variables of A', B', and C' indicate the returning coils. These three coils magnetically interact with four magnets in the magnet track. This is why this type of motor is often called a 3-4 combination motor. That is, 3 iron-core teeth and 4 magnets are a fundamental magnetic unit to generate thrust in such conventional iron-core motors. We define the length of this basic motor unit as λ_u . This parameter is related to other key geometric parameters of the motor with the relations of

$$\begin{aligned} \lambda_t &= \frac{\lambda_u}{3} = 16 \text{ mm} && (\because 3 \text{ coils/teeth per unit}) \\ \lambda_p &= \frac{\lambda_{pp}}{2} = \frac{\lambda_u}{4} = 12 \text{ mm} && (\because 4 \text{ magnets per unit}), \end{aligned} \quad (2.1)$$

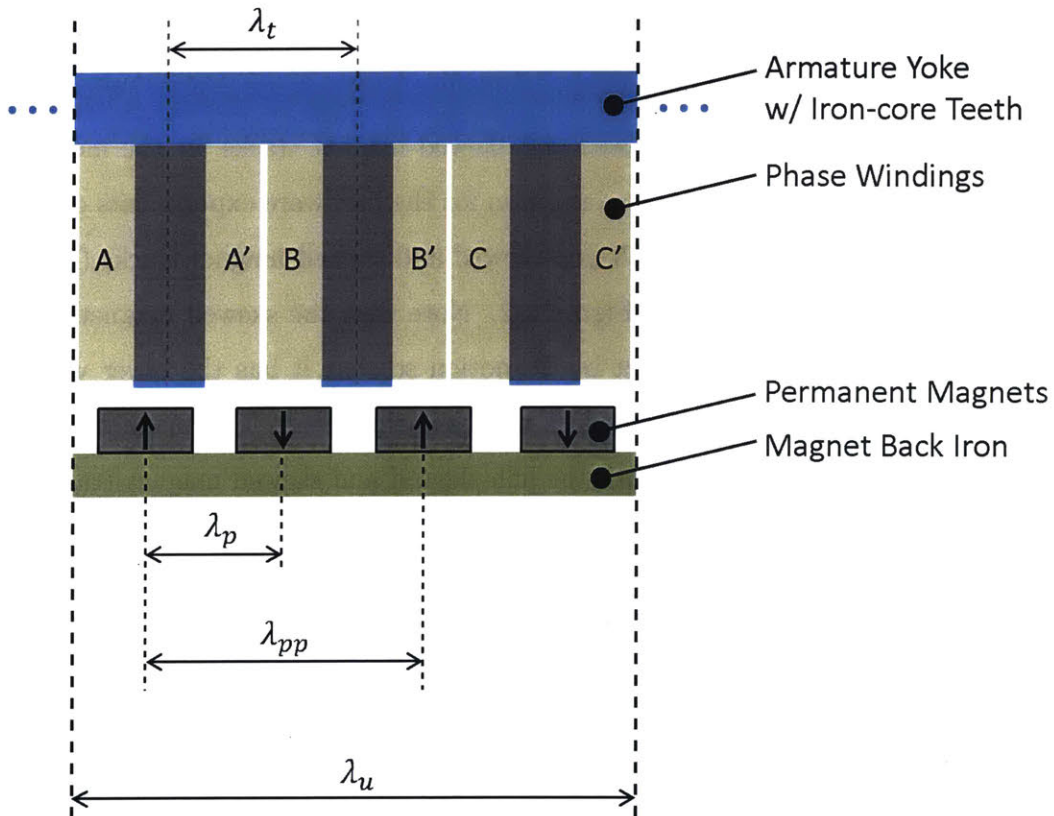


Figure 2-3: Schematic magnetic design of the conventional 3-4 combination linear iron-core motor.

where λ_t , λ_p , and λ_{pp} are the tooth pitch, the magnet pole pitch (e.g. from N to S), and the magnet pole-pair pitch (e.g. from N to N), respectively. Magnetic flux is interacted between the stator armature and the magnets to generate a force. In order to have the magnetic flux path closed, both the armature yoke and the magnet track have the back iron.

2.1.2 Simplified Analysis

In order to understand the magnetic force generation and its force harmonic content, we discuss the magneto-motive force (MMF) waveforms of the stator armature and the magnet track. The magnetic force of a motor is generated by two interacting magnetic fields, and it is proportional to the cross product of the MMFs of those interacting fields [54] as

$$F_{thrust} \propto \mathcal{F}_s \mathcal{F}_r \sin(\delta_{sr}) \quad (2.2)$$

where the vector components are the direct and quadrature axes, and where \mathcal{F}_s , \mathcal{F}_r , and δ_{sr} are the stator MMF amplitude, the rotor MMF amplitude, and the phase

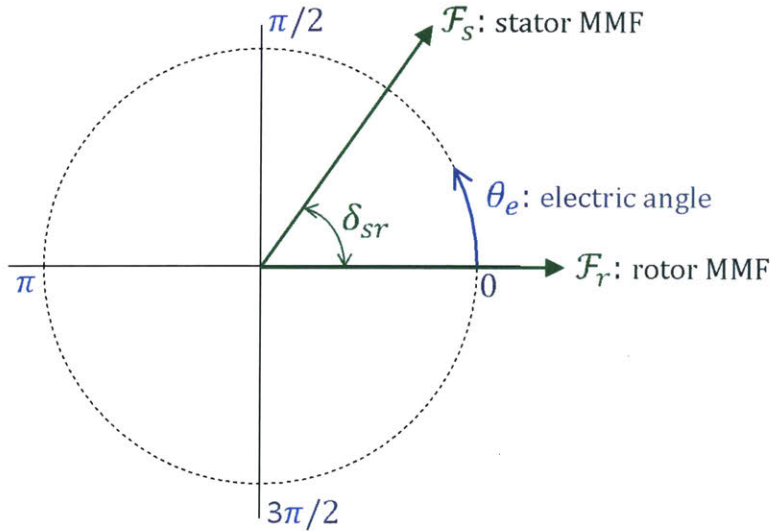


Figure 2-4: Magneto-motive force (MMF) vectors of the stator (\mathcal{F}_s) and magnet track (or rotor) (\mathcal{F}_r) in polar coordinates of the electrical angle, θ_e .

difference in the electrical angle between the stator and rotor MMFs, respectively. The relationship of these MMFs is illustrated in Figure 2-4. In our analysis, the electrical angle of $\theta_e = 2\pi$ corresponds to a linear position displacement by a distance equal to the magnet pole-pair pitch, λ_{pp} . As can be seen in the figure, the magnetic force is produced by the tendency of the rotor (magnet track) MMF, \mathcal{F}_r , to align with the stator MMF, \mathcal{F}_s , which is a traveling wave created by the commutation of the armature phase currents. To have the maximum thrust for a given magnetic design of a motor, \mathcal{F}_s has to lead or lag \mathcal{F}_r by an electrical angle of $\pi/2$, which means $\sin(\delta_{sr}) = 1$ in (2.2). The electrical angle definition and the commutation algorithm for the conventional iron-core motor are discussed in detail in Chapter 6.

The thrust force relation in (2.2) can be rewritten as

$$F_{thrust} \propto \sum_{n=1}^{\infty} \mathcal{F}_{s,n} \mathcal{F}_{r,n} \sin(\delta_{sr,n}) \quad (2.3)$$

so as to consider the harmonics (n) of the MMFs generating the force harmonics. Note that in the assumed periodic system, only like numbered harmonics generate thrust. From (2.3), we see that the ideal MMF waves for both the stator and the rotor are sinusoidal as shown in Figure 2-5 so that we have only the fundamentals to generate the thrust without any high harmonics. The red and green curves in the figure are the ideal sinusoidal MMF waves for the stator (red) and the rotor (green). Note that the stator MMF, \mathcal{F}_s leads the rotor MMF, \mathcal{F}_r by $\lambda_{pp}/4$, which corresponds to the electrical angle of $\pi/2$ as discussed earlier.

The realistic stator and rotor MMF waves of the conventional motor, however, are different from the ideal waveforms, as shown with the blue (stator) and black (rotor) curves in Figure 2-5. The stator MMF, which can be considered as the magnetic potential ψ_s at the air gap, is estimated with the relation of

$$\mathcal{F}_s = \psi_s = \mathcal{R}\phi = \left(\frac{l}{\mu A} \right) (AB) = \frac{B}{\mu} l = \oint H dl = Ni \quad (2.4)$$

where \mathcal{R} , ϕ , l , A , μ , B , H , and Ni are the magnetic reluctance of an iron-core

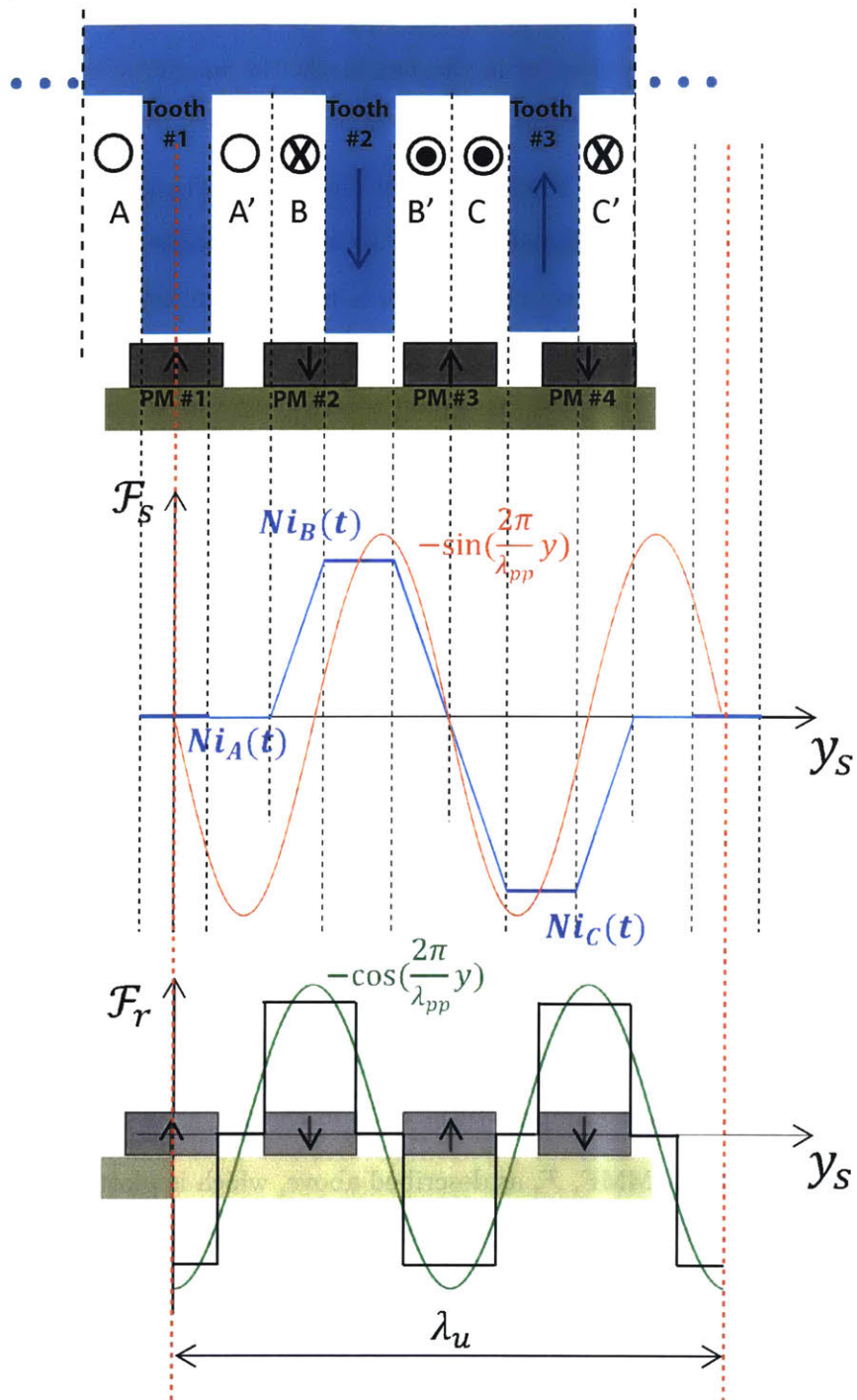


Figure 2-5: Magneto-motive force (MMF) waveforms of the stator and magnet track (or rotor) of the conventional linear iron-core motor.

tooth, the magnetic flux through the tooth, the characteristic length of the flux path, the cross-section area of the flux path, the magnetic permeability of the iron-core material, the magnetic flux density in the flux path, the magnetic field strength in the flux path, and the ampere-turns enclosed by the flux path, respectively.

At the instant depicted in Figure 2-5, the first tooth (Tooth#1) and the first magnet (PM#1) are instantaneously aligned so that the phase A coil needs to be turned off ($i_A(t) = 0$). This means that there is no potential drop or increase from the armature back iron to the tooth tip at the air gap. We thus also have zero potential, $\mathcal{F}_s = 0$ across Tooth#1, assuming a zero potential at the armature back iron. This zero potential continues through the slot area (with zero current density) until the start of the phase B coil. In order to generate a thrust in the rightward direction on the magnet track, the phase B and the phase C coils have to be turned on such that 1) the magnetic flux direction in Tooth#2 is the same as PM#2 to pull the magnet to the rightward direction, and is opposite to PM#3 to push it to the rightward direction, and 2) the magnetic flux direction in Tooth#3 is the same as PM#3 to pull it to the rightward direction, and is opposite to PM#4 to push it to the rightward direction. Thus, the magnetic potential at Tooth#2 is a positive constant while it is a negative constant value at Tooth#3. Note that we use the sign convention where the ampere-turns (Ni) is positive when it creates a magnetic flux downward as can be seen in Tooth#2 in the figure. The MMF, magnetic potential, changes linearly across a slot when there are energized coils because the potential change is proportional to the ampere-turns (Ni) in the slot as in (2.4).

We obtain the stator MMF, \mathcal{F}_s as described above, which is plotted with the blue curve in Figure 2-5. This realistic \mathcal{F}_s curve can be considered as a sampled version of the ideal sinusoidal waveform (red curve) with the iron-core tooth locations as the sampling points. As can be seen in the figure, the realistic \mathcal{F}_s waveform is coarsely sampled one so that it contains significant higher harmonics. The realistic MMF waveform of the magnet track (rotor), \mathcal{F}_r is plotted with the black curve in the figure with the same sign convention. This pulsating waveform of \mathcal{F}_r also contains significant higher harmonics. Since both the stator and rotor MMFs have such higher harmonic

content, we expect that the generated force by the conventional motor also contains high force harmonics as can be seen from (2.3). We present the force harmonic content of the conventional iron-core motor in Section 2.2.

2.2 Motor Performance in Simulation

In this section, we discuss the predicted motor performance of the conventional motor with a finite element model. The 2D finite element tool, called FEMM, is used since 1) it is computationally simpler than 3D tools and 2) it can capture the key motor performance including the thrust, cogging, and force ripple. We describe in this section a method to capture the effects of skewed magnets on the cogging and force ripple using the 2D tool. The force harmonics of the predicted force ripple are also discussed with the expected noise of the conventional 3-4 combination linear iron-core motor.

2.2.1 Finite Element Analysis Model

We create a 2D finite element model of the conventional linear iron-core motor, TL18 by Tecnotion, so as to predict its motor performance. Figure 2-6 shows a snapshot of the finite element (FE) model created in the 2D finite element program, called FEMM. The FE model has the magnetic configuration of the moving short magnet and the stationary long armature same as the commercial motor shown in Figure 2-1. This model has two basic motor units where a total of 8 magnets in the moving magnet track periodically interact with 6 coils/poles to produce a force. Note that the captured moment in the figure is when the moving magnet is located at the reference zero position. In the FE model, 1) the material magnetic nonlinearity is included, 2) the three phase currents are commutated, and 3) the impedance boundary conditions are used to mimic the behavior of an unbounded region [53, 55].

The motor depth in the direction of into-the-page (X-direction) is defined in the program, and we can utilize it to capture 2.5D performance such as the magnet skewing effect. The FE model can be divided into multiple segments in the X direction

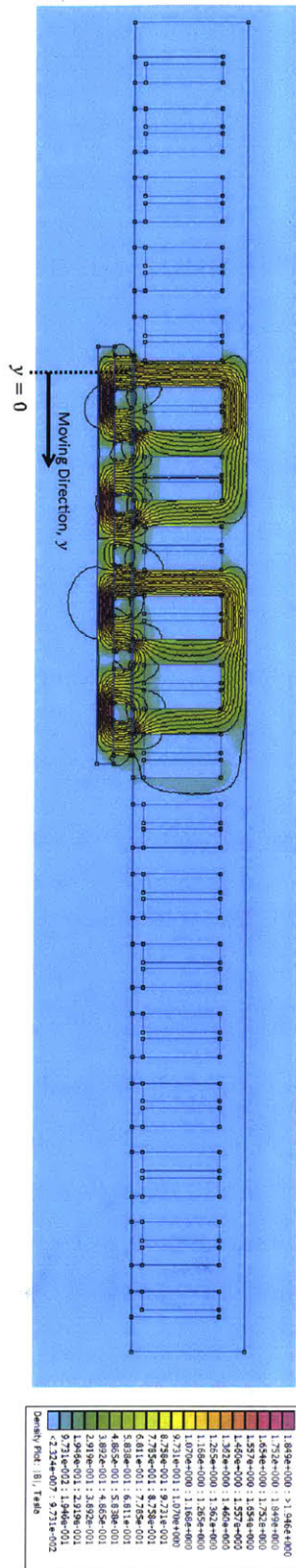


Figure 2-6: Finite element model of the conventional linear iron-core motor, with 4 pitches of magnets and coil currents of zero.

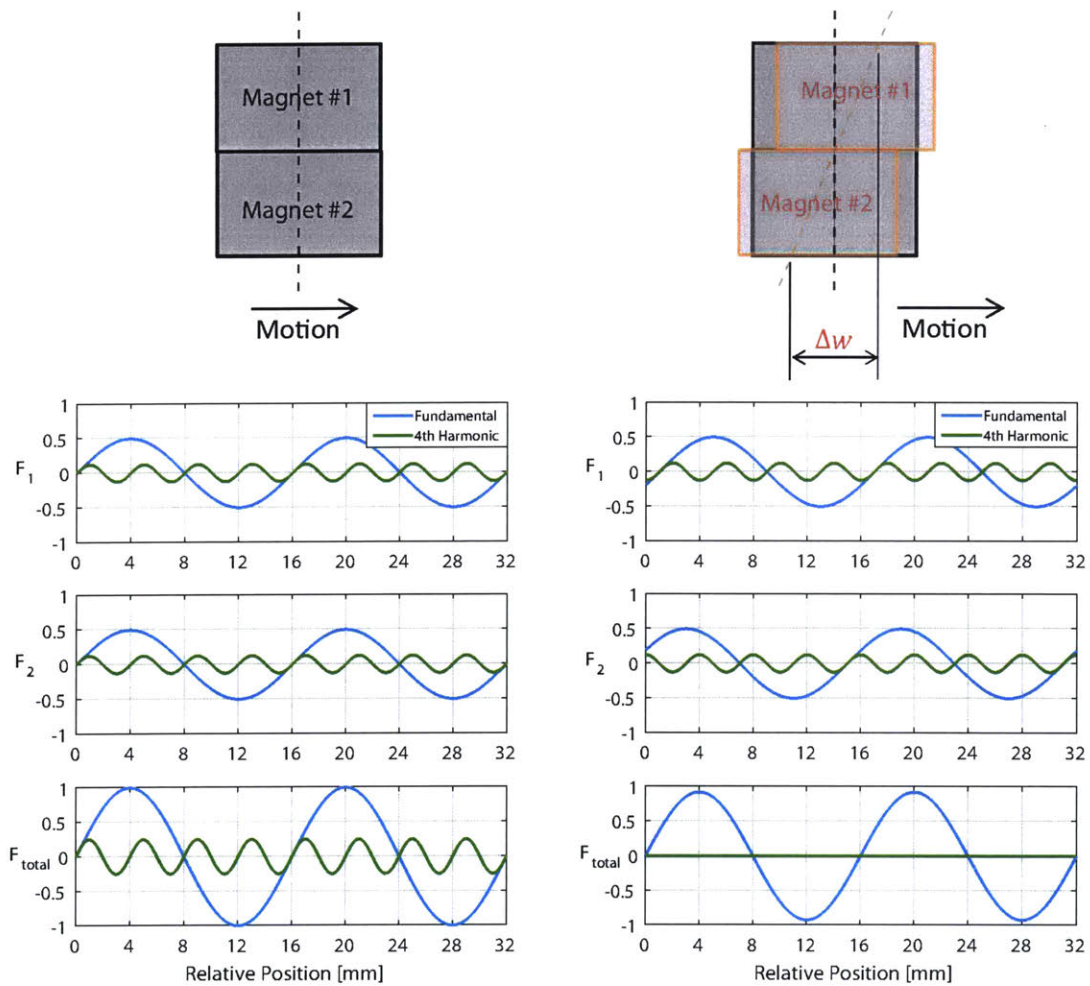


Figure 2-7: Schematic explanation of the magnet skewing effect in reducing the cogging force. Non-skewed magnet and related cogging harmonics (left) and skewed magnet and related cogging harmonics (right).

with shifted magnets in order to simulate the skewed magnet effect. Figure 2-7 schematically shows the magnet segmented into two pieces in the X direction. The left side in the figure shows two pieces of magnets with no shift to simulate the non-skewed magnet and its effect on the cogging force while the right side shows two pieces of magnets with the total shift of Δw to simulate the skewed magnet and its effect. Depending on the magnetic design of a motor, the cogging force can contain various harmonics. In the figure, we observe the fundamental (blue curve) and the fourth (green curve) harmonics of the cogging caused by Magnet#1 (F_1) and Magnet#2 (F_2). Note that the fundamental cogging period, $\lambda_{cogging}$ is set to 16 mm, which is the same cogging period of the conventional motor we use (TL18 by Tecnotion). The resultant cogging force by two magnet pieces is defined as $F_{total} = F_1 + F_2$. These forces are illustrated in the figure for both the non-skewed (left) and skewed (right) magnets.

For the case with the non-skewed magnet, the two magnet pieces, Magnet#1 and Magnet#2, are aligned with no shift. Thus, the cogging forces, F_1 and F_2 are identical and thus double both the fundamental and fourth harmonics as can be seen in the resultant force plot of F_{total} in the left side of the figure. For the skewed magnet case, we shift both magnet pieces to have a total shift of $\Delta w = \lambda_{cogging}/4 = 4$ mm. The corresponding cogging forces of F_1 and F_2 show the shifted fundamental and fourth harmonics according to the magnet shift. The resultant cogging force of the skewed magnet shows an elimination of the fourth harmonic (green curve) and a small reduction in the fundamental (blue curve). This is because the magnet shift of $\Delta w = 4$ mm is the same as the period of the fourth cogging harmonic, which makes the fourth harmonic components of F_1 and F_2 180°-out-of-phase and thus canceling.

We list below some of the interesting takeaways from the schematic explanation of the magnet skewing effect illustrated in Figure 2-7.

- We can well approximate the effect of skewed magnets on the cogging force using multiple segmented 2D finite element models. The skewed magnets help to eliminate or reduce the cogging force.

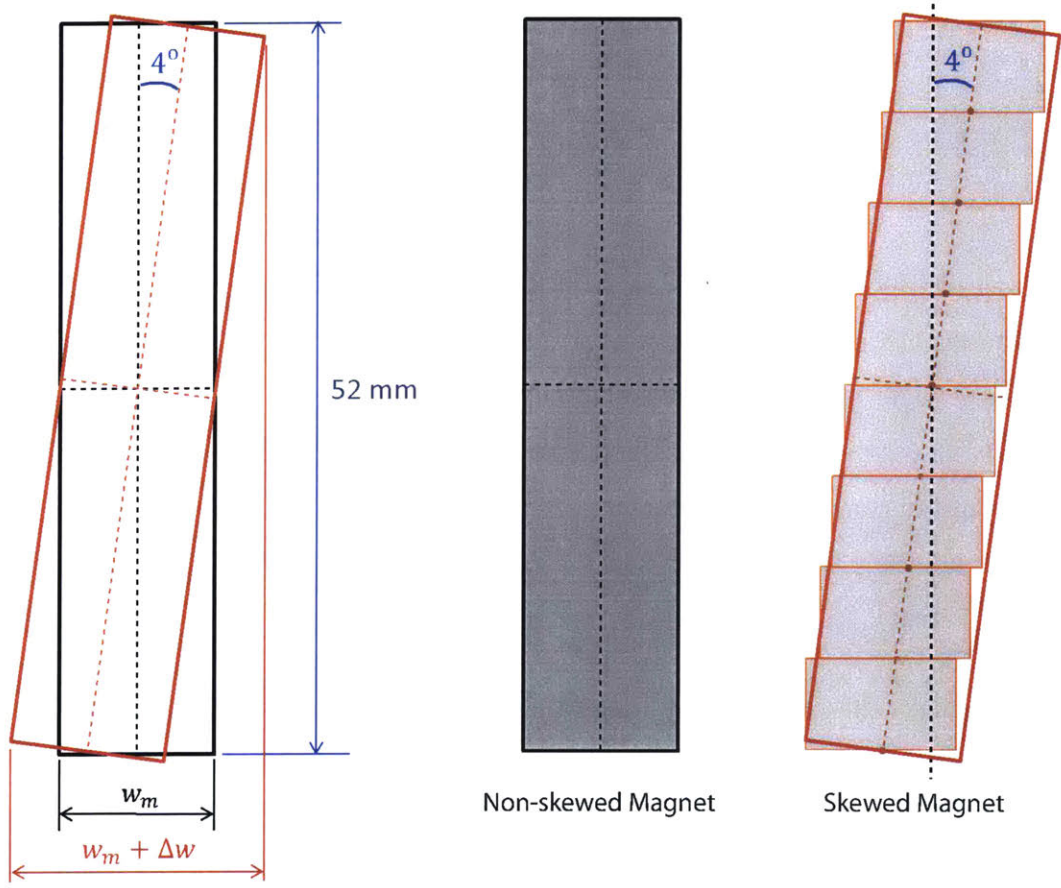


Figure 2-8: Segmented magnets in the 2D finite element model to approximately capture the magnet skewing effect of the conventional iron-core motor.

- The magnet skewing angle can be adjusted depending on which cogging harmonic we want to eliminate. The cogging harmonic, whose period is the same as the magnet shift Δw by the skewing angle, can be eliminated.

The conventional motor, TL18 by Tecnotion, has the motor depth of $D = 52$ mm and skewed magnets with a skewing angle of 4° . To simulate the skewed magnets, we divide the magnets into 8 segments in the motor depth direction as shown in Figure 2-8. The total magnet shift by the skewing angle of $\theta_{skew} = 4^\circ$ is

$$\Delta w = D \tan(\theta_{skew}) \approx 4 \text{ mm} = \lambda_t/4 = \lambda_{cogging}/4. \quad (2.5)$$

Note that the magnet shift is close to a fourth of the fundamental cogging period of the conventional motor. From this, we see that the skewed magnets with the skewing angle of 4° in the conventional motor are designed to reduce the fourth cogging harmonic. We present the relevant results on the predicted cogging and force ripple of the conventional motor in Section 2.2.2.

2.2.2 Cogging and Force Ripple

We calculate the cogging and force ripple of the conventional motor for both non-skewed and skewed magnets using the finite element model shown in Figure 2-6. For the skewed magnets, we use the method of magnet segments as illustrated in Figure 2-8. The calculated cogging force in both the normal and tangential directions are plotted in Figure 2-9 with non-skewed (blue curves) and skewed (red) magnets. Note that the cogging force shown in the figure is per motor basic unit of 3 iron-core teeth and 4 magnets. The FE model shown in Figure 2-6 has two units as discussed earlier, so we simply divide the calculated force by two.

The cogging force with the non-skewed magnets shows relatively sharper fluctuation, indicating more high harmonic contents, in both the normal and tangential directions. The fundamental cogging period is 16 mm, which is the same as the tooth pitch, λ_t as in (2.1). In the figure, we observe 4 notable fluctuating peaks within

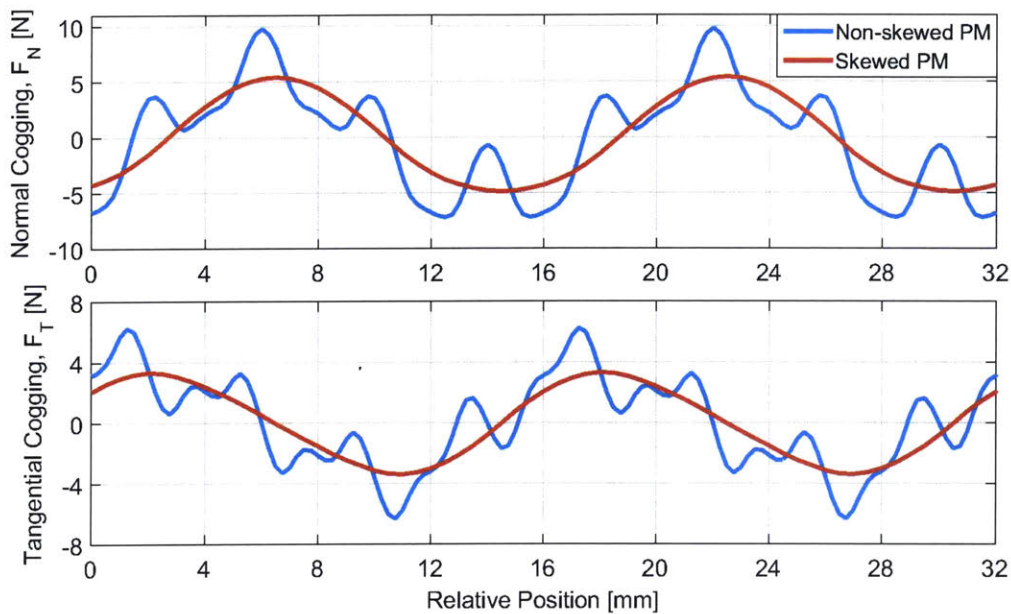


Figure 2-9: Simulated cogging force of the conventional iron-core motor with both non-skewed and skewed magnets. The cogging force is per basic motor unit. By unit, we mean the basic combination of 3 iron-core teeth and 4 magnets.

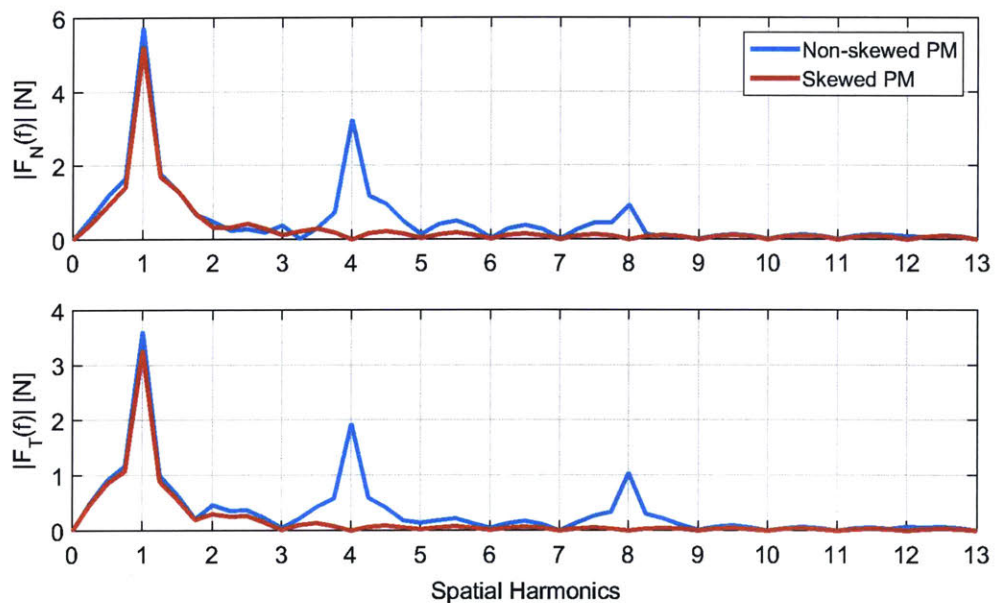


Figure 2-10: Simulated cogging force spectrum of the conventional iron-core motor with both non-skewed and skewed magnets.

this fundamental cogging period, thereby expecting a strong fourth harmonic in both directions. The cogging force with the skewed magnets, on the other hand, behaves close to sinusoidal waves with the period of 16 mm, showing mainly the fundamental component.

The harmonic components of the calculated cogging forces in both directions can be clearly observed in the spatial amplitude spectra shown in Figure 2-10. Note that in the amplitude spectra, we multiply the cogging period of 16 mm to the spatial frequencies to obtain the harmonics in the abscissa. Consistent with the results shown in Figure 2-9, the spectrum of the non-skewed magnet case also shows strong components at the multiples of the fourth harmonic as well as the fundamental. We observe that the cogging spectrum of skewed magnet case contains mainly the fundamental with the multiples of the fourth harmonic eliminated. This is because the skewing angle of 4° makes the magnet shift of $\Delta w = 4$ mm, which is exactly the same as a fourth of the cogging period as in (2.5). Note that the fundamental component of skewed magnet case is slightly smaller than that of non-skewed magnet case. This is also consistent with the result discussed earlier in Figure 2-7.

We list below a few remarks from the observation on the predicted cogging force of the conventional motor.

- The skewed magnets in the conventional 3-4 combination iron-core motor design are to reduce the high harmonics of the cogging force.
- The peak-to-peak cogging amplitude is reduced by 39.4 % (from 16.99 N to 10.29 N) and 46.7 % (from 12.58 N to 6.71 N) in the normal and tangential directions, respectively, by skewing the magnets with the angle of 4° . This is a significant reduction in cogging.
- However, the cogging fundamental is almost intact even with the skewed magnets. The majority of the cogging (specifically, 60.6 % and 53.3 % in the normal and tangential directions, respectively) remains.
- In order to eliminate the fundamental cogging too, the magnet shift would have to be equal to the full tooth pitch of 16 mm, which corresponds to a skewing

angle of about 17° . The large tooth pitch in the conventional motor design thus requires a large skewing angle in order to reduce the fundamental cogging. However, such a large skewing angle will compromise the thrust performance significantly, and is thus not generally used in practice.

- The cogging force harmonics can vibrate the moving stage, and can thus also radiate the acoustic noise as hypothesized in Chapter 1. The expected cogging-oriented noise will be at the frequency of

$$f_{cogging} = \frac{v_c}{\lambda_{cogging}/n} \quad (2.6)$$

where v_c , $\lambda_{cogging}$, and n are the constant velocity, fundamental cogging period, and cogging harmonic index, respectively. We discuss in detail this cogging-related noise in Chapters 6 and 7.

We also present the force ripple of the conventional motor predicted by the finite element model shown in Figure 2-6 so as to observe the force harmonic content in the magnetically generated force. Figure 2-11 shows the calculated force ripple of the conventional motor with both the non-skewed (blue curve) and skewed (red curve) magnets. Note that in these plots, we have subtracted the average thrust. The upper plot shows the force ripple in the normal direction, and the lower plot shows it in the tangential direction. Note that the force ripples in both directions are calculated for one motor unit of 3 iron-core teeth and 4 magnets. As can be seen in the figure, the force ripple with the non-skewed magnets shows higher fluctuations than that with the skewed magnets in both tangential and normal directions. Particularly, we observe four strong fluctuating peaks within the cogging fundamental period of 16 mm, indicating a strong fourth harmonic component.

The cogging harmonic content can be clearly observed with the amplitude spectra in Figure 2-12. As before, the blue curves show the spatial spectrum of the non-skewed magnet case while the red curves are for the skewed magnet case. The upper plot shows the force ripple spectrum in the normal direction, and the lower plot shows

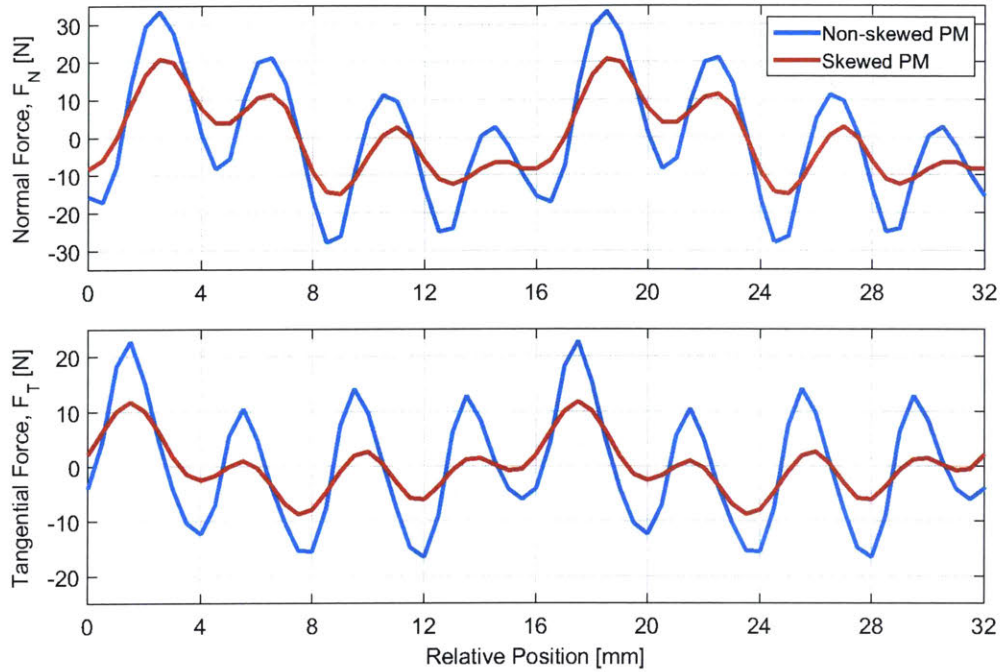


Figure 2-11: Simulated force ripple of the conventional iron-core motor with both non-skewed and skewed magnets. The force ripple is per basic motor unit. By unit, we mean the basic combination of 3 iron-core teeth and 4 magnets.

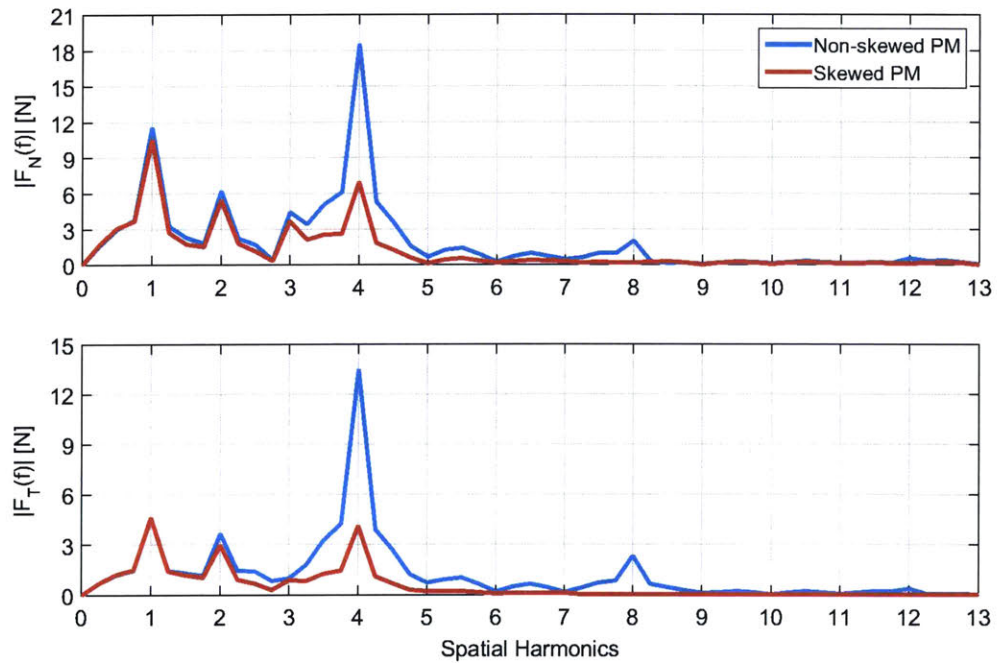


Figure 2-12: Simulated force ripple spectrum of the conventional iron-core motor with both non-skewed and skewed magnets.

it in the tangential direction. Note that in the amplitude spectra, we multiply the spatial frequencies by the cogging period of 16 mm so as to directly show the harmonic number in the abscissa. As expected from Figure 2-11, the spectra of the non-skewed magnet case shows strong fourth harmonics in both force directions, even stronger than the fundamental component. In addition, second and third harmonics, not observed from the cogging force in Figure 2-10, are generated by energizing the phase coils. With the skewed magnets, the cogging only shows the fundamental component as shown in Figure 2-10. However, when the motor is powered to generate thrust, the second, third, and fourth harmonics of the force ripple are observed with significant amplitudes. As discussed in Chapter 1, these high force harmonics of the conventional motor can vibrate the moving stage and so vibrate the machine frame and also emit acoustic noise during the motor's cyclic operations. Particularly, this stage vibration and the associated acoustic noise can be even more serious if the force harmonics excite the lumped and flexible stage dynamics. We present the relevant experimental data and discuss the motor noise caused by this high force harmonic content of the conventional motor in Chapter 6.

We list below our observations on the predicted force ripple of the conventional linear iron-core motor.

- The skewed magnets help reduce the force ripple in both the normal and tangential directions. The peak-to-peak force ripple amplitude is reduced with skewing by 41.8 % (from 61.53 N to 35.83 N) and 48.0 % (from 39.31 N to 20.46 N) in the normal and tangential directions, respectively. The force ripple reduction by the skewed magnet mainly comes from the fourth harmonic reduction as can be seen in Figure 2-12. Specifically, the fourth harmonic reduction ratios are 62.6 % (from 18.57 N to 6.95 N) and 69.4 % (from 13.52 N to 4.14 N) in the normal and tangential directions, respectively.
- Even with the skewed magnets, however, the conventional iron-core motor shows significant fundamental, second, third, and fourth harmonics in the force ripples in both force directions.

- The high force harmonics in the magnetically generated force by the conventional motor (either with skewed or non-skewed magnets) can cause the stage vibration and the associated acoustic noise, especially severe when the force harmonics excite the stage dynamics, as hypothesized in Chapter 1. We discuss this issue with experimental results in Chapter 6.

2.3 Summary

We discuss studies of the conventional 3-4 combination linear iron-core motor in this chapter. The conventional motor we use, TL18 by Tecnotion, is first introduced to discuss 1) the magnetic motor configuration of the moving short magnets with the stationary long armature, and 2) the magnetic design of 3 coils/poles periodically interacting with 4 magnets to generate a force. Using the magnetic design of the conventional motor, we present the ideal and realistic magneto-motive force (MMF) waves of the stator and the rotor (moving magnet track). Due to the magnetic design with a large tooth pitch and a conventional N-S magnet array, both the stator and rotor MMFs contain high harmonic contents. This results in high force harmonics in the magnetically generated force. These high force harmonics are responsible for the vibro-acoustic noise of the conventional motor. We present experimental results on this motor noise in Chapter 6.

In this chapter, we also discuss the predicted performance of the conventional 3-4 combination iron-core motor in terms of the cogging force and force ripple, which are drives for the motor noise. We use a 2D finite element model with the FEMM program in order to calculate the key motor performance. The cogging force and force ripples are compared between the cases of non-skewed magnets and skewed magnets. We also present the spectra of the calculated forces to discuss the spatial harmonic components. We summarize our understanding from the predicted performance of the conventional iron-core motor as follow:

- 1) The conventional motor with the non-skewed magnets shows a strong fourth harmonic component in the cogging and the force ripple.

- The multiples of the fourth harmonic in the cogging are the major components along with the fundamental.
 - The fourth harmonic is even stronger than the fundamental component in the force ripple with the non-skewed magnets, as shown in Figure 2-12.
- 2) Skewing the magnets helps reduce both the cogging and the force ripple.
- The conventional commercial motor has skewed magnets with a skewing angle of 4° which is associated with a magnet shift of 4 mm, which is the same as a fourth of the fundamental cogging period.
 - This results in reducing the fourth cogging and ripple harmonics as shown in Figures 2-10 and 2-12.
- 3) A significant amount of force components are still remaining even with skewing the magnets.
- The skewed magnets of the conventional motor are designed to reduce the high cogging harmonics, but do not address the fundamental cogging component. In order to reduce the fundamental cogging, the skewing angle has to be large enough to have the magnet shift to be the same as the full tooth pitch. This will result in significantly compromising the thrust. Such a large skew angle is not used in practice.
 - Even with the skewed magnets, the force ripple of the conventional motor contains strong fundamental, second, third, and fourth harmonic components as shown in Figure 2-12.

The magnetic design of the conventional 3-4 combination motor contains high harmonics in the stator and rotor MMFs which thus generate high force harmonics. Moreover, due to the magnetic design with a large tooth pitch, using the skewed magnets cannot significantly reduce the fundamental and some higher force harmonics of the conventional motor. This results in vibrating the stage and also radiating the acoustic noise as discussed in Chapter 1. We discuss the noise issue of the conventional

motor in detail in Chapter 6. Our new fine-tooth motor is designed to resolve this issue by having smoother stator and rotor MMFs. The new motor design details and the relevant experimental data on the motor performance improvements are discussed in Chapters 3 and 7, respectively.

Chapter 3

Fine-tooth Motor Modeling, Design, and Construction

In this chapter, we discuss the modeling, design, and construction of our new linear iron-core motor designed for higher thrust and lower force harmonics. As discussed in Chapter 2, the conventional 3-4 combination iron-core motor exhibits high force harmonics, which can cause stage vibrations and acoustic noise. In order to reduce the force harmonics and also increase the thrust at the same time, we take the design direction of having fine iron-core teeth closely packed together. This design approach and how it is different from the conventional iron-core motor design are discussed in the first section of this chapter.

We use a hybrid layer model as well as a finite element model to design our new motor. The hybrid layer modeling method is adapted from the work of Dr. Matthew Angle at MIT [3] where he uses the model to optimize the magnetic design of a rotary permanent magnet motor for the MIT Cheetah robot [56–58]. We introduce this modeling method and discuss some of the modification we made for our linear iron-core motor design in the second section. The design process of the new motor is discussed in detail in the following section where we select design parameters to optimize performance. This results in a design which outperforms the conventional motor. We present the expected performance of our new motor with the finalized design parameters, and show the construction details of the new motor at the end of

this chapter, followed by a summary.

3.1 Fine-tooth Motor

The magnetic force of a motor can contain high force harmonics depending on the magnetic design. As discussed in Chapter 2, the conventional 3-4 combination iron-core motor generates high force harmonics since its magnetic design produces high harmonics in the magneto-motive forces (MMFs) of both the stator and rotor (magnet track). In particular, the stator MMF waveform of such a motor is significantly coarse due to the smaller number (only 3 per unit) of iron-core teeth with the large tooth pitch ($\lambda_u/3$) as shown in Figure 2-5. Note that we define the motor unit length λ_u as the minimal length of a motor required to generate thrust: 3 iron-core teeth and 4 magnets for the conventional motor and one pole pair for our new motor as shown in Figure 3-1.

In order to generate smaller force harmonics, our new motor is designed to have multiple fine teeth with a small tooth pitch so as to create a stator MMF with reduced

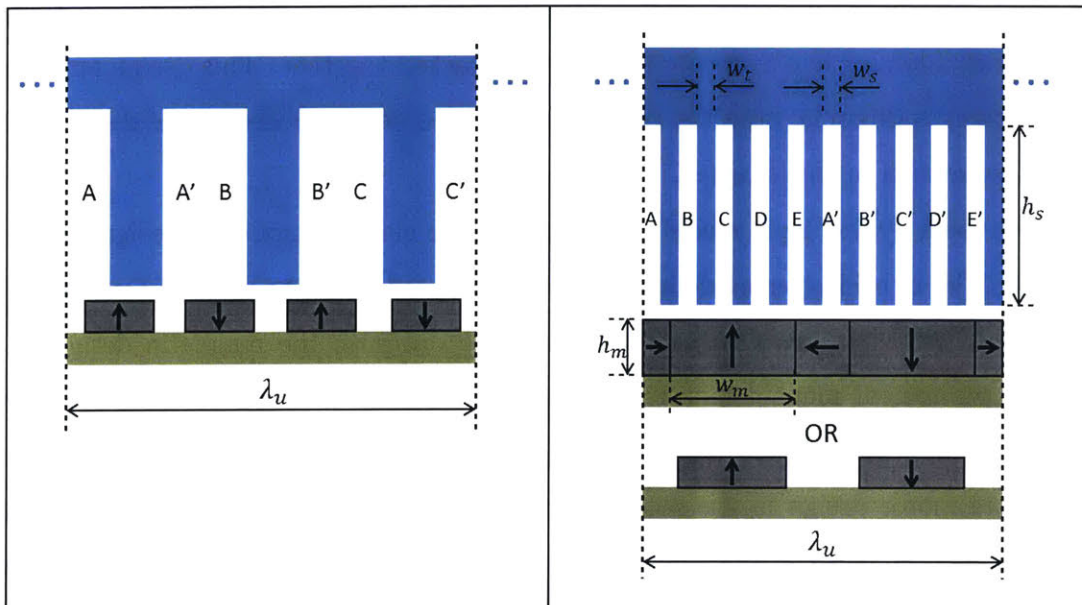


Figure 3-1: Schematic magnetic designs of a unit length of the conventional 3-4 combination motor (left) and our new fine-tooth motor (right).

harmonics. The schematic magnetic design is illustrated in Figure 3-1. Compared to the conventional iron-core motor design, our new motor has fine teeth, deep slots, and multiple phases. The schematic in the figure shows a 5-phase stator, but it can be any number of phases. Since we have fine teeth in our new motor design, we call our motor as a fine-tooth motor. As shown in the figure, the magnet array can be either a conventional N-S pattern or a Halbach array. Note that the Halbach array pattern, named after its inventor Klaus Halbach, produces magnetic fields with less harmonics, and enhances the field strength on one side while reducing it on the other side [59–63].

In this section, we study the magnetic design of our new fine-tooth motor to compare the MMFs of both the stator and magnet track to those of the conventional motor. We also obtain a simplified thrust equation using the MMFs, and discuss the pros and cons of our fine-tooth motor at the end of this section.

3.1.1 Simplified Analysis

The thrust force of a linear motor is generated by the tendency of two interacting magnetic fields to align their magnetic axes, and it is proportional to the cross product of two MMFs [54] as

$$F_{thrust} \propto \vec{\mathcal{F}}_s \times \vec{\mathcal{F}}_r = \mathcal{F}_s \mathcal{F}_r \sin(\delta_{sr}) \quad (3.1)$$

where $\vec{\mathcal{F}}_s$, $\vec{\mathcal{F}}_r$, \mathcal{F}_s , \mathcal{F}_r , and δ_{sr} are the stator MMF vector, rotor (magnet track) MMF vector, stator MMF amplitude, rotor MMF amplitude, and phase angle difference between the stator and rotor MMF vectors, respectively. The proportional factor is determined by the geometry of motor magnetic designs. The thrust force of our new motor can thus be written as

$$F_{thrust} = \left(\frac{\mu_0 N_{pp} D \pi}{g} \right) \mathcal{F}_s \mathcal{F}_r \sin\left(\frac{2\pi}{\lambda_{pp}} \Delta_{sr}\right), \quad (3.2)$$

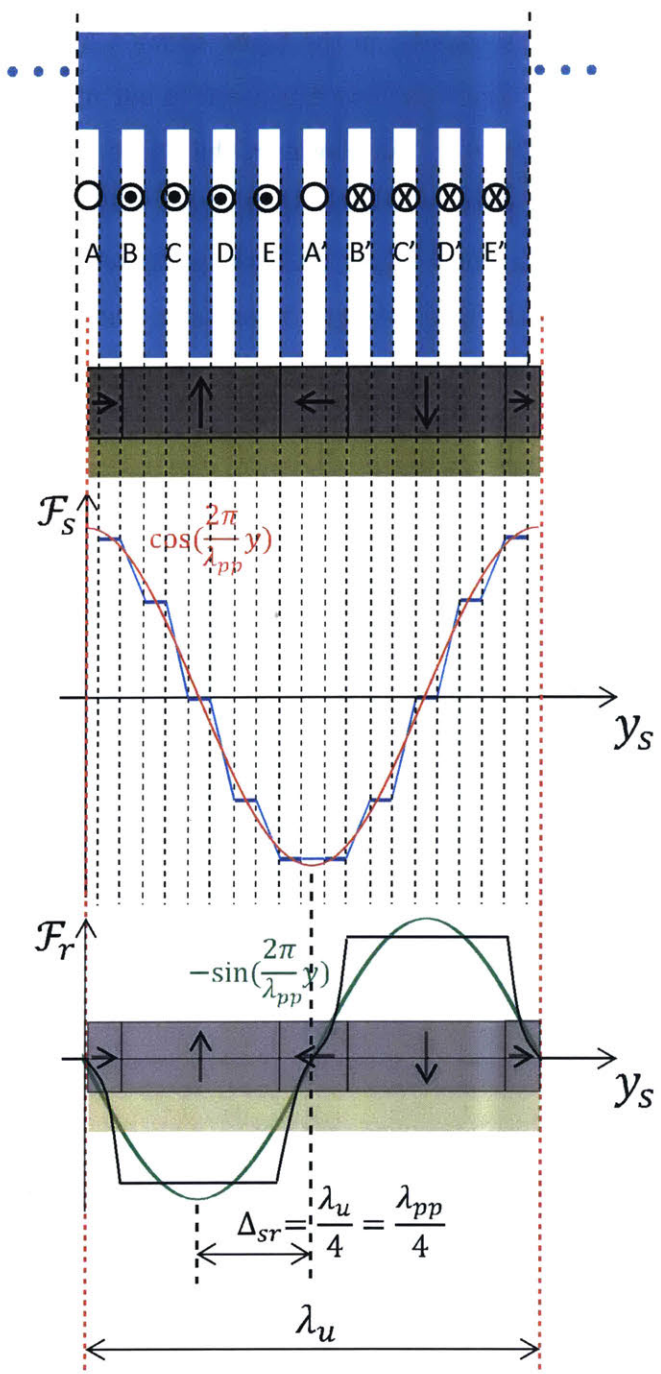


Figure 3-2: Magneto-motive force (MMF) waveforms of the stator and magnet track (or rotor) of our new fine-tooth motor.

where μ_0 , N_{pp} , D , g , λ_{pp} , and Δ_{sr} are the magnetic permeability of air, number of pole-pair, motor depth, air-gap distance, magnet pole-pair pitch, and phase position difference between the stator and rotor MMFs, respectively. Note that the phase angle difference, δ_{sr} in (3.1) is used in a vector diagram in [54] with polar coordinates. We replace δ_{sr} by $2\pi\Delta_{sr}/\lambda_{pp}$ to express the phase difference in terms of linear position. The phase position difference, Δ_{sr} is illustrated in Figure 3-2, and it is in the Y direction of the Cartesian coordinates. The thrust force equation in (3.2) is derived using the energy method described in [54]. This is a simplified force calculation with the assumptions of no material saturation and no leakage flux.

The thrust will contain high harmonics if the stator and rotor MMFs have high harmonics as can be seen in (3.1) and (3.2). This is why the conventional 3-4 combination motor has significant high force harmonic content as discussed in Chapter 2. We choose to have multiple fine teeth in our new motor design to reduce the force harmonics content by designing for relatively smooth stator and rotor MMFs as shown in Figure 3-2. The ideal desired MMF waveforms for both stator and rotor are sinusoidal as shown in the red and green curves in the figure so that we can have only the fundamental to generate the thrust without high harmonics. However, the MMFs cannot be harmonically pure in reality and behave like the blue and black curves in the figure. The realistic stator MMF can be considered as a sampled version of the ideal sinusoidal waveform with the iron-core tooth locations as the sampling points. Note that the MMF, which is the same as the magnetic potential, stays constant across a tooth and changes linearly across a slot because the potential change is proportional to the ampere-turns in the slot. We make the reasonable simplifying assumption that the potential varies linearly across the slot. The magnet track (rotor) MMF is also smoother with the Halbach array pattern than that of a conventional motor magnet track as shown in Figure 2-5. Since we have less harmonics in both the stator and rotor MMFs, when these interact, we expect less force harmonics in the magnetically generated force, and thereby less vibro-acoustic noise with our new motor. The force harmonic components of our new fine-tooth motor are discussed in Section 3.4, and the vibro-acoustic noise measurements are presented and compared in Chapter 7.

3.1.2 Pros and Cons

Here, we list the pros (+) and cons (−) of our new fine-tooth motor design compared to the conventional 3-4 combination motor.

(+) Our new fine-tooth motor will generate reduced force harmonics, and so is expected to emit less noise and vibration.

- Fine teeth densely placed together produce a smoother stator MMF with less high frequency harmonics.
- The Halbach magnet array not only produces a smoother rotor MMF with less high harmonics, but also generates higher force due to the enhanced magnetic field on the side of the working air-gap.

(+) Our new fine-tooth motor can generate higher thrust.

- Magnetic force is generated from the areas where the iron-core teeth ends are engaged with magnets, and our fine-tooth motor structurally contains more of such areas than the conventional motor.
- High force performance of our new fine-tooth motor is discussed in Sections 3.3 and 3.4.

(+) Cogging force can be reduced relatively easily so that we can expect less vibrations and acoustic noises caused by cogging.

- Cogging is a force fluctuation caused by the magnetic interaction between iron-core teeth and magnets. Cogging force can be eliminated, in theory, by skewing either the magnets or iron-core teeth to cover one full tooth pitch.
- The fine-tooth motor design allows reduced cogging with only slightly skewed magnets, and thus without compromising the thrust, due to the small tooth pitch.

(−) Our new fine-tooth motor is relatively difficult to manufacture.

- Unlike the lump-winding in the conventional 3-4 combination motor, the fine-tooth motor requires a multi-phase full-pitch winding. The overlapping of winding end-turns can make the motor construction difficult and increase the manufacturing time. The winding details and new motor construction are discussed in Section 3.5.
- The multi-phase full-pitch winding typically requires longer end-turns, thereby increasing the overall coil resistance and thus the conductor power loss. This issue is taken into account so as to fairly compare our new motor design to the conventional one in Sections 3.3 and 3.4.

3.2 Hybrid Layer Model

The thrust force equation in (3.2) can be useful to estimate the overall force level generated by different magnetic designs of a motor. However, it is limited for use in the motor design process in that 1) it does not capture the material nonlinearity and 2) it cannot estimate the cogging force. In the need of a more complete model, we adapted the hybrid layer modeling method invented by Dr. Angle at MIT [3] for our linear iron-core motor design. When it comes to a general design of a linear iron-core motor, we can mainly consider two sections: an armature core and a magnet track, as can be seen in Figure 3-3. The magnet track section consists of uniform layers of an air gap, a magnet array, and a back iron so that we can explicitly solve Maxwell's equations, which are linear in this region [64–66]. However, it is difficult to solve Maxwell's equations directly in the armature-core section due to its geometric complexity and nonlinear material properties. In this region, therefore, we use a lumped flux-tube model to solve the network of nonlinear reluctances. These two models can be combined at the motor working air-gap by matching the boundary conditions. Since the layer model is combined with the flux-tube model, it is called the hybrid layer model (HLM). [3]

In this section, we first present the solutions of the Maxwell model in the magnet track region. Maxwell's equations are solved at each boundary of the uniform layers

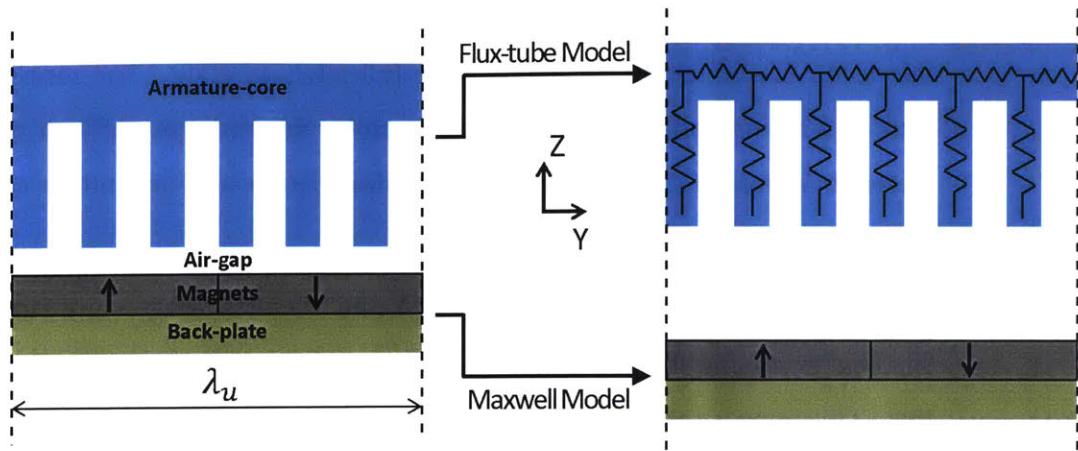


Figure 3-3: Hybrid layer model of a linear iron-core motor. Flux-tube model for the stator armature and Maxwell model for the magnet track (or rotor).

in Cartesian coordinates. For the magnet region, the Halbach magnet array pattern is taken into account. We also discuss the flux-tube model in the stator armature region and present the solutions of its equivalent magnetic circuit. The iteration process of these two models is then described. We compare the performance results of this hybrid layer modeling method to those of the finite element method (FEM) to confirm our model's fidelity at the end of this section.

3.2.1 Maxwell Model for Magnet Track

In the magnet track, we can explicitly solve Maxwell's equations since we have the uniform layers of the motor working air gap, magnet array, and magnet back iron. Figure 3-4 shows the coordinates to use in solving the Maxwell's equations within three regions of uniform layers for the magnet track section. Note that the figure shows an example schematic for a 3-phase motor, but it can have any number of phases. We solve for the magnetic scalar potential $\psi(y, z)$ in these uniform layers (3 regions) and for the magnetic fields at the boundaries. The boundaries are indicated with various z parameters, and their relationships are given by

$$\left\{ \begin{array}{l} z_4 = 0 \quad : \text{Bottom of magnet back iron = reference} \\ z_3 = z_4 + h_{mb} \quad : \text{Bottom of magnet array} \\ z_2 = z_3 + h_m \quad : \text{Upper surface of magnet array} \\ z_1 = z_2 + g \quad : \text{Tooth tip} \\ z_0 = z_1 + h_s \quad : \text{Bottom of slot} \\ z_u = z_0 + h_a \quad : \text{Upper surface of stator yoke,} \end{array} \right. \quad (3.3)$$

where h_{mb} , h_m , g , h_s , and h_a are the thickness of the magnet back iron, the thickness of the magnets, the air gap distance, the slot depth, and the thickness of stator back iron, respectively. We assume arbitrary Fourier transformable periodic fields with the period of the motor unit length λ_u , which is the same as the magnet pole pair pitch λ_{pp} .

Since we have the magnets, we solve Poisson's equation of

$$\nabla^2 \psi(y, z) = \nabla \cdot \vec{M} \quad (3.4)$$

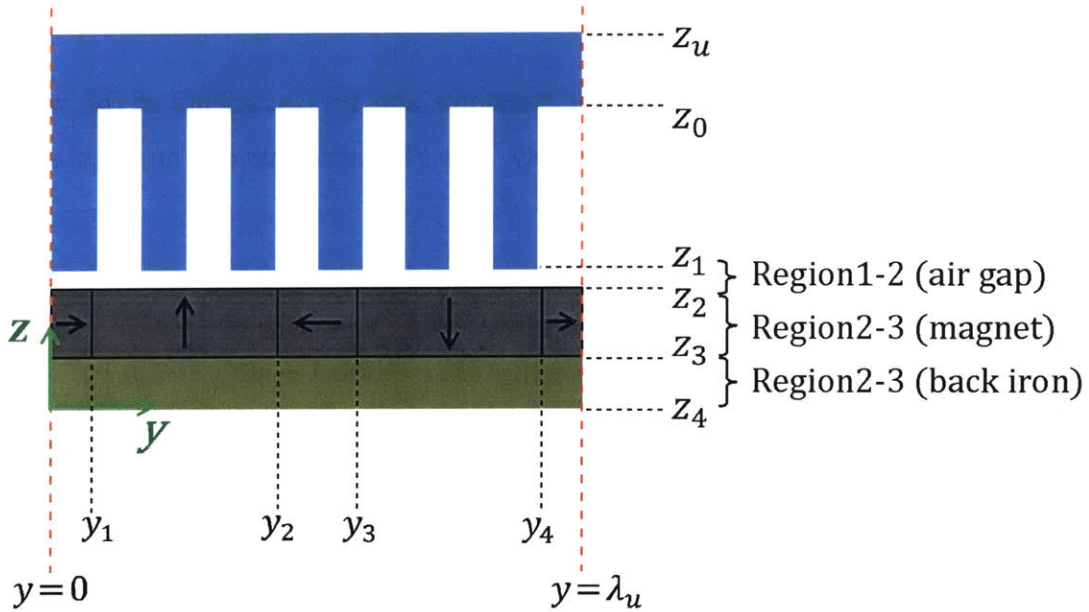


Figure 3-4: Example schematic of a 3-phase linear iron-core motor with Halbach magnet array in Cartesian coordinates.

where \vec{M} is the magnetization vector of the magnet array, which can be written as

$$\vec{M} = M_h(y) \vec{i}_y + M_v(y) \vec{i}_z \quad (3.5)$$

where $M_h(y)$, $M_v(y)$, \vec{i}_y , and \vec{i}_z are the horizontal-direction magnetization, vertical-direction magnetization, horizontal-direction (y) unit vector, and vertical-direction (z) unit vector, respectively. Note that the magnetizations are a function of y only since we assume the uniform magnetization in the normal (z) direction, i.e. the array is composed of blocks of uniform material. Figure 3-5 shows the magnetization functions $M_h(y)$ and $M_v(y)$ within one period of the motor unit λ_u . The magnet boundaries are $y = y_1, y_2, y_3$, and y_4 , consistent with the schematic shown in Figure 3-4. With this periodic magnetization, we can express both $M_h(y)$ and $M_v(y)$ in the form of Fourier Series (FS) as

$$\begin{aligned} M_v(y) &= \frac{a_{v0}}{2} + \sum_{k=1}^{\infty} \left[a_{vk} \cos\left(\frac{2\pi}{\lambda_u} ky\right) + b_{vk} \sin\left(\frac{2\pi}{\lambda_u} ky\right) \right] \\ M_h(y) &= \frac{a_{h0}}{2} + \sum_{k=1}^{\infty} \left[a_{hk} \cos\left(\frac{2\pi}{\lambda_u} ky\right) + b_{hk} \sin\left(\frac{2\pi}{\lambda_u} ky\right) \right] \end{aligned} \quad (3.6)$$

where k , a_{vk} , b_{vk} , a_{hk} , and b_{hk} are the harmonic and FS coefficients of the vertical and horizontal magnetizations, respectively. The FS coefficients can be calculated to be

$$\begin{aligned} a_{vk} &= \frac{M_0}{\pi k} \left[\sin\left(\frac{2\pi}{\lambda_u} ky_2\right) - \sin\left(\frac{2\pi}{\lambda_u} ky_1\right) - \sin\left(\frac{2\pi}{\lambda_u} ky_4\right) + \sin\left(\frac{2\pi}{\lambda_u} ky_3\right) \right] \\ b_{vk} &= \frac{M_0}{\pi k} \left[-\cos\left(\frac{2\pi}{\lambda_u} ky_2\right) + \cos\left(\frac{2\pi}{\lambda_u} ky_1\right) + \cos\left(\frac{2\pi}{\lambda_u} ky_4\right) - \cos\left(\frac{2\pi}{\lambda_u} ky_3\right) \right] \\ a_{hk} &= \frac{M_0}{\pi k} \left[\sin\left(\frac{2\pi}{\lambda_u} ky_1\right) - \sin\left(\frac{2\pi}{\lambda_u} ky_3\right) + \sin\left(\frac{2\pi}{\lambda_u} ky_2\right) - \sin\left(\frac{2\pi}{\lambda_u} ky_4\right) \right] \\ b_{hk} &= \frac{M_0}{\pi k} \left[-\cos\left(\frac{2\pi}{\lambda_u} ky_1\right) + \cos\left(\frac{2\pi}{\lambda_u} ky_3\right) - \cos\left(\frac{2\pi}{\lambda_u} ky_2\right) + \cos\left(\frac{2\pi}{\lambda_u} ky_4\right) \right]. \end{aligned} \quad (3.7)$$

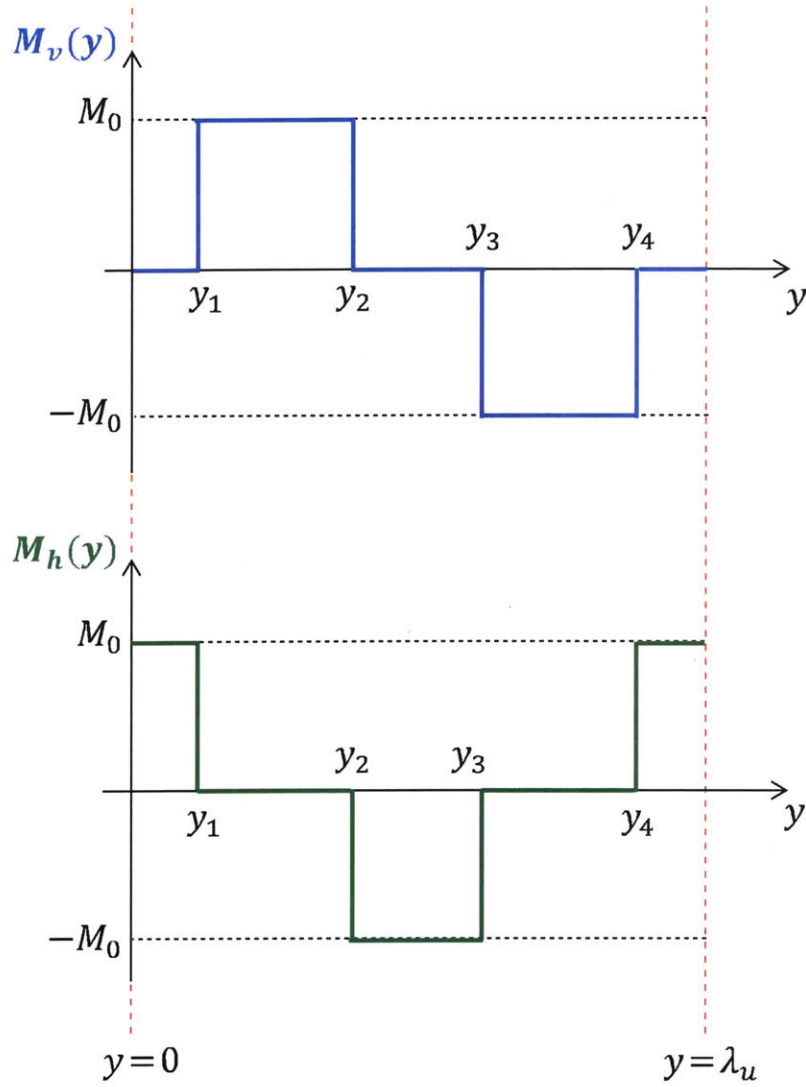


Figure 3-5: Vertical and horizontal magnetization waveform of the Halbach magnet array with the magnetization amplitude M_0 . Both magnetizations are a function of y and periodic with the period of $\lambda_u = \lambda_{pp}$. The locations of $y = y_1, y_2, y_3,$ and y_4 are the magnet boundaries as shown in Figure 3-4.

The general solution of the Poisson's equation in (3.4) can be divided into a homogeneous solution $\psi_h(y, z)$ and a particular solution $\psi_p(y)$, which can be solved by

$$\begin{aligned}\nabla^2\psi_h(y, z) &= 0 \\ \nabla^2\psi_p(y) &= \nabla \cdot \vec{M}.\end{aligned}\tag{3.8}$$

Note that the particular solution is assumed be a function of only y due to thin magnets. The general solution to the Poisson's equation is then obtained as in

$$\psi = \psi_h + \psi_p = \left(A \cos \frac{2\pi}{\lambda_u} ky + B \sin \frac{2\pi}{\lambda_u} ky \right) \left(C e^{\frac{2\pi}{\lambda_u} kz} + D e^{-\frac{2\pi}{\lambda_u} kz} \right) + \int M_h(y) dy.\tag{3.9}$$

where A , B , C , and D are the Poisson solution constants which are determined for each harmonic. We can obtain the magnetic field strength in both the normal (H_z) and tangential (H_y) directions using the scalar potential solution of the Poisson's equation in (3.9) by the relations of

$$\begin{aligned}H_z &= -\frac{\partial\psi}{\partial z} = \left(-L e^{\frac{2\pi}{\lambda_u} kz} + M e^{-\frac{2\pi}{\lambda_u} kz} \right) \cos \frac{2\pi}{\lambda_u} ky + \left(-N e^{\frac{2\pi}{\lambda_u} kz} + O e^{-\frac{2\pi}{\lambda_u} kz} \right) \sin \frac{2\pi}{\lambda_u} ky \\ H_y &= -\frac{\partial\psi}{\partial y} = \left(-N e^{\frac{2\pi}{\lambda_u} kz} - O e^{-\frac{2\pi}{\lambda_u} kz} \right) \cos \frac{2\pi}{\lambda_u} ky + \left(L e^{\frac{2\pi}{\lambda_u} kz} + M e^{-\frac{2\pi}{\lambda_u} kz} \right) \sin \frac{2\pi}{\lambda_u} ky - M_h(y)\end{aligned}\tag{3.10}$$

where L , M , N , and O are the resultant constants from the combinations of A , B , C , and D . Using (3.10), we can solve the magnetic fields at each boundary of the magnet track.

At the boundary of the tooth tip location ($z = z_1$), we obtain the normal direction magnetic flux density $B_z|_{z=z_1}$ and the tangential direction magnetic field $H_y|_{z=z_1}$ as in

$$\begin{aligned}
B_z|_{z=z_1} &= \mu_0 H_z|_{z=z_1} = \mu_0 H_\perp \\
&= \mu_0 \left(-L_{12} e^{\frac{2\pi}{\lambda_u} kz} + M_{12} e^{-\frac{2\pi}{\lambda_u} kz} \right) \cos \frac{2\pi}{\lambda_u} ky + \mu_0 \left(-N_{12} e^{\frac{2\pi}{\lambda_u} kz} + O_{12} e^{-\frac{2\pi}{\lambda_u} kz} \right) \sin \frac{2\pi}{\lambda_u} ky \\
&= a_\perp \cos \frac{2\pi}{\lambda_u} ky + b_\perp \sin \frac{2\pi}{\lambda_u} ky
\end{aligned} \tag{3.11}$$

$$\begin{aligned}
H_y|_{z=z_1} &= H_\parallel \\
&= \left(-N_{12} e^{\frac{2\pi}{\lambda_u} kz} - O_{12} e^{-\frac{2\pi}{\lambda_u} kz} \right) \cos \frac{2\pi}{\lambda_u} ky + \left(L_{12} e^{\frac{2\pi}{\lambda_u} kz} + M_{12} e^{-\frac{2\pi}{\lambda_u} kz} \right) \sin \frac{2\pi}{\lambda_u} ky \\
&= a_\parallel \cos \frac{2\pi}{\lambda_u} ky + b_\parallel \sin \frac{2\pi}{\lambda_u} ky
\end{aligned} \tag{3.12}$$

where H_\perp , H_\parallel , L_{12} , M_{12} , N_{12} , and O_{12} are the perpendicular magnetic field strength in the working air gap, the horizontal magnetic field strength in the air gap, and the field constants in Region1-2. Note that both $B_z|_{z=z_1}$ and $H_y|_{z=z_1}$ are also expressed in the form of Fourier Series since they are assumed to be periodic. We will discuss shortly how we can determine the FS coefficients a_\perp , b_\perp , a_\parallel , and b_\parallel .

We can obtain the magnetic fields at all boundaries ($z = z_2$, z_3 , and z_4) in the magnet track section in the same way described above. We can then organize the magnetic field equations in a matrix form of

$$A_{Maxwell} C = B_{Maxwell}, \tag{3.13}$$

where $A_{Maxwell}$, C , and $B_{Maxwell}$ are given in (3.14), (3.15), and (3.16), respectively. The matrix $A_{Maxwell}$ is determined by the motor geometry and is known for a given motor design. The column vector $B_{Maxwell}$ is the Fourier Series (FS) coefficients of magnetic fields in both the tangential and normal directions at each boundary in the magnet track. These FS coefficients can be solved directly at all boundaries, except for the air-gap region (a_\parallel and b_\parallel) whose magnetic fields should be calculated from the flux-tube model as discussed in the next subsection. The other column vector, C in (3.13) is the field coefficients in all three uniform layer regions.

(3.14)

$$A_{Maxwell} = \begin{bmatrix} e^{\frac{2\pi}{\lambda_u} kz_1} & e^{-\frac{2\pi}{\lambda_u} kz_1} & 0 & 0 & 0 & 0 & 0 & 0 & 0 & 0 & 0 & 0 & 0 \\ 0 & 0 & -e^{\frac{2\pi}{\lambda_u} kz_1} & -e^{-\frac{2\pi}{\lambda_u} kz_1} & 0 & 0 & 0 & 0 & 0 & 0 & 0 & 0 & 0 \\ -e^{\frac{2\pi}{\lambda_u} kz_2} & e^{-\frac{2\pi}{\lambda_u} kz_2} & 0 & 0 & e^{\frac{2\pi}{\lambda_u} kz_2} & -e^{-\frac{2\pi}{\lambda_u} kz_2} & 0 & 0 & 0 & 0 & 0 & 0 & 0 \\ 0 & 0 & -e^{\frac{2\pi}{\lambda_u} kz_2} & e^{-\frac{2\pi}{\lambda_u} kz_2} & 0 & 0 & e^{\frac{2\pi}{\lambda_u} kz_2} & -e^{-\frac{2\pi}{\lambda_u} kz_2} & 0 & 0 & 0 & 0 & 0 \\ e^{\frac{2\pi}{\lambda_u} kz_2} & e^{-\frac{2\pi}{\lambda_u} kz_2} & 0 & 0 & -e^{\frac{2\pi}{\lambda_u} kz_2} & -e^{-\frac{2\pi}{\lambda_u} kz_2} & 0 & 0 & 0 & 0 & 0 & 0 & 0 \\ 0 & 0 & -e^{\frac{2\pi}{\lambda_u} kz_2} & -e^{-\frac{2\pi}{\lambda_u} kz_2} & 0 & 0 & e^{\frac{2\pi}{\lambda_u} kz_2} & e^{-\frac{2\pi}{\lambda_u} kz_2} & 0 & 0 & 0 & 0 & 0 \\ 0 & 0 & 0 & 0 & -\mu_0 e^{\frac{2\pi}{\lambda_u} kz_3} & \mu_0 e^{-\frac{2\pi}{\lambda_u} kz_3} & 0 & 0 & \mu_c e^{\frac{2\pi}{\lambda_u} kz_3} & -\mu_c e^{-\frac{2\pi}{\lambda_u} kz_3} & 0 & 0 & 0 \\ 0 & 0 & 0 & 0 & 0 & 0 & -\mu_0 e^{\frac{2\pi}{\lambda_u} kz_3} & \mu_0 e^{-\frac{2\pi}{\lambda_u} kz_3} & 0 & 0 & \mu_c e^{\frac{2\pi}{\lambda_u} kz_3} & -\mu_c e^{-\frac{2\pi}{\lambda_u} kz_3} & 0 \\ 0 & 0 & 0 & 0 & e^{\frac{2\pi}{\lambda_u} kz_3} & e^{-\frac{2\pi}{\lambda_u} kz_3} & 0 & 0 & -e^{\frac{2\pi}{\lambda_u} kz_3} & -e^{-\frac{2\pi}{\lambda_u} kz_3} & 0 & 0 & 0 \\ 0 & 0 & 0 & 0 & 0 & 0 & -e^{\frac{2\pi}{\lambda_u} kz_3} & -e^{-\frac{2\pi}{\lambda_u} kz_3} & 0 & 0 & e^{\frac{2\pi}{\lambda_u} kz_3} & e^{-\frac{2\pi}{\lambda_u} kz_3} & 0 \\ 0 & 0 & 0 & 0 & 0 & 0 & 0 & 0 & -e^{\frac{2\pi}{\lambda_u} kz_4} & e^{-\frac{2\pi}{\lambda_u} kz_4} & 0 & 0 & 0 \\ 0 & 0 & 0 & 0 & 0 & 0 & 0 & 0 & 0 & 0 & -e^{\frac{2\pi}{\lambda_u} kz_4} & e^{-\frac{2\pi}{\lambda_u} kz_4} & 0 \end{bmatrix} \infty$$

$$C = \begin{bmatrix} L_{12} \\ M_{12} \\ N_{12} \\ O_{12} \\ L_{23} \\ M_{23} \\ N_{23} \\ O_{23} \\ L_{34} \\ M_{34} \\ N_{34} \\ O_{34} \end{bmatrix} \quad (3.15)$$

$$B_{Maxwell} = \begin{bmatrix} b_{\parallel} \\ a_{\parallel} \\ a_{vk} \\ b_{vk} \\ b_{hk} \\ a_{hk} \\ -\mu_0 a_{vk} \\ -\mu_0 b_{vk} \\ -b_{hk} \\ -a_{hk} \\ 0 \\ 0 \end{bmatrix} \quad (3.16)$$

The FS coefficients in the air-gap region (a_{\parallel} and b_{\parallel}) are the input to the Maxwell model given from the flux-tube model in the stator armature. The field coefficient vector C is then obtained by

$$C = A_{Maxwell}^{-1} B_{Maxwell}. \quad (3.17)$$

Once we have all the field coefficient values, we can obtain the magnetic fields at all regions in the magnet track. In the following subsections, we present the flux-tube model for the stator armature, and discuss the iteration scheme between two models for the completed hybrid layer model.

3.2.2 Flux-tube Model for Stator Armature

Due to the geometric complexity and material nonlinearity, it is difficult to directly solve Maxwell's equations in the stator armature. Thus, we use a lumped flux-tube model in this region to solve the equivalent magnetic circuit [3, 67–72] of the nonlinear reluctance network as shown in Figure 3-6. Note that the slot width is a bit exaggerated in the figure in order to clearly draw the reluctance links for the fringing fields in the slots. The magnetic flux ϕ 's are inputted from the Maxwell model using its output of B_{\perp} in the air gap by

$$\phi = B_{\perp} A_t \quad (3.18)$$

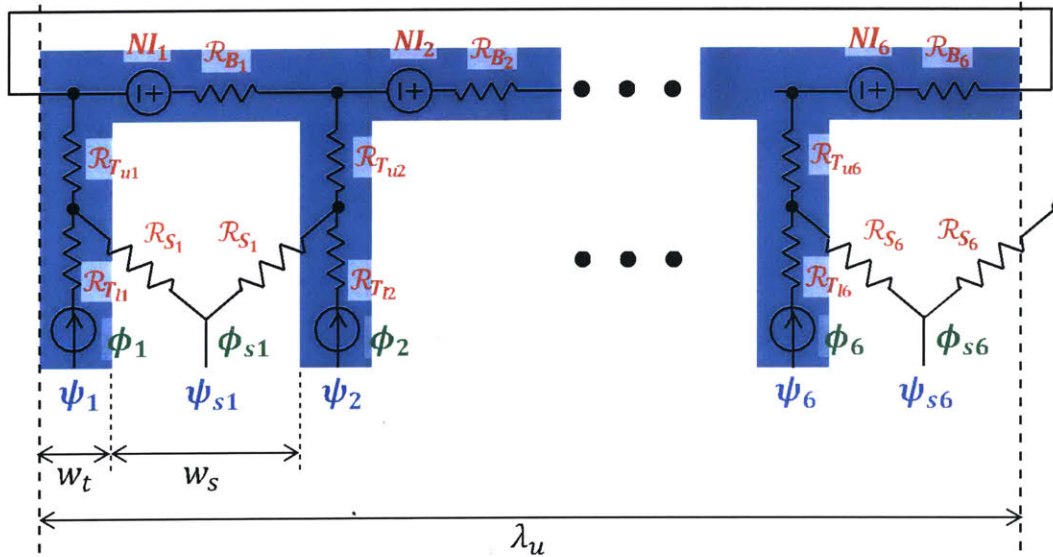


Figure 3-6: Network of nonlinear reluctances in the flux-tube model for the example 3-phase stator shown in Figure 3-3. The equivalent magnetic circuit is solved for the magnetic potential ψ 's when the magnetic flux ϕ 's are given as the input from the Maxwell model.

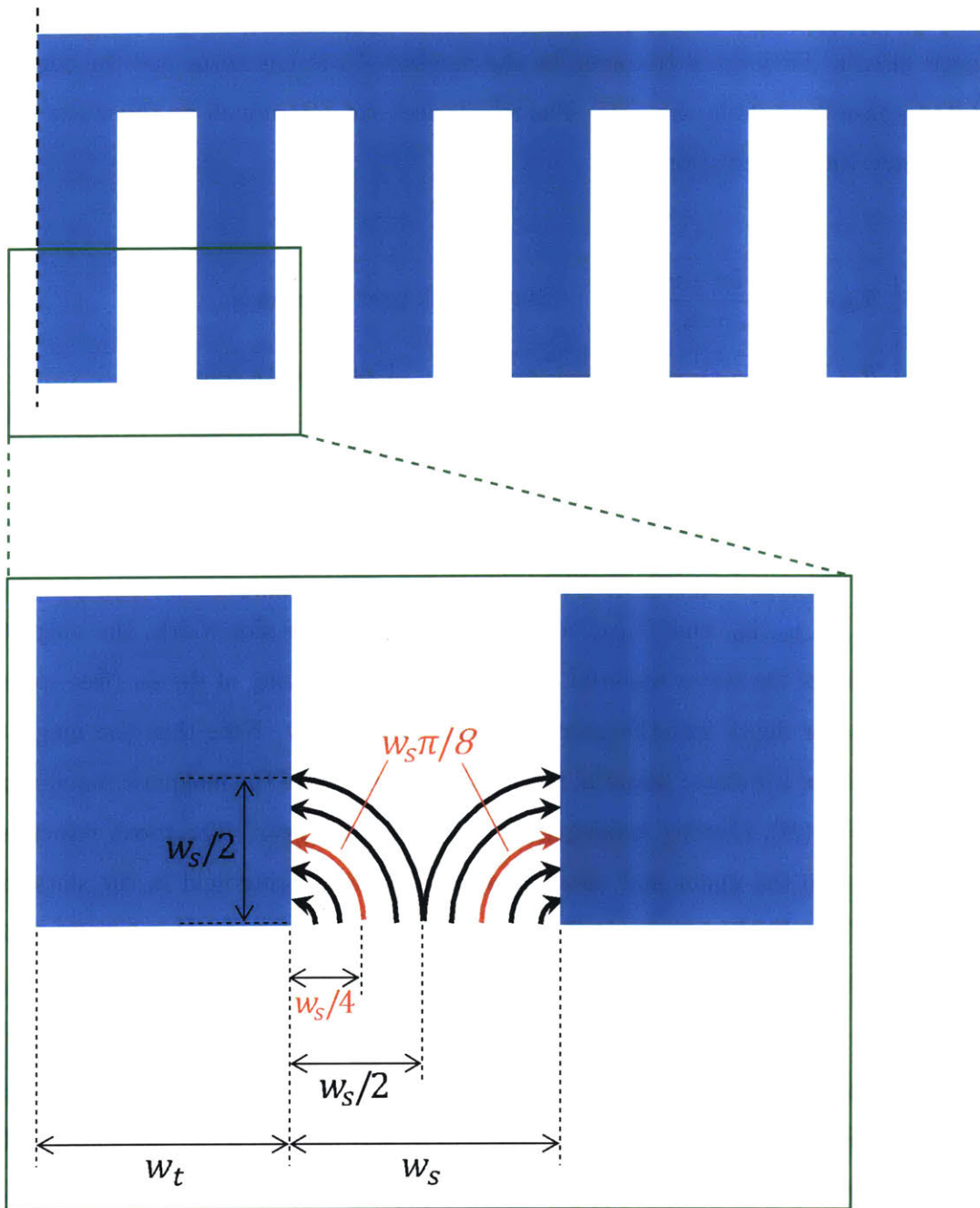


Figure 3-7: Schematic of assumed flux tube for the fringing fields in the slots. The magnified view of teeth and a slot is in the green box showing the characteristic length of $w_s\pi/8$ and the area of $(w_s/2)D_{motor}$, where D_{motor} is the depth of the motor into the page.

where A_t is the cross-section area of a tooth that the flux goes through. The ampere-turns NI 's are the magnetic potential to drive the magnetic flux to flow in the magnetic circuit. They are determined by the number of winding turns and the commutated phase currents in the slots. The reluctances are determined by the stator yoke geometry with the relations of

$$\left\{ \begin{array}{l} \mathcal{R}_B = \frac{w_t + w_s}{\mu_c(z_u - z_0)D_{motor}} \quad : \text{Stator back iron reluctance} \\ \mathcal{R}_{T_u} = \frac{(z_0 - z_1) - w_s/2 + (z_u - z_0)/2}{\mu_c w_t D_{motor}} \quad : \text{Upper tooth reluctance} \\ \mathcal{R}_{T_l} = \frac{w_s/2}{\mu_c w_t D_{motor}} \quad : \text{Lower tooth reluctance} \\ \mathcal{R}_s = \frac{w_s \pi / 8}{\mu_0 (w_s / 2) D_{motor}} \quad : \text{Slot fringing reluctance} \end{array} \right. \quad (3.19)$$

where w_t , w_s , μ_c , μ_0 , and D_{motor} are the tooth width, the slot width, the magnetic permeability of the stator material, the magnetic permeability of the air (free space), and the motor depth into-the-page direction, respectively. Note that the magnetic permeability of the stator material is a nonlinear function of the magnetic flux density as in $\mu_c = \mu_c(B)$, thereby making the reluctances nonlinear. The tooth reluctance is divided into the upper and lower ones to take the fringing field in the slots into account. The dividing point is the assumed upper limit of the slot fringing field, which is a half of the slot width, $w_s/2$. A circular shape is assumed for the fringing field [67].

We can solve the equivalent magnetic circuit using the standard electrical circuit techniques of Kirchoff's Voltage Law (KVL) and Kirchoff's Current Law (KCL). The relationship among the magnetic potential ψ 's, the ampere-turns NI 's, and the magnetic flux ϕ 's can be organized in a matrix form of

$$A_{flux} \vec{\phi} + A_{source} \overrightarrow{NI} = A_{mmf} \vec{\psi} \quad (3.20)$$

where A_{flux} , A_{source} , A_{mmf} , $\vec{\phi}$, \overrightarrow{NI} , and $\vec{\psi}$ are given in (3.21)-(3.24).

(3.21)

$$A_{flux} = \begin{bmatrix} 1 + \frac{\mathcal{R}_{I_{11}} + \mathcal{R}_{I_{v1}}}{\mathcal{R}_{D_1}} + \frac{\mathcal{R}_{I_{11}} + \mathcal{R}_{I_{v1}}}{\mathcal{R}_{D_6}} & \frac{\mathcal{R}_{I_{v1}} - \mathcal{R}_{I_{v2}}}{2\mathcal{R}_{D_1}} + \frac{\mathcal{R}_{I_{v1}}}{2\mathcal{R}_{D_6}} + \frac{1}{2} & -\frac{\mathcal{R}_{I_{12}} + \mathcal{R}_{I_{v2}}}{\mathcal{R}_{D_1}} & -\frac{\mathcal{R}_{I_{v2}}}{2\mathcal{R}_{D_1}} & 0 & 0 \\ \frac{2\mathcal{R}_{I_{11}}}{\mathcal{R}_{s_1}} & -1 & 0 & 0 & 0 & 0 \\ -\frac{\mathcal{R}_{I_{11}} + \mathcal{R}_{I_{v1}}}{\mathcal{R}_{D_1}} & \frac{\mathcal{R}_{I_{v2}}}{2\mathcal{R}_{D_2}} + \frac{\mathcal{R}_{I_{v2}} - \mathcal{R}_{I_{v1}}}{2\mathcal{R}_{D_1}} + \frac{1}{2} & 1 + \frac{\mathcal{R}_{I_{12}} + \mathcal{R}_{I_{v2}}}{\mathcal{R}_{D_2}} + \frac{\mathcal{R}_{I_{12}} + \mathcal{R}_{I_{v2}}}{\mathcal{R}_{D_1}} & \frac{\mathcal{R}_{I_{v2}} - \mathcal{R}_{I_{v3}}}{2\mathcal{R}_{D_2}} + \frac{\mathcal{R}_{I_{v2}}}{2\mathcal{R}_{D_1}} + \frac{1}{2} & -\frac{\mathcal{R}_{I_{13}} + \mathcal{R}_{I_{v3}}}{\mathcal{R}_{D_2}} & -\frac{\mathcal{R}_{I_{v3}}}{2\mathcal{R}_{D_2}} \\ 0 & 0 & \frac{2\mathcal{R}_{I_{12}}}{\mathcal{R}_{s_2}} & -1 & 0 & 0 \\ 0 & -\frac{\mathcal{R}_{I_{v2}}}{2\mathcal{R}_{D_2}} & -\frac{\mathcal{R}_{I_{12}} + \mathcal{R}_{I_{v2}}}{\mathcal{R}_{D_2}} & \frac{\mathcal{R}_{I_{v3}}}{2\mathcal{R}_{D_3}} + \frac{\mathcal{R}_{I_{v3}} - \mathcal{R}_{I_{v2}}}{2\mathcal{R}_{D_2}} + \frac{1}{2} & 1 + \frac{\mathcal{R}_{I_{13}} + \mathcal{R}_{I_{v3}}}{\mathcal{R}_{D_3}} + \frac{\mathcal{R}_{I_{13}} + \mathcal{R}_{I_{v3}}}{\mathcal{R}_{D_2}} & \frac{\mathcal{R}_{I_{v3}} - \mathcal{R}_{I_{v4}}}{2\mathcal{R}_{D_3}} + \frac{\mathcal{R}_{I_{v3}}}{2\mathcal{R}_{D_2}} + \frac{1}{2} \\ 0 & 0 & 0 & 0 & \frac{2\mathcal{R}_{I_{13}}}{\mathcal{R}_{s_3}} & -1 \\ 0 & 0 & 0 & 0 & -\frac{\mathcal{R}_{I_{13}} + \mathcal{R}_{I_{v3}}}{\mathcal{R}_{D_3}} & \frac{\mathcal{R}_{I_{v4}}}{2\mathcal{R}_{D_4}} + \frac{\mathcal{R}_{I_{v4}} - \mathcal{R}_{I_{v3}}}{2\mathcal{R}_{D_3}} + \frac{1}{2} \\ 0 & 0 & 0 & 0 & 0 & 0 \\ 0 & 0 & 0 & 0 & 0 & -\frac{\mathcal{R}_{I_{v4}}}{2\mathcal{R}_{D_4}} \\ 0 & 0 & 0 & 0 & 0 & 0 \\ -\frac{\mathcal{R}_{I_{11}} + \mathcal{R}_{I_{v1}}}{\mathcal{R}_{D_6}} & -\frac{\mathcal{R}_{I_{v1}}}{2\mathcal{R}_{D_6}} & 0 & 0 & 0 & 0 \\ 0 & 0 & 0 & 0 & 0 & 0 \end{bmatrix}$$

$$\left[\begin{array}{ccccccc}
0 & 0 & 0 & -\frac{\mathcal{R}_{I_{u6}}}{2\mathcal{R}_{D_6}} & -\frac{\mathcal{R}_{I_{16}}+\mathcal{R}_{I_{u6}}}{\mathcal{R}_{D_6}} & \frac{\mathcal{R}_{I_{u4}}}{2\mathcal{R}_{D_1}} + \frac{\mathcal{R}_{I_{u4}}-\mathcal{R}_{I_{u6}}}{2\mathcal{R}_{D_6}} + \frac{1}{2} \\
0 & 0 & 0 & 0 & 0 & 0 \\
0 & 0 & 0 & 0 & 0 & -\frac{\mathcal{R}_{I_{u4}}}{2\mathcal{R}_{D_1}} \\
0 & 0 & 0 & 0 & 0 & 0 \\
-\frac{\mathcal{R}_{I_{14}}+\mathcal{R}_{I_{u4}}}{\mathcal{R}_{D_3}} & -\frac{\mathcal{R}_{I_{u4}}}{2\mathcal{R}_{D_3}} & 0 & 0 & 0 & 0 \\
0 & 0 & 0 & 0 & 0 & 0 \\
1 + \frac{\mathcal{R}_{I_{14}}+\mathcal{R}_{I_{u4}}}{\mathcal{R}_{D_4}} + \frac{\mathcal{R}_{I_{14}}+\mathcal{R}_{I_{u4}}}{\mathcal{R}_{D_3}} & \frac{\mathcal{R}_{I_{u4}}-\mathcal{R}_{I_{u6}}}{2\mathcal{R}_{D_4}} + \frac{\mathcal{R}_{I_{u4}}}{2\mathcal{R}_{D_3}} + \frac{1}{2} & -\frac{\mathcal{R}_{I_{16}}+\mathcal{R}_{I_{u6}}}{\mathcal{R}_{D_4}} & -\frac{\mathcal{R}_{I_{u6}}}{2\mathcal{R}_{D_4}} & 0 & 0 \\
\frac{2\mathcal{R}_{I_{14}}}{\mathcal{R}_{s_4}} & -1 & 0 & 0 & 0 & 0 \\
-\frac{\mathcal{R}_{I_{14}}+\mathcal{R}_{I_{u4}}}{\mathcal{R}_{D_4}} & \frac{\mathcal{R}_{I_{u6}}}{2\mathcal{R}_{D_5}} + \frac{\mathcal{R}_{I_{u6}}-\mathcal{R}_{I_{u4}}}{2\mathcal{R}_{D_4}} + \frac{1}{2} & 1 + \frac{\mathcal{R}_{I_{16}}+\mathcal{R}_{I_{u6}}}{\mathcal{R}_{D_5}} + \frac{\mathcal{R}_{I_{16}}+\mathcal{R}_{I_{u6}}}{\mathcal{R}_{D_4}} & \frac{\mathcal{R}_{I_{u6}}-\mathcal{R}_{I_{u6}}}{2\mathcal{R}_{D_6}} + \frac{\mathcal{R}_{I_{u6}}}{2\mathcal{R}_{D_4}} + \frac{1}{2} & -\frac{\mathcal{R}_{I_{16}}+\mathcal{R}_{I_{u6}}}{\mathcal{R}_{D_5}} & -\frac{\mathcal{R}_{I_{u6}}}{2\mathcal{R}_{D_6}} \\
0 & 0 & \frac{2\mathcal{R}_{I_{16}}}{\mathcal{R}_{s_5}} & -1 & 0 & 0 \\
0 & -\frac{\mathcal{R}_{I_{u6}}}{2\mathcal{R}_{D_5}} & -\frac{\mathcal{R}_{I_{16}}+\mathcal{R}_{I_{u6}}}{\mathcal{R}_{D_5}} & \frac{\mathcal{R}_{I_{u6}}}{2\mathcal{R}_{D_6}} + \frac{\mathcal{R}_{I_{u6}}-\mathcal{R}_{I_{u6}}}{2\mathcal{R}_{D_5}} + \frac{1}{2} & 1 + \frac{\mathcal{R}_{I_{16}}+\mathcal{R}_{I_{u6}}}{\mathcal{R}_{D_6}} + \frac{\mathcal{R}_{I_{16}}+\mathcal{R}_{I_{u6}}}{\mathcal{R}_{D_5}} & \frac{\mathcal{R}_{I_{u6}}-\mathcal{R}_{I_{u4}}}{2\mathcal{R}_{D_6}} + \frac{\mathcal{R}_{I_{u6}}}{2\mathcal{R}_{D_5}} + \frac{1}{2} \\
0 & 0 & 0 & 0 & \frac{2\mathcal{R}_{I_{16}}}{\mathcal{R}_{s_6}} & -1
\end{array} \right]$$

(3.22)

$$A_{source} = \begin{bmatrix} -\frac{1}{\mathcal{R}_{B_1}} & 0 & 0 & 0 & 0 & 0 & 0 & 0 & 0 & 0 & \frac{1}{\mathcal{R}_{B_6}} & 0 \\ 0 & 0 & 0 & 0 & 0 & 0 & 0 & 0 & 0 & 0 & 0 & 0 \\ \frac{1}{\mathcal{R}_{B_1}} & 0 & -\frac{1}{\mathcal{R}_{B_2}} & 0 & 0 & 0 & 0 & 0 & 0 & 0 & 0 & 0 \\ 0 & 0 & 0 & 0 & 0 & 0 & 0 & 0 & 0 & 0 & 0 & 0 \\ 0 & 0 & \frac{1}{\mathcal{R}_{B_2}} & 0 & -\frac{1}{\mathcal{R}_{B_3}} & 0 & 0 & 0 & 0 & 0 & 0 & 0 \\ 0 & 0 & 0 & 0 & 0 & 0 & 0 & 0 & 0 & 0 & 0 & 0 \\ 0 & 0 & 0 & 0 & \frac{1}{\mathcal{R}_{B_3}} & 0 & -\frac{1}{\mathcal{R}_{B_4}} & 0 & 0 & 0 & 0 & 0 \\ 0 & 0 & 0 & 0 & 0 & 0 & 0 & 0 & 0 & 0 & 0 & 0 \\ 0 & 0 & 0 & 0 & 0 & 0 & \frac{1}{\mathcal{R}_{B_4}} & 0 & -\frac{1}{\mathcal{R}_{B_5}} & 0 & 0 & 0 \\ 0 & 0 & 0 & 0 & 0 & 0 & 0 & 0 & 0 & 0 & 0 & 0 \\ 0 & 0 & 0 & 0 & 0 & 0 & 0 & 0 & \frac{1}{\mathcal{R}_{B_5}} & 0 & -\frac{1}{\mathcal{R}_{B_6}} & 0 \\ 0 & 0 & 0 & 0 & 0 & 0 & 0 & 0 & 0 & 0 & 0 & 0 \end{bmatrix}$$

(3.23)

$$A_{mmf} = \begin{bmatrix} \frac{1}{\mathcal{R}_{B_1}} + \frac{1}{\mathcal{R}_{B_6}} & 0 & -\frac{1}{\mathcal{R}_{B_1}} & 0 & 0 & 0 & 0 & 0 & 0 & 0 & 0 & -\frac{1}{\mathcal{R}_{B_6}} & 0 \\ \frac{2}{\mathcal{R}_{s_1}} & -\frac{2}{\mathcal{R}_{s_1}} & 0 & 0 & 0 & 0 & 0 & 0 & 0 & 0 & 0 & 0 & 0 \\ -\frac{1}{\mathcal{R}_{B_1}} & 0 & \frac{1}{\mathcal{R}_{B_2}} + \frac{1}{\mathcal{R}_{B_1}} & 0 & -\frac{1}{\mathcal{R}_{B_2}} & 0 & 0 & 0 & 0 & 0 & 0 & 0 & 0 \\ 0 & 0 & \frac{2}{\mathcal{R}_{s_2}} & -\frac{2}{\mathcal{R}_{s_2}} & 0 & 0 & 0 & 0 & 0 & 0 & 0 & 0 & 0 \\ 0 & 0 & -\frac{1}{\mathcal{R}_{B_2}} & 0 & \frac{1}{\mathcal{R}_{B_3}} + \frac{1}{\mathcal{R}_{B_2}} & 0 & -\frac{1}{\mathcal{R}_{B_3}} & 0 & 0 & 0 & 0 & 0 & 0 \\ 0 & 0 & 0 & 0 & \frac{2}{\mathcal{R}_{s_3}} & -\frac{2}{\mathcal{R}_{s_3}} & 0 & 0 & 0 & 0 & 0 & 0 & 0 \\ 0 & 0 & 0 & 0 & -\frac{1}{\mathcal{R}_{B_3}} & 0 & \frac{1}{\mathcal{R}_{B_4}} + \frac{1}{\mathcal{R}_{B_3}} & 0 & -\frac{1}{\mathcal{R}_{B_4}} & 0 & 0 & 0 & 0 \\ 0 & 0 & 0 & 0 & 0 & 0 & \frac{2}{\mathcal{R}_{s_4}} & -\frac{2}{\mathcal{R}_{s_4}} & 0 & 0 & 0 & 0 & 0 \\ 0 & 0 & 0 & 0 & 0 & 0 & -\frac{1}{\mathcal{R}_{B_4}} & 0 & \frac{1}{\mathcal{R}_{B_5}} + \frac{1}{\mathcal{R}_{B_4}} & 0 & -\frac{1}{\mathcal{R}_{B_5}} & 0 & 0 \\ 0 & 0 & 0 & 0 & 0 & 0 & 0 & 0 & \frac{2}{\mathcal{R}_{s_5}} & -\frac{2}{\mathcal{R}_{s_5}} & 0 & 0 & 0 \\ -\frac{1}{\mathcal{R}_{B_6}} & 0 & 0 & 0 & 0 & 0 & 0 & 0 & -\frac{1}{\mathcal{R}_{B_5}} & 0 & \frac{1}{\mathcal{R}_{B_6}} + \frac{1}{\mathcal{R}_{B_5}} & 0 & 0 \\ 0 & 0 & 0 & 0 & 0 & 0 & 0 & 0 & 0 & 0 & \frac{2}{\mathcal{R}_{s_6}} & -\frac{2}{\mathcal{R}_{s_6}} & 0 \end{bmatrix}$$

$$\vec{\phi} = \begin{bmatrix} \phi_1 \\ \phi_{s1} \\ \phi_2 \\ \phi_{s2} \\ \phi_3 \\ \phi_{s3} \\ \phi_4 \\ \phi_{s4} \\ \phi_5 \\ \phi_{s5} \\ \phi_6 \\ \phi_{s6} \end{bmatrix}, \quad \vec{NI} = \begin{bmatrix} NI_1 \\ 0 \\ NI_2 \\ 0 \\ NI_3 \\ 0 \\ NI_4 \\ 0 \\ NI_5 \\ 0 \\ NI_6 \\ 0 \end{bmatrix}, \quad \vec{\psi} = \begin{bmatrix} \psi_1 \\ \psi_{s1} \\ \psi_2 \\ \psi_{s2} \\ \psi_3 \\ \psi_{s3} \\ \psi_4 \\ \psi_{s4} \\ \psi_5 \\ \psi_{s5} \\ \psi_6 \\ \psi_{s6} \end{bmatrix} \quad (3.24)$$

The magnetic flux vector $\vec{\phi}$ is inputted from the output of the Maxwell model as in (3.18). We can then solve for the magnetic potential vector $\vec{\psi}$ using the relation of

$$\vec{\psi} = A_{mmf}^{-1}(A_{flux}\vec{\phi} + A_{source}\vec{NI}). \quad (3.25)$$

Note that we solve for the case of a 3-phase stator as shown in Figure 3-6, however, a similar analysis can be applied to other multi-phase cases. The magnetic potential obtained by (3.25) is at the motor working air gap. Using this, we can calculate the magnetic field strength in the air gap as

$$H_{\parallel} = \frac{d\psi}{dy}. \quad (3.26)$$

This air gap magnetic field strength H_{\parallel} is the output of the flux-tube model, which is used as the input to the Maxwell model to provide the FS coefficients a_{\parallel} and b_{\parallel} in (3.12) and (3.16). We discuss in the following subsection the iteration process of these two models to have the completed hybrid layer model.

3.2.3 Iteration of Hybrid Layer Model

Figure 3-8 shows the overall iteration schematic of the hybrid layer model. We first assume the air-gap magnetic flux density in the normal direction, B_{\perp} to calculate the air-gap magnetic flux, ϕ as in (3.18). This magnetic flux is the input to the flux-tube model where we solve the network of nonlinear reluctances to obtain the magnetic scalar potential, ψ in the motor working air-gap. As shown in the figure, the magnetic equivalent circuit is written in a matrix form of (3.20). We solve for ψ by (3.25) with the input of ϕ and the given ampere-turns of NI . The calculated air-gap potential ψ is the output of the flux-tube model, and this is used to obtain the tangential direction air-gap field, H_{\parallel} as in (3.26). We input this magnetic field to the Maxwell model, and solve for the air-gap flux density, B_{\perp} . In the magnet track section, we analytically solve the magnetic fields in both the tangential and normal directions at each boundary, and write the equations in a matrix form of (3.13), as

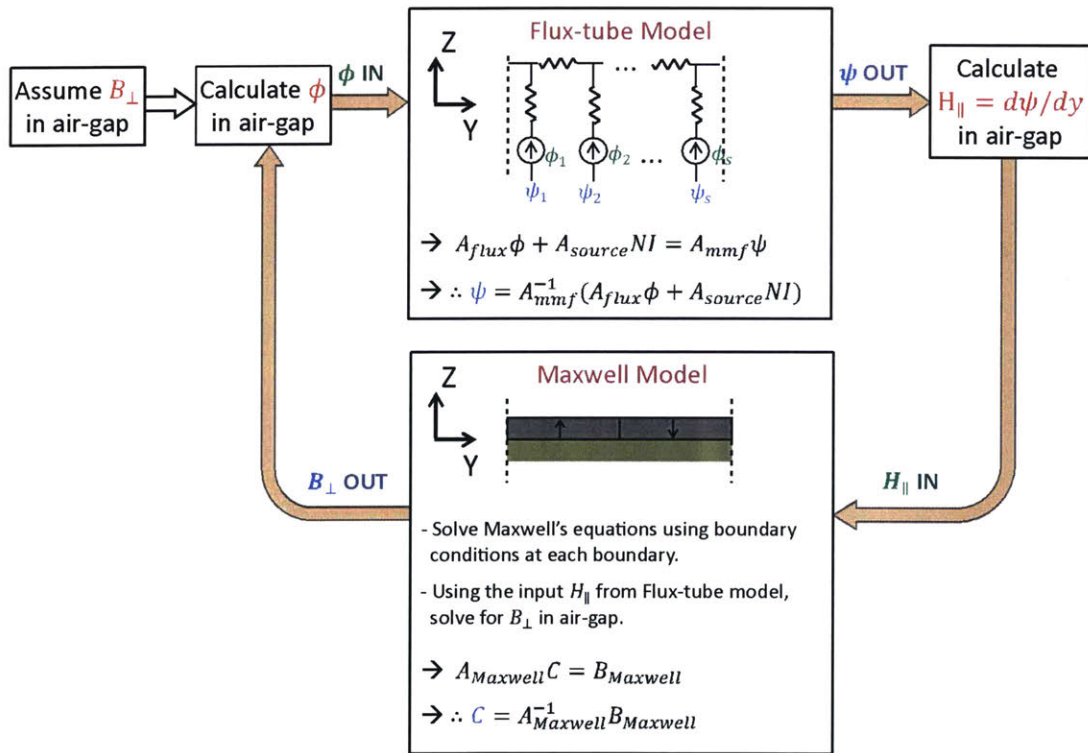


Figure 3-8: Iteration schematic of the hybrid layer model (HLM) between the flux-tube model in the armature core and the Maxwell model in the magnet track.

shown in the figure. Once the vector C is calculated by (3.17), the Poisson solution coefficients (L_{12} , M_{12} , N_{12} , and O_{12}) can be used to obtain the normal direction air-gap magnetic flux density, B_{\perp} as in (3.11). This flux density is again inputted to the flux-tube model, thereby closing the iteration loop. This iteration continues until the change in the air-gap flux ϕ falls into a predefined tolerance [3]. When the iteration loop converges, we calculate the thrust force or cogging force using the calculated magnetic fields in the working air-gap using the Maxwell stress tensor, τ_m as in

$$F = \int \tau_m dA = \int \mu_0 H_{\perp} H_{\parallel} dA \quad (3.27)$$

where A is the force generating area in the working air-gap of a motor, and $\mu_0 H_{\perp}$ and H_{\parallel} are obtained by (3.11) and (3.12), respectively. We present the performance tests of our hybrid layer model in Section 3.2.4.

3.2.4 Performance Compared to Finite Element Method

In order to test the hybrid layer modeling method in the linear iron-core motor application, we compare the model performance of the hybrid layer model (HLM) to the finite element method (FEM) in predicting relevant magnetic functions. Note that we use the 2D finite element software, called FEMM.

Figure 3-9 shows the calculated air-gap magnetic flux density of a linear iron-core motor with 6 teeth/slots per pole over the length of 4 pole pairs. Both the normal- and tangential-direction flux densities are simulated by the FEM (blue solid line) and the hybrid layer model (red dotted line). As shown in the figure, the two simulation results overlap closely, showing that the hybrid layer model has a reasonable fidelity to the FEM. Note that we observe a bit of discrepancy at the ends. This is due to the fact that the hybrid layer model is inherently periodic, but the FEM is not. The finite element model has a finite length so that it captures the magnetic end effects while the hybrid layer model does not, which explains these discrepancies.

We also compare the computed cogging force as shown in Figure 3-10. The cogging is calculated for motion over two tooth pitches (4 mm). As can be seen in the figure,

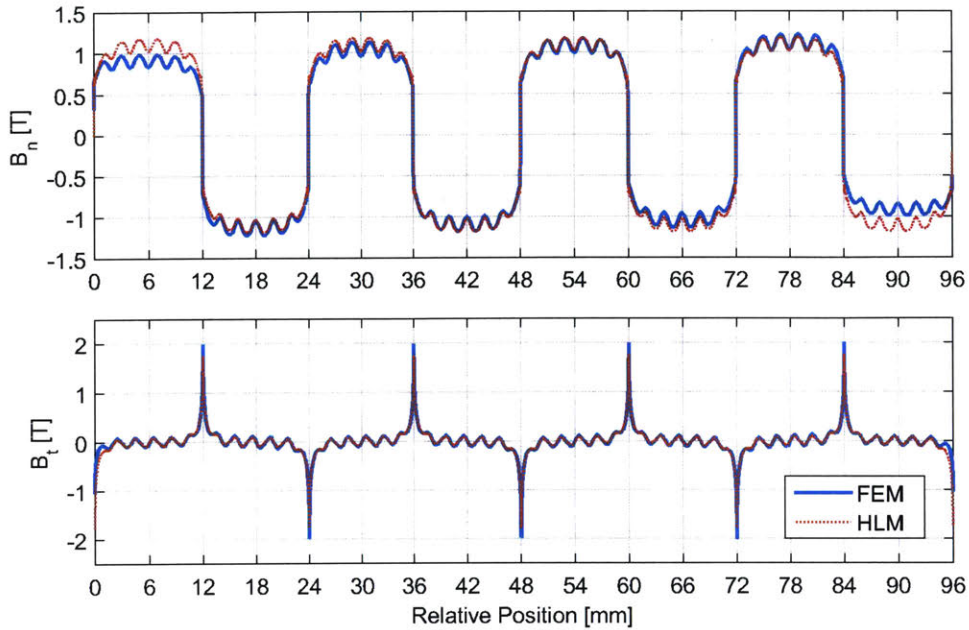


Figure 3-9: Simulated air-gap magnetic flux density by both the finite element method (blue solid line) and our hybrid layer model (red dotted line). Magnetic flux density in Tesla in both the normal (upper) and tangential (lower) directions.

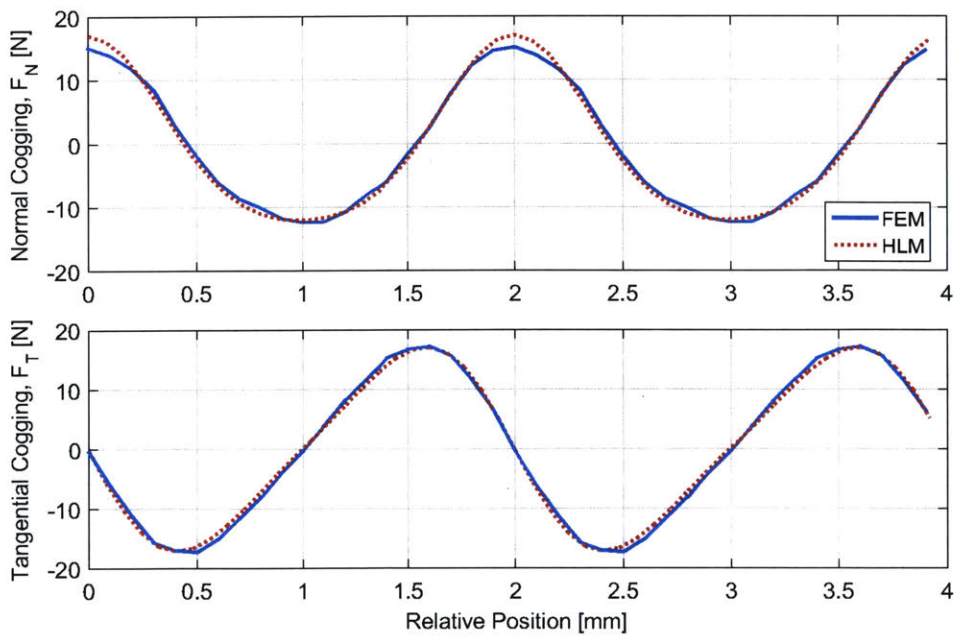


Figure 3-10: Computed cogging force by both the finite element method (blue solid line) and our hybrid layer model (red dotted line). Cogging force in Newtons in both the normal (upper) and tangential (lower) directions.

the cogging period is same as the tooth pitch in both the normal and tangential directions. From this cogging comparison also, we observe the hybrid layer model agrees with results from FEM. In addition, the hybrid layer model has the advantage of much shorter calculation time. For the estimation of the air-gap flux density in Figure 3-9, the hybrid layer model takes only 0.15 second while the FEM takes 317 seconds, showing about 99.95 % calculation time reduction. For the cogging force estimation, the calculation time is also significantly reduced from 5624 seconds (more than one and a half hours) by the FEM to 4 seconds by the hybrid layer model. This faster calculation property together with the high fidelity of the hybrid layer model helps reduce the design time when we have a number of magnetic design variants to compare for optimizing the motor performance. Note that the hybrid layer model works well for lower excitation currents, but ran into problems with convergence at higher currents where iron core saturation is significant. Thus we were unable to use the hybrid layer model for prediction of the motor performance at high currents. It will be a future effort to make it work well at high currents. We discuss a possible approach in Chapter 8. We therefore use this hybrid layer modeling method in conjunction with the FEM in the design process of our new fine-tooth motor, as discussed in Section 3.3.

3.3 New Motor Design Process by Motor Performance Comparison

In this section, we discuss the design process of our new fine-tooth motor. Given that our new fine-tooth motor design in general produces less force harmonics and facilitates the cogging reduction by skewing magnets, the major design objective in this section is to optimize motor design parameters to have higher force performance than the conventional 3-4 combination motor. We introduce the specific design parameters of our new motor, and discuss in detail the selection process of each parameter throughout this section. We use both the hybrid layer model (HLM) and the finite element method (FEM) to determine the parameters. In Section 3.4, we present

the final design parameters with a few practical design modifications and discuss the expected motor performances of our new fine-tooth motor with the final design parameters compared to the conventional motor.

3.3.1 Design Parameters

The schematic design of our new fine-tooth motor is shown in the right-side of Figure 3-1, and the relevant parameters are listed in Figure 3-11. The design parameters are categorized into two groups of the stator armature section and the magnet track section. For the stator armature, the number of phase, N_{slot} which is the same as the number of teeth/slots per pole needs to be determined along with the size of teeth and slots. Note that we keep one-to-one ratio between the widths of tooth (w_t) and slot (w_s). The slot depth is represented by the slot aspect ratio, R_{slot} . We also determine how many winding turns, N are used for the armature with which wire gauge, AWG . For the magnet track design, the Halbach array ratio needs to be decided and it is represented by the fraction of vertical magnets, f_{magnet} out of a pole pitch. We need to also determine the magnet thickness as a parameter of the magnet aspect ratio, PM_{thick} . These design parameters are determined to have high force performance in terms of shear stress and acceleration. We discuss in detail the selection process of each parameter in Sections 3.3.2 and 3.3.3.

Stator Armature	
N_{slot}	Number of slots per pole (# of phase)
w_t, w_s	Tooth and slot width (assumed one-to-one)
R_{slot}	Slot aspect ratio ($h_s = R_{slot} \times w_s$)
N	Number of winding turns
AWG	Wire gauge for winding
Magnet Track	
f_{magnet}	Fraction of vertical magnet ($f_{magnet} = w_m/\lambda_p$)
PM_{thick}	Magnet aspect ratio ($h_m = PM_{thick} \times w_m$)

Figure 3-11: Design parameters of our new fine-tooth motor.

3.3.2 Design Parameter Selection by HLM

We first discuss the design parameters to determine by the hybrid layer model. The number of phases in the stator armature and the Halbach array ratio in the magnet track are determined by using the hybrid layer model to simulate the force performance.

Number of Phases

In order to determine how many number of phases to use in our new fine-tooth motor, we calculate motor shear stress per power versus the number of phase as shown in Figure 3-12. We use the hybrid layer model for the force calculation for each case while keeping the other geometric parameters the same. The shear stress means a magnetic pressure in the working air-gap of a motor, which tells how forceful the motor is. The power dissipation level is also taken into account by dividing the shear stress for a fair comparison.

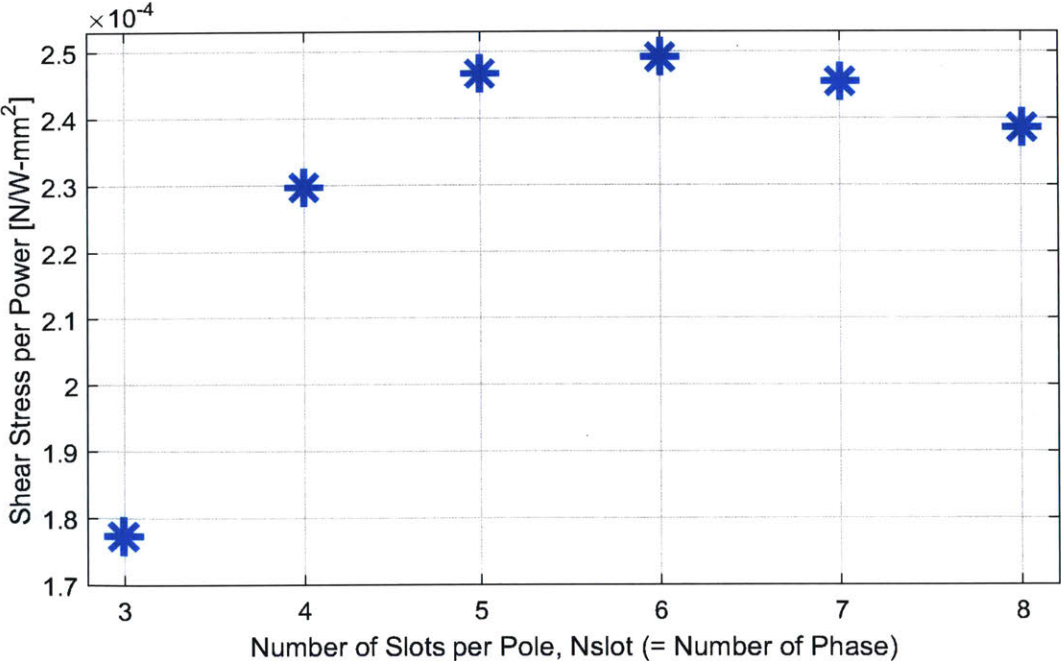


Figure 3-12: Shear stress per power versus the number of motor phases. Shear stress per power is simulated by our hybrid layer model. Power is calculated over a motor unit, which is one pole-pair.

As can be seen in the figure, 5 to 7 phases show relatively higher shear per power performance than the other cases. Among these three cases, we select the 5-phase motor design due to a few practical reasons: 1) For the constant tooth and slot size, the motor design with the higher number of phases would have a higher attractive force. We plan to use air bearings to eliminate any mechanical contacts and the associated vibration, and there is a limitation in the preloading force the air bearings can resist. The relation between the motor attractive force and the air bearing preload are discussed in Chapter 5. 2) For a full-pitch winding, the higher number of phases would require larger overlapping areas for the winding end-turns, thereby making the winding process more difficult and time consuming. The winding scheme and constructed stator armature are presented in Section 3.5.

Halbach Magnet Array Fraction

We choose to use the Halbach magnet array pattern 1) to increase the thrust by the enhanced magnetic field strength in the working air-gap side and 2) to smoothen the rotor (magnet track) MMF waveform to reduce the high harmonic contents as shown in Figure 3-2. The Halbach array pattern contains permanent magnets magnetized both vertically (Z-direction) and horizontally (Y-direction), and it is important to determine the ratio between them since the generated force depends on it. The Halbach magnet array ratio is represented by the fraction of the vertical magnets, f_{magnet} out of a pole pitch as written in

$$f_{magnet} = \frac{w_m}{\lambda_p} \quad (3.28)$$

where w_m and λ_p are the width of the vertical magnets and the magnet pole pitch, respectively.

In order to determine this ratio, we calculate the thrust using the hybrid layer model to plot the normalized thrust versus the vertical magnet fraction, f_{magnet} as shown in Figure 3-13. For this calculation, the stator armature geometry and the magnet thickness are kept the same while only changing the fraction value. We select

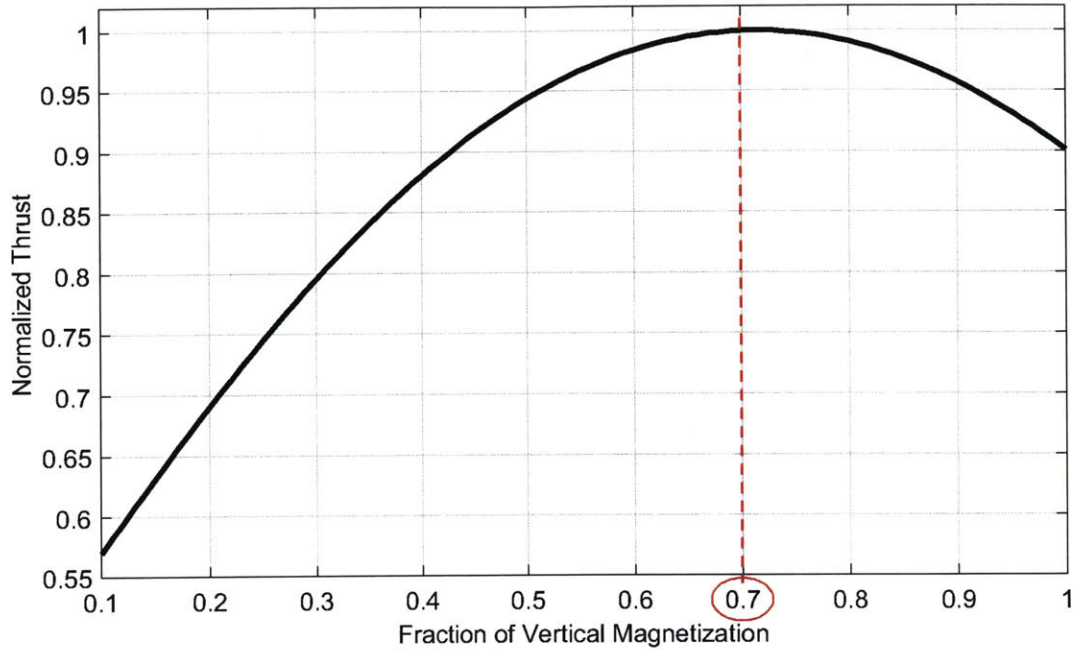


Figure 3-13: Normalized thrust versus Halbach array ratio, f_{magnet} . Thrust force is simulated by our hybrid layer model.

$f_{magnet} = 0.7$, which shows the maximum thrust in the plot. This means that our fine-tooth motor will have 70 % vertical magnets and 30 % horizontal magnets in the moving magnet tracks. This result is similar to that of Ofori [63]. Pictures of the constructed magnet tracks of our new motor are shown in Section 3.5 and their drawings are documented in Appendix A.

3.3.3 Design Parameter Selection by FEM

Despite of the advantages of high fidelity and reduced calculation time, the hybrid layer model is limited in that the model at present does not converge when the material is highly saturated, as shown in Figure 3-14. We speculate that this is due to the fact that the flux-tube model in the stator armature does not contain any leakage paths as shown in Figure 3-6 and in [3]. This makes it difficult to use the hybrid layer modeling method to predict the motor performance at high flux density levels. For this reason, we use the finite element method (FEM) for the selection process

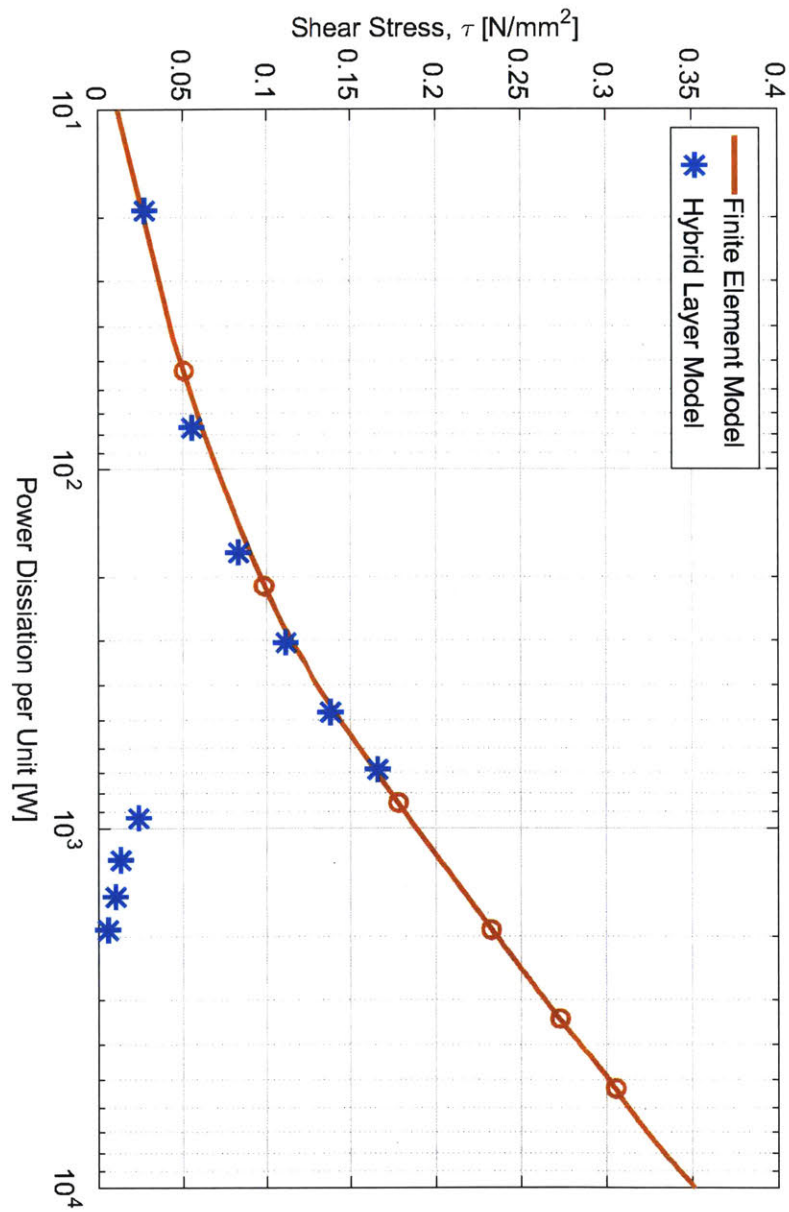


Figure 3-14: Simulated shear stress versus power dissipation per unit 1) to compare our hybrid layer model (HLM) to the finite element model (FEM) and 2) to observe the non-convergence issue of HLM at high currents. The shear stress and power are calculated with the motor design parameters of Case 1 in Figure 3-15 for both HLM (orange curve) and FEM (blue asterisk). The hybrid layer model begins to fail at around 900 W per unit in this case. The meaning of the ordinate and abscissa will be explained shortly in the text.

Fine-Tooth Motor	Input Variables							Output Parameters		
	$w_t = w_s$	R_{slot}	PM_{thick}	N	AWG	Current, I [A]	Common	P_{diss} [W]	J_{max} [A/mm ²]	Comparing Parameters
Case.1	1.5 mm	10	1	42	23	[0,5,10,20,30,40,50,100]	- $N_{slot} = 5$ - $f_{magnet} = 0.7$	2.120 I ²	3.878 I	- Shear stress [N/mm ²] - Final stage accel. [m/s ²] - Force Density [N/kg]
Case.2	1.8 mm	10	1	42	21	[0,5,10,20,30,40,50,100]		1.416 I ²	2.440 I	
Case.3	1.8 mm	15	1	42x1.5= 63	21	[0,5,10,20,30,40,50,100]/1.5	- Amp-turns	2.124 I ²	2.440 I	
Case.4	1.8 mm	20	1	42x2= 84	21	[0,5,10,20,30,40,50,100]/2	- N40 magnets	2.832 I ²	2.440 I	
Case.5	2.0 mm	10	1	42	20	[0,5,10,20,30,40,50,100]	- Halbach array	1.167 I ²	1.930 I	
Case.6	2.5 mm	10	1	42	18	[0,5,10,20,30,40,50,100]	- Skewed PM - Gap: 500um	0.803 I ²	1.214 I	Limiting Factors
Case.7	2.5 mm	10	1	42x2= 84	21	[0,5,10,20,30,40,50,100]/2		3.220 I ²	2.440 I	- RMS current density, J_{rms} due to heat - Current amplitude due to power amplifier - Total power due to wall power limit
Case.8	2.0 mm	15	1	42x1.5= 63	20	[0,5,10,20,30,40,50,100]/1.5	- $N_{slot} = 5$ - $f_{magnet} = 0.7$	1.751 I ²	1.930 I	
Case.9	2.0 mm	15	0.7	42x1.5= 63	20	[0,5,10,20,30,40,50,100]/1.5	- Amp-turns	1.751 I ²	1.930 I	
Case.10	2.0 mm	15	0.5	42x1.5= 63	20	[0,5,10,20,30,40,50,100]/1.5	- N40 magnets - Halbach array	1.751 I ²	1.930 I	
Case.11	2.0 mm	15	0.3	42x1.5= 63	20	[0,5,10,20,30,40,50,100]/1.5	- Skewed PM - Gap: 250um	1.751 I ²	1.930 I	
Tecnotion Motor				141	SWG 22	[0,5,10,20,30,40,50,100]	- Skewed PM - Gap: 500um or 250um	2.580 I ²	2.520 I	

Figure 3-15: Table of various cases to determine design parameters. Four different groups are color-coded for the selection process of five design parameters, w_t ($= w_s$), R_{slot} , PM_{thick} , N , and AWG .

of the design parameters that affect the motor force performances. We predict and compare the shear stress and stage acceleration at a wide power range in various cases to optimize each parameter value. Figure 3-15 shows the various cases of design parameters with four different color-coded groups: tooth/slot width w_t ($= w_s$), slot aspect ratio R_{slot} , magnet aspect ratio PM_{thick} , winding turns N , and wire gauge AWG . The selection process of the design parameters is described as follows.

- 1) For each parameter (color-coded) group, we change only that parameter value while keeping the other the same and select the value that shows the maximum force performance. The force performance is compared in terms of shear stress in [N/mm²] and stage acceleration in [m/s²].

- The shear stress, τ is obtained by

$$\tau = \frac{F_{thrust}}{A} \quad [\text{N/mm}^2] \quad (3.29)$$

where F_{thrust} is the calculated thrust force of a fine-tooth motor by the finite element method, and A is the force-generating area (= magnet array length \times motor depth) in the working air-gap of a motor.

- The stage acceleration, A_{stage} is estimated for a double-sided motor configuration with a stage mass of $M_{stage} = 10$ kg, using the formula of

$$A_{stage} = \frac{F_{thrust}}{M_{stage} + M_{magnet}} \quad [\text{m/s}^2] \quad (3.30)$$

where M_{magnet} is the mass of the moving magnet tracks used for the double-sided motor configuration.

- Note that we use a 2D finite element model as it is computationally much simpler than a 3D model, and captures the key motor design issues including the thrust, cogging, and force ripple. For a real motor design, a 3D FEM model could be used to optimize final details.
- 2) In order to compare the force performance among various design variants of the fine-tooth motor and also to that of the conventional motor, we plot the shear stress and the stage acceleration against the power dissipation per unit and the RMS current density.
- The power dissipation per unit, $P_{diss,unit}$ is the instantaneous peak conductor power loss of

$$P_{diss,unit} = I_p^2 R \quad [\text{W}] \quad (3.31)$$

where I_p and R are the instantaneous peak current and coil resistance over a basic motor unit. The basic unit means the minimal motor magnetic configuration to generate thrust, which consists of 3 iron-core teeth and 4 magnets for the conventional motor and one pole pair for our new fine-tooth motor. The shear stress in (3.29) and the acceleration in (3.30) are compared at the same power levels of one basic motor unit for a fair comparison between two different (conventional and our fine-tooth) motors.

- The RMS current density is the root mean square of instantaneous current density in wire (current divided by a wire cross-section area in [A/mm²]) over a certain velocity trajectory. We calculate the RMS current density in wire by assuming a simple trapezoidal velocity profile with the stage acceleration estimated as mentioned above (3.30), the maximum velocity of $V_{max} = 2.4$ m/s, and the travel length of $Y_{max} = 350$ mm, using the relations of

$$\begin{aligned}
 t_1 &= \frac{V_{max}}{A_{stage}} \quad [\text{s}] \\
 t_2 &= \frac{Y_{max}}{V_{max}} \quad [\text{s}] \\
 J_{rms} &= \sqrt{\frac{2t_1 J_{peak}^2}{t_1 + t_2}} \quad [\text{A/mm}^2],
 \end{aligned} \tag{3.32}$$

where t_1 , t_2 , and J_{peak} are the acceleration/deceleration time, the time from zero to the end of the constant velocity period, and the peak current density in wire to achieve the require acceleration, respectively. Note that the time duration of t_1+t_2 is the half period of a stage cycle. It is important to compare the force performance against the RMS current density in wire because J_{rms} is directly related to the thermal limit of a motor.

- 3) In the following subsections, we present $(\tau - P_{diss,unit})$, $(\tau - J_{rms})$, $(A_{stage} - P_{diss,unit})$, $(A_{stage} - J_{rms})$ plots to compare the force performance between our fine-tooth motor and the conventional motor for optimizing each of our new motor design parameters.

Tooth/Slot Width

In order to determine the tooth/slot width $w_t (= w_s)$ in the blue group in Figure 3-15, we calculate the shear stress and the stage acceleration for all four cases and compare their performances to those of the conventional 3-4 combination motor as shown in Figures 3-16 to 3-19. For all plots in Figures 3-16 to 3-19, the light blue curve is the simulated result of the conventional 3-4 combination motor as a reference, and all the other lines are the design variants of our new fine-tooth motor.

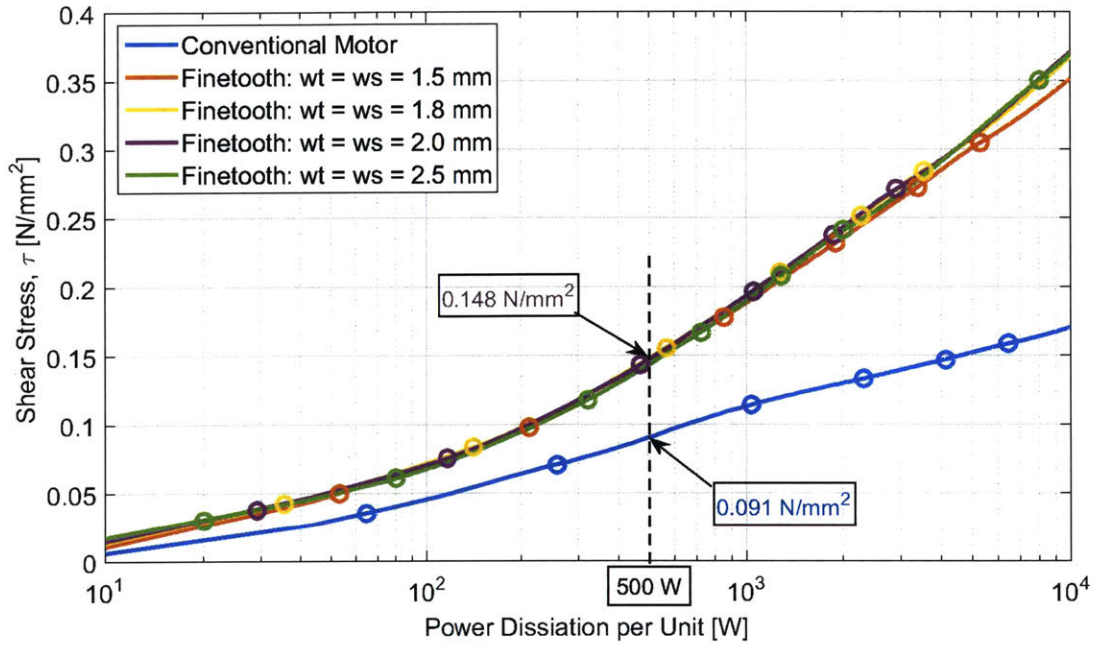


Figure 3-16: Simulated shear stress in (3.29) versus power dissipation per unit in (3.31). By unit, we mean the minimal motor magnetic configuration required to generate a thrust, which consists of 3 iron-core teeth and 4 magnets for the conventional motor and one pole pair for our new fine-tooth motor.

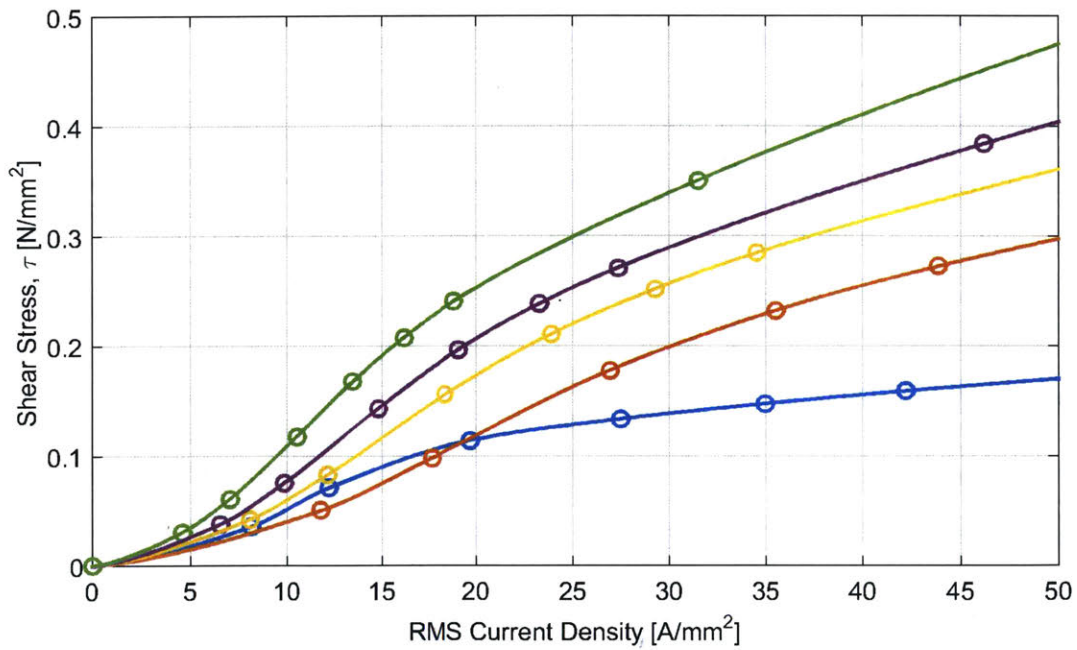


Figure 3-17: Simulated shear stress in (3.29) versus RMS current density in wire in (3.32). Shear stress performance of the conventional motor in light blue line serves as a design reference.

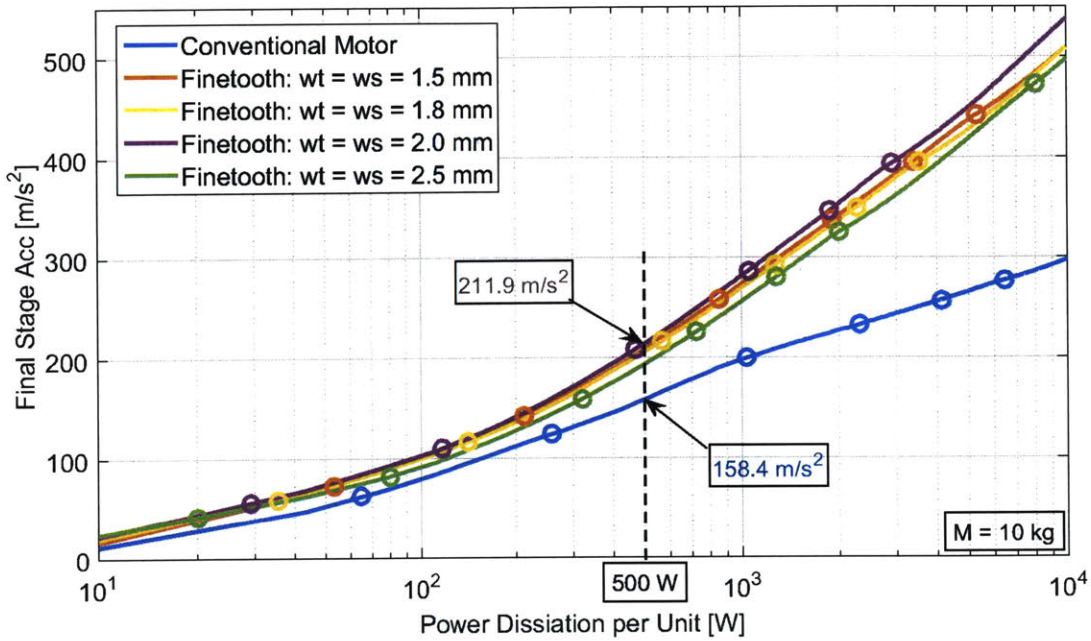


Figure 3-18: Simulated stage acceleration in (3.30) versus power dissipation per unit in (3.31). As before, by unit, we mean the minimal motor magnetic configuration required to generate a thrust. The stage acceleration is estimated for a double-sided motor configuration with a stage mass of 10 kg.

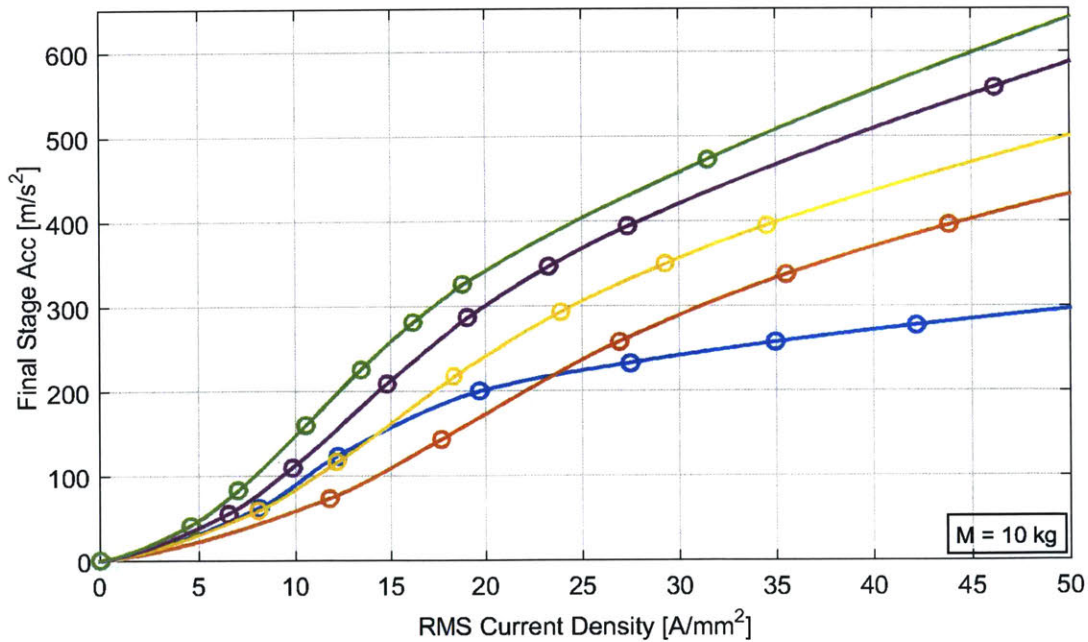


Figure 3-19: Simulated stage acceleration in (3.30) versus RMS current density in wire in (3.32). The stage acceleration is estimated for a double-sided motor configuration with a stage mass of 10 kg.

The first thing to notice in Figure 3-16 is that regardless of the tooth width values, our new fine-tooth motor always shows higher shear stress at all power levels than the conventional motor. For instance, at the practical power level of 500 W per motor unit, the fine-tooth motor with $w_t = w_s = 2$ mm shows the shear stress of 0.148 N/mm^2 , which is about 63 % higher than the conventional motor shear stress of 0.091 N/mm^2 at the same power level. The steeper slopes at higher power levels indicate even more potential to a significant shear stress increase with our new fine-tooth motor design.

The reason why we have almost identical ($\tau - P_{diss,unit}$) curves for all fine-tooth motor design variants in Figure 3-16 is because both the shear stress and the power dissipation decrease as the tooth width increases. We keep the ampere-turns the same for all cases, and so expect the same thrust. However, as w_t increases, the force-generating area increases and the coil resistance decreases (\because thicker wires are used for wider slots), thereby decreasing both τ and $P_{diss,unit}$.

In Figure 3-17, the shear stress is plotted against the RMS current density in the wire windings up to 50 A/mm^2 , which is almost the thermally-limited value for a heavily-liquid-cooled motor in high power machines such as a lithography scanner. As can be seen in the figure, the fine-tooth motor designs with $w_t \geq 2$ mm show higher shear stress than the conventional motor at all current density levels. Among these three cases, we select the parameter value of $w_t = 2$ mm since it is expected to produce the maximum stage acceleration at our testbed's practical power level of 500 W per motor unit, as shown in Figure 3-18. In addition, we can see that the selected parameter value of $w_t = 2$ mm also guarantees higher stage acceleration than the conventional motor at all RMS current density levels as shown in Figure 3-19.

Slot Aspect Ratio

We obtain the same force performance plots for the red group in Figure 3-15 to determine the optimal slot aspect ratio. Figures 3-20 to 3-23 show the plots and compare the force performance of fine-tooth motor design variants to the conventional motor. The light blue line is again the conventional motor as a reference, and all the

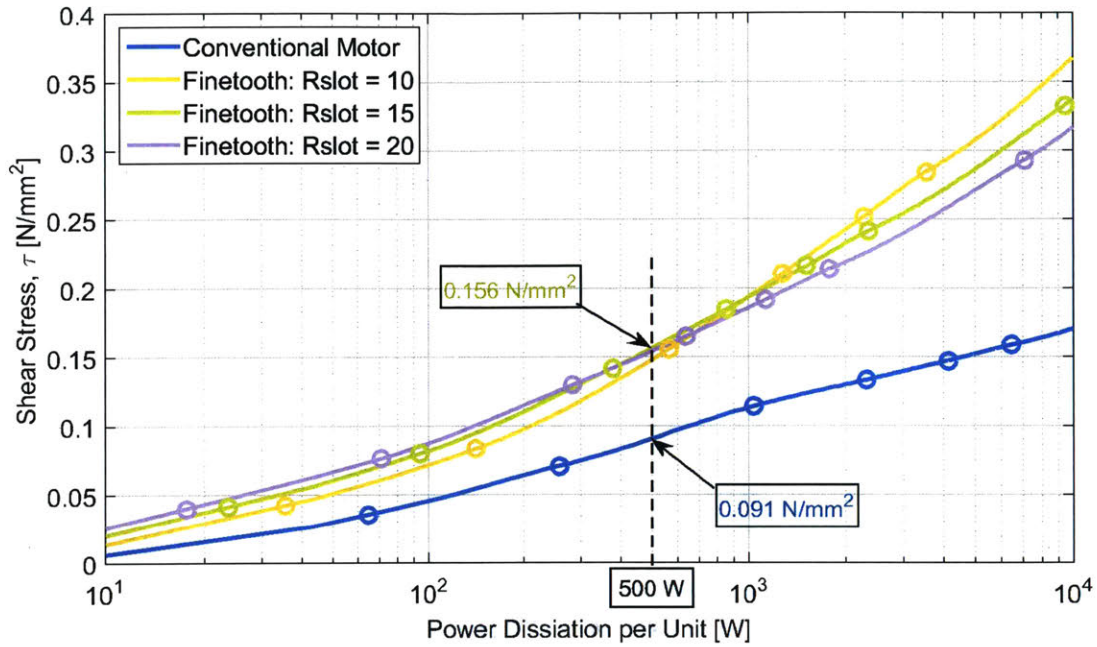


Figure 3-20: Simulated shear stress in (3.29) versus power dissipation per unit in (3.31). By unit, we mean the minimal motor magnetic configuration required to generate a thrust.

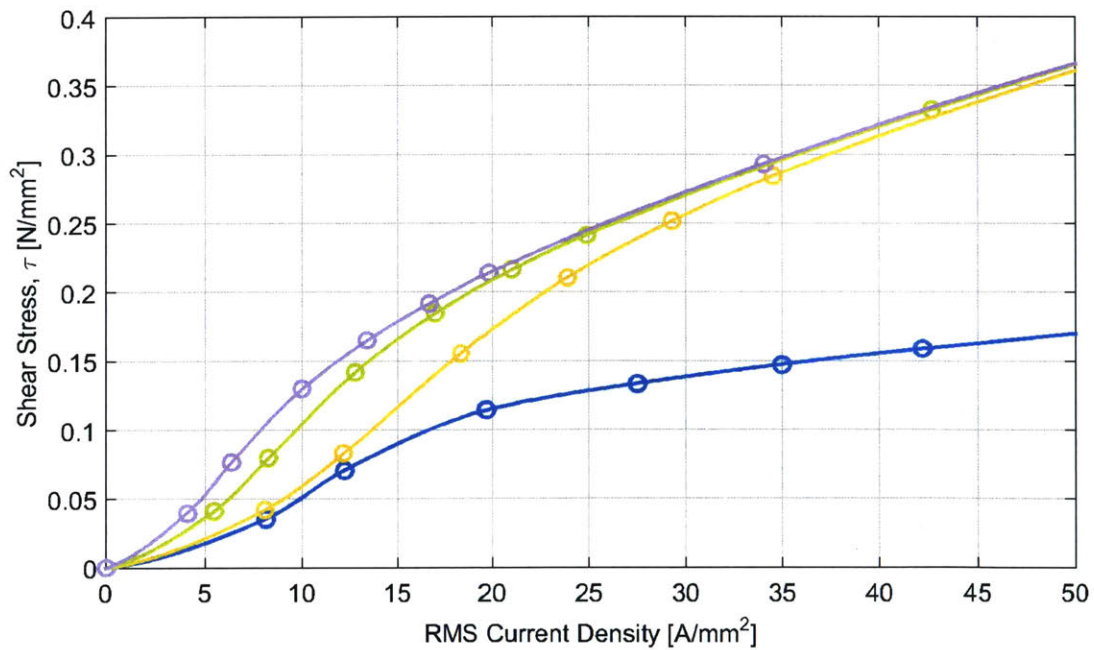


Figure 3-21: Simulated shear stress in (3.29) versus RMS current density in wire in (3.32). Shear stress performance of the conventional motor in light blue line serves as a design reference.

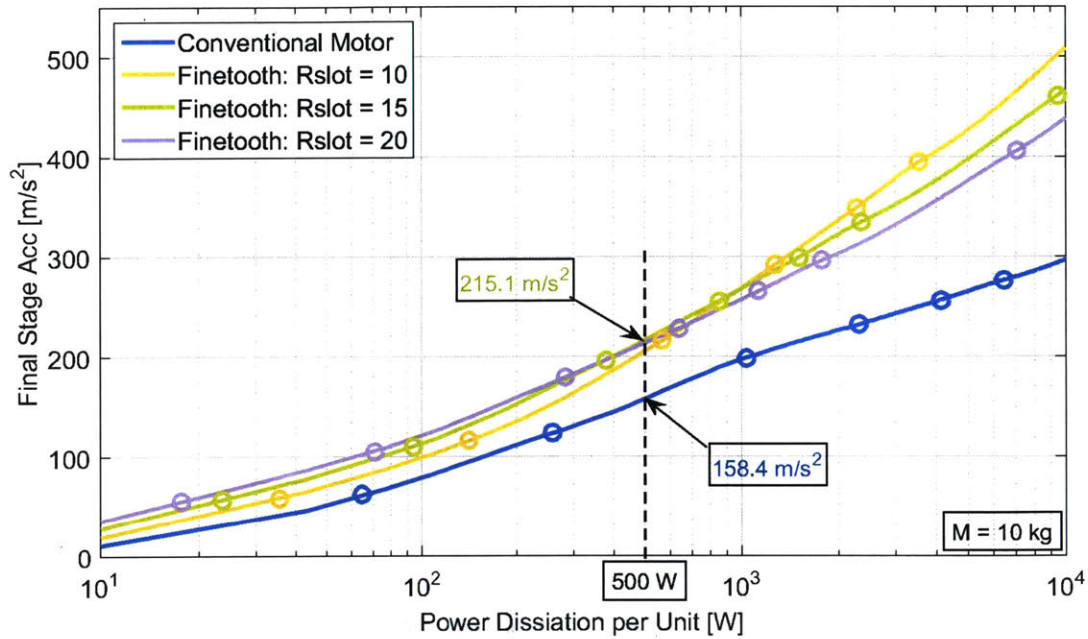


Figure 3-22: Simulated stage acceleration in (3.30) versus power dissipation per unit in (3.31). By unit, we mean the minimal motor magnetic configuration required to generate a thrust. The stage acceleration is estimated for a double-sided motor configuration with a stage mass of 10 kg.

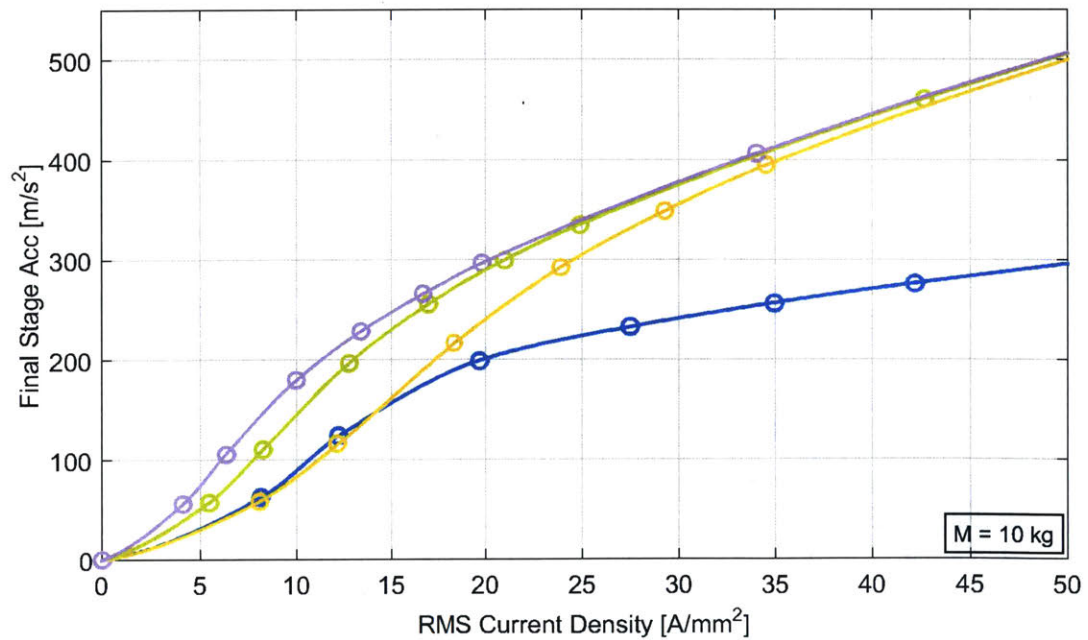


Figure 3-23: Simulated stage acceleration in (3.30) versus RMS current density in wire in (3.32). The stage acceleration is estimated for a double-sided motor configuration with a stage mass of 10 kg.

other lines are for the fine-tooth motor with different R_{slot} values. As observed before, our fine-tooth motor designs show higher shear stress performance at all power levels than the conventional motor, regardless of the slot aspect ratio.

Figure 3-20 shows that the fine-tooth motor designs with higher slot aspect ratio start with higher shear stress at a low power range, but the slopes decrease faster at a high power level. This is because the designs with deeper slots are more prone to flux leakage when the material is saturated. The leakage effect results that the parameter value of $R_{slot} = 15$ generates the highest shear stress of 0.156 N/mm^2 at 500 W per motor unit, which is about 71 % increase from the conventional motor shear of 0.091 N/mm^2 at the same power level. We observe the similar behavior in the stage acceleration versus power plot in Figure 3-22, leading us to select the slot aspect ratio value of $R_{slot} = 15$ for our new fine-tooth motor. Figures 3-21 and 3-23 show that we can expect both the shear stress and stage acceleration to be higher than the conventional motor at all times with the selected parameter value of $R_{slot} = 15$.

Number of Winding Turns and Wire Gauge

For the purple group in Figure 3-15, we compare the cases of less turns with thicker wire and more turns with thinner wire while keeping the ampere-turns the same. For these two cases, we calculate the shear stress performance versus both the power dissipation per unit and the RMS current density in wire, and compare them to each other and to the conventional motor, as shown in Figures 3-24 and 3-25. As can be seen in both figures, we observe the same performance for the two different cases of less turns with thicker wire (green solid line) and more turns with thinner wire (gray dashed line). This is because 1) we keep the ampere-turns and the stator armature geometry the same so that the shear stress is the same for both cases, and 2) we use twice more turns with a half cross-section wire for the case of more turns with thinner wire, thereby making the winding coil resistance 4 times higher while having half current for the same ampere-turns. This keeps the power dissipation in (3.31) the same for both cases. These are the reasons why we have the identical results for both cases in Figures 3-24 and 3-25.

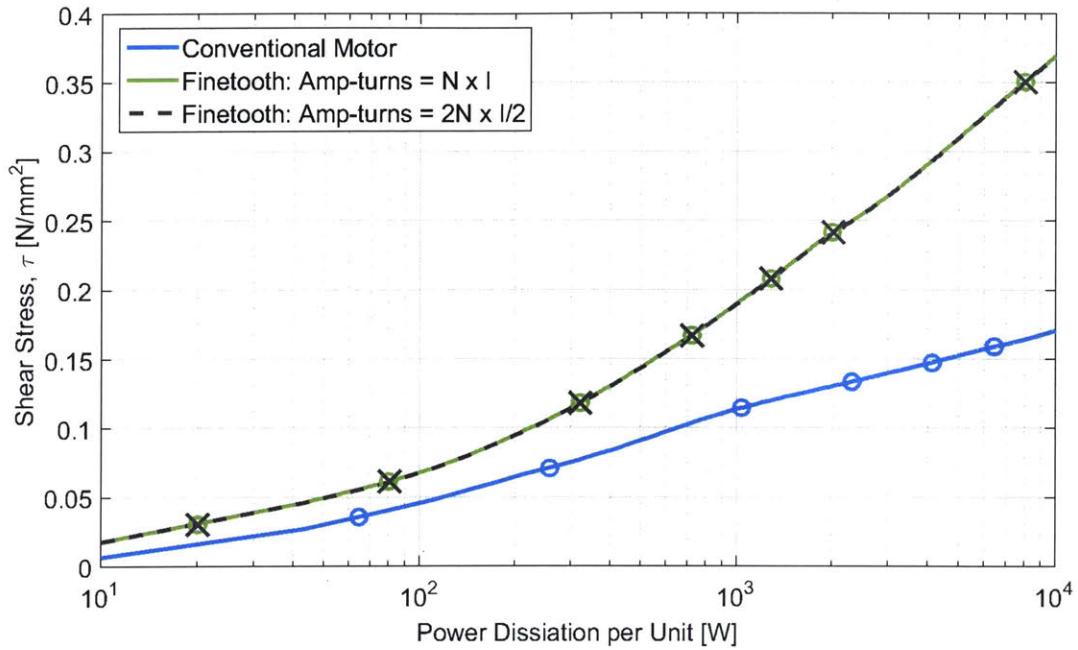


Figure 3-24: Simulated shear stress in (3.29) versus power dissipation per unit in (3.31). By unit, we mean the minimal motor magnetic configuration required to generate a thrust.

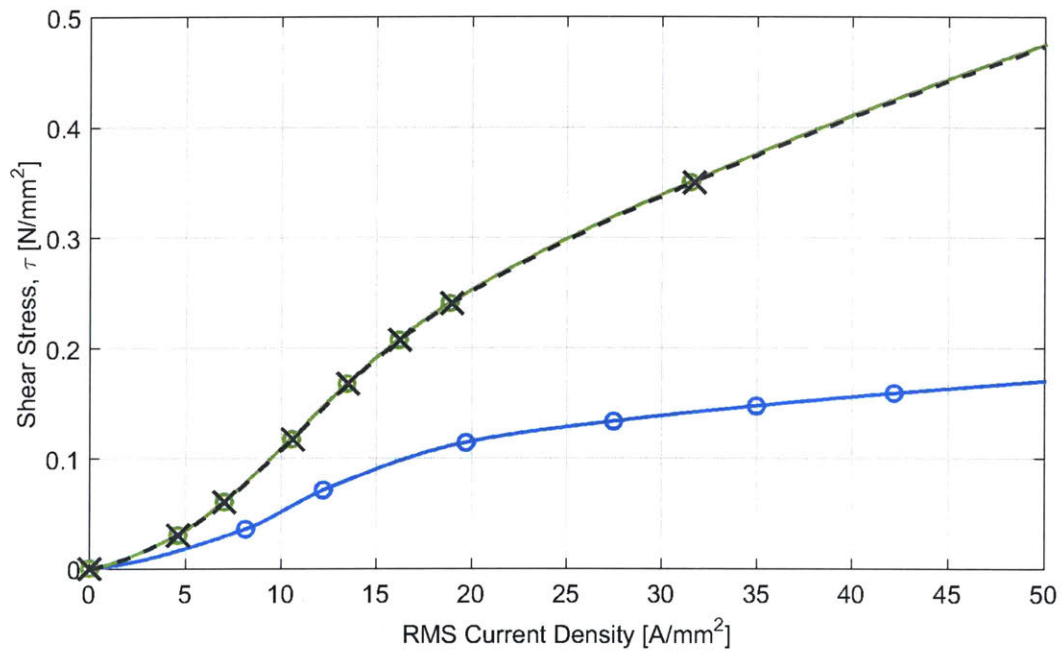


Figure 3-25: Simulated shear stress in (3.29) versus RMS current density in wire in (3.32). Shear stress performance of the conventional motor in light blue line serves as a design reference.

Given that both cases of less turns with thicker wire and more turns of thinner wire are expected to produce the same force performance, the selection between them can depend on a few practical issues including a winding fill factor, power electronics ratings, and winding difficulty. We present the finally chosen values for the number of winding turns and the wire gauge for our new fine-tooth motor, and discuss the practical reasons for the selection in Section 3.4.

Magnet Thickness

We take the same procedure to compare the force performances with different parameter values in the green group in Figure 3-15 so as to determine the magnet thickness of our new fine-tooth motor. Figures 3-26 to 3-29 compare the shear stress and stage acceleration of the new motor design variants of the magnet thickness. First thing to notice is that regardless of the magnet thickness, our new fine-tooth motor shows the higher shear stress and acceleration than the conventional motor at all power and current density levels. Note that our fine-tooth motor is expected to generate higher shear stress and acceleration even with the same magnet array pattern and same thickness as the conventional motor, as shown in Figures 3-26 and 3-28 with the black line. The force performances are then enhanced further when the Halbach array pattern is used with thicker magnets. Note that we use the Halbach magnet ratio with the vertical magnet fraction of $f_{magnet} = 0.7$ as selected in the previous subsection.

We observe in Figures 3-26 and 3-27 that the fine-tooth motor designs with $PM_{thick} \geq 0.5$ (green, red, and blue curves) show significant shear stress increases compared to the conventional motor design (light blue curve). Among these three candidates, we select the parameter value of $PM_{thick} = 0.5$ since it is expected to result in the maximum possible stage acceleration at our testbed's practical power level of 500 W per motor unit as shown in Figure 3-28. For thicker magnets, we know we will have higher shear stress. However, the moving mass will also increase with thicker magnets, thereby decreasing the overall stage acceleration. In other words, using thickest magnets does not mean the highest acceleration. All in all, $PM_{thick} = 0.5$

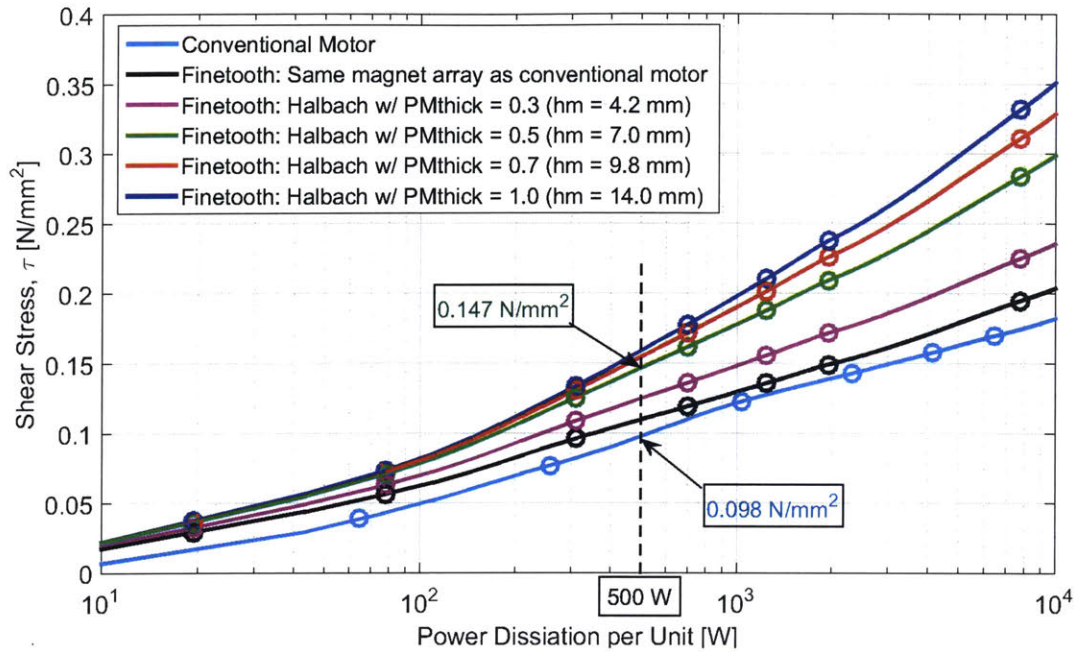


Figure 3-26: Simulated shear stress in (3.29) versus power dissipation per unit in (3.31). By unit, we mean the minimal motor magnetic configuration required to generate a thrust.

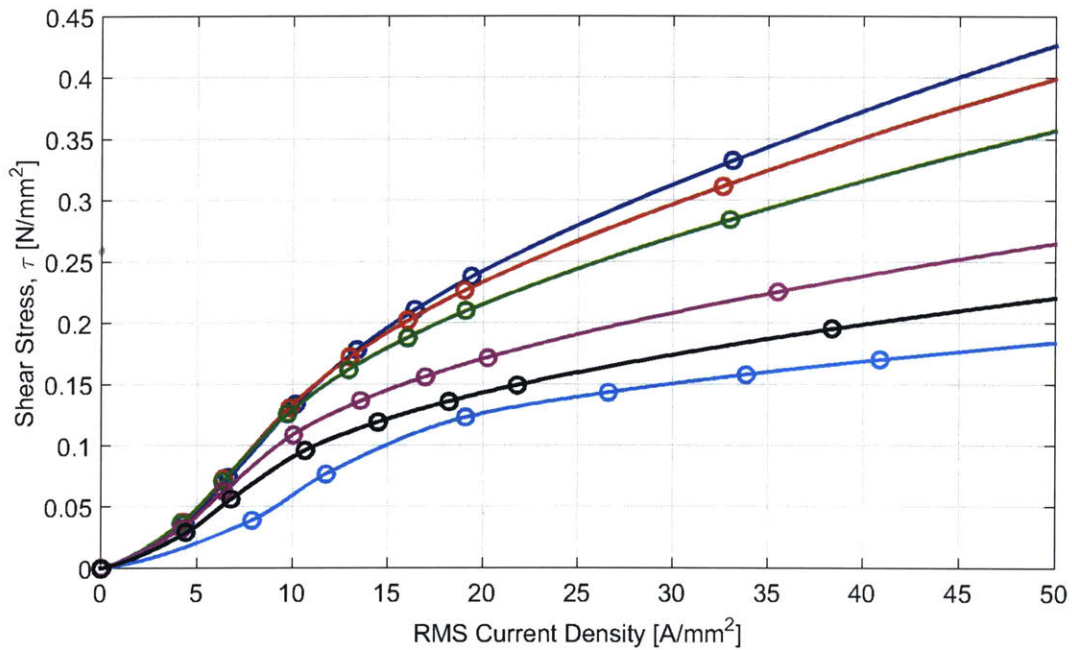


Figure 3-27: Simulated shear stress in (3.29) versus RMS current density in wire in (3.32). Shear stress performance of the conventional motor in light blue line serves as a design reference.

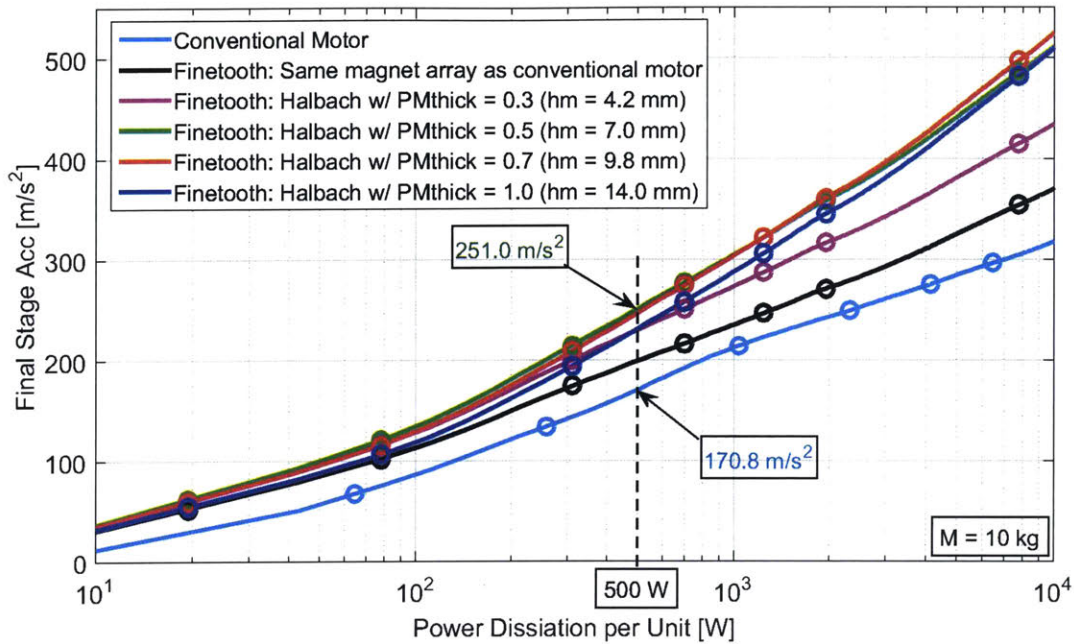


Figure 3-28: Simulated stage acceleration in (3.30) versus power dissipation per unit in (3.31). By unit, we mean the minimal motor magnetic configuration required to generate a thrust. The stage acceleration is estimated for a double-sided motor configuration with a stage mass of 10 kg.

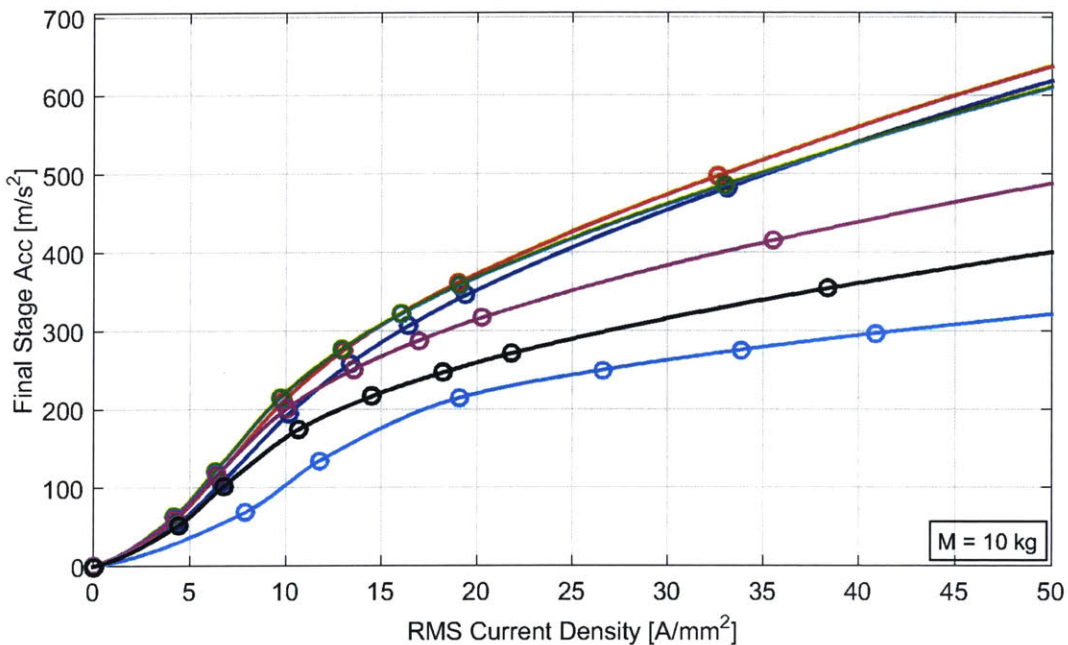


Figure 3-29: Simulated stage acceleration in (3.30) versus RMS current density in wire in (3.32). The stage acceleration is estimated for a double-sided motor configuration with a stage mass of 10 kg.

shows to produce the maximum stage acceleration of 251.0 m/s² at the power level of 500 W per motor unit, which is about 47 % higher than the acceleration of 170.8 m/s² by the conventional motor at the same power level. The selected parameter value of $PM_{thick} = 0.5$ means that our new fine-tooth motor has the magnet thickness of 7 mm. The final magnet array drawings are documented in Appendix A, and the constructed magnet tracks are shown in Section 3.5.

3.4 Final Design of New Fine-tooth Motor

In this section, we present the final design parameters determined through the selection process discussed in the previous section. The final values of the design parameters are organized in Figure 3-30 along with several relevant information. We design our fine-tooth motor to have five phases with the tooth/slot width of 2 mm. This results in the tooth pitch λ_t , the magnet pole pitch λ_p , and the fundamental unit

Stator		Reason
Material	Cobalt Iron (Hyperco50) \longrightarrow Silicon Iron (M-19)	- Cost
Lam. Cost	\$9.5k/stator $\xrightarrow{80\% \downarrow}$ \$2.0k/stator	- Lead time
Lead time	6-7 weeks \longrightarrow 3 weeks	
N_{slot}		5
w_t, w_s [mm]		2
R_{slot}		15
N	63 \longrightarrow 126	- Easier handling
AWG	20 \longrightarrow 23	- End-turn reduction
Magnet Track		
f_{magnet}		0.7
PM_{thick}		0.5
Back iron	Cobalt Iron w/ 3mm thick \longrightarrow C1018 steel w/ 4.76mm thick	- Cost, Lead time (pre-ground plate) - Structural integrity

Figure 3-30: Final design parameters of a new fine-tooth motor using silicon-iron stator material to reduce prototype cost.

length λ_u as

$$\begin{aligned}\lambda_t &= w_t + w_s = 4 \text{ mm} \\ \lambda_p &= N_{slot}(w_t + w_s) = 20 \text{ mm} \\ \lambda_u &= \lambda_{pp} = 2\lambda_p = 40 \text{ mm}\end{aligned}\tag{3.33}$$

where λ_{pp} is the magnet pole-pair pitch. The slot aspect ratio is selected as $R_{slot} = 15$, and this makes the slot depth h_s as

$$h_s = w_s \times R_{slot} = 30 \text{ mm}.\tag{3.34}$$

For the magnet track, the sizes of vertical and horizontal magnets are

$$\begin{aligned}w_{m,vertical} &= f_{magnet}\lambda_p = 14 \text{ mm} \\ w_{m,horizontal} &= (1 - f_{magnet})\lambda_p = 6 \text{ mm} \\ h_m &= w_m \times PM_{thick} = 7 \text{ mm}\end{aligned}\tag{3.35}$$

where $w_{m,vertical}$, $w_{m,horizontal}$, and h_m are the width of vertical magnets, width of horizontal magnets, and magnet thickness, respectively. The completed drawings of our new fine-tooth motor with the final design parameters can be found in Appendix A.

We discuss in this section some of the practical modifications we made for the final motor design, and present the expected motor performances of the fine-tooth motor with the final design.

3.4.1 Practical Design Modification

As shown in Figure 3-30, we make several design modifications for practical reasons, each of which is discussed as below.

- 1) Stator material is changed from the cobalt iron (Hyperco50) to the silicon iron (M-19).

- The cobalt iron was first selected for the stator material due to its high saturation limit of about 2.4 T. This material was used to obtain the force performance estimations in Figures 3-16 to 3-29 for both the conventional motor and our new motor designs.
 - The cobalt iron, however, is much more expensive and its lead time was too long for our experimental testbed. To reduce the cost and the turnaround time, we changed the stator material to the silicon iron (M-19). Since this material has a lower saturation limit of about 1.8 T as compared with the cobalt iron, we expect our new motor to be relatively more prone to flux leakage. However, we confirm in Section 3.4.2 that our new fine-tooth motor can provide higher shear stress than the conventional motor even with this material change. cobalt iron should be considered for future designs.
- 2) We decided to use thinner wires to wind more turns.
- We first selected 20 AWG with 63 turns per slot since we can have a higher fill factor with thicker wires in general.
 - However, we realized that using thick wires makes the winding more difficult and time-consuming. For the multi-phase full-pitch winding, the end-turns have to be reformed to deal with the overlapping issue. For thick wires, the end-turn reformation is more difficult due to their high stiffness, thereby requiring more time and even longer end-turn length.
 - For the purpose of easier winding and end-turn reduction, we chose to use 23 AWG with 126 turns per slot. Since the ampere-turns are kept the same, we expect no force performance reduction as shown in Figures 3-24 and 3-25. The completed stator armature with the windings is shown in Figure 3-41.
- 3) We decided to use a general purpose C1018 steel for the magnet back iron rather than the cobalt iron.

- The cobalt iron was first selected for the magnet back iron material in the attempt of decreasing the moving mass by reducing the back iron thickness (to about 3 mm) due to the advantage of higher saturation limit.
- We changed to a pre-ground C1018 steel to reduce the cost and the lead time, and made it thicker (to 4.76 mm) so as to have higher structural integrity.
- The expected acceleration is confirmed to be higher than the conventional motor even with this change of the magnet back iron. We present the relevant results in Section 3.4.2.

3.4.2 Performance Expectation of Final New Motor Design

In this subsection, we describe the expected motor performance of our final motor design in terms of thrust and force ripple, and compare these results to the conventional motor. The thrust performance is shown with the shear stress and the stage acceleration versus the power and RMS current density. The force fluctuation performance is presented to observe and compare the force harmonic components between our new motor and the conventional 3-4 combination motor.

Thrust Performance Comparison

Figures 3-31 to 3-34 show the shear stress and stage acceleration performances predicted for this revised practical design. In all figures, the light blue lines are for the conventional 3-4 combination motor and the black lines are for our new fine-tooth motor with the final design parameters shown in Figure 3-30. Even with the practical design modifications discussed in the previous subsection, our new fine-tooth motor shows higher shear stress and higher acceleration than the conventional motor at every power and current density level. Note that in Figures 3-31 and 3-33, we use the power dissipation per length in the unit of [W/mm], rather than the power dissipation per unit as in Section 3.3. This is to take the motor unit length difference into account to have a fair comparison on the motor force performance between two

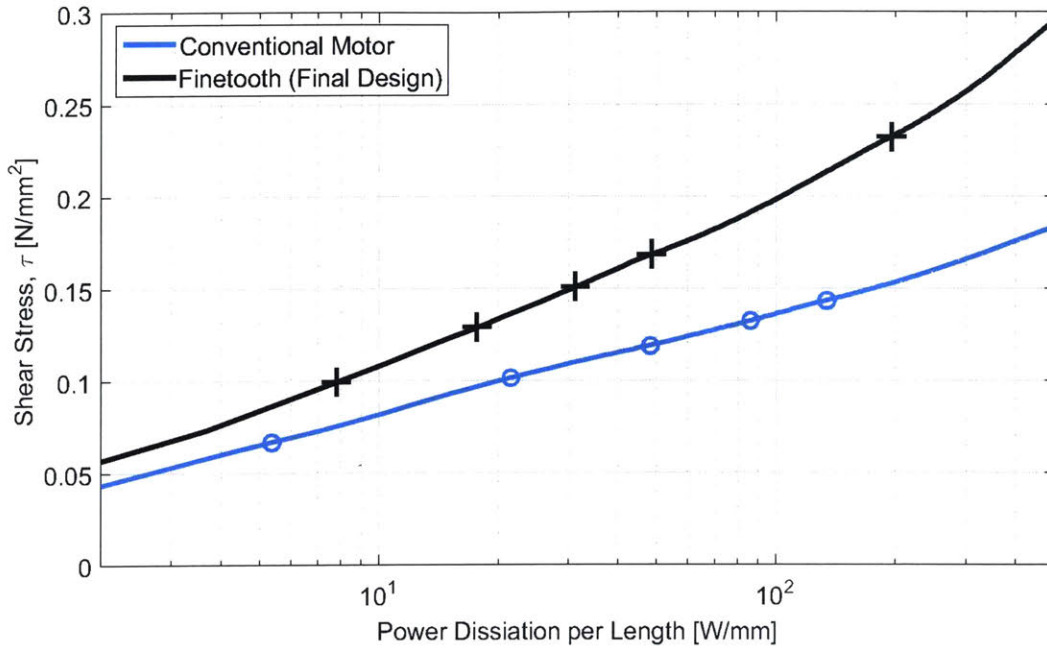


Figure 3-31: Simulated shear stress in (3.29) versus power dissipation per unit in (3.31). By unit, we mean the minimal motor magnetic configuration required to generate a thrust. Comparison between the conventional motor (light blue line) and our new fine-tooth motor with final design parameters (black line).

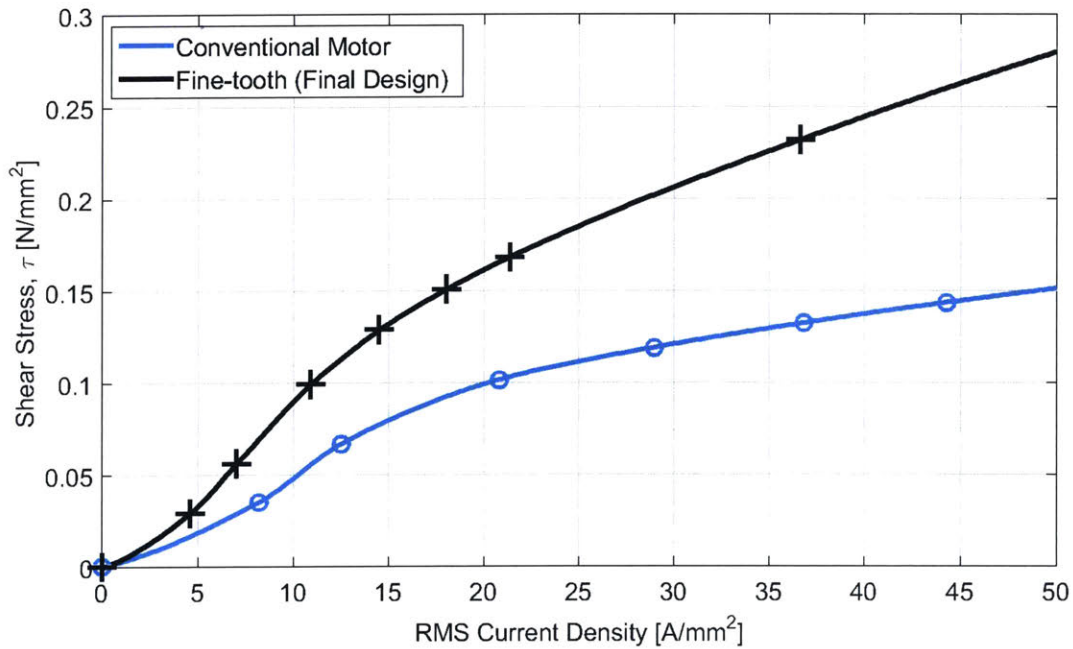


Figure 3-32: Simulated shear stress in (3.29) versus RMS current density in wire in (3.32). Comparison between the conventional motor (light blue line) and our new fine-tooth motor with final design parameters (black line).

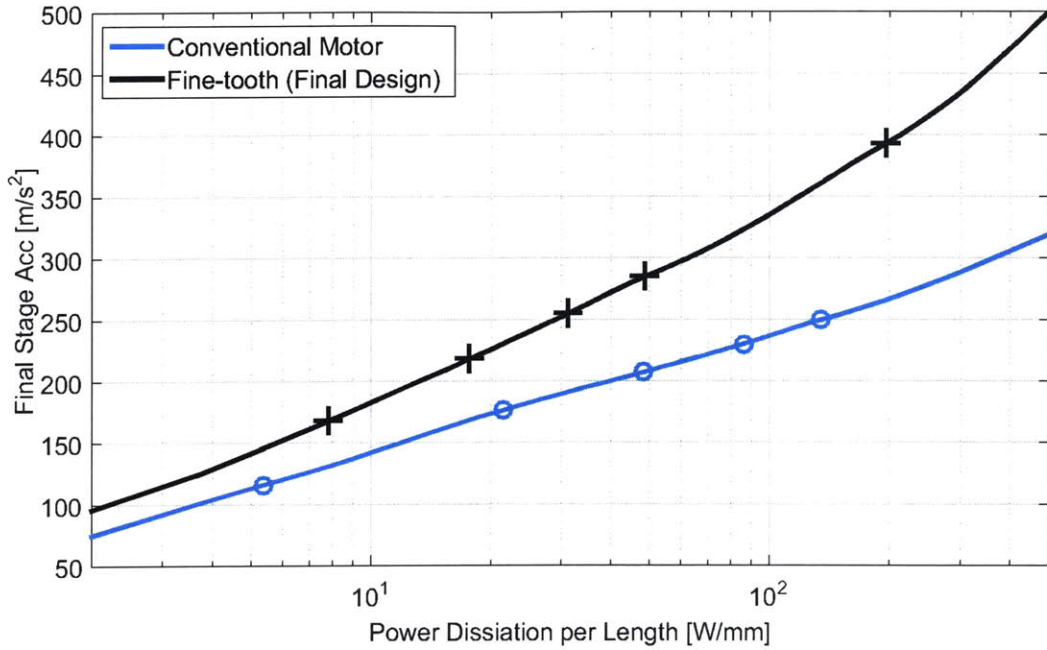


Figure 3-33: Simulated stage acceleration in (3.30) versus power dissipation per unit in (3.31). By unit, we mean the minimal motor magnetic configuration required to generate a thrust. Comparison between the conventional motor (light blue line) and our new fine-tooth motor with final design parameters (black line).

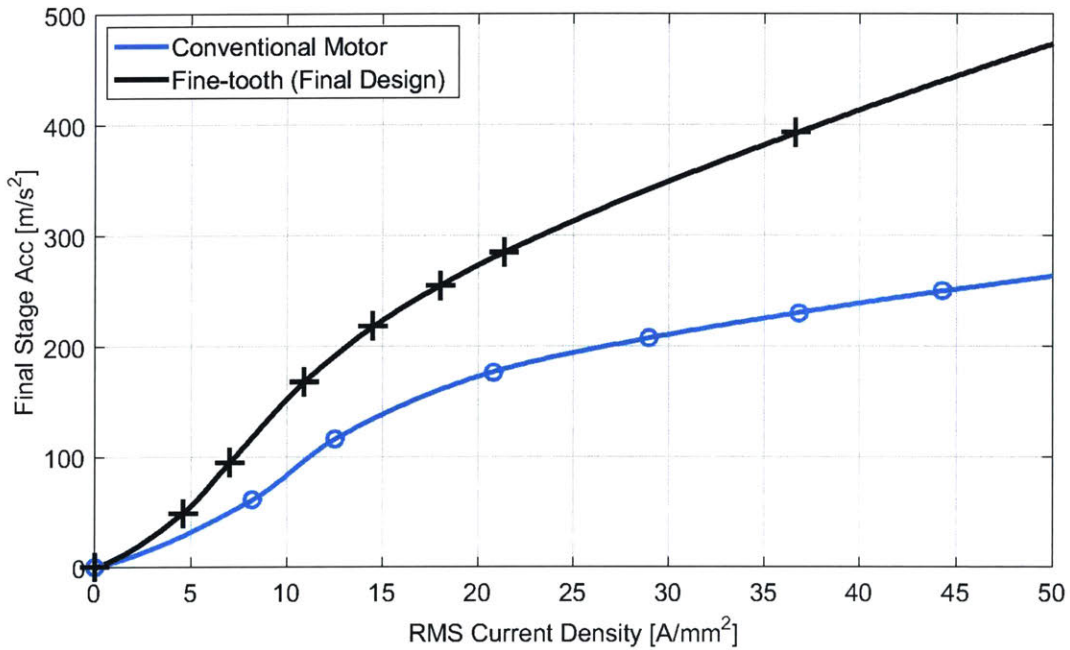


Figure 3-34: Simulated stage acceleration in (3.30) versus RMS current density in wire in (3.32). Comparison between the conventional motor (light blue line) and our new fine-tooth motor with final design parameters (black line).

different motors. Specifically, the motor unit length λ_u is 48 mm for the conventional motor and 40 mm for our new fine-tooth motor.

The fine-tooth motor is expected to generate a shear stress of 0.115 N/mm^2 at a lower power level of 10 W/mm , showing approximately 28 % increase over the conventional motor's shear stress of 0.090 N/mm^2 at the same power level. At the maximum RMS current density of 50 A/mm^2 , we observe even higher shear stress increase of about 84 % from 0.167 N/mm^2 ($\approx 24 \text{ psi}$) by the conventional motor to 0.308 N/mm^2 ($\approx 45 \text{ psi}$) by our new fine-tooth motor. The acceleration predictions in Figures 3-33 and 3-34 also show the similar results of our new fine-tooth motor showing significant force enhancement. The simulated result of enhanced force performance of our new fine-tooth motor is experimentally validated in Chapter 7.

Force Fluctuation Comparison

We discuss how our new fine-tooth motor design contains less force harmonics in Section 3.1. Here we confirm that argument by observing the predicted force ripple and its harmonics generated by our fine-tooth motor. Figure 3-35 compares the force ripples of the fine-tooth motor with the final design parameters (black line) to the conventional motor (light blue line). The upper plot is for the force ripple in the normal direction, and the lower one is for the tangential direction. Note that skewed magnets are used for both motors.

As shown in Figure 3-35, our fine-tooth motor generates smaller force ripple. Specifically, we have a significant peak-to-peak force ripple reduction with the ratio of 9-to-1 and 5-to-1 in the normal and tangential directions, respectively. We can also observe that our new motor contains less force harmonics from the spatial spectrum of the force ripples in Figure 3-36. The conventional motor has a strong fundamental harmonic along with the second, third, and also fourth harmonics of significant amplitudes. On the other hand, our new fine-tooth motor exhibits almost solely the fundamental harmonic without any notable high harmonics due to the smoother stator and rotor MMFs as shown in Figure 3-2.

We expect that the advantage of having less force harmonics will lead to less motor

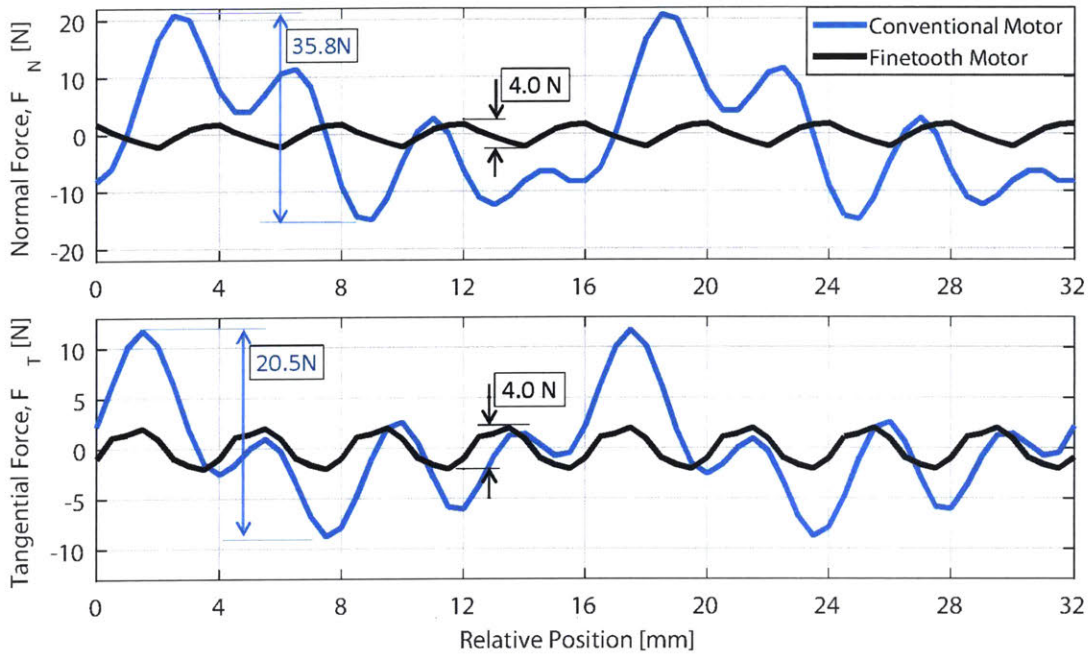


Figure 3-35: Simulated force ripple comparison between the conventional motor (light blue line) and our new fine-tooth motor with final design parameters (black line).

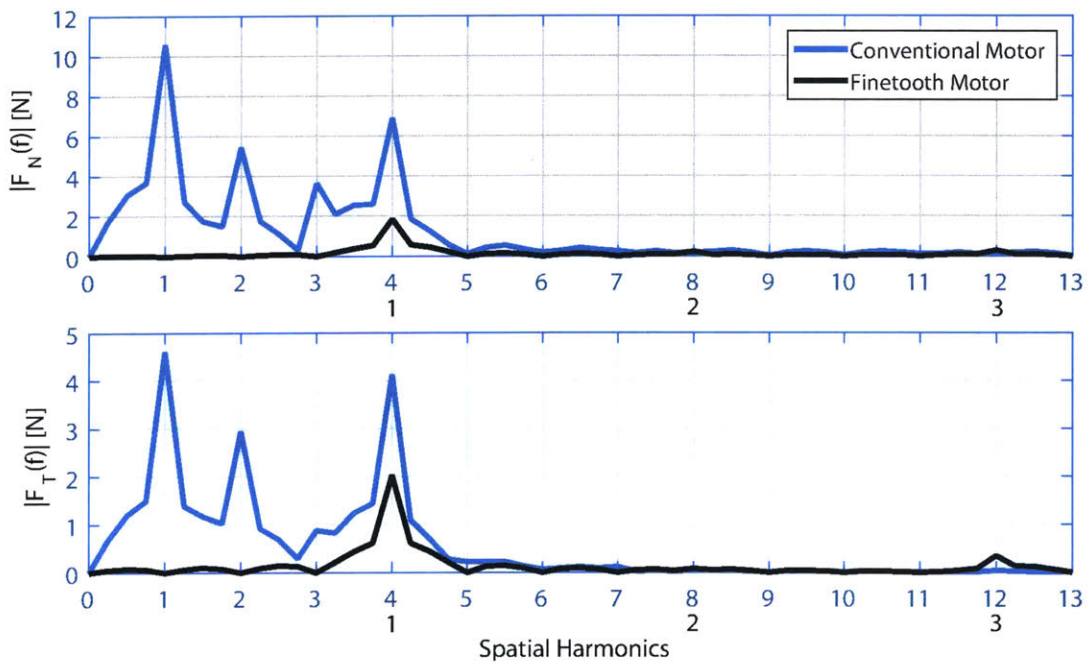


Figure 3-36: Simulated force ripple spectrum comparison between the conventional motor (light blue line) and our new fine-tooth motor with final design parameters (black line).

noise as discussed in Chapter 1. In Chapters 6 and 7, we present experimental results to validate this expectation and show how much less noise we can have with our new fine-tooth motor compared to the conventional 3-4 combination motor.

3.5 Construction of New Fine-tooth Motor

In this section, we present the construction of our new fine-tooth motor¹ based on the final design discussed in the previous section. We first discuss the stator armature construction in terms of stator laminations, coil windings, wirings, and cabling. The fabrication process of Halbach magnet array is then presented along with the pictures of the completed magnet tracks. For the detailed drawings of stator laminations and moving magnet tracks, please refer to Appendix A.

3.5.1 Stator Armature

Figure 3-37 shows the pictures of the stator laminations, fabricated by Polaris Laser Laminations, with the total length of 728 mm and the total number of 180 slots. The U.S. quarter coin in the pictures serves as a size reference. The silicon iron M-19 laminations are laser-cut and stacked to have the motor depth of 52 mm, which is the same depth as the conventional iron-core motor, TL 18 by Tecnotion. Note that the mounting slots in the back yoke of the stator laminations are for dove-tail inserts used to mount the stator in the experimental testbed. The drawing of the dove-tail inserts is documented in Appendix A, and how they are used to mount the stator armature is discussed in Chapter 5.

Our new fine-tooth motor has five phases, so we have a total of 36 ($=180/5$) basic winding regions as shown in Figure 3-38. These winding regions are divided into four sections to distribute the motor driving power. The 5-phase coils are wound in each section as shown with the winding scheme of section #1 in the figure. We use the double-layer and full-pitch winding method for each phase as color-coded in the winding schematic: red, orange, yellow, green, and blue for the phase A, B, C, D, and

¹We thank Fred Sommerhalter for his fabrication of these challenging motor components.

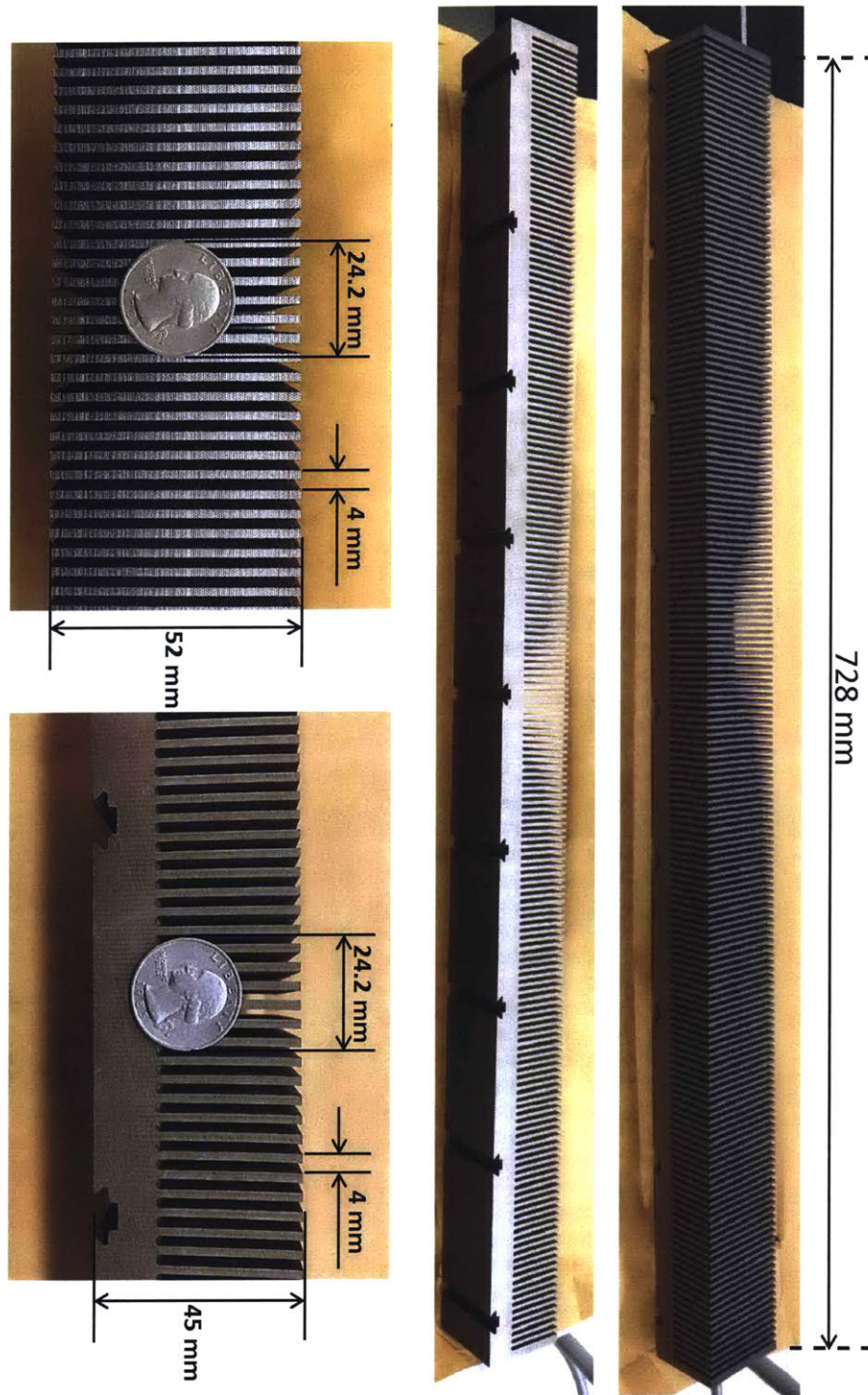


Figure 3-37: Pictures of stator laminations showing the total length of 728 mm and the tooth pitch of 4 mm. Quarter is for a size reference.

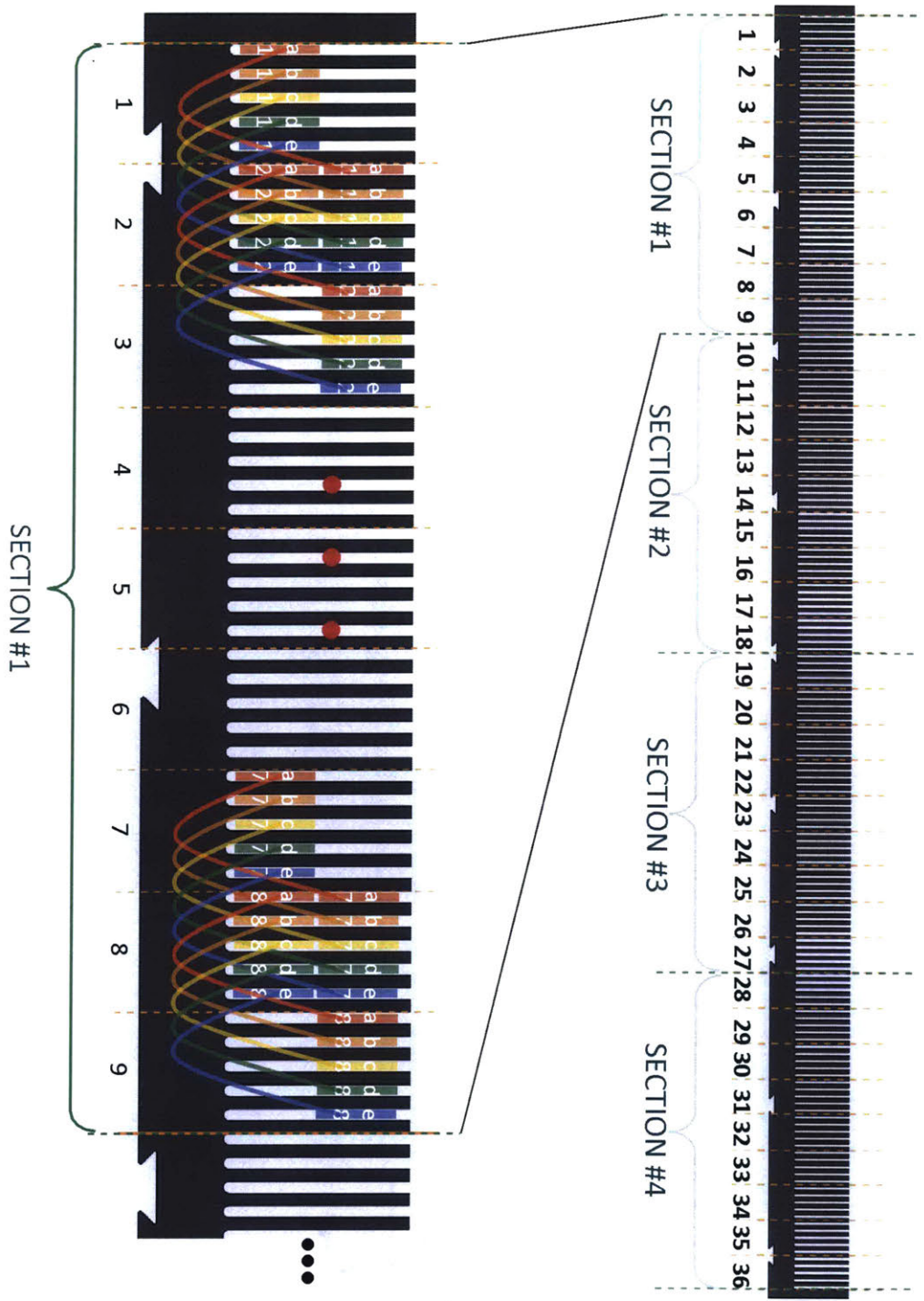


Figure 3-38: Winding scheme of 5-phase double-layered full-pitch concentrated windings for the newly-designed fine-tooth motor stator.

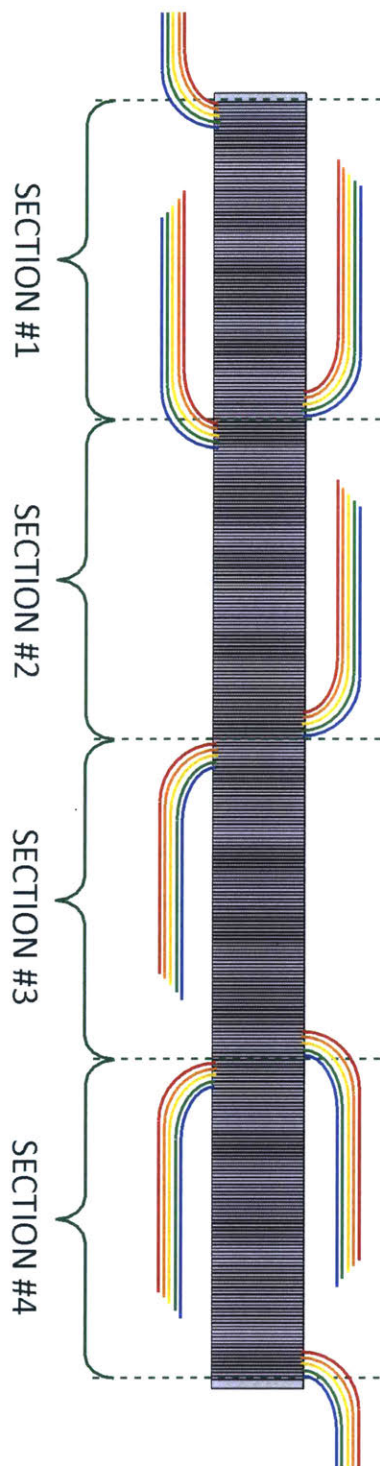


Figure 3-40: Cabling scheme of our newly-designed fine-tooth motor. Total of 40 cables for 20 resultant phase winding coils (5-phase coils per section) with 10 cables brought out to each corner.

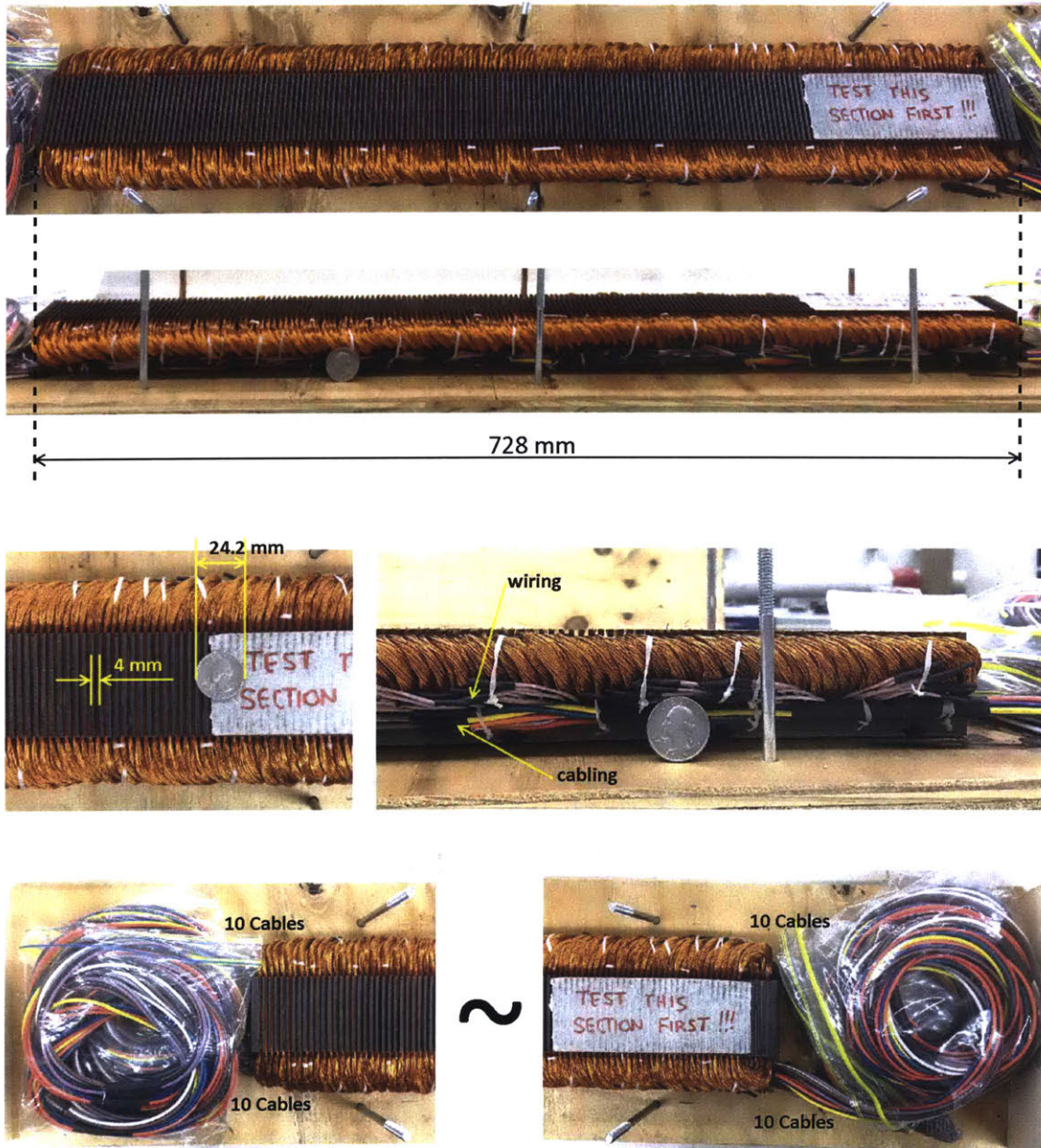


Figure 3-41: Completed stator armature with all the winding, wiring, and cabling. Quarter is for a size reference.

Figure 5-24. To tackle this challenging issue of cable packaging, we bring out a total of 10 cables at each corner to effectively utilize the limited space under the winding end-turns, as schematically shown in Figure 3-40.

Figure 3-41 shows the pictures of the completed stator armature with all the windings, wirings, and cablings. The U.S. quarter coin is again used as a size reference. The total of 175 coils are inserted one by one in the total number of 180 narrow and deep slots, and all these coils are wired in series for each phase per section. Then, all the resultant winding coils are brought out by the lead cables, as shown in the pictures, to be connected to the multiple power amplifiers.

3.5.2 Magnet Tracks

The moving magnet tracks are also fabricated to be operated with the stator armature previously presented. We use the Halbach magnet array for our new fine-tooth motor as discussed in Sections 3.3 and 3.4, and Figure 3-42 shows its assembly process. First, the assembly template made by a non-magnetic material is positioned on top

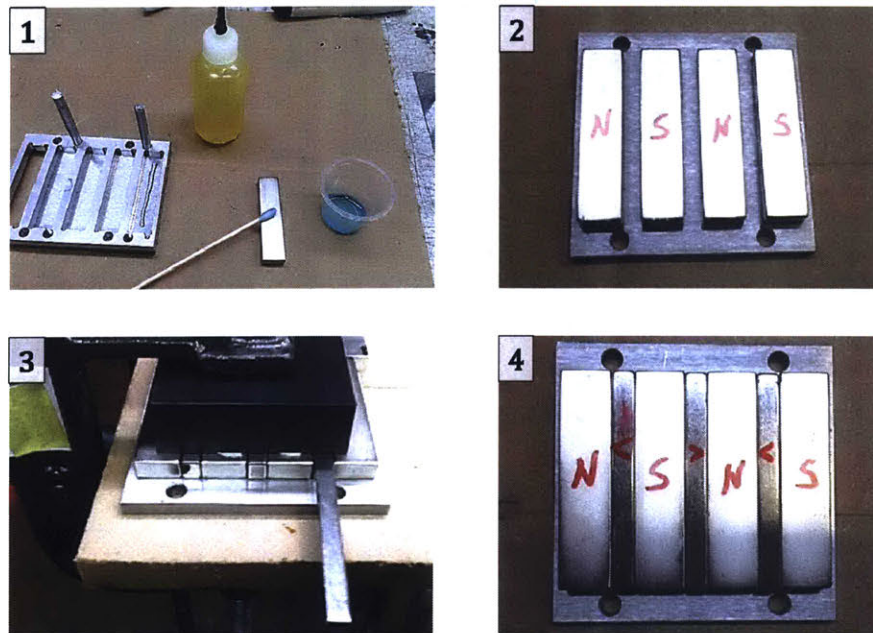


Figure 3-42: Assembly process of Halbach magnet array. Photos courtesy of Fred Sommerhalter.

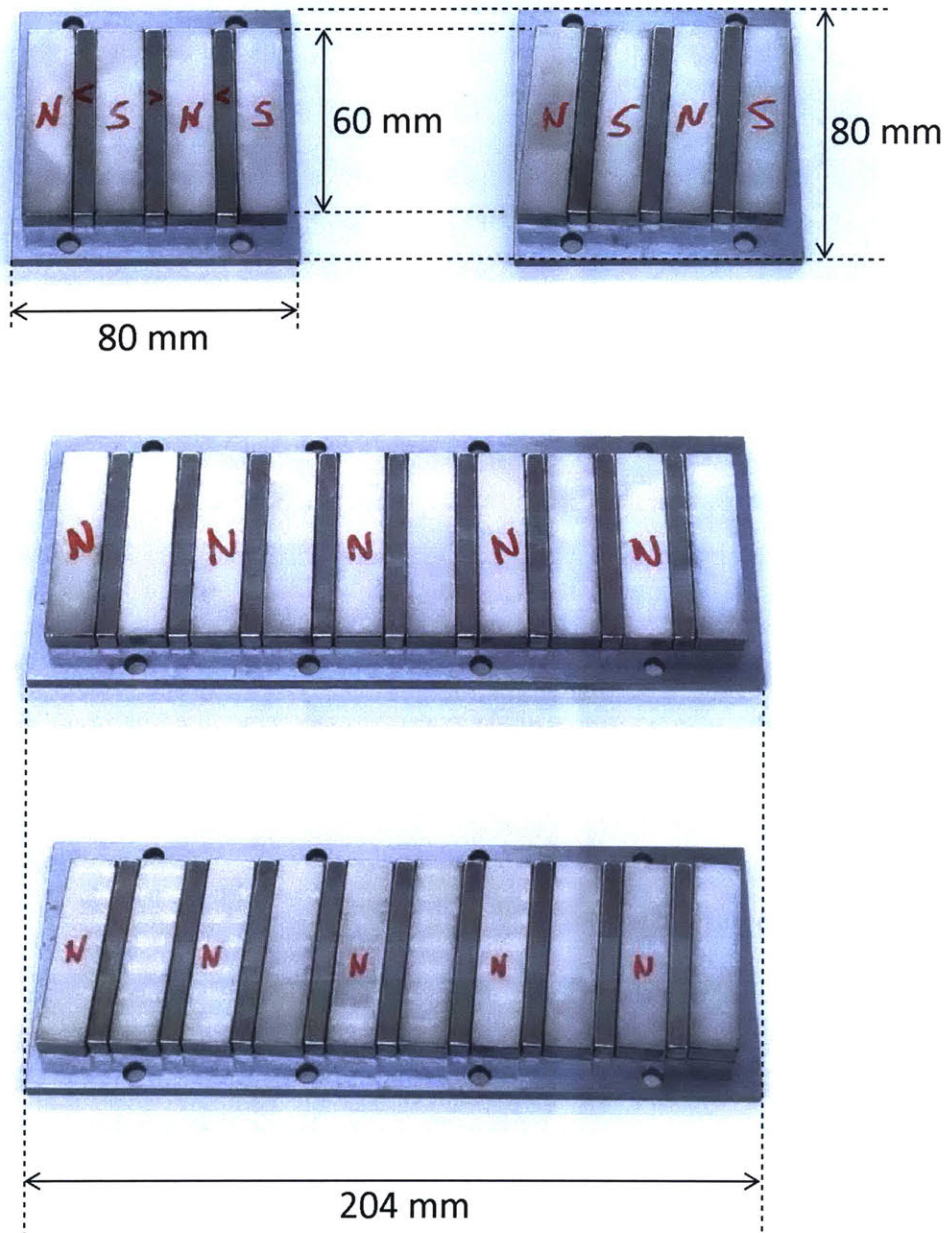


Figure 3-43: Completed Halbach array magnet tracks with both non-skewed and skewed magnets. The short tracks are for the single-sided motor configuration and the long ones for the double-sided configuration. We thank Fred Sommerhalter for the fabrication of the magnet tracks.

of the magnet back iron. The adhesive is applied on those portions of the back iron for the vertical magnets. The vertical magnets are then inserted in the template.

It is very difficult to directly insert the horizontal magnets between the vertical magnets since they tend to flip themselves to be aligned with the vertical magnets. To facilitate the horizontal magnets assembly, Fred Sommerhalter used a vice to create a flat top on the vertical magnets and insert the horizontal ones from the side. These pictures of Halbach magnet assembly process are for the non-skewed magnet tracks, but the same procedure can be taken for the skewed magnet tracks too. Figure 3-43 shows the completed moving magnet tracks in both non-skewed and skewed versions. The shorter tracks are for the single-sided motor configuration in the scope of this Ph.D research work, and the longer tracks are for the double-sided motor configuration in the future work. Note that the longer magnet tracks cannot be used in our experimental testbed for the single-sided configuration because the motor attractive force would be too large for air-bearings to work against. The details on the motor attractive force and air-bearings used in our testbed are discussed in Chapter 5. We use both non-skewed and skewed magnet tracks for our noise experiments to investigate the cogging-oriented noise. The relevant results are discussed in Chapter 7.

3.6 Summary

In this chapter, we discuss the modeling, design, and construction of our new fine-tooth motor. In contrast to the conventional 3-4 combination motor design, we take the design direction of having multiple fine teeth closely placed together with the Halbach magnet array for the advantages listed as below.

- The multi-phase (5-phase in our final design) fine-tooth stator design helps reduce the high harmonic contents in the stator MMF.
- The Halbach magnet array helps reduce the high harmonics in the rotor (magnet track) MMF.

- The generated force by our fine-tooth motor, therefore, contains less force harmonics, thereby expected to emit less noise.
- The fine-tooth design facilitates cogging reduction by using skewed magnets without compromising the thrust. The cogging force reduction is expected to lead to the cogging-related noise reduction of our new fine-tooth motor.
- The multi-phase fine-tooth stator with the Halbach magnet array also helps increase the shear stress to have higher force performance than the conventional motor.

We determine the specific design parameters of our new fine-tooth motor using the hybrid layer model and the finite element method. In the parameter selection process, we calculate and compare the shear stress and stage acceleration versus the power dissipation and RMS current density. We consider many different design variants and select the parameter values to yield the maximum force performance in terms of shear stress and acceleration. Our fine-tooth motor with the final design parameters shows great potential to increase the force performance compared to the conventional 3-4 combination motor. Furthermore, the force harmonics are also compared to confirm that our new fine-tooth motor contains much less force harmonics than the conventional motor. The expected motor performances discussed in this chapter are experimentally validated in Chapters 6 and 7.

We also present in this chapter the new motor fabrication details for both the stator armature and moving magnet tracks. The experimental linear stage testbed to test our new fine-tooth motor as well as the conventional motor is discussed in detail in Chapter 5. The comprehensive experimental results on the motor noise issue are presented in Chapters 6 and 7, where we show the improved force and noise performances of our new fine-tooth motor compared to the conventional motor.

Chapter 4

Experimental Testbed Design

In this chapter, we discuss experimental testbed designs to have various functionalities required for the motor vibro-acoustic noise experiments. The experimental linear stage testbed needs to be able to accommodate both the conventional 3-4 combination iron-core motor and our newly-designed fine-tooth motor in the single- and double-sided configurations. The testbed design should also include measuring systems for the real-time stage position and direct motor force measurements. We discuss these design targets with other important system requirements in the first section. Various conceptual designs to fulfill the requirements are presented in the following section. The structural designs of the stage testrig can be substantially different depending on the motor magnetic configurations, for example, which part is long or short and which is moving or stationary. We present hand sketches of possible stage concept designs for each case, and discuss the pros and cons of each design to converge into one promising conceptual design. In the last section, we present design details of the converged stage configuration, including base structures and bearings. The final design of the experimental testbed is illustrated in detail with CAD models at the end of this chapter, followed by a summary.

4.1 Functional Requirements

The basic purpose of the experimental testbed is 1) to facilitate vibro-acoustic noise experiments so that we can understand and resolve the noise issue of linear iron-core motors and 2) to test our newly-designed fine-tooth motor to experimentally validate its performance. In order to meet these objectives, the linear stage testrig is required to have certain functionalities, and we list these requirements in this section.

#1. The experimental testbed is required to have *hardware flexibility* to accommodate two different linear motors in four different configurations.

- We investigate the vibro-acoustic noise issues of both the conventional iron-core motor, TL18 model by Tecnotion, and our new fine-tooth motor. These motors are different in design and size, so a large enough volumetric margin is required.
- The testbed needs to be structured in four different configurations of single-sided and double-sided stage with either the conventional or new motor. Independence of one side from another is, therefore, required. Note that we study the noise issues of the single-sided configuration with both motors in the scope of this thesis, and pursue the topic of the double-sided motor configuration as a future work.
- The stage setup needs to be disassembled and reassembled relatively easily, and the assembly process needs to be repeatable.

#2. The experimental testbed is required to have *air bearings* to isolate only the magnetic source of the motor vibro-acoustic noise.

- Bearings are needed to provide a linear motion in one direction while constraining the other degrees of freedom. The most widely-used rolling-element bearings, however, require mechanical contacts and so generate vibrational and acoustic noises unrelated to motor operation.
- In order to avoid extraneous mechanical noise sources and isolate the magnetic noise sources of the motors, the usage of air bearings is required.

#3. The experimental testbed is required to provide *a long enough travel length* to be able to study the motor noise issue during constant velocity regions with various speed levels.

- The maximum stage velocity we target for our testrig is 2.4 m/s, which is on the same order of magnitude with the scanning speed of a lithography machine. In order to maintain this level of velocity constant over a substantial period of time for meaningful noise data, it is necessary to have a total travel length larger than 300 mm.
- The travel range of the conventional iron-core motor (192 mm) is limited by the length of the commercially available model (Tecnotion TL18), not by the testbed structure. However, the stage structure needs to be designed 1) to accommodate our new fine-tooth motor with 728 mm length as discussed in Chapter 3 and 2) to provide the travel range larger than 300 mm.

#4. The experimental testbed is required to *deal with high reaction forces* during high-acceleration operations.

- We run the single-sided testbed at the maximum acceleration of 45 m/s² (≈ 4.5 G) and plan in a future study to drive the double-sided motor up to about 20 G. At these high acceleration cycles, the motor reaction force becomes very significant and needs to be handled not to cause any serious excitation to the rest of the system and even to other equipment nearby.
- The high reaction force can be handled 1) by a balance mass which moves in the opposite direction to dissipate the reaction energy and to keep the force from being transmitted to the rest of the system and 2) by a very high mass ratio between stationary and moving masses to minimize the reaction dynamics.
- For a balance mass, a ratio of about 10-to-1 or higher is required while a much larger ratio of about 100-to-1 is necessary for a stationary reaction mass.

#5. The experimental testbed is required to *measure the moving stage position in real-time*.

- Position sensors are required for the testbed to provide real-time position to the commutation algorithm and to the position feedback controller so that we can control the motors to perform the noise experiments.
- The real-time position information needs to be available throughout the entire travel range with the desired resolution less than or equal to $1\ \mu\text{m}$ and the RMS position tracking error less than $10\ \mu\text{m}$ during a constant velocity region, required for the long-stroke reticle stage of a lithography scanner.

#6. The experimental testbed is required to *directly measure the motor force such as cogging* to understand the force harmonics exerted on the stage during cycle operations.

- We speculate that the motor force harmonics act on and vibrate the moving stage, thereby radiating acoustic noise. In this sense, it is important to be able to directly measure the forces, especially the cogging, to study the harmonics.
- A force sensor or a dynamometer is required to do this task for the experimental testbed.

#7. *Vibrational and acoustic noise measurement systems* are required to investigate the motor vibro-acoustic noise issues.

- Accelerometers are needed to measure the vibrational noise of both the conventional iron-core motor and new fine-tooth motor.
- Microphones are needed to measure the acoustic noise emitted by both the conventional and new motors. Microphones with the audible frequency range of 20 Hz to 10 kHz are required.

- Selected accelerometers, microphones, and necessary electric accessories are presented in Chapter 5.

We present in the following section various conceptual designs of the experimental testbed considering the requirements discussed above.

4.2 Conceptual Designs

The structural designs of the experimental stage setup are mainly subject to the magnetic configuration of the motor armature and magnet track. Namely, depending on which part is moving or stationary and which is long or short, we can have four different major configurations of 1) moving short magnet with stationary long armature, 2) stationary long magnet with moving short armature, 3) moving long magnet with stationary short armature, and 4) stationary short magnet with moving long armature. In the design process, we generated concepts for each of these four configurations to understand and compare one design to another. Hand sketches of the testbed system for each case are presented in the following subsections along with the pros and cons of each design. Note that the design sketches are based on the double-sided motor configuration, but the single-sided design configuration simply requires the removal of the upper half.

4.2.1 Moving Short Magnet and Stationary Long Coil

There can be many different designs to achieve the magnetic configuration of moving short magnet and stationary long armature (or coil to be simpler), and one possible design is sketched in Figure 4-1 with corresponding coordinates. The front view shows the upper and lower armatures, and the moving magnet track in between. The whole system is installed on a large (1.2 m × 0.9 m) and heavy granite table to provide a high mass ratio and handle the expected high reaction force. Note that only a half of system is depicted for simplicity in the front view sketch about the symmetry line. The dynamometers are installed on the bottoms of the stationary armatures to

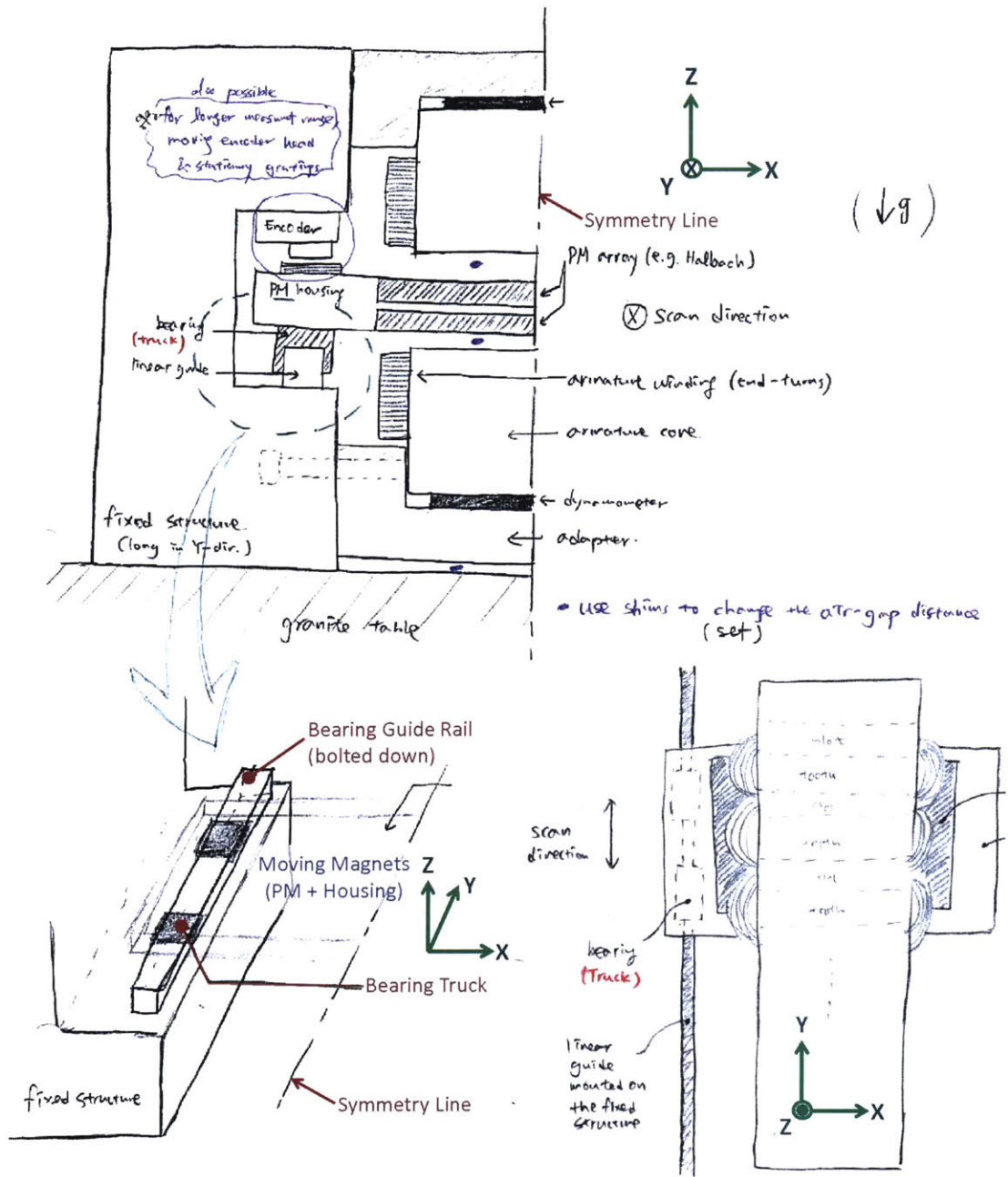


Figure 4-1: Hand sketch of a possible stage design with moving short magnet and stationary long coil. Front view (upper), isometric view (lower left), and top view (lower right).

directly measure the motor force. We configure the dynamometer using four triaxial load cells; its details are discussed in Chapter 5. The motor air gap can be established by using shims, especially of non-magnetic material when directly used in the motor air gap. There are also position sensors, which consist of an encoder read-head and linear scale to obtain the real-time position of the moving stage. Note that in this configuration, we must have the read-head on the moving short magnet track and the encoder scale on the longer stationary structure, so as to have a long measurement range. The moving stage is guided in the Y scan direction by the bearing system with the bearing trucks on the stage and linear guide rails on a fixed structure as shown in the isometric view of the sketch. Note that the bearing system is schematically drawn with trucks and linear rails, but we ultimately plan to utilize air bearings as discussed in the previous section. Detailed air bearing designs and the design process are presented in Section 4.3.1.

In this design variant, the moving portion is the short magnet track as shown in the top view, so we can achieve a higher acceleration for the same magnetic force exerted on both the armature and the magnets. It is also beneficial to have moving magnets in that we can minimize the number of umbilical cables. In addition, these sketches in Figure 4-1 show modular designs where 1) the single- and double-sided configurations can be independent by attaching or detaching the upper armature module and 2) the motor can be changed to a different kind without fully disassembling the stage structure.

Another possible design with the magnetic configuration of moving short magnet and stationary long coil is shown in Figure 4-2. This design is basically a 90°-rotated version of the previous design. Here, we use commercially available cast-iron angle plates as a base structure to hold the stationary long armatures. The angle plates can be translated on the table top to set or adjust the motor air gap with the help of shims and as allowed by oval openings of the top plate as depicted in the magnified view. In this design, it might be easier to disassemble and reassemble the armatures 1) for single- and double-sided configurations and 2) when changing the motor, since we always have easy access to the mounting area from the backs of the angle plates. One

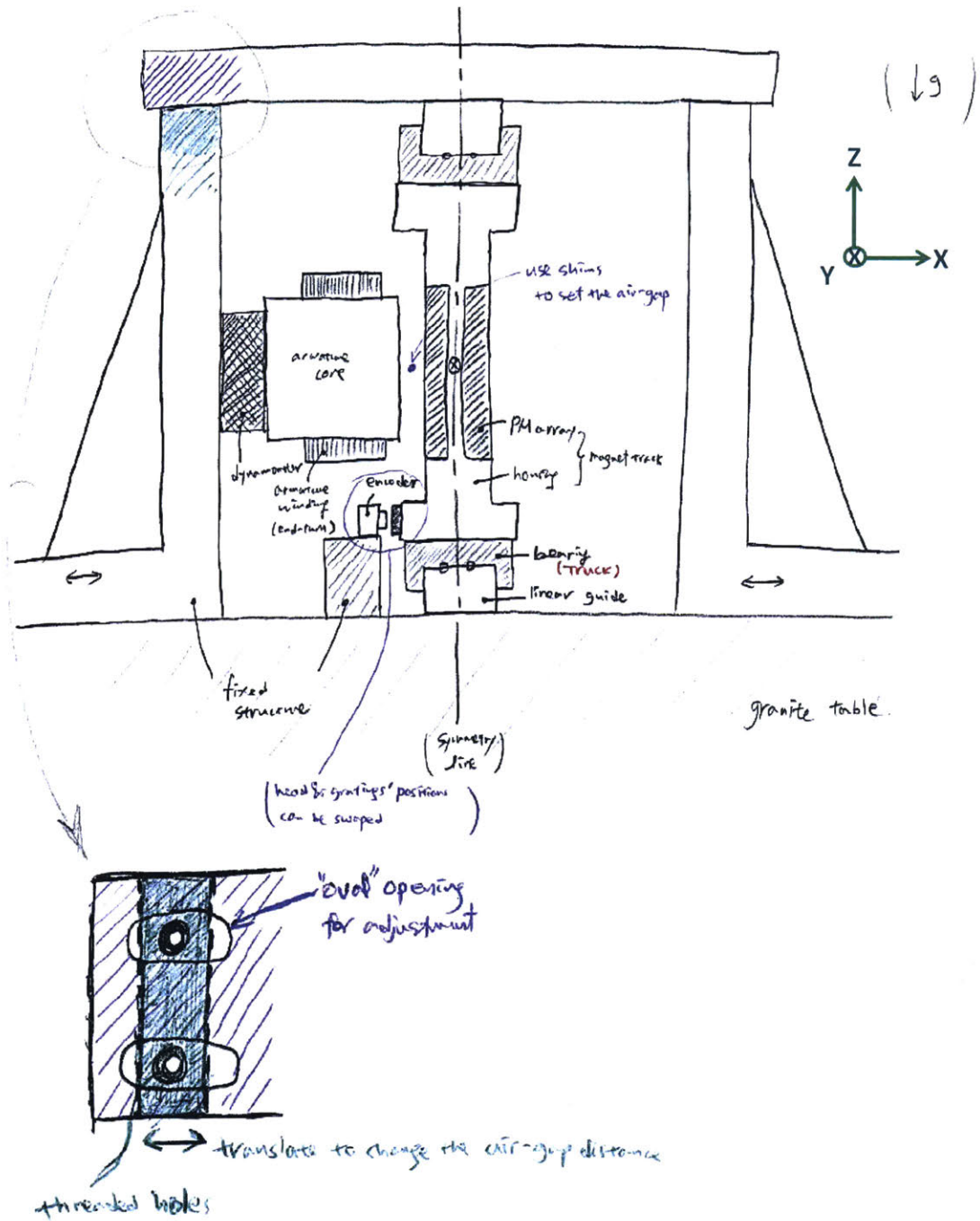


Figure 4-2: Hand sketch of a possible stage design with moving short magnet and stationary long coil. Essentially a 90°-rotated version of the previous concept.

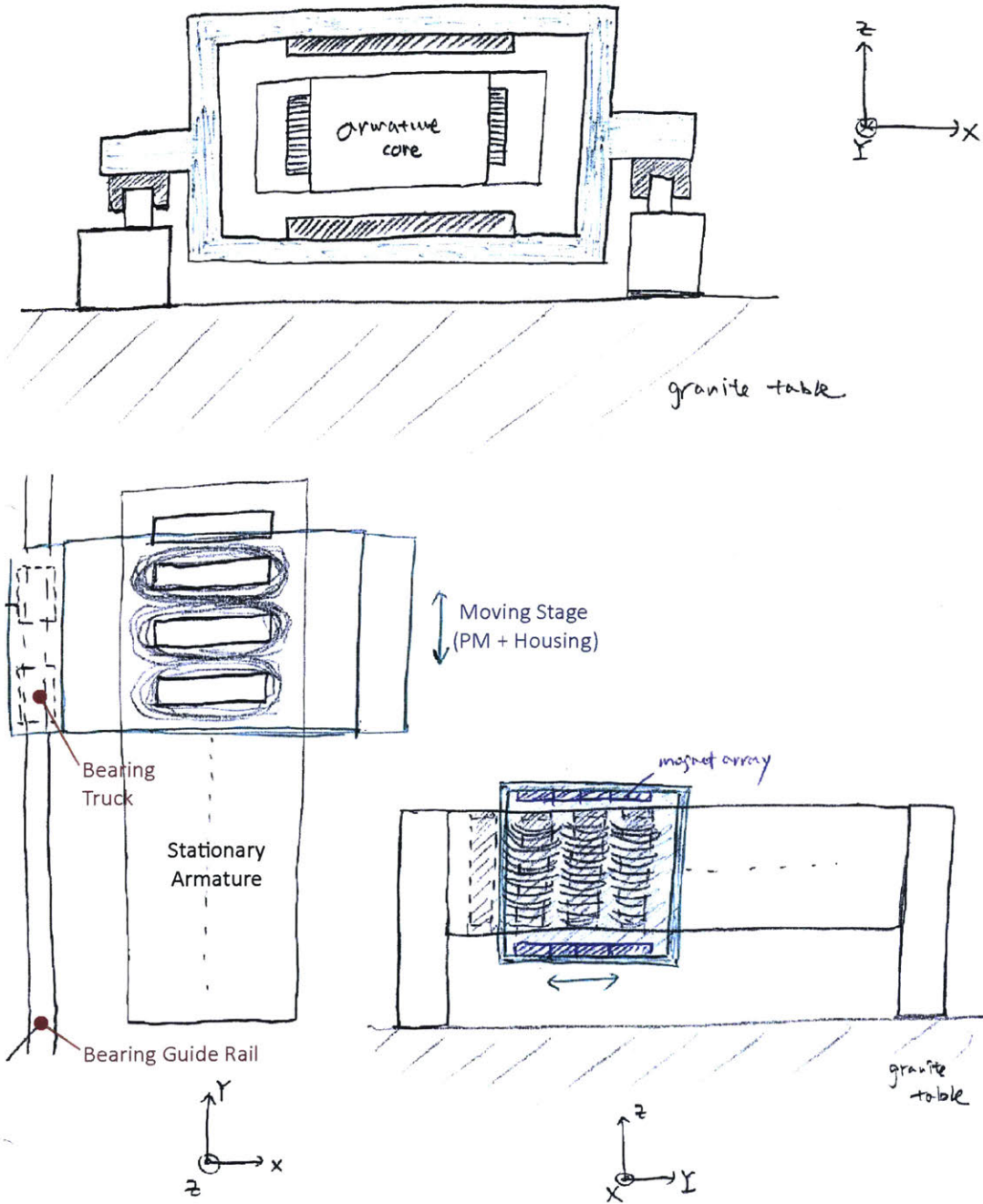


Figure 4-3: Hand sketch of a possible stage design with moving short magnet and stationary long coil. Moving magnets are configured outside. Front view (upper), top view (lower left), and side view (lower right).

drawback of this design is however that the armature is simply hanging as a cantilever, thereby causing a constant moment in the θ_Y -direction on the dynamometer by its own weight. This moment might make it difficult to set the preload uniformly to the load cells forming the dynamometer.

If we place the moving short magnets outside, we can have another possible design configuration as shown in Figure 4-3. Unlike the previous designs where the short magnets are sandwiched by two armatures, the magnet arrays are split into the upper and lower parts of the moving stage structure. The long iron-core armature in the middle can be made out of two regular armatures mounted back to back. Note that if only for the double-sided configuration, the iron-core armature can be customized as one piece without a back yoke since the magnetic flux can return through the magnet track. In this design, it is easy to switch between single- and double-sided configurations by simply adding or taking apart one of the magnet tracks. There are however a few disadvantages in this design that 1) the stage structure required to split the magnet tracks increases the moving mass, thereby decreasing the acceleration and 2) the long stationary armature required to have a long travel range might sag in the middle because it can be only held at the ends as shown with the side view in Figure 4-3.

Among the three different conceptual designs for the case of moving short magnet and stationary long coil, the first one in Figure 4-1 meets the requirements better, and we briefly list the pros (+) and cons (-) of this design.

- (+) The moving mass of magnet tracks is smaller than the iron-core armatures so that we can increase the stage acceleration for the same magnet force.
- (+) The long and heavy armatures add significant mass to the stationary portion of the system. With these heavy armatures together with the base structures and the granite table against the light moving magnets, we can achieve a high mass ratio to handle the expected high reaction force.
- (+) We can minimize the number of moving cables, so the assembly can be simpler and the undesired cable dynamics can be minimized.

(–) Longer armatures than magnets mean that there are parts of coils which are not engaged with magnets. These un-engaged coils increase the electric power dissipation. To avoid this, we can divide the armature into several sections and selectively turn off the un-engaged windings. This however requires the increased number of power amplifiers and also might cause the traveling of heat along the long armature. Such moving heat sources are troublesome in precision machines, as thermal deformation then never reaches steady-state. In the lithography use case, it will likely be best to operate all coils, and accept the large power dissipation.

4.2.2 Stationary Long Magnet and Moving Short Coil

In this subsection, we discuss the second magnetic motor configuration of stationary long magnet and moving short coil, which is the opposite of the previous magnetic structure. Hand sketches of one possible design with such a magnetic configuration are shown in Figure 4-4. The overall testbed structure stays the same, but in this design, the magnet tracks are long, stationary, and located outside, while the moving iron-core armature is sandwiched between the upper and lower magnet tracks. The side-view sketch schematically shows a conventional 3-phase armature with the coils lump-wound on iron cores. This moving short armature is placed between two magnet tracks without a back yoke. As before, the motor air gap can be set or adjusted by using shims, and the modular design helps the disassembly and reassembly process for changing motors or switching between single- and double-sided configurations. A similar design, but a 90°-rotated version is depicted in Figure 4-5. In this design, compared to one in Figure 4-2, the moment exerted on the dynamometer in the θ_Y -direction is smaller due to the lower weight and the shorter moment arm, so the cantilever effect might not be as problematic as before.

The moving short armature designs in Figures 4-4 and 4-5 are advantageous in that: 1) all the coils are always engaged with magnets and so there is no unnecessary power consumption, and 2) not many power amplifiers are required, so the electric assembly can be simpler. In fact, only one commercial 3-phase power amplifier is

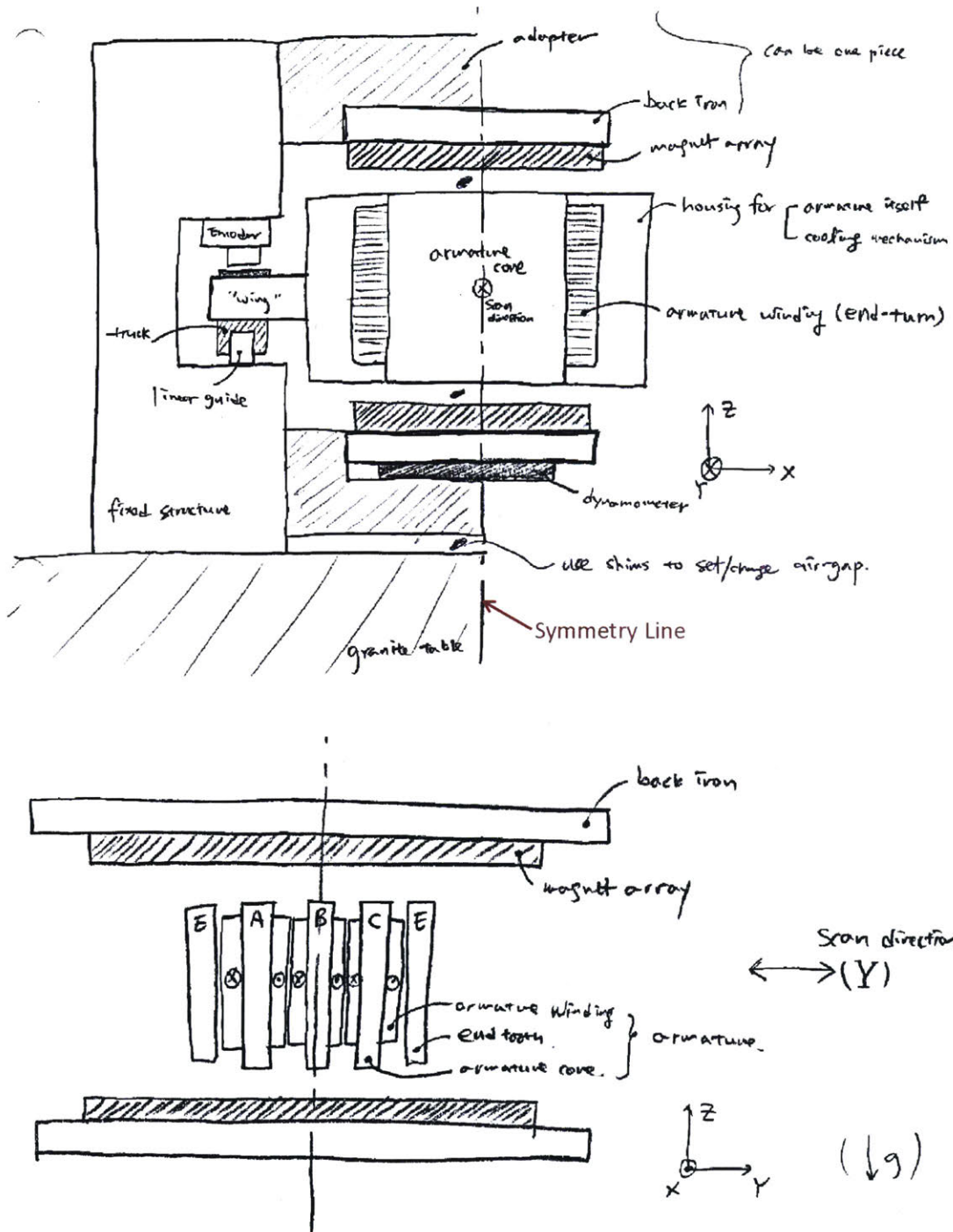


Figure 4-4: Hand sketch of a possible stage design with stationary long magnet and moving short coil. Front view of overall structure (upper) and side view of motor magnetic configuration (lower).

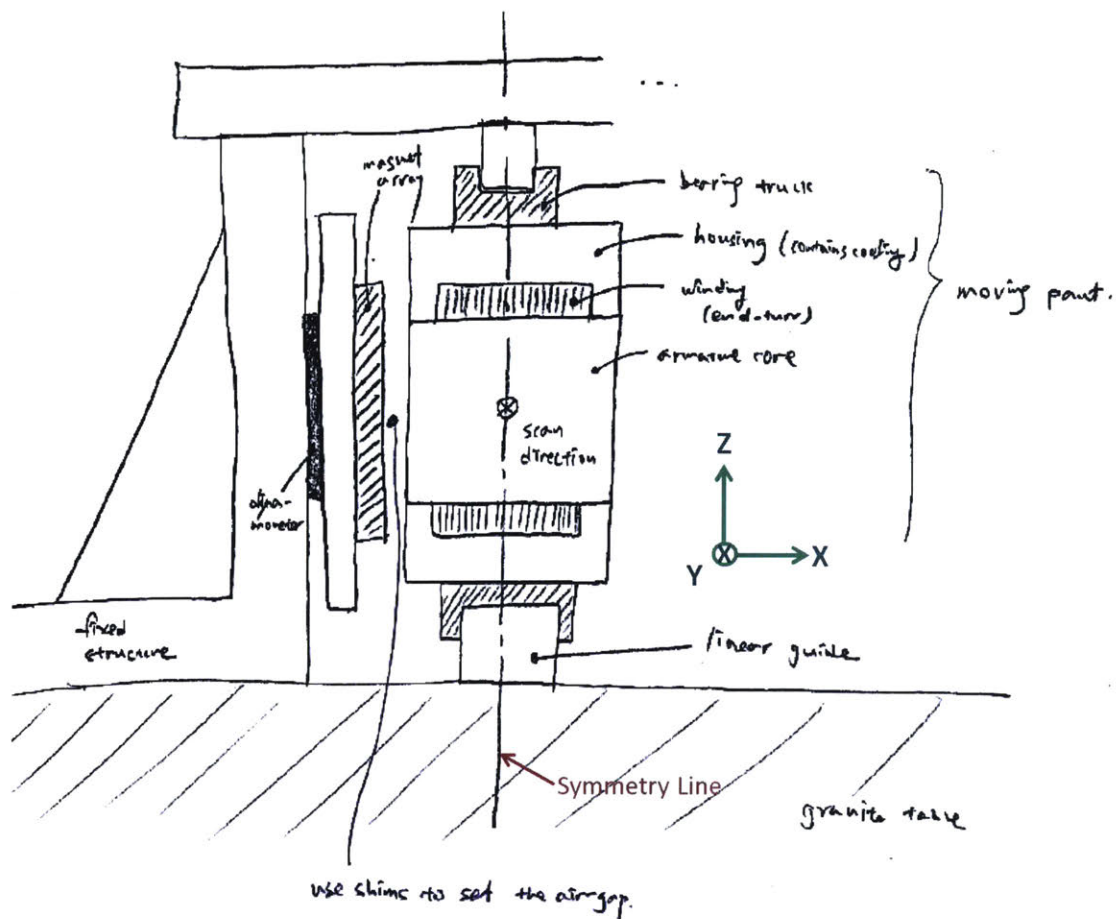


Figure 4-5: Hand sketch of another possible stage design with stationary long magnet and moving short coil. Essentially a 90°-rotated version of the previous concept.

enough to drive a conventional 3-phase motor when the armature is short and moving. These are some of the reasons why the magnetic motor configuration of stationary long magnet and moving short coil is the most common type in industry. However, one of the biggest drawbacks of this configuration for our purpose is that the moving mass of the iron-core armature will be larger than the moving mass in the case of moving short magnets. This can be a significant loss in the aspects of 1) achievable stage acceleration and 2) mass ratio between stationary and moving parts for the reaction force handling. This becomes more problematic if we add a liquid cooling mechanism to the moving armature, as will be required for thermal management at high acceleration. Note that we choose not to implement the cooling structure in our experimental testbed since we can run experiments for a short duty cycle so as not to

approach thermal limits. For commercial-level motor designs, however, the cooling is one of the most important design aspects to ultimately consider, especially for high-power applications such as a lithography scanner. In addition to the disadvantage of increasing the moving mass, the armature contains numerous coils and possibly water supply lines so that we have to deal with a large number of moving umbilical cables in this magnetic configuration. This might complicate the assembly process and require more effort to deal with the associated cable dynamics.

We briefly summarize below the pros (+) and cons (–) of designs with the magnetic motor configuration of stationary long magnet and moving short coil.

- (+) All coils in the armature are engaged with magnets at all times and so no unnecessary power dissipation is needed.
- (+) The motors can be driven with the minimal number of power amplifiers: namely, as small as one amplifier for a conventional 3-phase armature and 5 amplifiers at most for our 5-phase fine-tooth motor armature.
- (–) The moving mass of the iron-core armature is larger than the case of moving short magnets.
 - The achievable stage acceleration decreases.
 - The mass ratio between stationary and moving parts decreases and so the system might be more affected by the high reaction force.
- (–) There are more umbilical cables attached to the moving part than for the case of moving short magnets.

4.2.3 Moving Long Magnet and Stationary Short Coil

The third magnetic motor configuration is with a moving long magnet and stationary short coil. A simple hand sketch of such a configuration is shown in Figure 4-6. In fact, this design can be seen as either moving long magnet with stationary short coil or stationary long magnet with moving short coil depending on our choice of

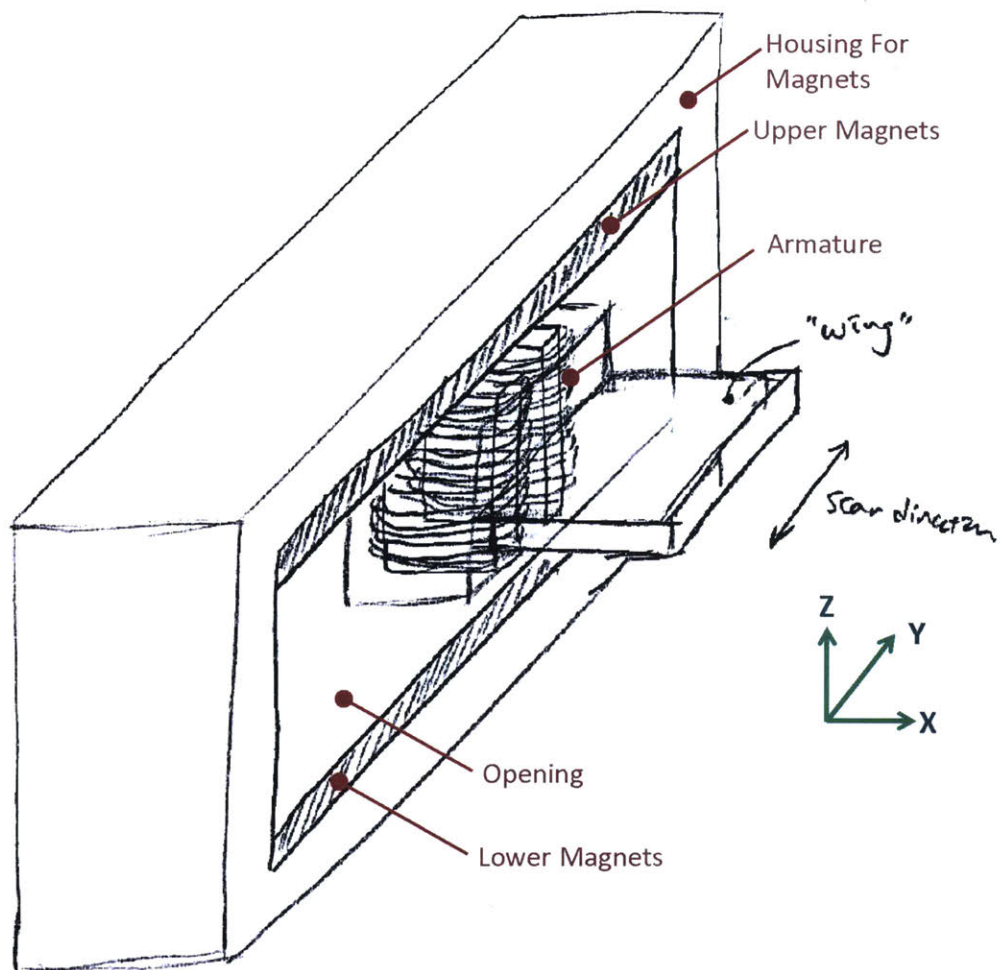


Figure 4-6: Hand sketch of a possible stage design with moving (or stationary) long magnet and stationary (or moving) short coil.

which is the moving part. If we choose to move the armature and guide its motion accordingly with bearing systems, then we would have a design similar to Figure 4-4. If we choose, however, to move the long magnet tracks, then we have a design of the magnetic motor structure of moving long magnet and stationary short coil. Similarly, this configuration of moving long magnet can also be achieved in the same design shown in Figure 4-1 if we make the moving magnet tracks longer and the stationary armatures shorter.

In both possible designs (moving magnets outside or inside) of the long-moving-magnet case, we keep the advantages of having short armatures. However, the moving

mass is still larger than the case of moving short magnet and this is a critical disadvantage when considering our testbed's purpose of high acceleration.

A brief list of the pros (+) and cons (−) of this long-moving-magnet case is summarized as below.

- (+) All coils are engaged with magnets at all times, so there is no unnecessary power consumption and the number of power amplifiers can be minimized.
- (+) The number of umbilical cables is minimized.
- (−) The moving mass is larger than the case of moving short magnets, so we lose in the aspect of achievable stage acceleration.
- (−) The linear guide rails or guide surfaces for bearings are required to be inefficiently long.

4.2.4 Stationary Short Magnet and Moving Long Coil

The final motor configuration variant is with stationary short magnet and moving long coil. One possible design of this configuration is illustrated in Figure 4-7. As can be seen in the figure, this design is a switched (between moving and stationary parts) version of Figure 4-1 with the long moving armatures outside. Similarly, we can have the moving long armature inside by switching the moving and stationary parts of the design shown in Figure 4-3.

As discussed in the previous subsection, one of our design targets is to have high stage acceleration. In this sense, the configuration with long and heavy moving armatures needs to be avoided. Moreover, this motor structure keeps the disadvantages of having longer armatures than magnets, which gives another reason to avoid this design approach. We provide a brief list of the pros (+) and cons (−) of this long-moving-armature case as below.

- (+) None.
- (−) The moving mass is the biggest among the four different motor configurations.

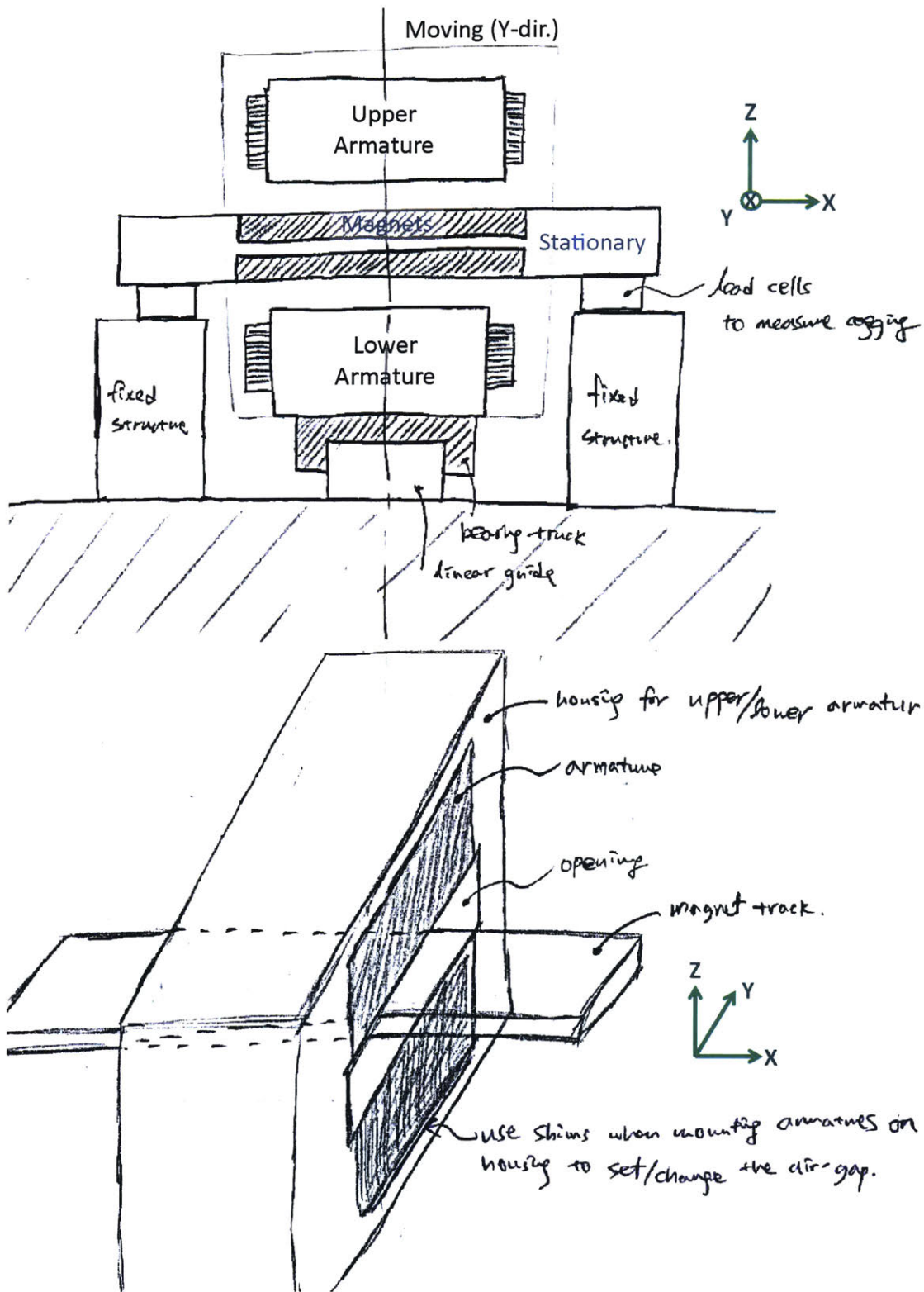


Figure 4-7: Hand sketch of a possible stage design with stationary short magnet and moving long coil. Front view (upper) and isometric view (lower).

- (–) The mass ratio between stationary and moving masses is the lowest among the four basic configurations.
- (–) The number of moving umbilical cables is the largest among the four configurations.
- (–) Not all coils are engaged with magnets, so there is unnecessary power loss by energizing those un-engaged windings. The windings can be divided into multiple sections to avoid this power dissipation issue, but it requires more power amplifiers.
- (–) The linear guide rails or guide surfaces for bearings are needed to be inefficiently long.

4.3 Design Selection

In the previous section, possible testbed designs for four different motor configurations are presented, and the pros and cons of each design are discussed. We choose to converge on the magnetic configuration of *moving short magnet and long stationary coil* for the reasons listed below.

- *Low moving mass*
 - High achievable stage acceleration.
 - High mass ratio between stationary and moving parts to handle the expected high motor reaction forces.
- *Minimized number of moving cables*
 - All winding cables are stationary, and only required umbilical cables are for the encoders and the air supply for the air bearings.
 - This makes it easier to assemble the testbed and handle undesired cable dynamics.

- *Multiple number of power amplifiers to drive individual coils*

- The coils not engaged with magnets can be selectively turned off to save unnecessary power consumption.
- If the heat travel is a more critical factor than the power, then we can choose to energize all coils at all times.

In this section, we present more detailed and practical designs of the magnetic motor configuration with the moving short magnets and the long stationary coils. We first introduce base structures, which provide 1) mounting areas to upper and lower armatures and 2) long and well-ground bearing guide surfaces. As discussed in Section 4.1, we desire to use air bearings to avoid possible mechanical noise sources and isolate the magnetic noise source of the motors. Depending on the types of air bearings and their preloading methods, the stage structure design will be different. We discuss various feasible designs in the following subsection and converge to finalize the design. We show three-dimensional CAD models of the finalized testbed design in both single- and double-sided configurations at the end of this section.

4.3.1 Base Structure and Bearing Selection

We had extensive discussion about air bearing types and possible bearing structure designs with Drew Devitt, the chief technology officer (CTO) of New Way Air Bearings. He proposed using two long guide bars that New Way had in possession from a previous project. A picture of these guide bars is shown in Figure 4-8¹. We choose to use these bars as our base structures for the reasons listed below.

- The guide bars already have well-ground top and side guide surfaces for air bearings to run against.
- They are long enough (1040 mm and 1295 mm) to provide a long travel range.

For the conventional Tecnotion motor, the travel length is limited by the length

¹We appreciate New Way Air Bearings' kind offer for the guide bars, and thank Drew Devitt for sharing ideas on air bearing configurations.

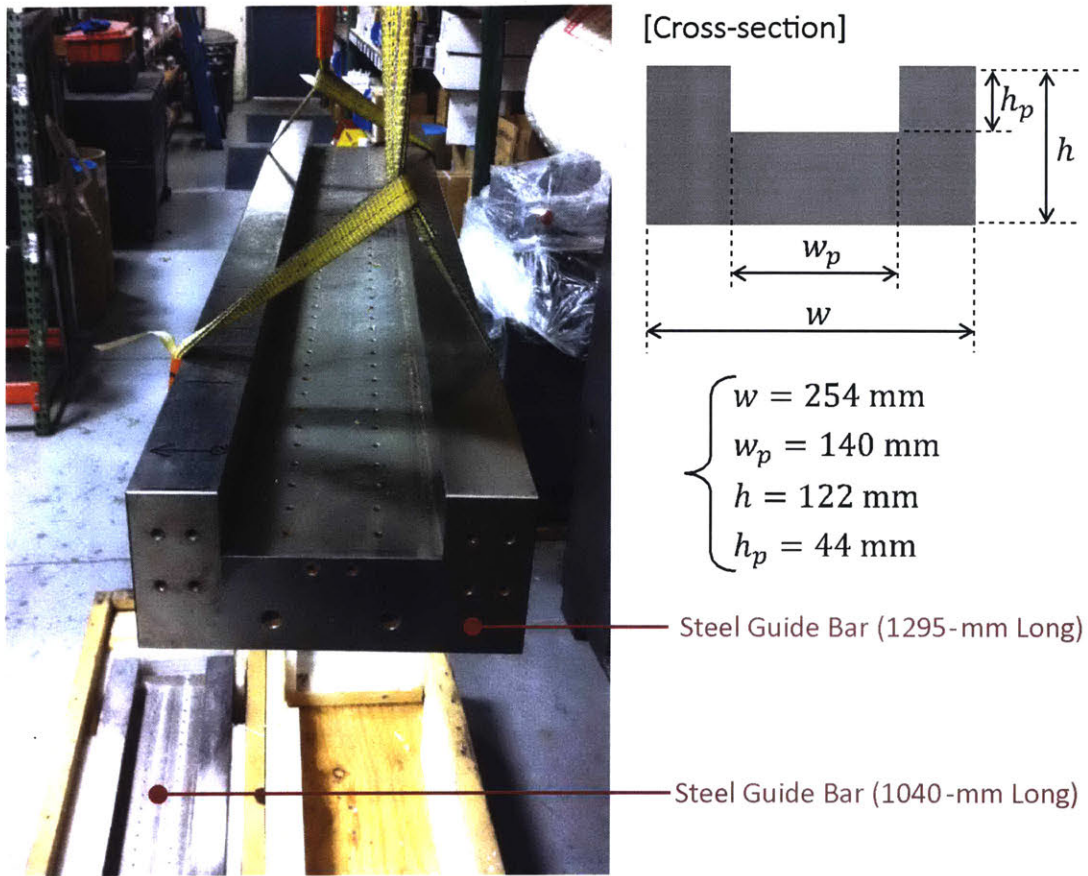


Figure 4-8: Picture of base guide bars with the same cross-section area, but with the different length of 1040 mm and 1295 mm.

of commercially available armatures. However, we can easily obtain the required travel of 300 mm by using these long guide bars together with our newly-designed fine-tooth motor.

- They have a pocketed area suitable to mount both the conventional and new motors. Specifically, the 1040-mm long bar has a pocket of 140 mm × 1040 mm, which are able to accommodate both 77 mm × 336 mm conventional Tecnotion armature and 110 mm × 728 mm fine-tooth motor armature.
- The guide bars are made of steel, and weigh about 226 kg (1295-mm long bar) and 184 kg (1040-mm long bar). These heavy base structures together with the

granite table can provide a high mass ratio to handle the expected high reaction force of the motors.

- Two guide bars with the same cross section area as shown in Figure 4-8 can provide a symmetric structure for the double-sided motor configuration.
- New Way kindly offered to provide the guide bars to us at very low cost. We are grateful for this important contribution to our project.

We consider various types of air bearings and corresponding stage structure designs using these base guide bars. The moving stage designs can be different depending on what types of air bearings to use and how they are preloaded. We discuss several different designs in the following subsections with the pros and cons of each design.

Air Bearings Preloaded by Air Bearings

In order for air bearings to work, the bearings have to be floated by compressed air and also at the same time pressed down by a preloading force against a guide surface. There can be many different ways of preloading, and one of the simplest ways is to use the same bearings in the opposite direction. Figure 4-9 shows one possible design in the front and isometric views with corresponding coordinates. As discussed earlier, we take the magnetic motor configuration of moving short magnet and stationary long coil. Air bearings are used both on the top and bottom of the moving stage to constrain its motion in the Z direction, and also symmetrically both sides for the lateral constraint in the X direction. Note that the air bearings in the sketches are schematically represented by bonded air bearings, but we can readily use other types of bearings with different mounting details. We discuss the selected bearing types and mounting methods in Section 4.3.2.

This preloading method by opposing bearings is conceptually simple. However, in order to realize it in practice, we need to have two parallel flat guide surfaces in each constraining direction. Therefore, a total of four flat guide surfaces have to be parallel in our case of constraining motions in both the X and Z directions, and all these guide surfaces with the tolerance less than a few micro-meters are

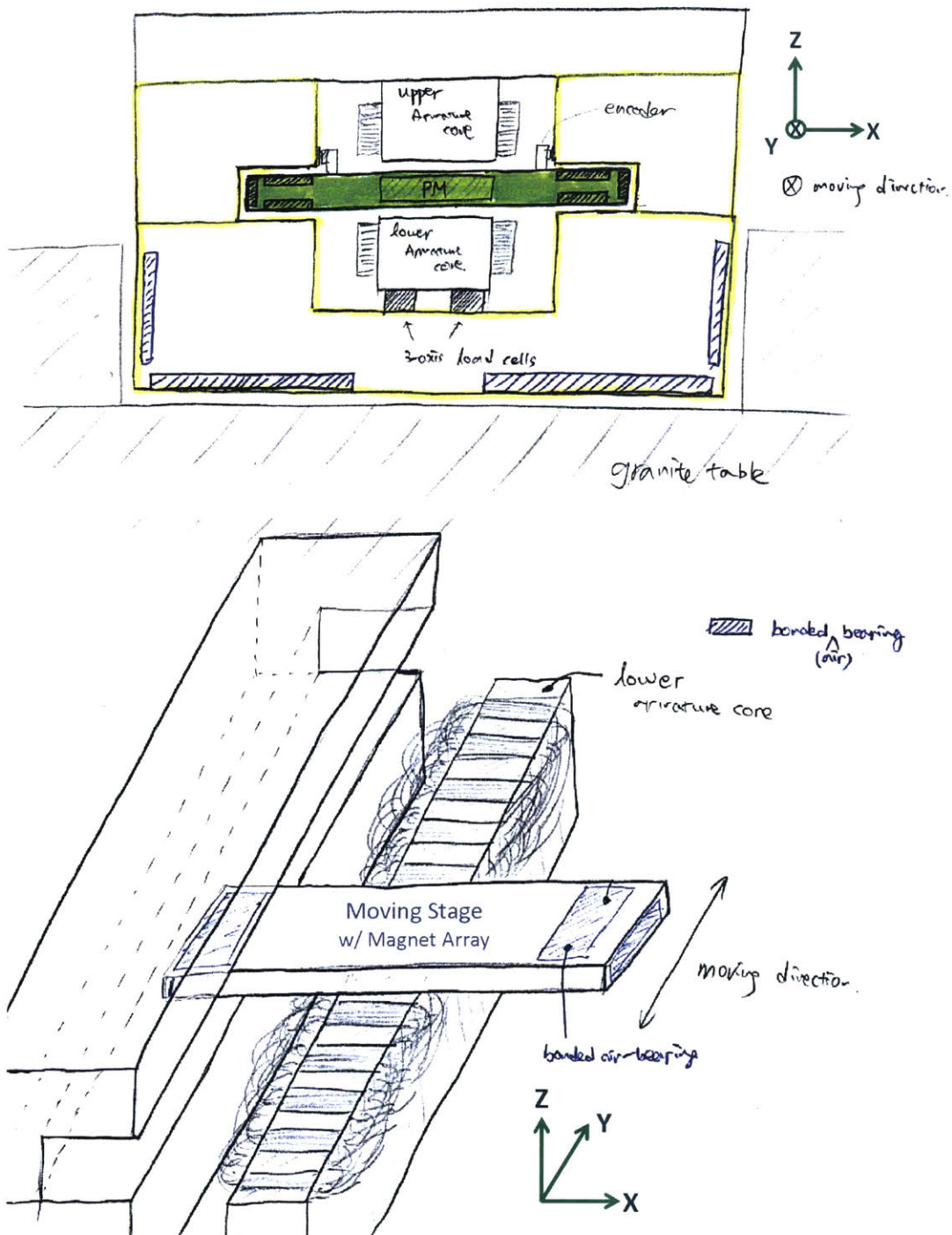


Figure 4-9: Hand sketch of a possible design with air bearings symmetrically preloaded by other air bearings. Front view (upper) and isometric view (lower).

needed even for the single-sided motor configuration. This complicates the overall structure assembly. Moreover, there have to be at least two different air supply lines so that we can adjust the air pressure to cope with different preloading levels required by changing motors (conventional or new motor) or switching motor configurations (single- or double-sided configuration).

Note that this design includes a possibility to use the base structure as a balance mass to dissipate the reaction energy. The flat surface of the granite table can be the guide surface, and with a proper selection of air bearing size, the bearings can be well preloaded by the weight of the base structure. The lateral motion of the balance mass can be constrained by opposing side bearings against additional guide surfaces as shown in the sketch. We choose not to use the balance mass method for the single-sided motor configuration since 1) we have a high mass ratio between stationary and moving masses and 2) our target acceleration for the single-sided configuration is not too high, namely about 45 m/s^2 . However, we might need to apply the balance mass approach for the double-sided motor configuration in the future work because we target to drive the double-sided motor at an acceleration as high as 200 m/s^2 (20 G).

Air Bearings Preloaded by Vacuum

In order to avoid using counter guide surfaces, we can preload air bearings by vacuum. One possible design with the vacuum preloaded (VPL) air bearings is shown in Figure 4-10. The top bearings are vacuum-preloaded, so the entire bearing systems can be operational with one base guide bar. This allows the single-sided motor configuration to be a stand-alone system without the need for the entire upper structure. For the side bearings, we can either use regular air bearings preloaded by opposing bearings from the other side or apply VPL bearings on only one side. There is a trade-off in this choice. Using opposing bearings on both sides might provide higher stiffness, but it can cause a bending moment on the stage as depicted in Figure 4-10 with the blue dashed line. With VPL bearings on one side, we can avoid the bending moment, but the stiffness might be lower. We discuss this issue further when we

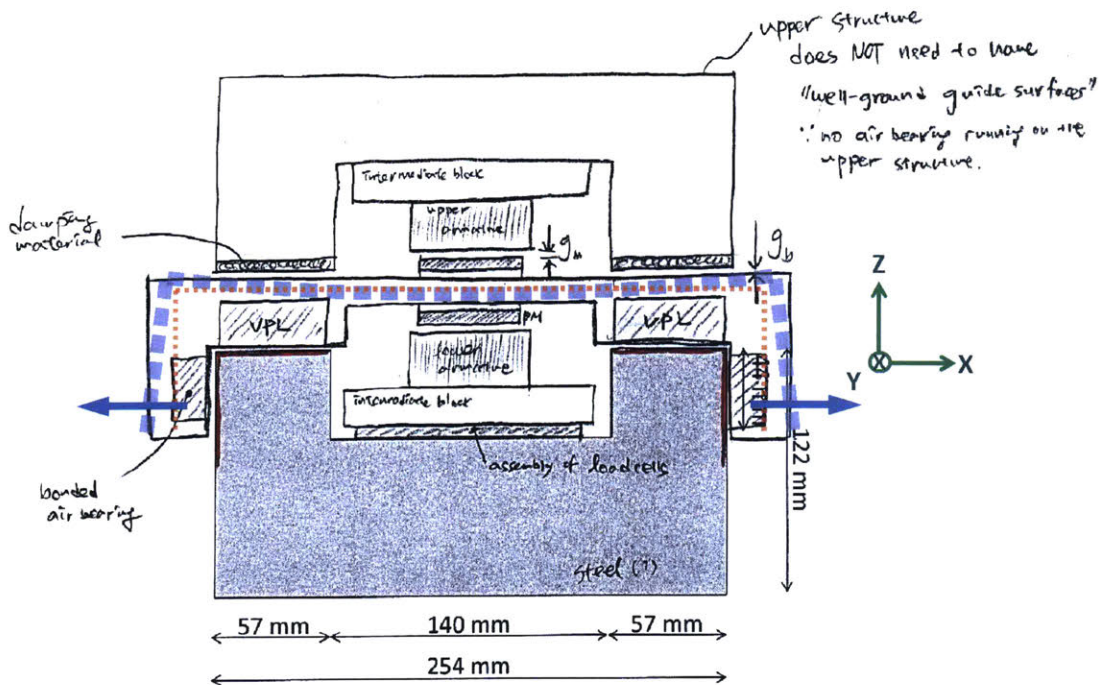


Figure 4-10: Hand sketch of a possible design with vacuum preloaded (VPL) air bearings.

present the final testbed design in Section 4.3.2.

The VPL bearings are advantageous in that we can float and hold them down simultaneously against one flat guide surface. However, since such a bearing shares the bearing surface for both pressured air and vacuum, it is not space-efficient and also provides less stiffness. For example, a circular VPL bearing with 50 mm diameter (S205001 by New Way) has the stiffness of $13 \text{ N}/\mu\text{m}$ at the air pressure of 60 psi while a regular bearing with the same size (S105001 by New Way) has the stiffness of $58 \text{ N}/\mu\text{m}$, which is about 4.5 times higher. This means that we need to use 4.5 times larger area to achieve the same level of bearing stiffness. Considering the pre-defined top guide surface area of the base bar, this requires the moving stage to have larger length in the Y direction, thereby 1) significantly losing the total travel range and 2) lowering the achievable acceleration due to the mass increase of the stage structure.

Air Bearings Preloaded by Magnets

Another way to preload the air bearings without the need of counter flat surfaces is to use magnetic forces. In fact, in many cases, an array of magnets are used with steel straps to provide proper preloading forces to air bearings. For our case, however, the base guide bar itself is made of steel and we can directly take advantage of this material property. Figure 4-11 shows hand sketches of one possible design with air bearings preloaded by magnets. The hand sketch of the top view schematically shows the arrangements of top air bearings and preloading magnets. The magnetic pressure is in general higher than the vacuum used in VPL bearings, so it is more space-efficient to use the magnetic preloading. Specifically, the magnetic pressure by a neodymium magnet with the residual flux density, B_r of 1.4 T is about 780 kPa, which is obtained by

$$\frac{B_r^2}{2\mu_0} = \frac{(1.4 \text{ T})^2}{2 \times 4\pi \times 10^{-7} \text{ Tm/A}} \approx 780 \text{ kPa} \quad (4.1)$$

where μ_0 is the magnetic permeability of the air. This is higher than the vacuum range, commonly used for VPL bearings, of 5 to 25 inHg (≈ 17 to 85 kPa). Accordingly, by magnets, we can preload the same air bearings at the same level with only about 10 % of the guide surface area compared to the vacuum, thereby not compromising the total travel length and the achievable stage acceleration.

In order to accommodate both the single- and double-sided configurations with either conventional or new motor, we need to be able to control the preloading force. One possible way as indicated in Figure 4-11 is to change magnets, using the magnet pockets in the stage, with different sizes for different preloading levels. Another, more practical and simpler, way is to use threaded studs to adjust the magnetic gap between magnets and the guide surface, as shown in Figure 4-12. We discuss these preloading magnets further with other design details to finalize the experimental testbed design in the following subsection.

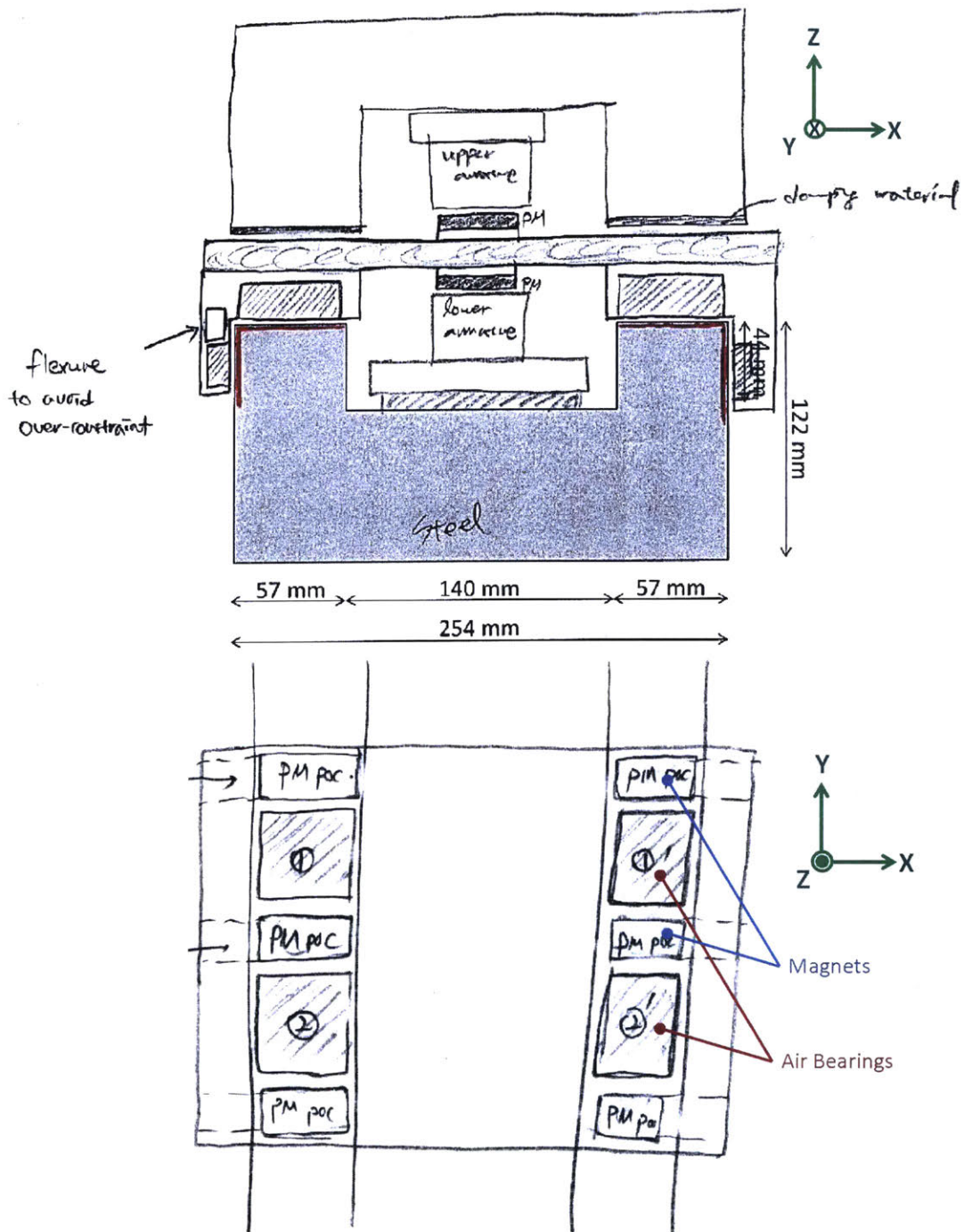


Figure 4-11: Hand sketch of another possible design with air bearings preloaded by magnets. Front view (upper) and top view (lower).

4.3.2 Selected Testbed Design and CAD models

Based on the requirements discussed in Section 4.1, we select the experimental testbed design to have the magnetic motor configuration of moving short magnet and stationary long coil. Also, the bearing systems with the magnetic preload and corresponding stage design are chosen for the reasons mentioned in the previous subsection. Here, we discuss and summarize the finalized design details of the experimental testbed to see how the selected design meets the requirements presented in Section 4.1. We also show the CAD models of the finalized testbed design for both single- and double-sided configurations with either the conventional Tecnotion motor or our newly-designed fine-tooth motor. Note that the drawings of all the components in the final design of the stage testbed are documented in Appendix A.

- #1. The selected testbed design has the *hardware flexibility* to accommodate single- and double-sided motor configurations with both conventional Tecnotion and newly-designed fine-tooth motors.
 - The pocketed area of the 1295-mm long base guide bar has large enough volumetric margin to accommodate motor armatures of both motors as shown in Figures 4-13 and 4-15.
 - The use of air bearings preloaded by the magnetic force allows the independent system of the single-sided motor configuration for both conventional and new motors as shown in Figures 4-13 to 4-16. The 1295-mm long guide bar is used as the lower base structure and the shorter 1040-mm guide bar is utilized as the base of upper motor structure for the double-sided configuration.

- #2. The selected testbed design uses *air bearings* to avoid the noise caused by mechanical contacts.
 - Four rectangular (not circular) air bearings are used against the top guide surfaces to take full advantage of the available guide surface area. Two

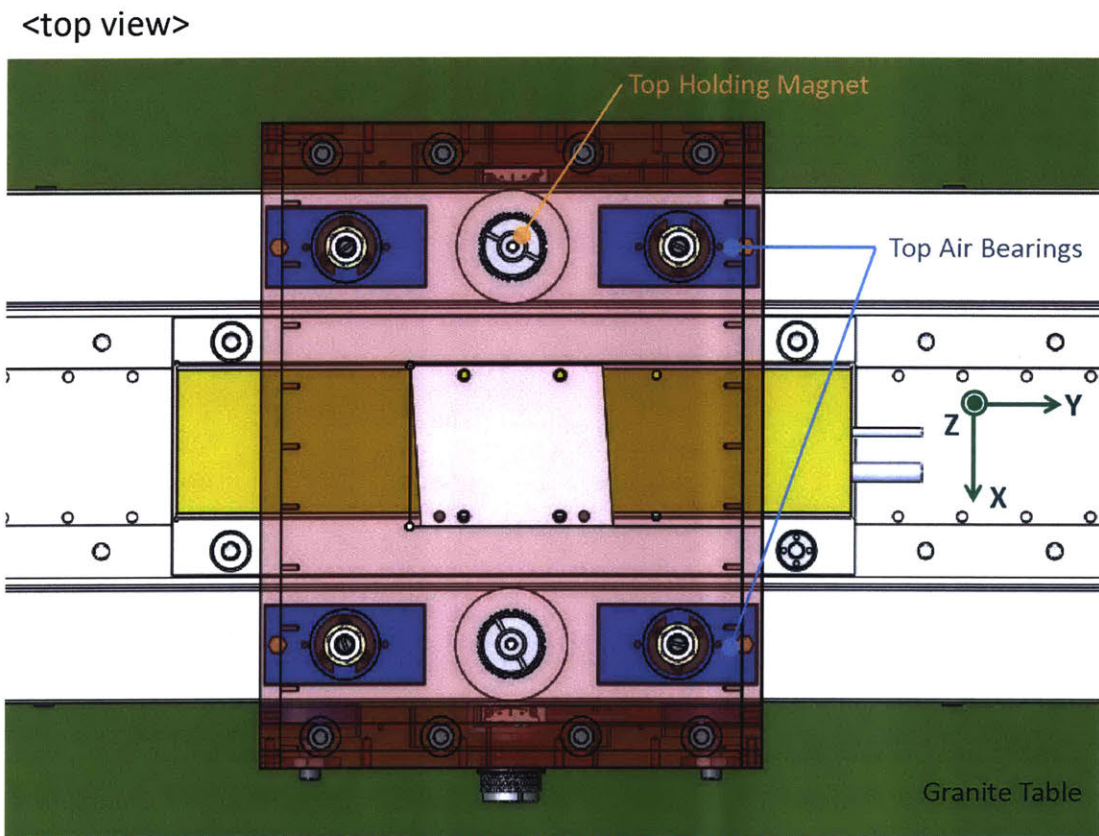
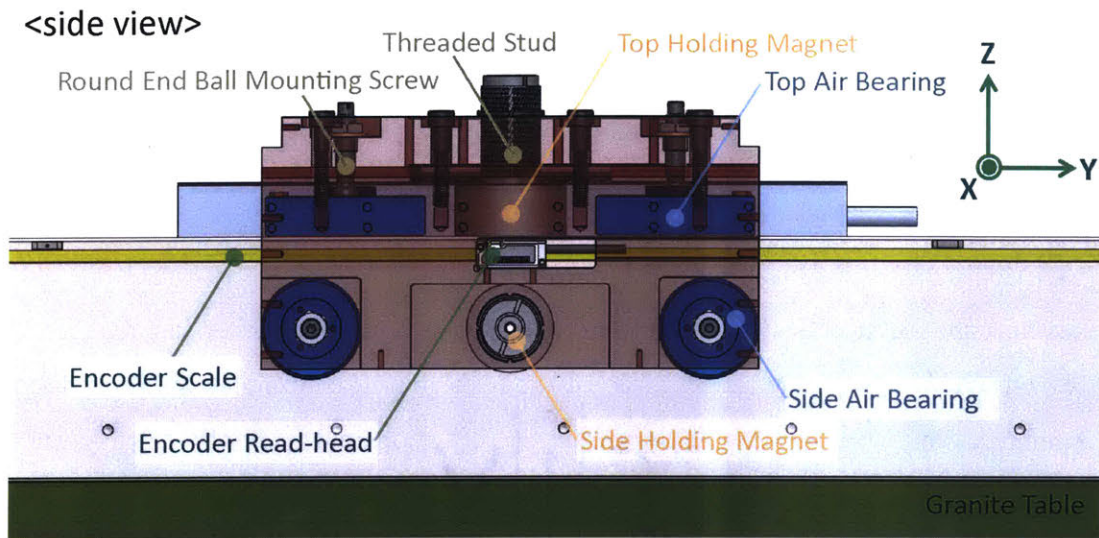


Figure 4-12: CAD model of selected testbed design showing mounting details of air bearings and holding magnets. Side view (upper) and Top view (lower).

circular air bearings are used on only one side to avoid a bending moment on the stage structure while providing the necessary lateral motion constraint. Both top and side air bearings are preloaded by magnets as shown in Figure 4-12.

- We choose to use holding magnets (magnets with steel housings) to apply the air bearing preload because 1) we have limited area and 2) holding magnets are stronger than simple magnets with the same size. The holding magnets are pre-assembled with threaded studs so that we can simply adjust the magnetic gap to control the preloading force.
- We select to use the round end ball mounting screws (S8013B16 and S8013B17 by New Way) to mount the air bearings as shown in Figure 4-12. The round end balls allow the air bearings to stay parallel against the flat guide surfaces even in cases of stage bending modes.

#3. The selected testbed design provides *a long enough travel length* by using the long base guide bars.

- The long guide bar together with the long armature of the newly-designed fine-tooth motor provides the total stage travel length up to 450 mm. Specifically, it is the length between shock absorbers at the ends, 700 mm, subtracted by the stage length in the Y scan direction, 250 mm as shown in Figure 4-16.
- The stage travel length with the conventional motor is limited by the length of the commercially available armature, TL18 by Tecnotion. The total travel range is up to 192 mm, which is the length between armature's end teeth, 288 mm subtracted by the length of the moving magnet track, 96 mm as shown in Figure 4-14.

#4. The selected testbed design provides *a high mass ratio* to handle the expected high reaction force of the motors.

- The mass ratio between stationary and moving masses of the single-sided

motor configuration is about 100-to-1. The stationary mass mainly composed of the granite table and 1295-mm long base bar is about 1140 kg and the moving stage mass is designed to be about 11.5 kg. When we drive the stage at the acceleration of 45 m/s^2 with a 350 mm travel, the base experiences about 0.45 m/s^2 acceleration and moves only 3.5 mm.

- The mass ratio of the double-sided motor configuration is about 115-to-1, where the stationary mass (granite table + two guide bars) is about 1325 kg and the same moving mass of 11.5 kg.

#5. The selected testbed design has *encoder systems* to measure the moving stage position.

- To be able to measure the stage position over a long travel range, the encoder read-heads are mounted on the side plates of the moving plate, and the encoder scales are attached to the side surfaces of the long base guide bar as shown in Figure 4-12.
- The encoder systems are used on both sides in order to cancel out any possible wobbling motion in the θ_z direction. The position resolution is determined by the interpolation rate we choose and it can affect the motor vibro-acoustic noise issue. We discuss in detail this topic in Chapters 5 and 6.

#6. The selected testbed design has the *dynamometer* to directly measure the motor force such as cogging.

- We choose to use four triaxial load cells to configure the dynamometer under the stationary armature by using the stator mounting plate as shown in Figures 4-13 and 4-15.
- Selected load cells and installation details of the dynamometer in the testbed with both conventional and new motors are discussed in Chapter 5.

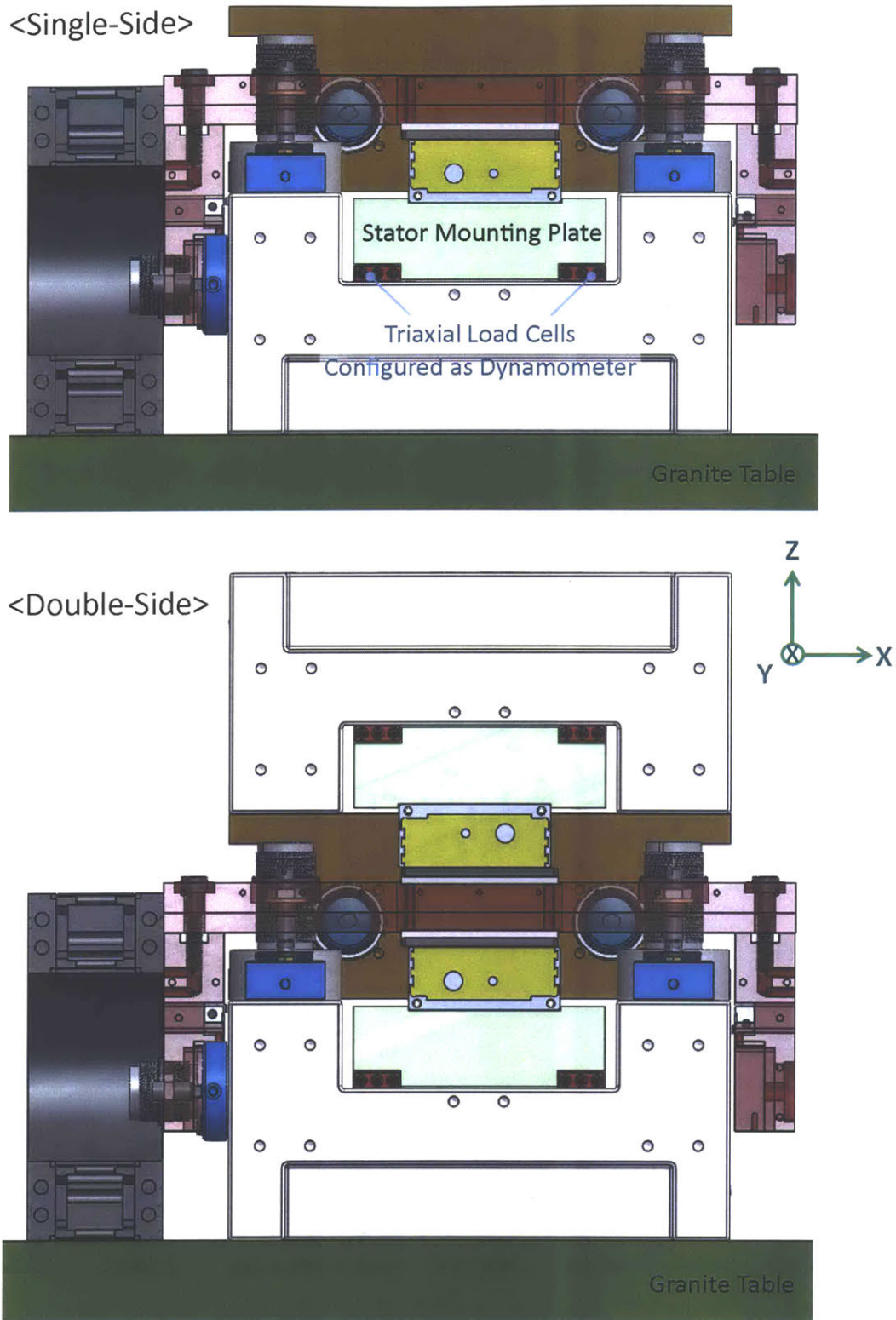


Figure 4-13: Front views of selected testbed design with the conventional Tecnotion Motors both for single-sided (upper) and double-sided (lower) configurations.

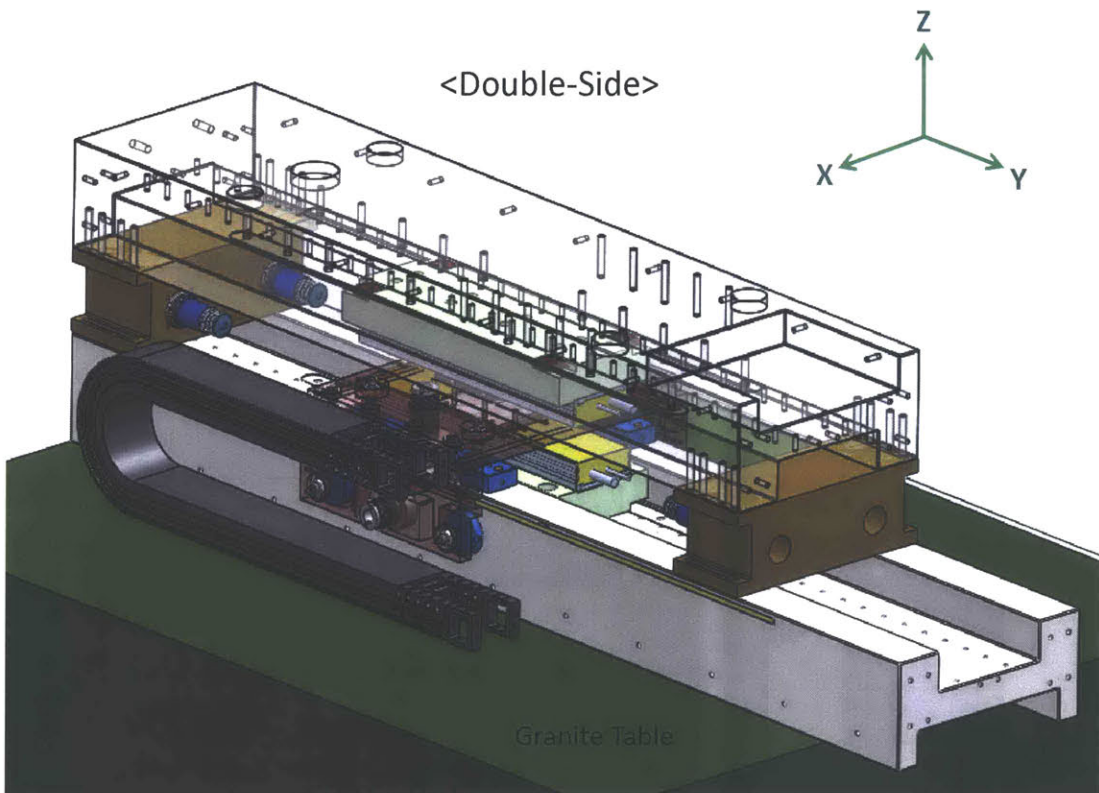
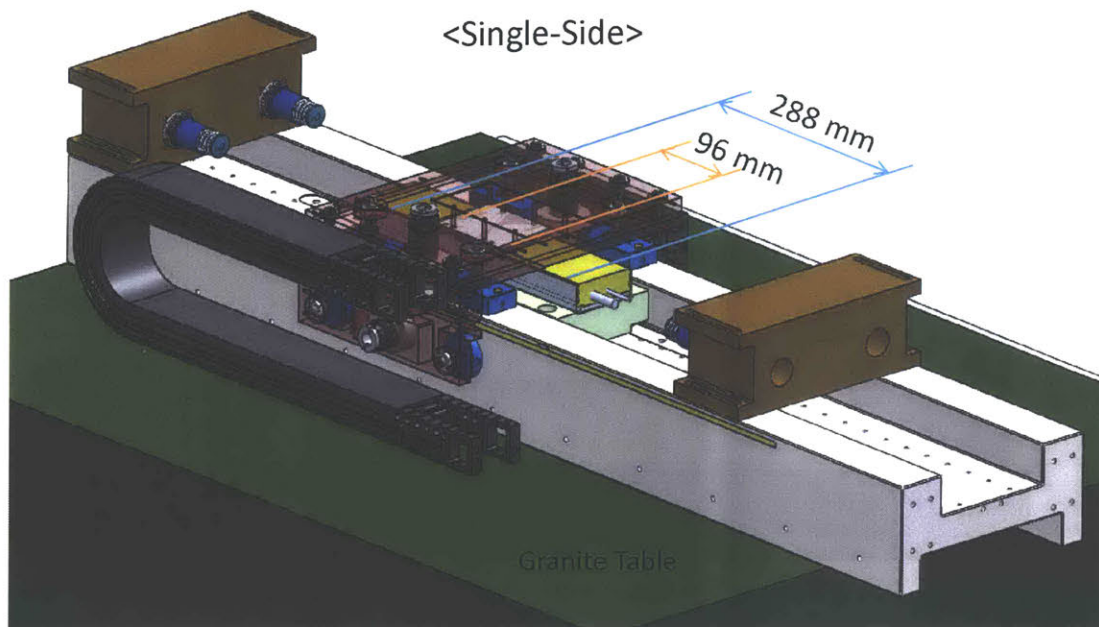


Figure 4-14: Isometric views of selected testbed design with the conventional Tecno-tion Motors both for single-sided (upper) and double-sided (lower) configurations.

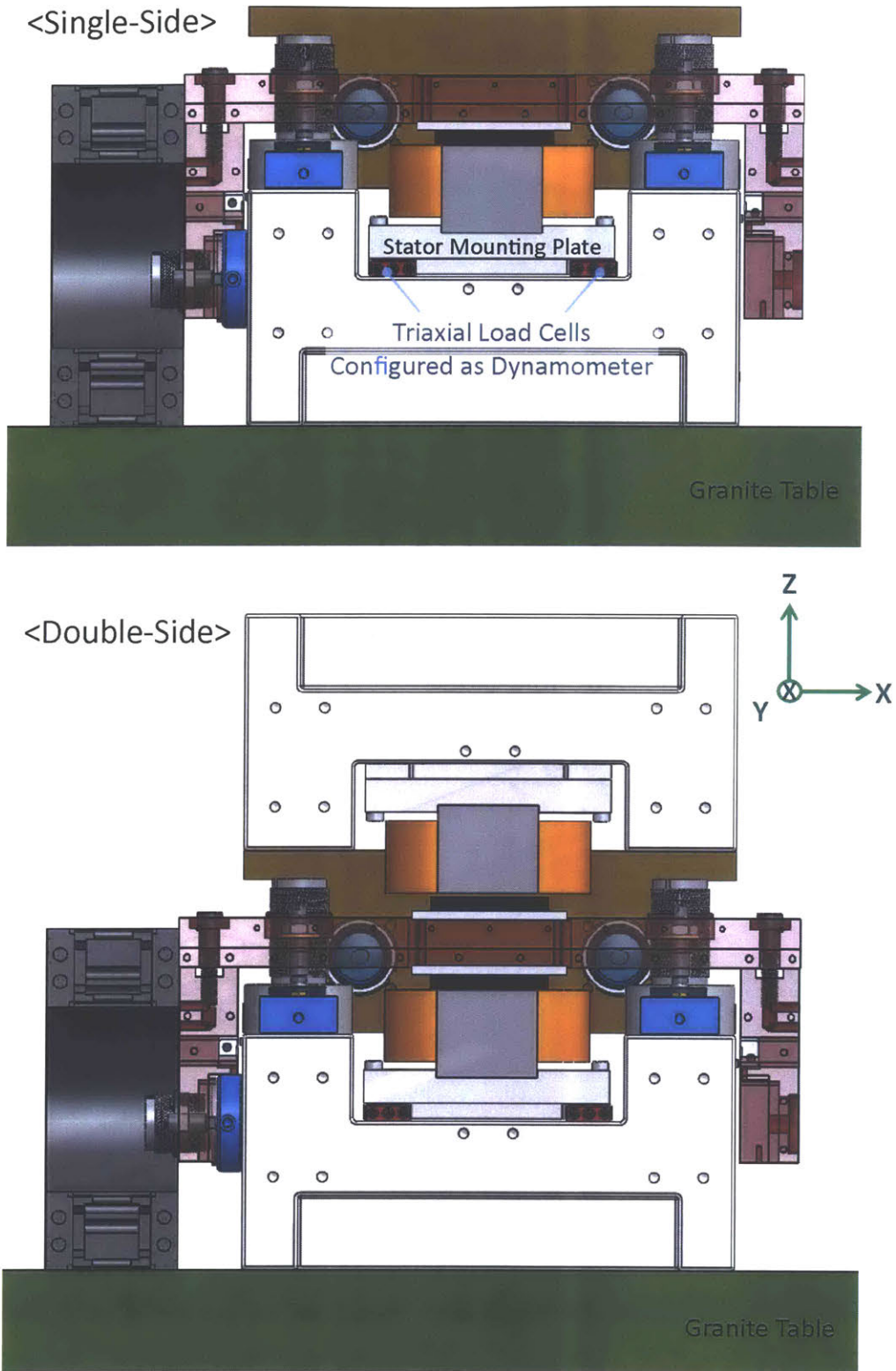


Figure 4-15: Front views of selected testbed design with our newly-designed fine-tooth Motors both for single-sided (upper) and double-sided (lower) configurations.

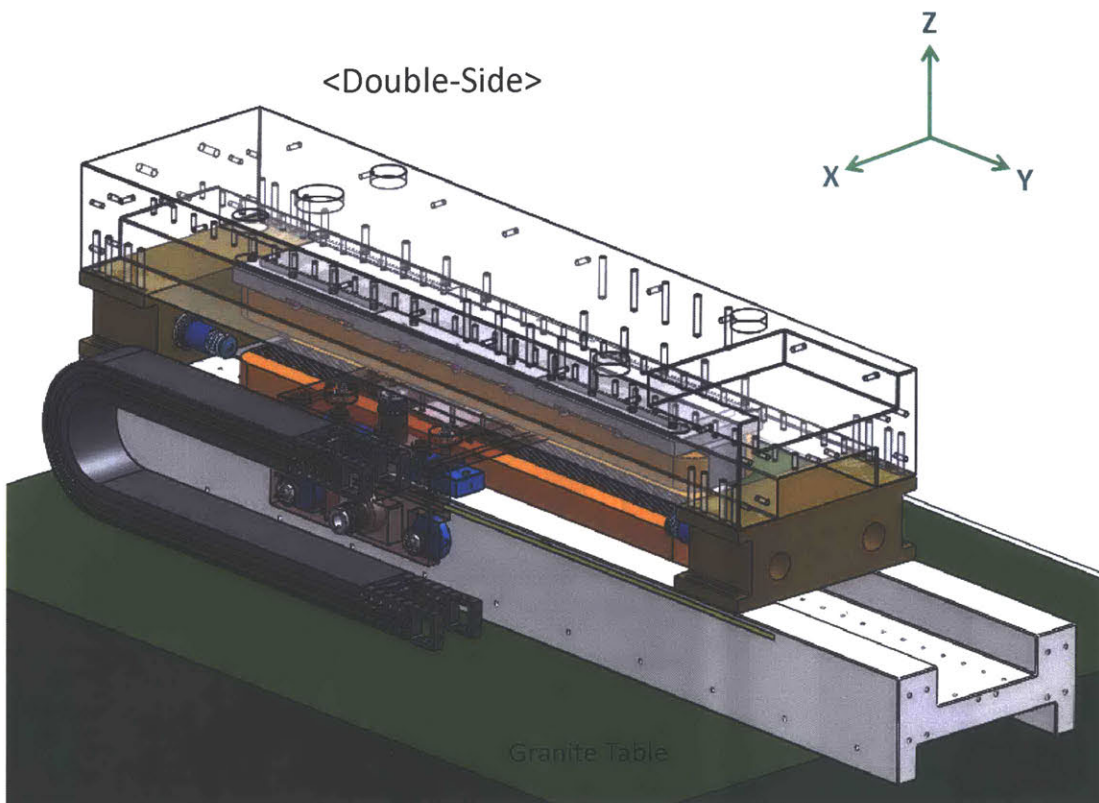
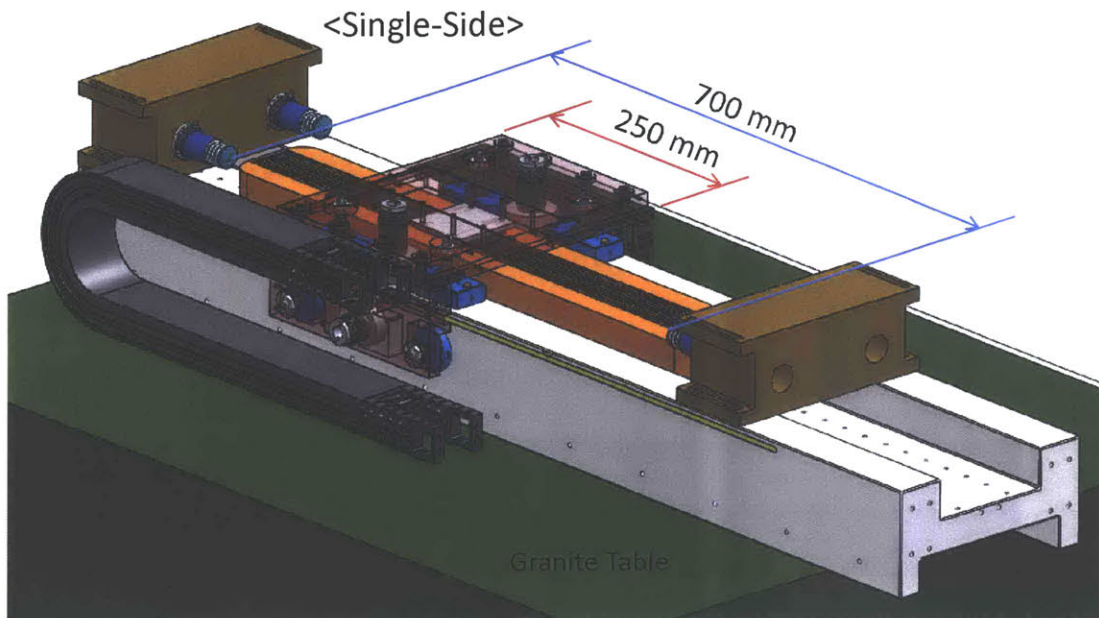


Figure 4-16: Isometric views of selected testbed design with our newly-designed fine-tooth Motors both for single-sided (upper) and double-sided (lower) configurations.

#7. We discuss *vibro-acoustic noise measurement systems* in Chapter 5.

- Accelerometers and microphones are used to measure the motor vibro-acoustic noises. The measured noise data of both conventional and new motors is presented in Chapters 6 and 7.

4.4 Summary

In this chapter, we present and compare various designs of the experimental linear stage testbed. The design targets and testbed requirements are discussed, and conceptual designs are converged to meet these requirements. Among four possible magnetic configurations depending on which part is moving or stationary and which is long or short, we select the motor configuration with the moving short magnets and stationary long coils due to the major advantages of 1) low moving mass, 2) high achievable stage acceleration, and 3) minimal number of moving umbilical cables.

Within the selected magnetic configuration, a variety of stage design details with different types of air bearings are discussed and compared. We choose the air bearings preloaded by the holding magnets against the steel guide bar to 1) avoid the need of multiple counter flat surfaces and 2) save the guide surface area to secure the long travel range. The holding magnets are attached to the threaded studs so that we can simply adjust the magnetic gap between the magnets and the guide surface to control the preloading force for different testbed configurations. We design the air bearings to be mounted by the round ball end mounting screws so that the bearing surfaces can maintain the parallelism to the flat guide surfaces even when the stage structure experiences the bending modes.

The experimental testbed design also has the required measurement systems. Two sets of optical encoder systems are used on both sides to measure the stage position in real-time. The encoder read-heads are designed to be mounted on the moving stage while the long linear scales are fixed on the side surfaces of the base bar so that we can measure the stage position throughout the whole travel length. The testbed design also provides the direct force measurement by the dynamometer configured with four

triaxial load cells sandwiched by the stator mounting plate and the base structure. We present various views of the CAD models of the finalized testbed design, showing that the design requirements are fulfilled.

We discuss in Chapter 5 the construction of the experimental testbed following the finalized design presented in this Chapter. The constructed stage testbed is used to conduct the extensive experiments to investigate and solve the motor vibro-acoustic noise issues. The experimental results are discussed in Chapter 6 for the conventional Tecnotion motor and in Chapter 7 for our newly-designed fine-tooth motor.

Chapter 5

Experimental Testbed Construction

In this chapter, we show the hardware components and construction process of our experimental setup based on the finalized design discussed in the previous chapter. There are many mechanical and electrical components involved in this testbed construction from air bearings and linear motors to power amplifiers. The assembly process requires careful handling and craft for these numerous parts to properly work in harmony, and we discuss the detailed process in this chapter.

As discussed in the previous chapter, our experimental setup is designed to accommodate two different linear motors: the conventional 3-4 combination motor and our newly-designed fine-tooth motor. In the first section, we start with the overall stage construction and discuss how a conventional motor is installed in the testbed. Then, we show the assembly process for the testbed with our new motor in the second section. Switching out the linear motors requires some key hardware modifications including redesign of a part, disassembly of the currently installed motor, installment of a new motor, and adjustment of air bearings. We present all the necessary details step-by-step in this chapter. In addition to the stage testbed itself, we need to also prepare the measurement systems to conduct full-scale experiments. Motor noises are measured in terms of vibration and sound, so in the last section, the measuring devices and necessary components to compose the measurement systems are discussed.

The drawings of testbed components are provided in Appendix A, and the information of vendors and manufacturers we worked with is given in Appendix B. The

data sheets and necessary specifications can be found by visiting the relevant websites listed in the appendix.

5.1 Linear Stage Testbed with Conventional Motor

We first assemble the linear stage testbed with a conventional motor. The completed assembly with a conventional 3-4 combination motor is shown in Figure 5-1. The construction involves many different hardware components and subsystems, which are assembled to provide necessary functionalities for the noise investigation such as zero-friction air bearings and direct force measurement with a dynamometer. In this section, we present descriptions of each assembly step and preliminary test results of the various functions in detail.

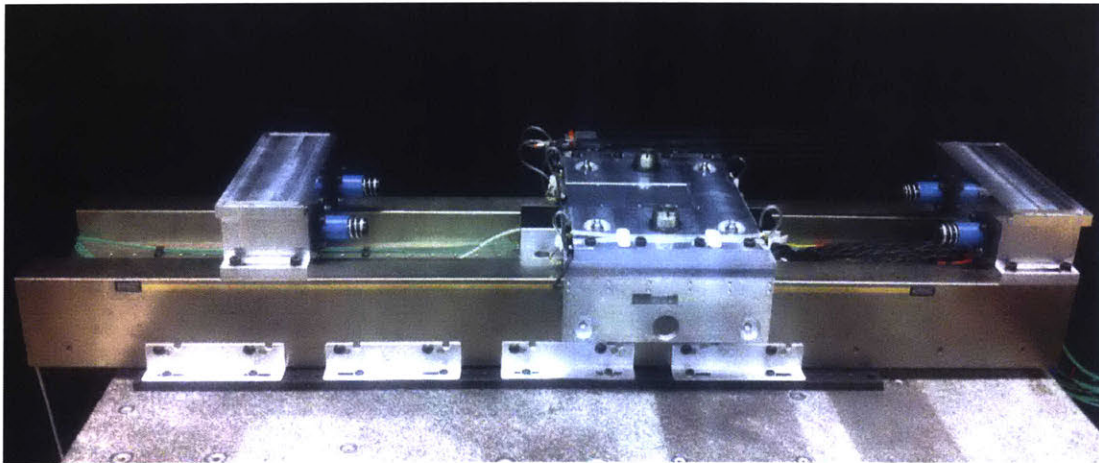


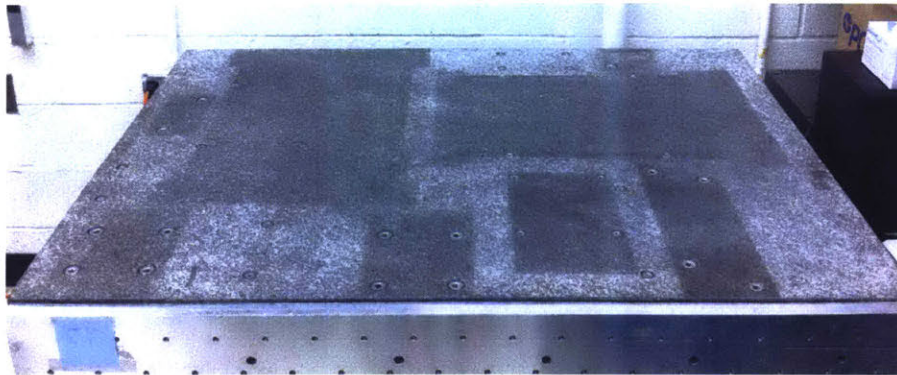
Figure 5-1: The completed assembly of the linear stage setup with a conventional 3-4 combination motor (TL18 by Tecnotion).

5.1.1 Steel Guide Bar

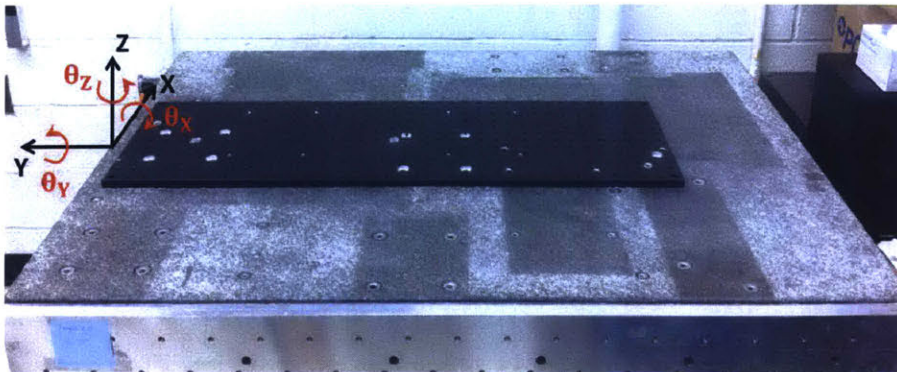
We utilize a steel guide bar, shown in Figure 5-3, as a base structure for our linear stage testbed. This guide bar is 51-in long (in the scan direction), 10-in wide (in the cross-scan direction), and 5-in tall, and weighs 200 pounds. This guide bar not only serves as a base structure, but also provides well-ground guide surfaces for the air

bearings. Some of key aspects of this steel bar are listed as below, and each aspect will be elaborated in the following subsections.

- A dynamometer is formed by four triaxial load cells in the pocket.
- A motor armature is installed in the pocket as the stationary part of actuator.
- Air bearings run against the well-ground guide surfaces (top and side).
- The steel guide bar itself is used to provide magnetic preloading for the air bearings.
- Linear encoder gratings are installed on the well-ground side surfaces to give linear position measurement.



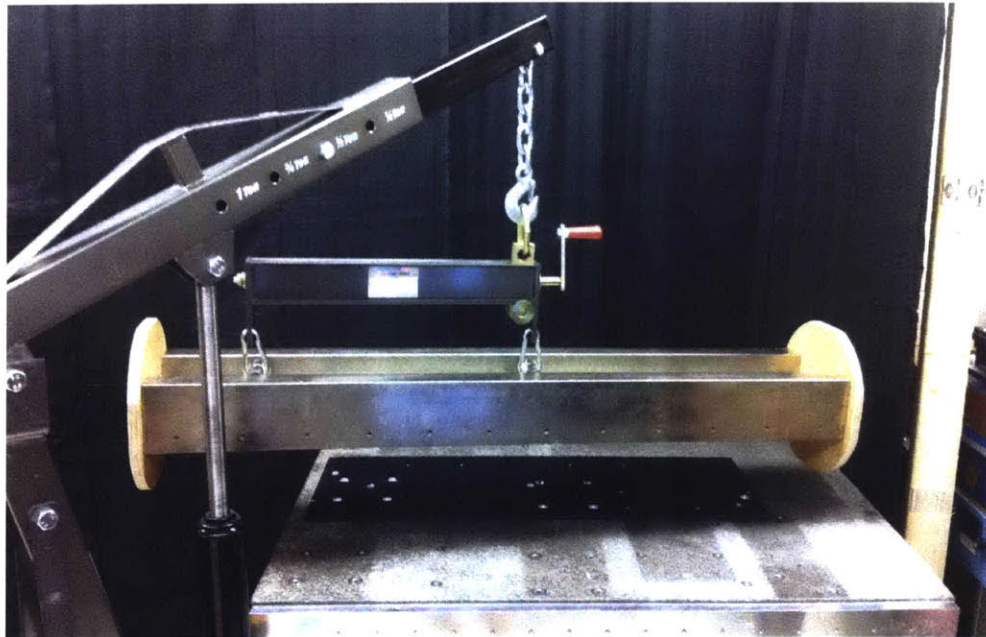
(a) Granite table with randomly-placed threaded holes



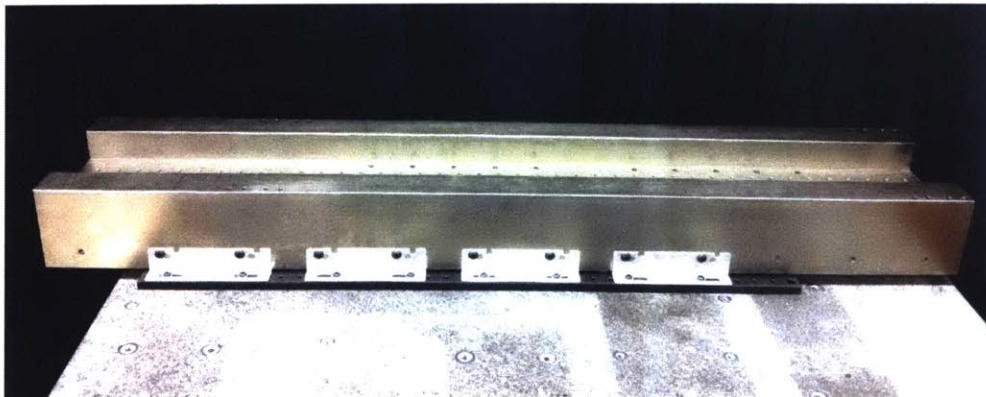
(b) Breadboard as an intermediate mounting plate

Figure 5-2: Mounting plate on a granite table for the guide bar to be firmly installed.

Before starting the stage assembly, the mounting plate for the base structure is first prepared on a granite table, as shown in Figure 5-2. The granite table we have in Precision Motion Control Lab was formerly the base of a diamond turning machine, and so it has several inserted threaded holes. These holes are distributed in a non-uniform way, so we use an aluminum intermediate breadboard that provides mounting holes prepared for the base to be mounted. Figure 5-2b shows the intermediate breadboard plate bolted down to the granite table.



(a) Guide bar lifted by an engine hoist



(b) Guide bar mounted on a granite table

Figure 5-3: 51-inch steel guide bar (donated by New Way Air Bearings) mounted on the granite table by an intermediate breadboard and L-brackets.

The granite table, which weighs about 900 kg, provides a high mass ratio (moving mass to stationary mass) to deal with the expected high reaction force by linear motors mostly in the Y scan direction, as indicated in Figure 5-2b. This high reaction force in the Y-direction can cause a significant reaction moment in the θ_Z -direction, if off-centered. Therefore, the intermediate breadboard is mounted in a way that the base structure and the reaction force point are located at the center in the X-direction. There does remain coupling into the θ_X -direction, because this reaction force is applied above the table's center of mass.

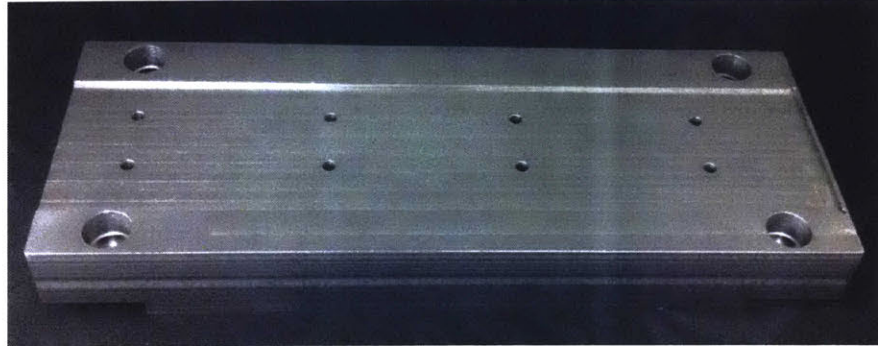
Once the mounting plate is prepared, the 51-in steel guide bar is lifted by an engine hoist with proper adjustment of a leveler to be positioned over the mounting area, as shown in Figure 5-3a. The guide bar is then gently placed on top of the intermediate breadboard and firmly mounted using pre-prepared L-brackets as shown in Figure 5-3b. The base structure is now ready for other components to be installed, and we will continue the testbed construction process with forming and implementing a dynamometer in the pocket of the guide bar.

5.1.2 Dynamometer

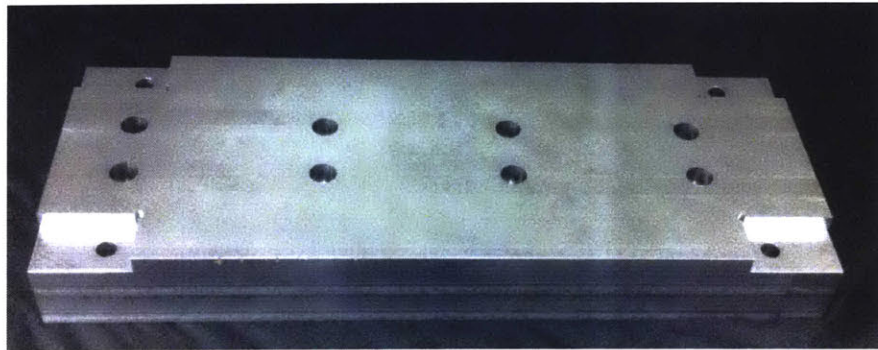
The testbed implements direct force measurements with a dynamometer using four Kistler 9250A4 triaxial load cells sandwiched between two rigid and flat plates. The stator mounting plate, shown in Figure 5-4, is used as the dynamometer top plate, and the base guide bar is the bottom plate. A stator of conventional linear iron-core motor (TL18 by Tecnotion) is mounted on the pocketed area of the mounting plate as shown in Figure 5-4a. Four load cells are accommodated at the four corners of the plate bottom as shown in Figure 5-4b.

The load cells we use for our customized dynamometer, shown in Figure 5-5a, are quartz force sensors, 9250A4 by Kistler, to measure the three orthogonal force components. With a preload of 25 kN, each load cell can measure up to ± 2.5 kN in in-plane directions (namely, X and Y) and ± 5 kN in out-of-plane direction (Z). The customized dynamometer formed with four of these load cells then has the force measurement range of ± 10 kN in X and Y, and ± 20 kN in Z direction. The data

sheet and user manual of these load cells can be found in the websites documented in Appendix B, and the drawing of the mounting plate is documented in Appendix A.



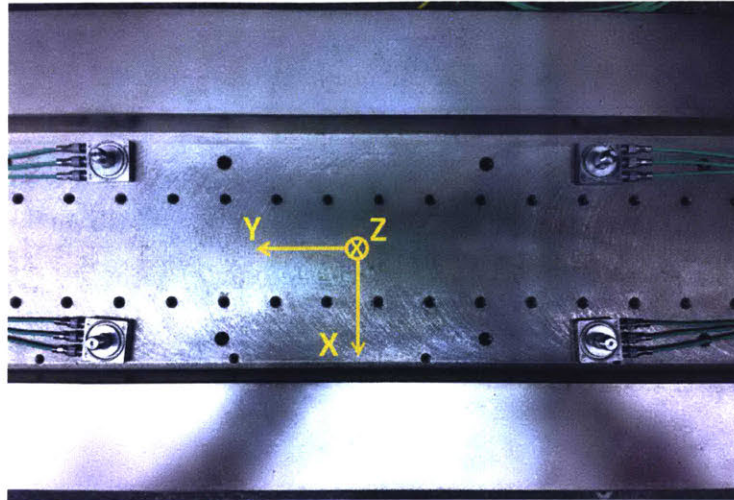
(a) Top view of dynamometer top plate



(b) Bottom view of dynamometer top plate

Figure 5-4: Heat treated 1045 steel mounting plate for the stator serves also as the dynamometer top plate, where the four corner pockets accommodate four Kistler 9250A4 triaxial load cells.

In order to form a dynamometer, the four load cells are first placed on the pocketed area of the base guide bar with pretensioning bolts as shown in Figure 5-5a. Note that it is important to match all the orthogonal measurement directions of each load cell so that the force measurements of all four load cells in each direction can be correctly summed, not canceling one from another. The top plate with a stator pre-assembled is then installed on top of those load cells to complete the dynamometer as shown in Figure 5-5b. The ring nuts are fastened over the pretensioning bolts to provide the desired preload of 100 kN. It is important to preload each load cell uniformly by 25 kN, so some key steps are listed as following. More detailed steps can be found in the user manual of Type 9250A4 by Kistler.



(a) Four triaxial load cells pre-located on the base guide bar



(b) Formed dynamometer with stator mounted on top

Figure 5-5: Formed dynamometer installed on the base guide bar to provide direct force measurements in all three directions.

- 1) Connect all four F_Z cables in parallel to sum the Z-direction charge signal and thus the force.
- 2) Connect the summed output to a charge amplifier input and connect the amplifier output to an oscilloscope to monitor the preloading force.
- 3) Fastening the ring nuts in the order of sensor#1-3-2-4-1-3... to preload the load cells by the same amount each step.
- 4) Preload the load cells up to the total of 100 kN.

Our customized dynamometer is completed, and we test it to validate the force measuring performance in all three transitional directions. Figures 5-6 to 5-8 show the force measurements over time while a hand-held force-meter is used to exert a semi-constant force of 35 to 40 N in each direction.

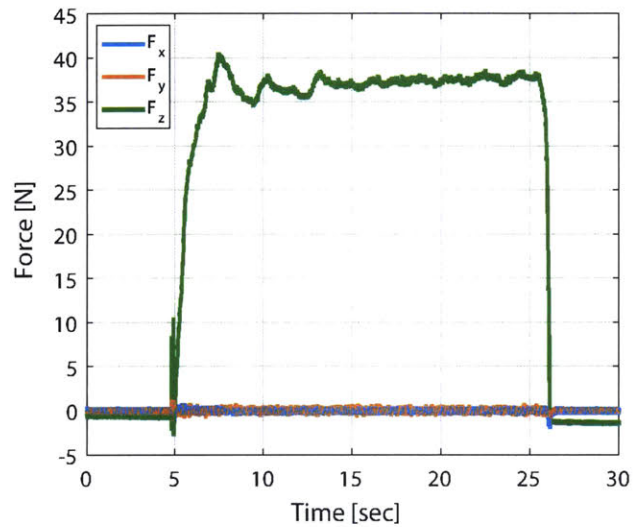


Figure 5-6: Dynamometer Z-direction force measurement test with a force-meter exerting +Z force of 35 to 40 N.

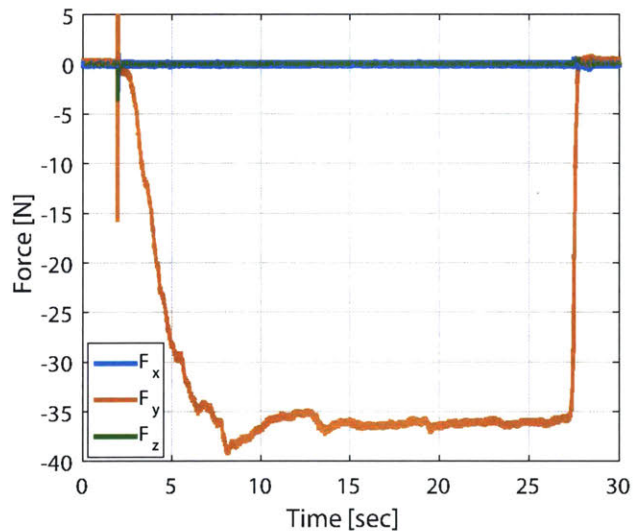
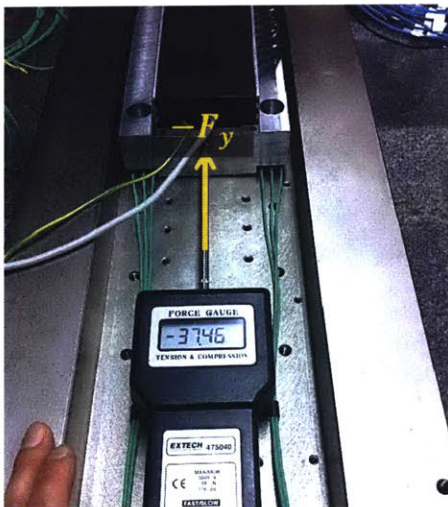


Figure 5-7: Dynamometer Y-direction force measurement test with a force-meter exerting -Y force of -35 to -40 N.

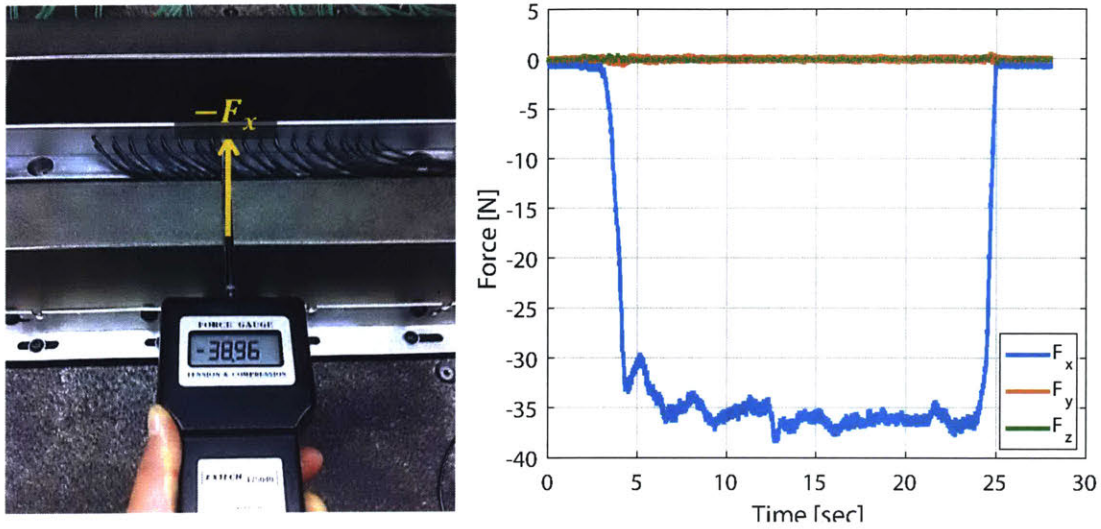


Figure 5-8: Dynamometer X-direction force measurement test with a force-meter exerting -X force of -35 to -40 N.

The figures show correct readings for the exerted force in each direction, validating the force measuring performance of our dynamometer. The sign convention for each direction is also described in the figures. This dynamometer meets our need for the direct force measurement, and are used to directly measure motor force fluctuations, such as cogging, in later chapters.

5.1.3 Stage with Air Bearings

The armature of a conventional linear motor is installed on top of our customized dynamometer, which forms the stationary part of the motor together with the base guide bar. In this subsection, we describe the installation of the moving part, which is the stage containing a magnet track. Before the direct installment on the base structure, the moving stage is first pre-assembled with aluminum plates, air bearings, air paths, fine-threaded studs, and preloading magnets, as shown in Figure 5-9. Detailed views of stage bottom are shown in Figure 5-10 with the full visibility of four top and two side air bearings. This stage carries a permanent magnet track, which is the moving part of a linear motor in our experimental setup. In both figures, a magnet track is not yet assembled, but it is mounted on the bottom pocket surface

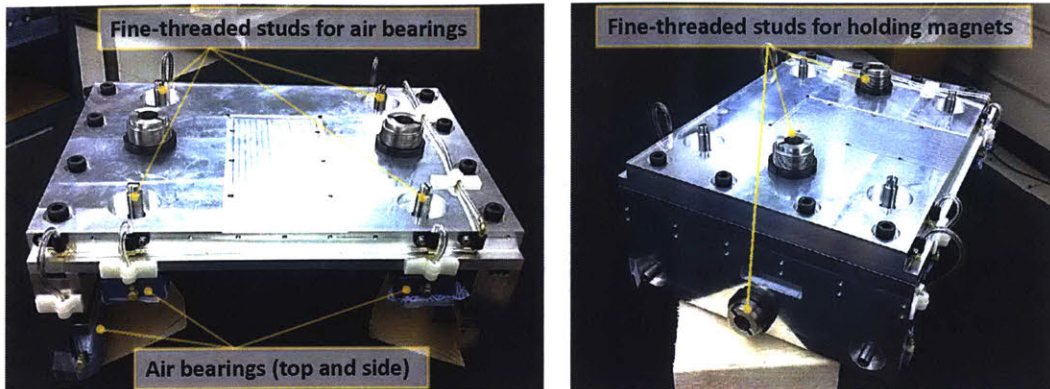


Figure 5-9: Pre-assembled moving stage with four top air bearings, two side air bearings, air paths, and preloading holding magnets.

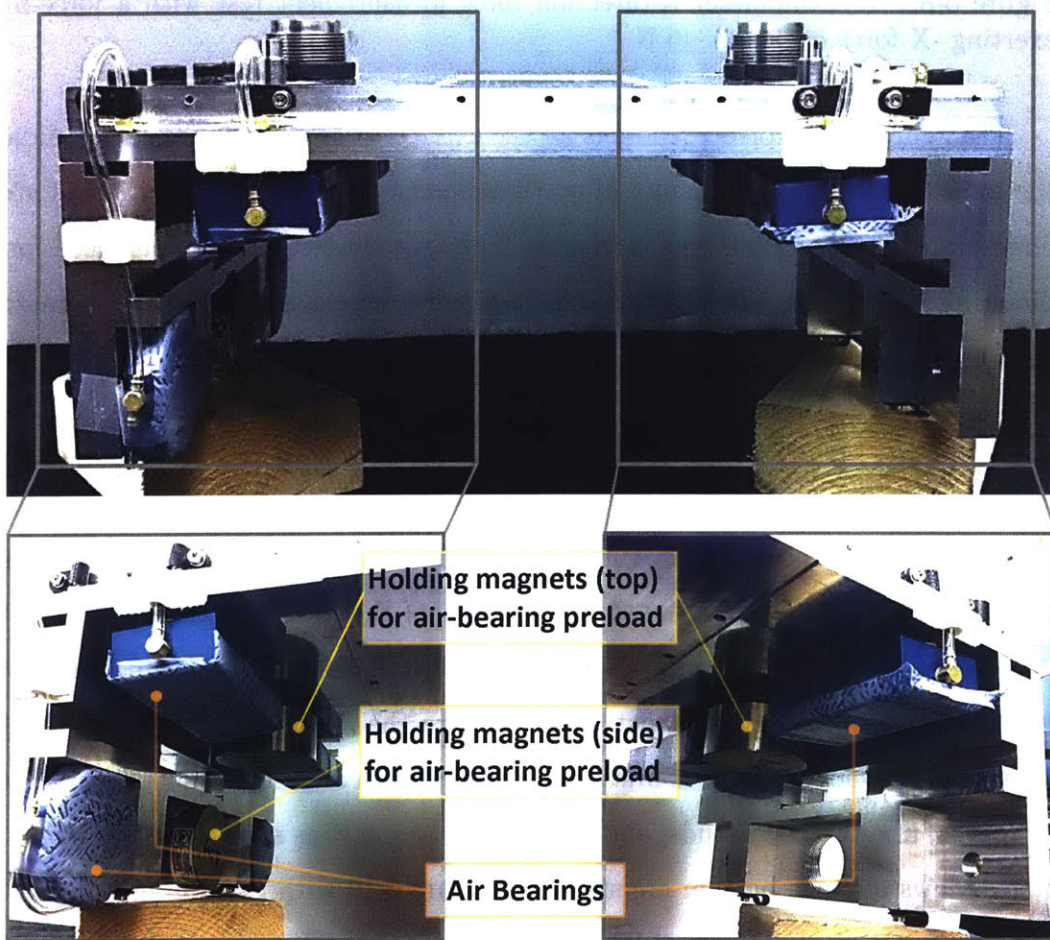


Figure 5-10: Detailed bottom views of the pre-assembled moving stage before being installed on the base guide bar. Patterned material protects face of air bearings, and is removed before operation.

when we conduct full-scale experiments.

We use rectangular air bearings (40mm×80mm, S124002 by New Way Air Bearings) to run on somewhat narrow (55mm width) top guide surfaces while constraining the out-of-plane motion of the stage, and circular air bearings (50mm dia., S105001 by New Way Air Bearings) on a side surface to constrain the cross-scan motion. Both top and side air bearings are preloaded by the attractive force using holding magnets against the steel guide bar. It is important to note the advantages of holding magnets over simple permanent magnets, which is listed as below.

- By concentrating magnetic flux with a steel housing, a holding magnet is much stronger than a permanent magnet in the same size, which is significantly beneficial when the volume is highly limited as in our case.
- By closing magnetic flux with a steel housing, there will be no magnetic interference with nearby components.

The holding magnets are implemented with fine-threaded studs, and the amount of preloading force can be controlled by these studs to achieve desired flying height and stiffness of the air bearings. Figure 5-11 shows finite element analysis models for top and side holding magnets, and calculated preloading forces according to the gap between bearings and steel guide surfaces. The permanent magnets used are cylindrical neodymium N52 magnets and housed with 1018 steel. The thickness of steel housing is determined to avoid material saturation, and the maximum magnetic flux density calculated, in Figure 5-11, with the gap of 250 μm is about 1.4 T , which is well below the material saturation limit of 1018 steel, 1.8 T . Dimensions and design details of our holding magnets are provided in Appendix A.

The pre-assembled moving stage is then installed on the base guide bar as shown in Figure 5-12. When no air flows, the holding magnets tightly clamp the air bearings against the guide surfaces, not allowing the stage to move. When the compressed air (e.g. at 80 psi) runs, the air pressure between bearings and guide surfaces makes the bearings float, allowing a smooth motion to the stage. The flying height of air

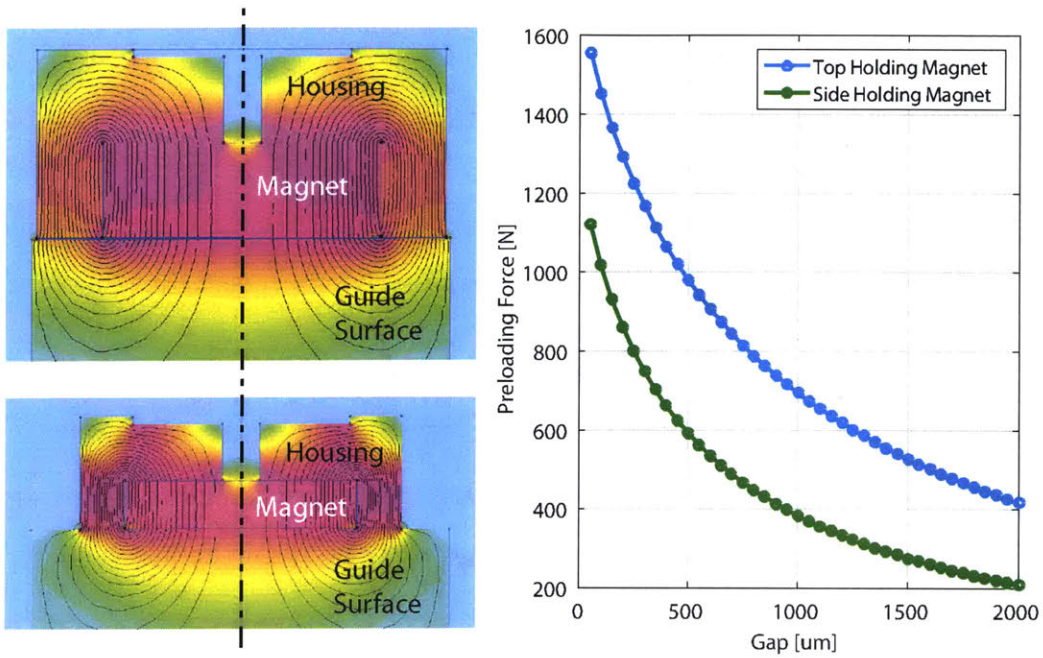


Figure 5-11: Simulated preloading force versus gap curves of holding magnets (right) by finite element analysis with models of top holding magnet (upper left) and side holding magnet (lower left).

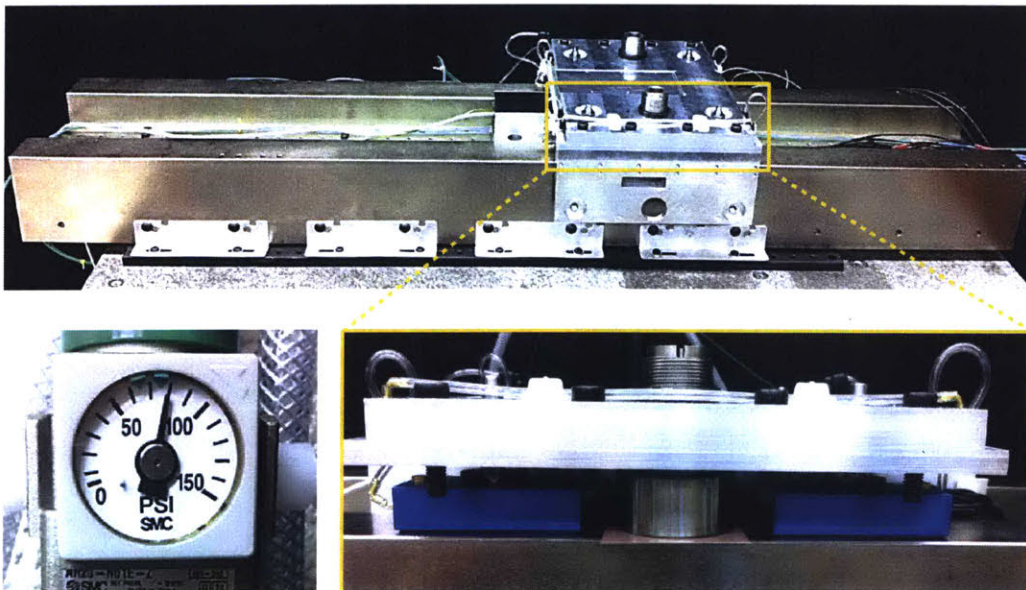


Figure 5-12: Moving stage installed on the base guide bar with air bearings preloaded by holding magnets against the well-ground guide surfaces. Pressure gauge shows our operation air pressure of 80 psi (lower left), and a magnified view shows how air bearings and a holding magnet are engaged against the guide surface (lower right).

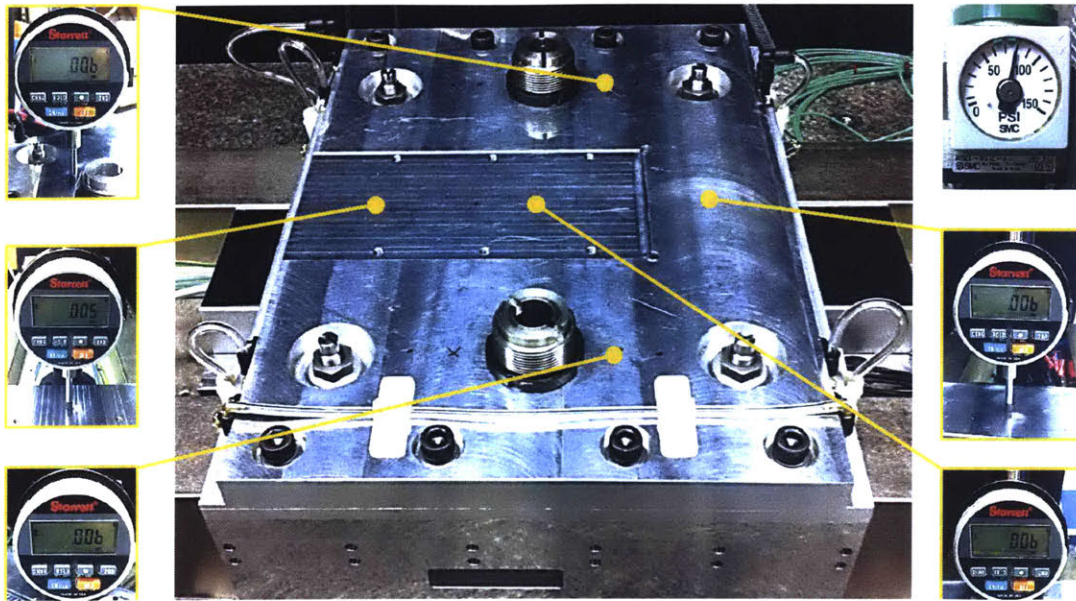


Figure 5-13: Stage flying height measured at five different points by a dial gauge showing the average flying height of $6 \mu\text{m}$ at the air pressure of 80 psi.

bearings are determined by the net force of the air pressure we give and the preloading force by holding magnets.

The resultant flying height of the top air bearings is measured at various points using a dial gauge with the resolution of $1 \mu\text{m}$. Measurements at five different stage points are shown in Figure 5-13. The dial indicator is referenced to zero when the air is off, and measures the incremental height change when the compressed air is turned on at 80 psi. As shown in the figure, the average flying height is about $6 \mu\text{m}$ at an air pressure of 80 psi, which is within the recommended operating range of 5 to $7 \mu\text{m}$ provided by the air bearing manufacturer, New Way Air Bearings. Since the flying height is determined and stabilized by using the correct preload, it is important to adjust this properly depending on whether a magnet track is installed or not, and also when motors are changed. With a conventional linear motor we use (TL18 by Tecnotion), the holding magnet gap distance is set to 0.4 mm before installing the magnet track, and is adjusted to 0.95 mm after mounting the magnet track so as to take the motor attraction into account and maintain the flying height of about $6 \mu\text{m}$. Appropriate adjustments are made when changing the motor to our new fine-tooth

motor as discussed in detail in Section 5.2. Note that the flying height of the side air bearings is set to about $12\ \mu\text{m}$, and is maintained at this height regardless of any changes of magnet track presence or a motor replacement, since these do not change the net force in the lateral direction.

5.1.4 Position Sensors

We implement linear position sensors to be able to measure the real-time position of the moving stage. It is of great help to have a moving stage to assist in applying a linear scale with correct alignment, especially for a long scale such as 1 meter in our case. Renishaw RGSZ20 tape linear scales with the pitch of $20\ \mu\text{m}$ are first attached on both sides of the base guide bar, using a scale applicator that helps feed the scale while slowly moving the stage. Renishaw T1001 encoder read-heads are then installed on the side plates of the stage with proper clearances to correctly read the gratings. An encoder system installed on the left side of the testbed is shown in Figure 5-14.

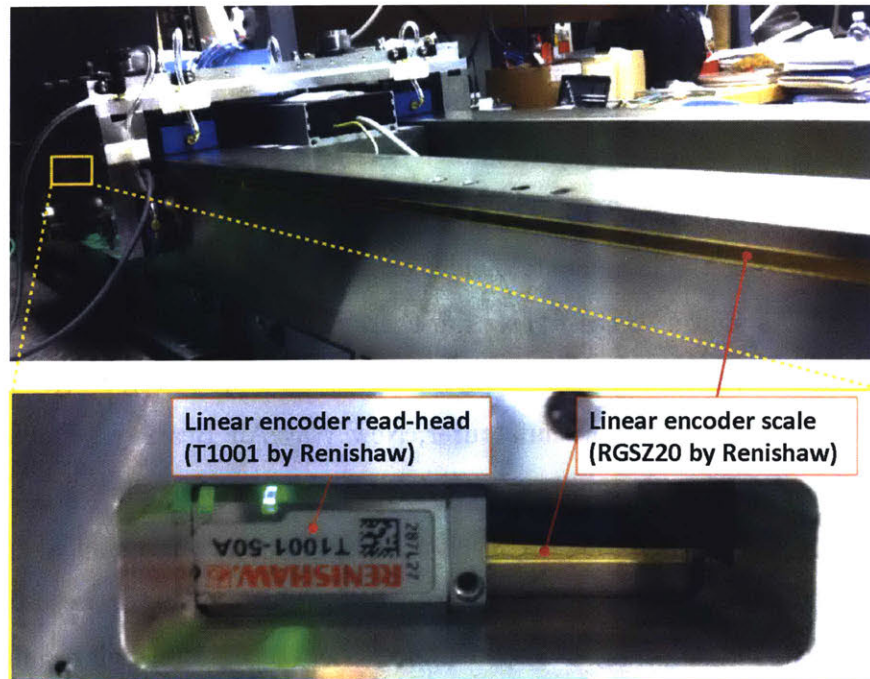


Figure 5-14: Linear encoder system using a scale on the base and a read-head on the moving stage. Green LED on the read-head indicates correct clearance associated with a normal signal level of 70 % to 135 %.

The sine-and-cosine output (with the pitch of 20 μm) of the encoder read-head is connected to an interface where the readout is interpolated and converted to a quadrature (A-quadrature-B) form. We have two types of interfaces with a final interpolated resolution of 1 μm (interpolation of $\times 20$) and 0.1 μm (interpolation of $\times 200$), and we discuss relevant issues of which interpolating rate to choose in Chapter 6. The final A-quadrature-B outputs are decoded by an FPGA counter programmed in a real-time controller (NI PXI-8110 by National Instruments) equipped with an FPGA card (NI PXI-7854R) running at 80 MHz¹. The counts are then utilized as a position feedback in a real-time position control loop, which is discussed in Chapters 6 and 7.

Note that it is important to properly ground and shield the electric connections not to lose any counts. We have observed wrong readings of real-time stage position due to lost counts, and later found it was a grounding issue. This problem was resolved by connecting the outer shield of read-head cable to the system earth ground.

5.1.5 Shock Absorbers and Cable Carrier

It is important to prepare for stage cycle failure modes so as to be safe at all times and to avoid any serious damage to the system. Thus, we use shock absorbers at both ends of travel to be able to safely and passively stop the stage in an emergency runaway situation. The shock dampers are specified for a working mass of 20 kg and a maximum speed of 10 m/s, which are well above our stage of about 10 kg running below 3 m/s. We install these devices on spacers, which are also designed for the double-sided motor configuration. They are shown in Figure 5-15 together with a picture of shock absorber itself and a square flange. The shock absorbers are aligned so that the stage hits both dampers simultaneously in an emergency stop, so that 1) the collision energy is distributed evenly to both dampers and 2) any reaction moment exerted on the stage is minimized.

Another necessary component we discuss in this subsection is the cable carrier. Since we choose to work with moving magnets, not moving coils, the number of moving cables are minimized, but still there are total of three cables in motion: one air supply

¹We appreciate NI's kind donation of these systems to our lab.

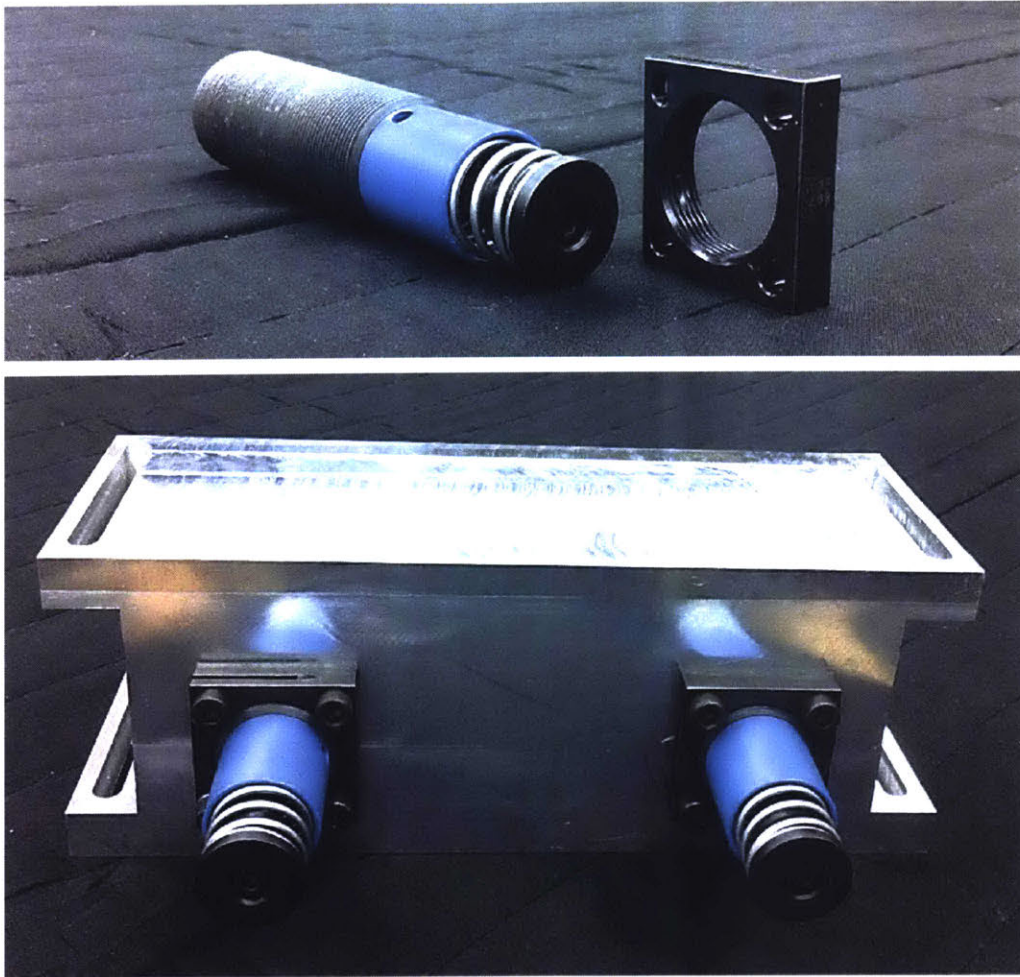


Figure 5-15: Shock absorbers (SCS33-25 by ACE) installed on a spacer to provide enough damping to stop the stage in case of motor or control failure.

hose and two encoder cables. At our targeted high acceleration, these cables might have problematic dynamics, which can disturb the stage significantly. In this sense, a cable carrier is an essential element to guide the cables in a deterministic way, thereby suppressing cable dynamics as well as protecting against cable damage.

The most common structure of a cable carrier consists of parallel side links joined by crossbars. This linked mechanism has several drawbacks including link wear and short lifetime, but the most serious issue for our experiments is the acoustic noise caused by such links and joints. When a linked cable carrier is operating, clicking

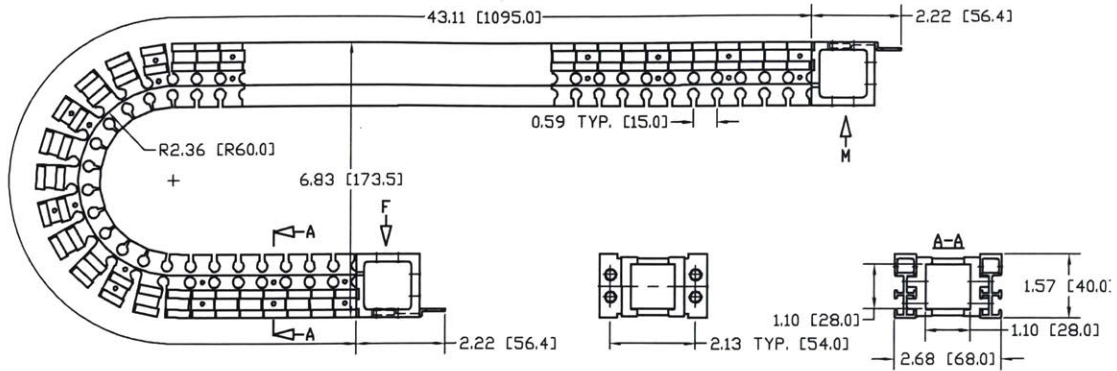


Figure 5-16: Schematic of low-noise and low-vibration link-less cable carrier provided by the manufacturer, Tsubaki KabelSchlepp. Link-free and hinge-free design with side-bands made of continuously extruded polymers.



Figure 5-17: Stage testbed with a link-less and hinge-less cable carrier (Quantum 040-28 by Tsubaki) carrying encoder cables and air inlet tubing. Cable stresses are isolated by strain reliefs.

noises are emitted, exciting almost all frequencies and thereby corrupting our acoustic noise measurements. To avoid this issue, we choose a link-less cable carrier for our experimental setup, and its schematic is shown in Figure 5-16². Due to the link-free

²Thank you to Dr. Stephen Ludwick for suggesting this type of carrier.

and hinge-free design with small pitch, this type of cable carrier shows very low noise and vibration, and is suitable for high acceleration and high speed as in our case. The stage with the cable carrier (Quantum 040-28 by Tsubaki) installed is shown in Figure 5-17. Note that it is important to use strain reliefs to keep stresses from being transmitted to the stage.

5.1.6 Power Electronics

In this subsection, we discuss power electronics required to drive the motors we use. The conventional linear iron-core motor we choose to work with is by Tecnotion, and

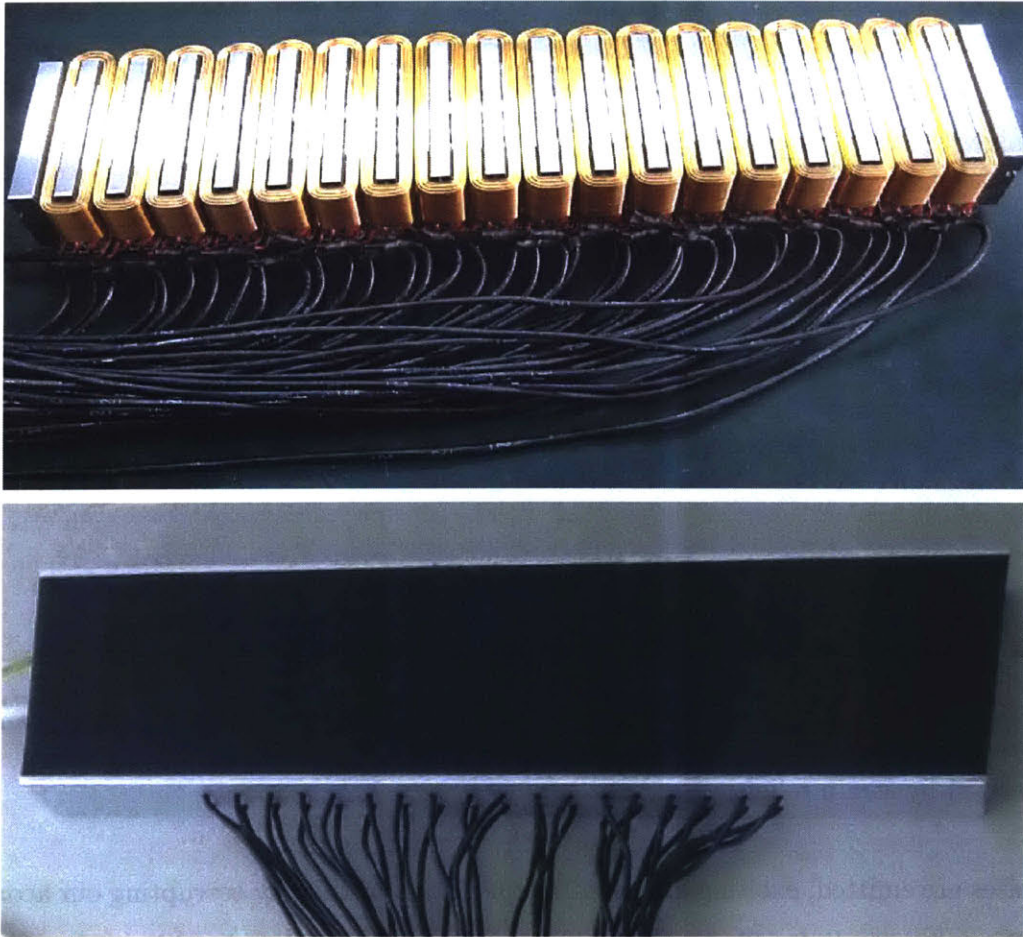


Figure 5-18: Power electronics drive target of multiple individual coils on a Tecnotion motor armature: 18 coils exposed before potting (upper) and potted stator (lower). Upper photo courtesy of Tecnotion.

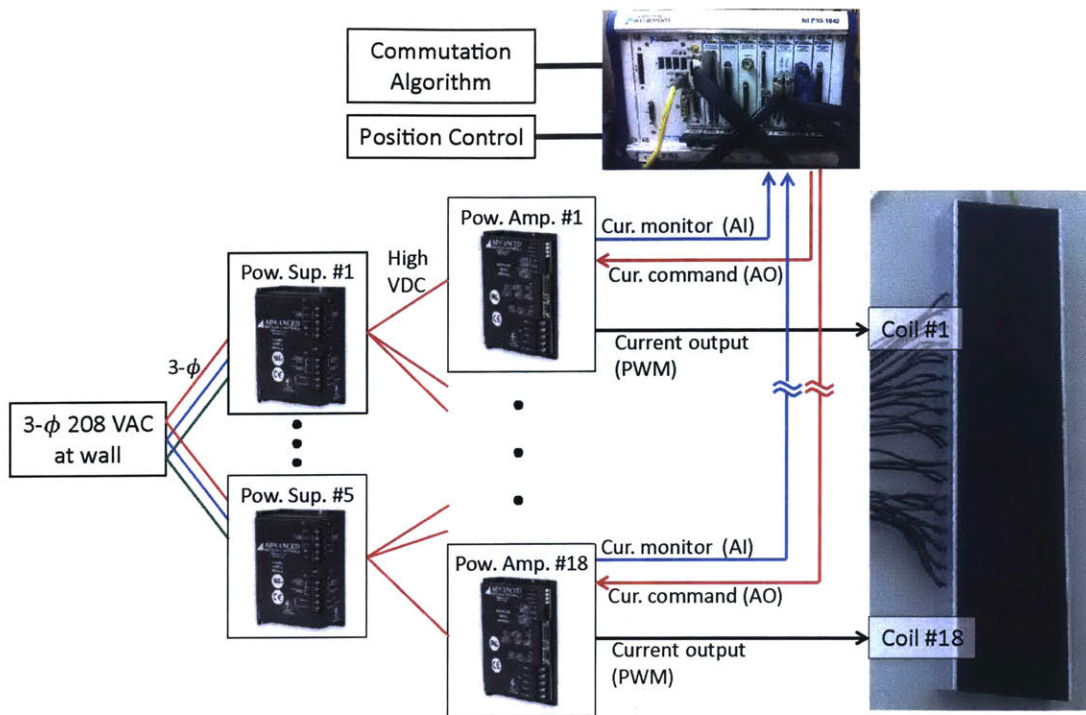


Figure 5-19: Schematic of power electronics configuration with 5 power supplies and 18 power amplifiers.

its stator armature is shown in Figure 5-18³. It is a 3-4 combination motor, and there are 6 sets of 3 coils individually wound on iron cores, resulting in total of 18 coils to drive. Each coil is driven by one power amplifier (B30A40 by AMC), which is a PWM drive switching at 20 kHz with an internal current controller of 2 kHz bandwidth. A total of 18 amplifiers are powered by 5 power supplies (PS30 by AMC), which rectify 3-phase 208 VAC to 300 VDC. Figure 5-19 schematically shows the power electronics connections. To drive the coils of the Tecnotion stator, current reference signals are commanded by the real-time controller to the amplifiers, and we can monitor the current outputs using a data acquisition card (NI PXI-6259) in real-time. A total of 18 analog output channels and 18 differential analog input channels are used to support all 18 amplifiers. Current command signals are determined by a commutation algorithm and the position controller, which are discussed in Chapter 6.

³We appreciate the help of Tecnotion on customizing the armature coil separation, especially thank you to Erwin Hofste.



Figure 5-20: Customized rack for 5 power supplies and 18 power amplifiers: front view (left) and rear view (right).

Figure 5-20 shows a customized rack for the power electronics. The front view shows a total of 5 power supplies on the lower part of the rack and 18 power amplifiers mounted on the upper part. The rear view shows power connections from the 3-phase 208 VAC line to the power supplies, and signal connections from our real-time controller to the amplifiers via terminal blocks.

The description of the assembly process of linear stage testbed with the conventional motor is now completed both mechanically and electrically. We describe commutation, position control, and experimental investigation on the motor noise issues of this stage setup with the conventional motor in Chapter 6.

5.2 Testbed Modification for New Fine-tooth Motor

In this section, we describe hardware modifications on the testbed to exchange the actuating system from a conventional 3-4 combination motor to our new fine-tooth motor discussed in Chapter 3. The completed assembly of our experimental setup

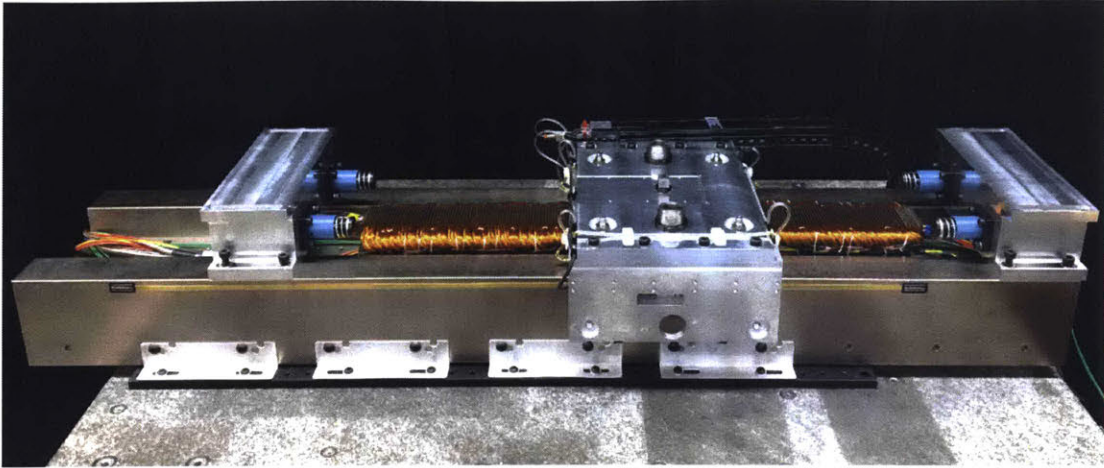


Figure 5-21: The completed assembly of the linear stage setup with our new fine-tooth motor.

with the new motor is shown in Figure 5-21. Since our new motor has a different size from the conventional motor (TL18 by Tecnotion), the mounting plate has to be redesigned and reconstructed, and the dynamometer has to be reconfigured with this new mounting plate. The air bearings do not have to be disassembled, but the preloading force needs to be adjusted to take the higher motor attractive force into account. In addition, there are a total of 20 coils to drive as discussed in Chapter 3, so two more power amplifiers need to be added and the electric connections for power electronics have to be rearranged. We discuss details of these modifications in the following subsections.

5.2.1 Stator Mounting Plate Redesign and Reconstruction

The linear stage setup with the conventional Tecnotion motor has a relatively short travel length of 192 mm since we use a commercially available iron-core motor (TL18 by Tecnotion). To use the full length available on the base guide bar, we designed our new fine-tooth motor to have a total length of 728 mm, which provides a travel up to 450 mm. Also, the stator and magnet track of new motor are thicker than those of Tecnotion motor while the distance between the pocket surface of the base and bottom surface of stage is constant. To accommodate these changed dimensions, we

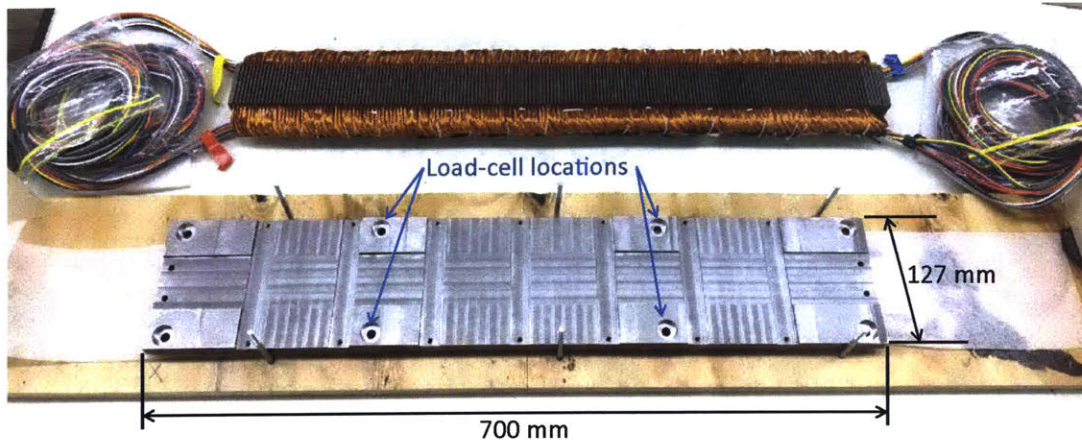


Figure 5-22: Mounting plate for the new fine-tooth motor, also serving as a top plate for the dynamometer formed by four load cells located as indicated.

designed and constructed a new mounting plate, which is shown in Figure 5-22 along with our new fine-tooth motor. Note that the new mounting plate is long and thin, and thus prone to warp if wrongly treated and machined. To avoid this issue and maintain appropriate overall flatness, we choose a ductile cast iron, which is relatively more stable than drawn and rolled carbon steel, and has similar level of stiffness. This mounting plate also serves as the dynamometer top plate sandwiching four load cells against the base guide bar. We discuss its details in the following subsection.

5.2.2 Dynamometer Reconfiguration

The dynamometer has to be reconfigured with the new mounting plate. To this end, the stage needs to be moved aside and the existing dynamometer top plate has to be disassembled to expose the load cells in place as shown in Figure 5-5a. We then place the new mounting plate on top of these four load cells as shown in Figure 5-23. Note that this time we do not pre-assemble the stator and mounting plate unlike the case with the conventional motor. This is due to the limited pocket area and protruding end-turns of new motor armature blocking the access to ring nuts used for preloading load cells. Given this situation, we first install the mounting plate to form the dynamometer and apply correct amount of preload to load cells by fastening ring nuts in the order described in the previous section. Then, the new motor stator is

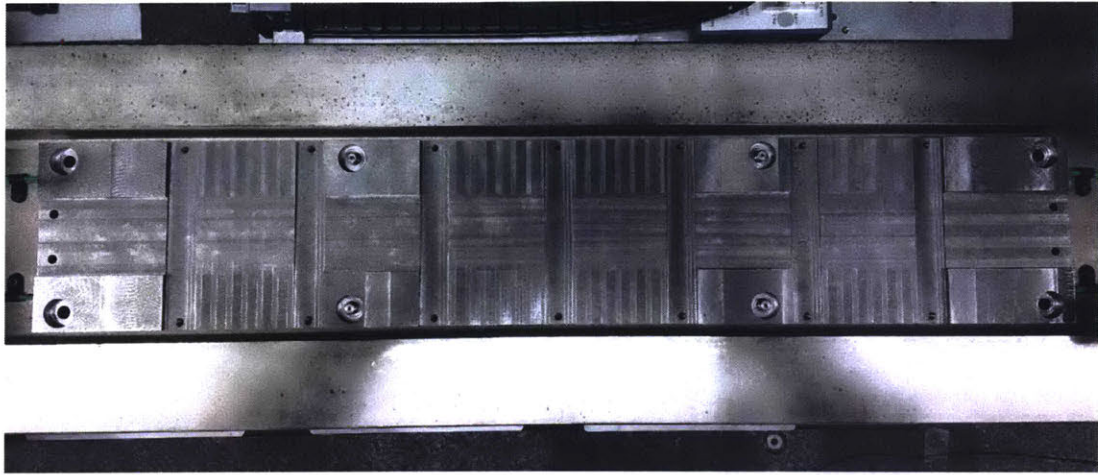


Figure 5-23: New mounting plate placed on top of four load cells forming the dynamometer.

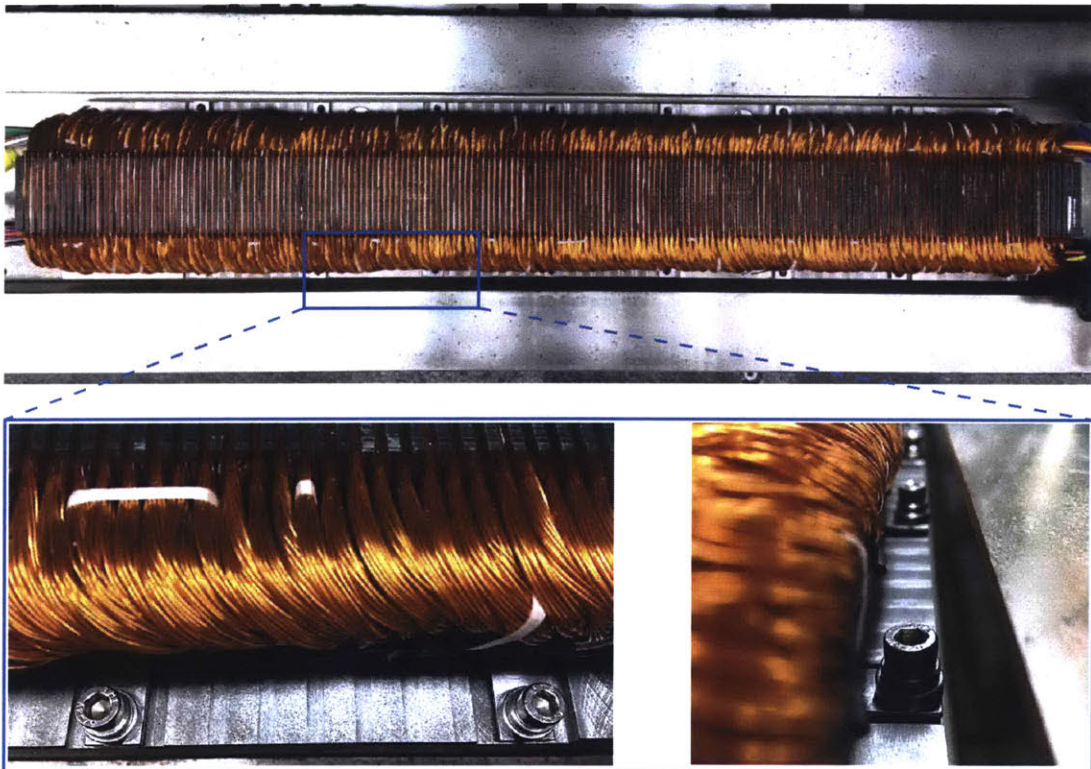


Figure 5-24: New fine-tooth stator mounted on the dynamometer. Long dove-tail inserts are used to clamp the stator down on the mounting plate.

mounted afterward as shown in Figure 5-24. Long dove-tail bars are inserted at the back yoke of stator and bolted down at both sides, thereby tightly clamping down the stator against the mounting plate. Note that we use spherical leveling washers to accommodate the bending of long dove-tails inserts, as shown with the magnified views in Figure 5-24.

5.2.3 Airbearings Adjustment

The air bearings and the stage do not need to be disassembled when exchanging the actuating system to the new fine-tooth motor. However, the top air-bearing preload has to be adjusted since the attractive force of a fine-tooth motor (~ 1509 N) is much higher than the conventional motor (~ 685 N) due to larger engagement between iron-core teeth and permanent magnets. The attractive force of the new motor is measured at about 1500 N at the magnetic air-gap of $550 \mu\text{m}$. This provides the majority of the required air-bearing preload. Accordingly, the holding magnet gap is increased

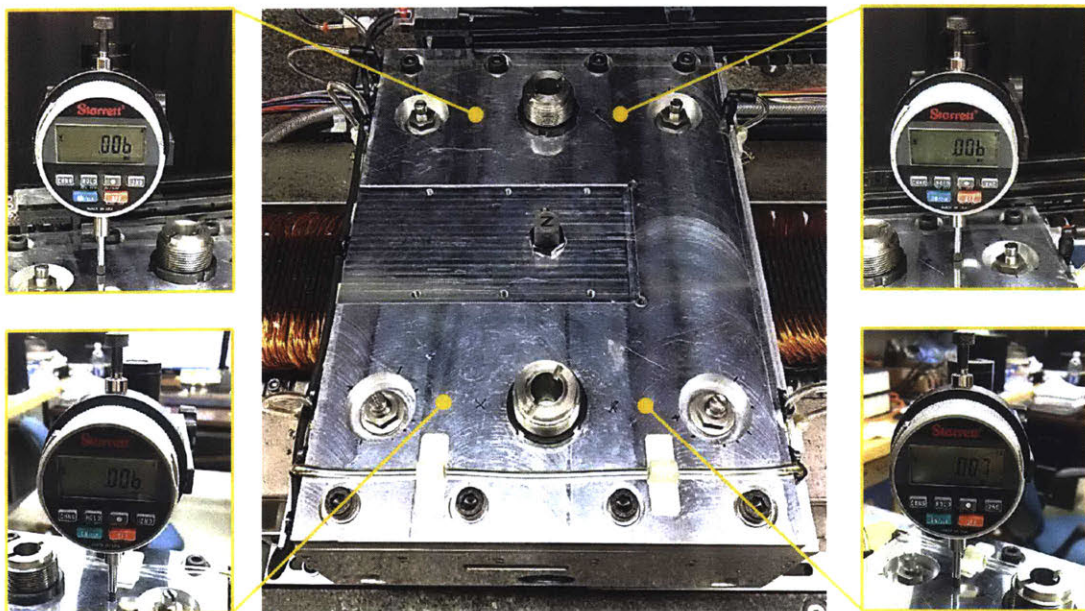


Figure 5-25: Top air bearing flying height measured at four corners on the stage by a dial indicator with the resolution of $1 \mu\text{m}$, showing the average flying height of $6 \mu\text{m}$ at the air pressure of 80 psi.

to 2.75 mm (from 0.95 mm with the Tecnotion motor) to maintain the nominal air-bearing flying height of 6 μm . We measure the top bearing flying height in the same way discussed in the previous section by using a dial gauge, and the measurement results are shown in Figure 5-25. The average flying height measured is 6 μm at the air pressure of 80 psi.

5.2.4 Power Electronics Reconnection

The last modification to complete the linear stage testbed with the new fine-tooth motor is to reconnect the power electronics. As discussed in Chapter 3, the phase windings of new motor armature are grouped in four sections so that we can distribute power loads to the existing multiple amplifiers. The armature has five-phase windings in each section, so there are a total of 20 coils to drive. We add two more amplifiers (B30A40 by AMC) to the rack shown in Figure 5-20, and connect them to the coils. Additional analog outputs in the real-time controller are also used to command current reference signals to those added amplifiers. We discuss a five-phase commutation algorithm and position control to make the system operational for the full-scale experiments in Chapter 7.

5.3 Noise Measurement Systems

In this section, we introduce noise measurement systems to investigate the vibro-acoustic noise from both conventional and new motors. It is important to have both vibration and sound noise data so that we can understand the noise emission mechanisms. To this end, we have two independent measurement systems, each for vibration noise and acoustic noise. The details on each measurement device are discussed in the following subsections.

5.3.1 Vibration Measurement System

Vibration can be measured by accelerometers. Figure 5-26 shows single-axis and triaxial accelerometers we use for the measurements. The single-axis accelerometer, 353B15 by PCB Piezotronics, has a nominal frequency range of 1 to 10,000 Hz with the nominal sensitivity of 10 mV/G while the triaxial one, 356A26, has 1 to 5000 Hz with 50 mV/G. Lists of detailed specifications for both devices are provided by the manufacturer, PCB Piezotronics, whose information is documented in Appendix B. Among many mounting methods, we use the adhesive Petro Wax, with mounting bases to fix the accelerometers. This approach can facilitate location changes without compromising the measuring frequency range too much. The sensor outputs are processed through signal conditioners (482C by PCB Piezotronics), and the resultant voltage outputs are read by a data acquisition card (NI PXIe-6363) in a real-time controller (NI PXIe-8133) running a measurement loop with the sample rate of 50 kHz.

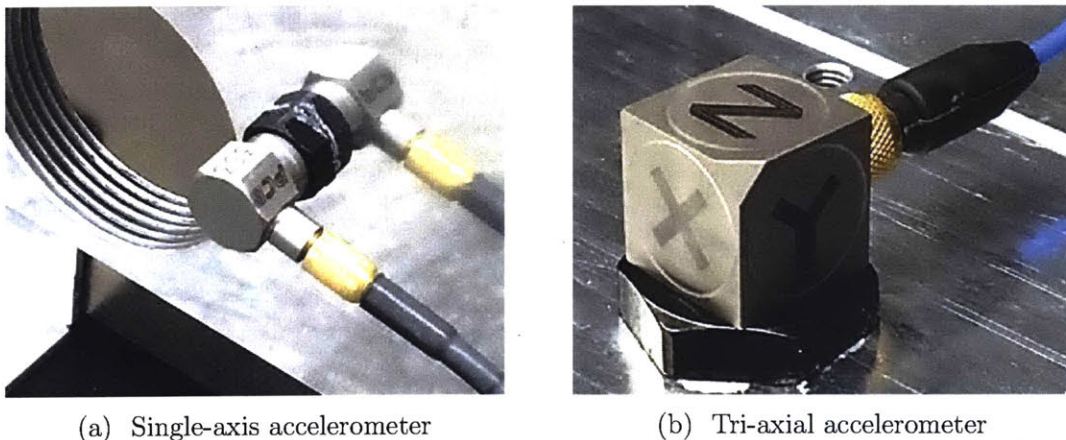


Figure 5-26: Single-axis (353B15) and triaxial (356A26) accelerometers, by PCB Piezotronics, to measure vibration noise of our linear stage testbed.

The raw measurement data from these accelerometers is used to investigate the motor noise mostly in metadata forms such as cumulative amplitude spectrum (CAS) and spectrogram as detailed in Chapters 6 and 7.

5.3.2 Acoustic Noise Measurement System

Acoustic noise can be measured by a set of microphone systems. Figure 5-27 shows a microphone we use for the measurement. The frequency range of this device for ± 2 dB is 20 to 10,000 Hz with the nominal sensitivity of 45 mV/Pa. Detailed specifications can be found at the website of PCB Piezotronics which is documented in Appendix B. The sensor outputs go through the same signal conditioners as accelerometers, and are sampled at 50 kHz in a measurement loop run by the real-time controller (NI PXIe-8133).



Figure 5-27: Microphone, 130E20 by PCB Piezotronics, to measure acoustic noise emitted from the experimental motor setup.

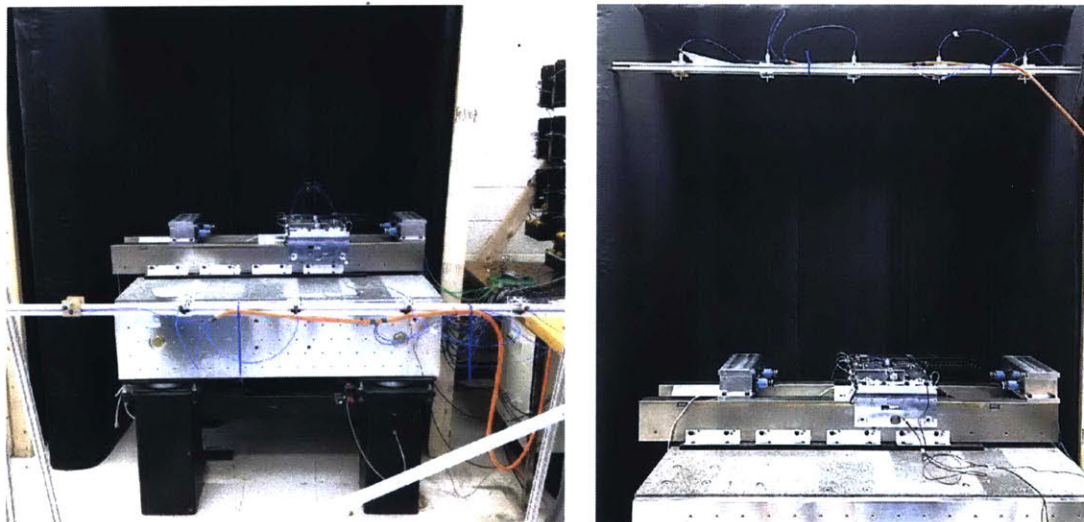


Figure 5-28: Microphone array to measure the motor acoustic noise both from side (left) and above (right).

We measure the motor acoustic noise by an array of microphones, shown in Figure 5-28, installed 1 m away both from above and the side of the testbed. The raw and metadata from these microphones are compared to those of accelerometers for the motor noise investigation, and its details are discussed in Chapters 6 and 7.

5.4 Summary

In this chapter, we discuss the construction of experimental testbed to accommodate both the conventional Tecnotion motor and our new fine-tooth motor. Assembly process of various mechanical and electrical components is described in detail, and functions of these parts are tested. We provide a list of important aspects of our experimental testbed and its functionalities.

- The experiment testbed has various mechanical functions to help the motor noise investigation.
 - Air bearings are used in the stage setup to avoid the noise generation by mechanical contacts.
 - Top and side air bearings run at 80 psi with the flying heights of 6 μm and 12 μm , respectively.
 - The granite table and the steel base guide bar provide a mass ratio of about 100-to-1 with respect to the moving stage mass of about 11.5 kg. This high mass ratio is advantageous for handling the high reaction force of the motor.
 - The shock absorbers at both travel ends keep the stage operation safe and prevent hardware damage in the case of motor or control failure.
 - The link-free and hinge-free cable carrier suppresses undesired cable dynamics without vibrations and noises, thereby not compromising the motor vibro-acoustic noise measurements.
- Many electric systems are used to power and control the linear stage testbed.

- Multiple power supplies (PS30 by AMC) and power amplifiers (B30A40 by AMC) drive individual phase coils of motor armatures. The power amplifier is a PWM drive switching at 20 kHz and has an internal current controller with 2 kHz bandwidth.
 - The real-time controller (NI PXI-8110) allows the position feedback control loop to run deterministically at 10 kHz with a commutation algorithm. We discuss in detail the commutation scheme and position controller design of both the conventional and new fine-tooth motors in Chapters 6 and 7.
 - The real-time processor (NI PXIe-8133) controls a measurement loop to measure both vibrational and acoustic noises at the sample rate of 50 kHz. The measured noise data is presented in Chapters 6 and 7.
- Various measurement systems are installed to help run experiments on the motor vibro-acoustic noise issues.
 - Optical linear position sensors are used to provide a real-time position feedback to the position controller. The interpolated resolutions can be chosen to be either 1 μm or 0.1 μm .
 - The dynamometer configured by four triaxial load cells directly measures the motor forces (e.g. cogging).
 - The single-axis and triaxial accelerometers measure the vibrational noise of the experimental testbed driven by either the conventional Tecnotion motor or our newly-designed fine-tooth motor..
 - The array of microphone systems measure the acoustic noise emitted by the testbed with either the conventional or our new motor.

We utilize these functions of the experimental testbed to investigate the motor vibro-acoustic noise issues. Comprehensive experiments are performed and relevant results are discussed in detail for both the conventional Tecnotion motor and our fine-tooth motor in Chapters 6 and 7.

Chapter 6

Experiments with Conventional 3-4 Combination Motor

In this chapter, we present the development of a controller for our experimental setup with the conventional linear motor so as to conduct full-scale experiments on motor noise issues. We begin with discussion on commutation algorithm and position control of the conventional linear motor with the combination of 3 phases and 4 magnets. Commutation requires information on the geometric configuration between magnets and iron-core teeth so that we can define a electric reference position. We utilize back EMF measurements to this end, and the details are discussed in the first section together with a commutation algorithm and position control loop design.

In the following section, we present comprehensive experimental results on the vibro-acoustic noise of the conventional motor (TL18 by Tecnotion) at various motor operation status. The conventional iron-core motor emits significant noise even when stationary. We first discuss the cause and the resolution of such stationary noise. We then present extensive experimental data on the motor cycle noise measured while cycling the stage at various profiles. Using the test results, we discuss the root causes of the motor noise and its mechanism. The key results on the vibro-acoustic noise emitted by the conventional linear motor are summarized at the end of this chapter.

6.1 Control of Conventional Motor

In this section, we present the commutation algorithm and the position controller design of the conventional linear iron-core motor (TL18 by Tecnotion). Commutation is basically to switch (or regulate) currents at the right time to produce a traveling MMF wave and generate controlled thrust in a desired direction. It requires knowing the location of the moving magnet track. We discuss a simple method to do that task using the measured back EMF. We also discuss in detail the design process of a position controller, and present the tracking performance of the closed position loop in this section.

6.1.1 Zero Electric Position

We need to know the position of a moving magnet track to correctly commute phase currents, and this can be achieved by defining a reference zero position. Figure 6-1 schematically shows the geometric configuration between magnets and iron-core teeth. A conventional 3-4 combination is shown in the figure where three phases and four magnets compose a basic unit to produce thrust. The period of this basic unit is the same as two magnet pole-pair pitches, $2\lambda_{pp}$ ($= 2 \times 24$ mm) as shown in Figure 6-1. We set the desired zero position when the first tooth is aligned with the eighth magnet (PM8) as illustrated in the figure. Once we correctly set this position as our zero position reference, we can always know the present location of the moving magnet track using the real-time encoder outputs.

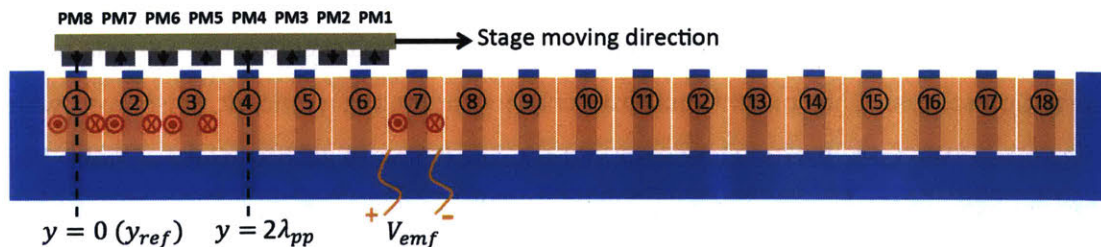


Figure 6-1: Schematic of conventional 3-4 combination linear iron-core motor configuration indicating the desired zero reference position, y_{ref} . By 3-4 we mean the motor periodically includes 3 coils/poles for every 4 magnets.

In order to set the zero electric position as a reference, we measure the back EMF from one of the armature coils while moving the magnet track in one direction. Any coil out of the total of 18 windings can be used for this purpose, but we choose to measure the back EMF of the coil number 7, as indicated in Figure 6-1, for calculation simplicity since it is the same phase (namely, phase A) as the first coil, and is distanced as a multiple of the basic unit length. We list a few key steps to define the zero position as below.

- 1) Place the moving magnet track at a random, but repeatable position such as one of the stable equilibrium points given by cogging stiffness, and set that location as an initial zero position. Note that we can also use one of the reference marks in the encoder scale to set the initial zero position.
- 2) Prepare to read the back EMF of the seventh coil by connecting the coil leads to an analog input channel of our data acquisition card (National Instruments PXI-6259).
- 3) Move the stage in one direction at approximately uniform velocity while measuring both the stage position and the back EMF, and plot the back EMF voltage as a function of the position.
- 4) Zero crossings of the back EMF curve show locations where a permanent magnet is exactly aligned with the coil ($d\lambda/dt = 0$). We thus can calculate how much our initial zero position is shifted from a desired reference point by looking at the back EMF zero crossings.
- 5) Reset the initial position by the shifted amount, thereby allowing our desired position to be set as the zero reference.

Following the above steps, we obtain a back EMF curve versus the stage position as shown in Figure 6-2, where the curve is categorized in three regions. Physical explanation for each region is illustrated in Figure 6-3. The first region is when the magnet track is approaching the seventh coil, so the first magnet (PM1) starts

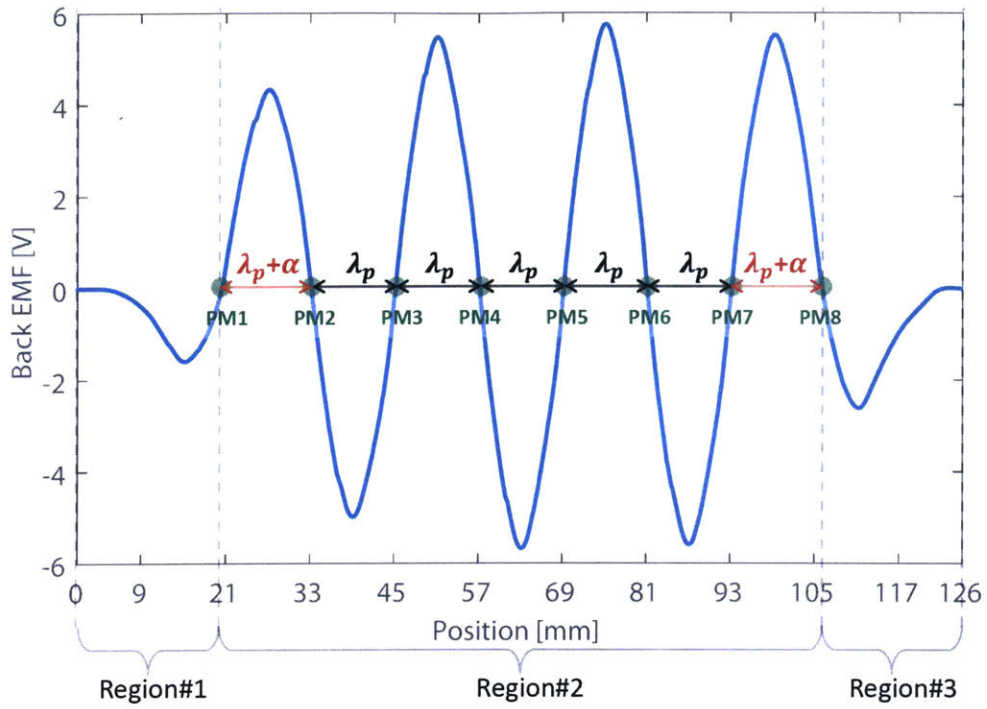


Figure 6-2: Measured back EMF of coil #7 in the Tecnotion TL18 conventional iron-core stator showing the zero-crossings with the interval of pole pitch, $\lambda_p = 12$ mm.

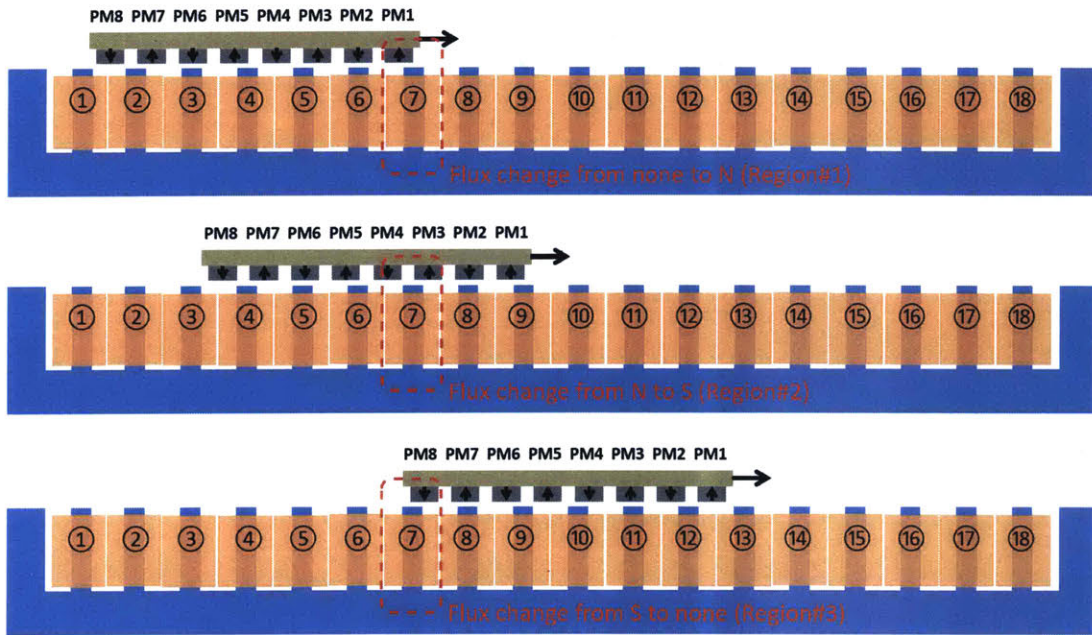


Figure 6-3: Schematic explanation of the measured back EMF of coil #7, region-by-region.

engaging with the coil. Similarly, the last region is when the magnet track is exiting the coil so that PM8 is gradually less engaged with the coil.

The second region begins with the first zero crossing, which is when PM1 is aligned with the seventh tooth/coil. In this region, there are a total of 8 zero crossings and 7 local peaks as expected by 8 magnets with alternating magnetization directions (N-S-N-S-N-S-N-S). The amplitude of the back EMF is determined by the time rate change of flux linkage according to Faraday's law, as shown in (6.1) where V_{emf} , λ_{PM} , and v_y are the back EMF, flux linkage of the coil due to the magnets, and velocity in the scan direction, respectively. Note that the minus sign in the equation is by Lenz's law indicating the direction of induced current (by back EMF) is such that it generates magnetic flux to oppose the flux change. Given this relation, we can see how the back EMF peaks in region#2 in Figure 6-2 are in similar, but not exactly the same magnitude because the stage is moved manually, and thus the velocity is not constant, via

$$V_{emf} = -\frac{d\lambda_{PM}}{dt} = -\frac{d\lambda_{PM}}{dy} \frac{dy}{dt} = -\frac{d\lambda_{PM}}{dy} v_y. \quad (6.1)$$

We also observe that the peak amplitudes in the first and last regions are much smaller than those in the second region, even given the manual stage movement. This is also due to the Faraday's law in (6.1) where flux change amount determines the induced voltage amplitude. As shown in Figure 6-3, the flux linked by the coil changes from none to N and from S to none in the first (#1) and last (#3) regions, respectively, while it changes from N to S or vice versa in the middle (#2) region, thereby boosting the value of the $d\lambda_{PM}/dt$ term.

The important information we need to use from the measured back EMF is the location of the zero crossing points. The measured back EMF curve in Figure 6-2 shows the average period of λ_{pp} , the magnetic pole-pair pitch, which gives us the zero crossing distance of $\lambda_p = \lambda_{pp}/2 = 12$ mm as the pole pitch (namely, from a north to south pole or vice versa). Note that the first and last zero crossing distance in region#2 is a bit larger than the pole pitch, λ_p , and this is due to the magnetic end

effect. In order to set the zero reference position, we need to see how much the zero crossing points are shifted from the initial position we chose. To this end, the zero crossing point where PM4 is aligned with the coil is considered. As can be seen from Figure 6-1, this zero crossing point should be located at $y = \lambda_{pp} = 48$ mm if the initial zero is the same as our desired reference position. However, from the measurement, we have the zero crossing of PM4 at $y = 57$ mm, which indicates a shift of 9 mm. We reset the initial position as -9 mm, rather than zero, so that we can have the desired reference position defined as zero.

6.1.2 Commutation

In this subsection, we present the algorithm to commutate the phase currents using the correctly defined zero position. Figure 6-4 schematically shows where and how to commutate the three phase currents based on the position of the moving magnet track. Since we use the conventional 3-4 combination motor, we have the geometric relations of

$$\begin{aligned} 4\lambda_p &= 2\lambda_{pp} = 3\lambda_t = 48 \text{ mm} \\ \lambda_t - \lambda_p &= 2\lambda_{pp}/3 - \lambda_{pp}/2 = \lambda_{pp}/6 = 4 \text{ mm} \end{aligned} \tag{6.2}$$

where λ_{pp} , λ_p , and λ_t are the magnet pole-pair pitch, the pole pitch, and the iron-core tooth pitch, respectively. The physical configuration of the motor in the figure can be considered as a snapshot at the moving magnet position of $y = 0$. At this instant, the phase A has to be turned off while the phase B and C are energized to be magnetized in upward and downward directions, respectively, in order to drive the magnet track to the indicated direction (rightward). The thrust generation can be considered as a tendency of permanent magnets to align in the same direction of electromagnets which are the iron-core teeth driven by the phase windings. Note that the winding direction is indicated in Figure 6-4 such that a positive current generates an upward magnetic flux in an iron-core tooth. Given this sign convention, at the instantaneous zero position, the phase A current, i_A has to be zero and the phase B and C currents,

i_B and i_C , need to be positive and negative, respectively, as shown in the plots in the figure.

When the magnet track is slightly moved in the positive direction, $y = 0^+$, the phase A turns on such that it directs the flux upward to repel PM8, so i_A needs to be positive at that instant. Phase A keeps this positive value until the next magnet with an opposing magnetization aligns with the phase A coil, which is when the direction of phase A current flips. This is what we see in the i_A plot in Figure 6-4 starting positive at $y = 0^+$ and flipping sign at multiples of $\lambda_p = \lambda_{pp}/2$, thereby having a period of λ_{pp} .

The commutation waveforms of phase B and C are simply a shifted version of phase A. As for the phase B current, it starts out as positive at $y = 0$ as discussed earlier, and instantaneously becomes zero and flips the sign when PM7 is aligned with the first phase B coil, which is at $y = \lambda_t - \lambda_p = \lambda_{pp}/6$ as shown in (6.2). The same reasoning goes to the phase C, and the resultant commutation laws are depicted in Figure 6-4 as a squarewave form. Three phase currents are shifted from each other by one third of its period, and it can be written as

$$\begin{cases} i_A = I_p \text{square} \left(\frac{2\pi y}{\lambda_{pp}} \right) \\ i_B = I_p \text{square} \left(\frac{2\pi}{\lambda_{pp}} \left(y + \frac{\lambda_{pp}}{3} \right) \right) = I_p \text{square} \left(\frac{2\pi y}{\lambda_{pp}} + \frac{2\pi}{3} \right) \\ i_C = I_p \text{square} \left(\frac{2\pi}{\lambda_{pp}} \left(y - \frac{\lambda_{pp}}{3} \right) \right) = I_p \text{square} \left(\frac{2\pi y}{\lambda_{pp}} - \frac{2\pi}{3} \right) \end{cases} \quad (6.3)$$

where the function $\text{square}(\cdot) = \text{signum}(\sin(\cdot))$ indicates a periodic squarewave function and I_p is a peak current value. In a simple motor system without a position sensor, this squarewave commutation can be achieved by correctly positioned Hall sensors, switching current directions at right moments. However, since we have position sensors in our stage setup, we can generate commutation waveforms of any desired shapes, and do not require Hall cells. For our experiments, we use squarewave and sinewave commutations to compare the motor noise. The sinewave commutation algorithm is written as

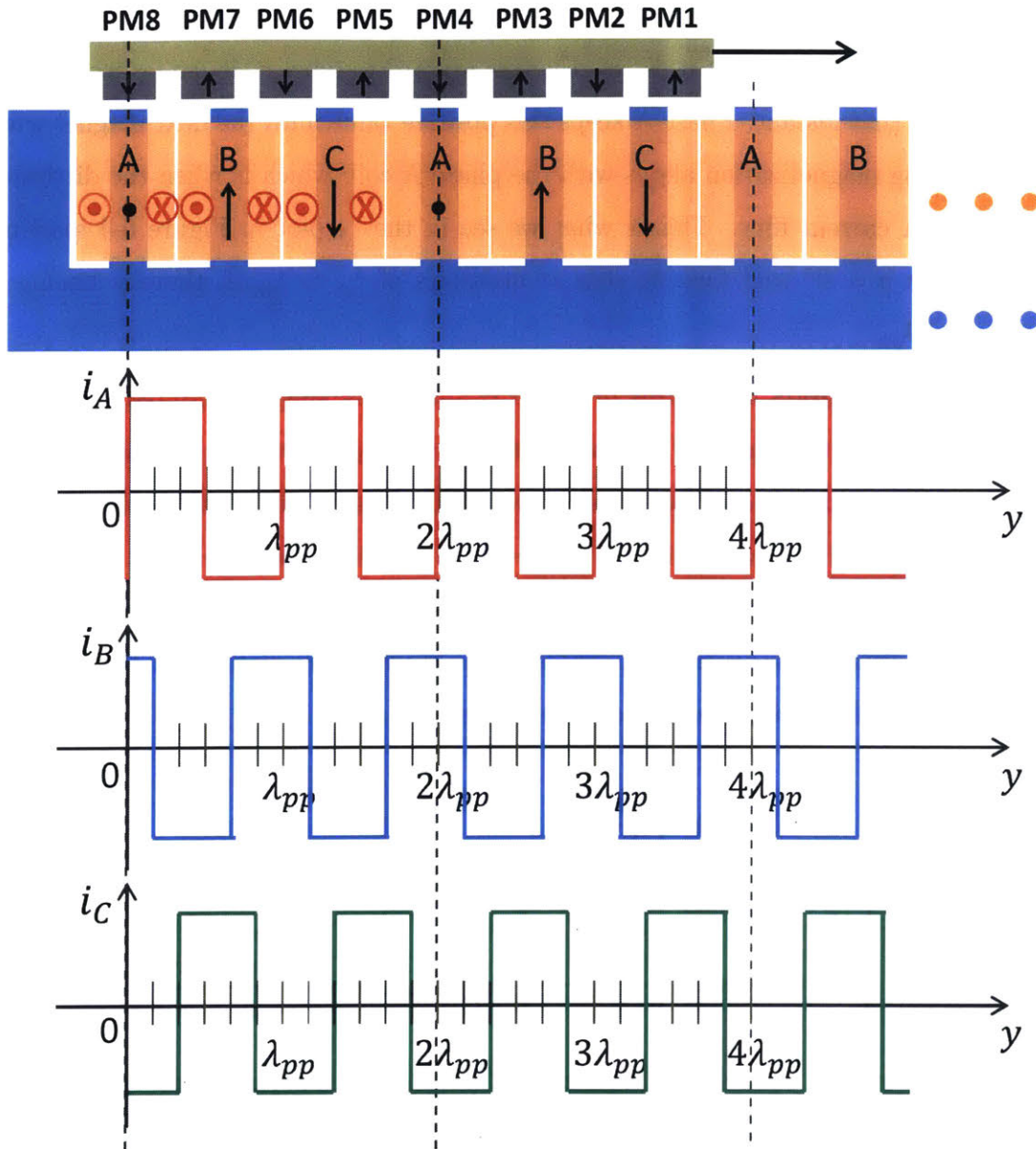


Figure 6-4: Squarewave commutation algorithm for the conventional Tecnotion TL18 three-phase iron-core motor. Magnet track shown is located at the zero reference position. Phase difference is one third of pole-pair pitch, $\lambda_{pp}/3$ from one phase to another.

$$\begin{cases} i_A = I_p \sin\left(\frac{2\pi y}{\lambda_{pp}}\right) \\ i_B = I_p \sin\left(\frac{2\pi}{\lambda_{pp}}\left(y + \frac{\lambda_{pp}}{3}\right)\right) = I_p \sin\left(\frac{2\pi y}{\lambda_{pp}} + \frac{2\pi}{3}\right) \\ i_C = I_p \sin\left(\frac{2\pi}{\lambda_{pp}}\left(y - \frac{\lambda_{pp}}{3}\right)\right) = I_p \sin\left(\frac{2\pi y}{\lambda_{pp}} - \frac{2\pi}{3}\right). \end{cases} \quad (6.4)$$

The commutation algorithm is implemented in a real-time controller (National Instruments PXI-8110), and the three-phase currents are commanded to the power amplifiers. As discussed in Chapter 5, we have a total of 18 amplifiers so as to drive the 18 coils individually. Thus, in order to implement 3-phase commutation, the coil currents have to be assigned as $i_{1,4,7,10,13,16} = i_A$, $i_{2,5,8,11,14,17} = i_B$, and $i_{3,6,9,12,15,18} = i_C$.

6.1.3 Position Control

The commutation current amplitude I_p , shown in (6.3) and (6.4), is determined by the position controller based on how much thrust (acceleration) is needed to follow a commanded trajectory. Figure 6-5 schematically shows the position feedback control loop we implement on our stage testbed. The conventional motor (TL18 by Tecnotion) together with power amplifiers and commutation algorithms forms a plant with the phase current amplitude, I_p and real-time stage position, y as an input and output, respectively. Note that sinewave commutation is shown in the figure, but as discussed earlier, we can programmatically control the commutation waveform in any desired shape.

We use a loop shaping technique to design the position controller. To that end, it is important to measure and understand the frequency responses of the plant and the loop return ratio. Figure 6-6 shows how we measure these frequency responses using a digital signal analyzer (DSA) designed in Labview by our lab, Precision Motion Control Laboratory (PMCL) at MIT. It is not impossible to measure the plant frequency response in an open loop configuration, but since our plant is basically a double-integrator, the stage may drift away and possibly run out of travel range

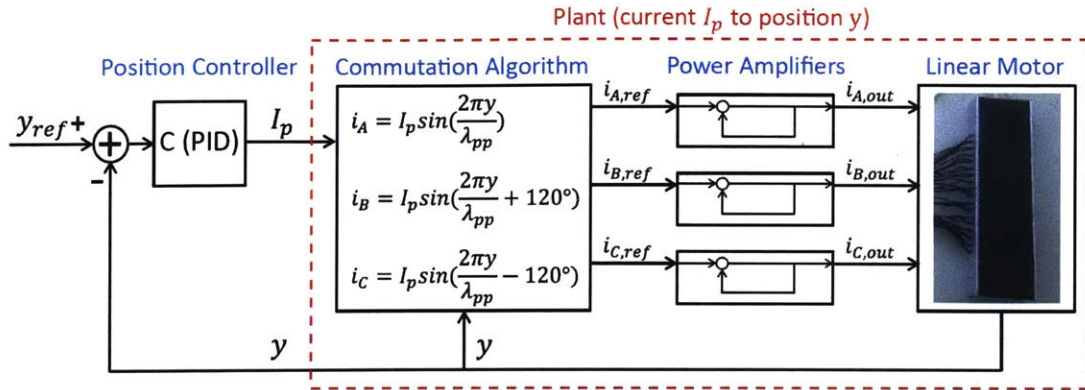


Figure 6-5: Schematic of position control loop with a plant of linear motor system, power amplifiers, commutation law, and a PID (lead-lag) controller.

while measuring the frequency response. To eliminate this DC drift issue, we design and implement a low bandwidth controller first, and use the schematic shown in the left side of Figure 6-6 to measure the plant response in closed loop. The DSA provides swept sine excitation as a disturbance while the position reference is set to zero, and it gathers the input (CH1) and output (CH2) to/from our plant to calculate its magnitude ratio and phase difference as written in

$$\left| \frac{CH2}{CH1} \right| = |P|, \quad \angle \frac{CH2}{CH1} = \angle P. \quad (6.5)$$

The measured plant frequency response is shown in Figure 6-7 as a blue line with data points. One might expect a pure double integrator behavior since the plant is simply a mass floating on air bearings pushed by a thrust force. The response shows, however, a plateau at DC and a resonance at about 4.5 Hz, which indicates that there is some kind of stiffness involved. This low-frequency resonance stems from the cogging force, which is an AC-coupled force fluctuation caused by the geometric saliency of the iron-core teeth engaged with the magnets. When we measure the frequency responses, we place the stage at an equilibrium position created by the cogging force, and the swept sines excited by our DSA perturb the stage about that point. This makes the stage experience the cogging stiffness, thereby showing the low-frequency resonant peak in our measured plant frequency response. To validate

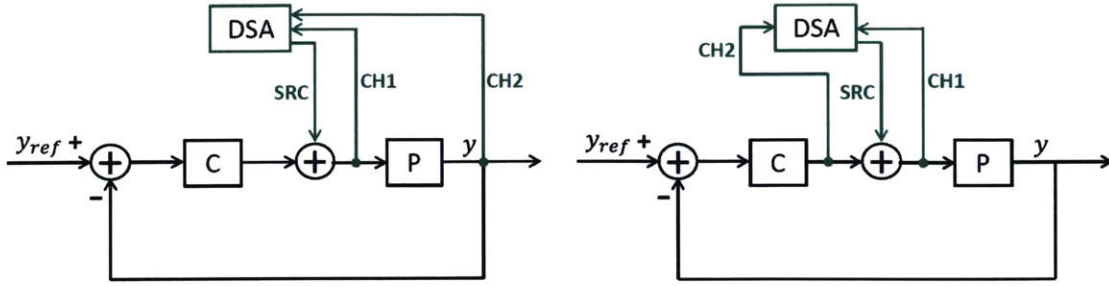


Figure 6-6: Schematic for measuring the relevant frequency responses of control loop: plant (left) and loop transmission (right).

this, we obtain a time response of stage position to a perturbation about the same equilibrium point as shown in Figure 6-8. The time response shows an oscillation with the average period of about 0.22 sec, which is equivalent to about 4.5 Hz we observe in our measured frequency responses.

The measured plant frequency response is fitted with a second order model as

$$P_{model}(s) = \frac{A}{s^2 + 2\zeta w_n s + w_n^2} e^{-\tau_d s}, \quad (6.6)$$

where A ($= 3136$), ζ ($= 0.05$), w_n ($= 28.9 \text{ rad/s}$), and τ_d ($= 300 \mu\text{s}$) are the plant gain, damping coefficient, resonant frequency, and system delay, respectively. These values are chosen to fit the measured frequency response. The fitted curve is shown in Figure 6-7 as a red solid line overlapped on the measured plant data.

Using the plant frequency response, we design a lead-lag compensator to shape the loop return ratio targeting a crossover, f_c , at 100 Hz with a phase margin, ϕ_{PM} of 45° . The controller we use is in the form of

$$C(s) = K \text{lead}(s) \text{lag}(s) = K \frac{\alpha\tau s + 1}{\tau s + 1} \frac{T_i s + 1}{T_i s} \quad (6.7)$$

where K , α , τ , and T_i are the loop gain, phase lead ratio, lead time constant, and lag time constant, respectively. The phase lead ratio, α determines how much phase lead we can get at the crossover, and it can be calculated by

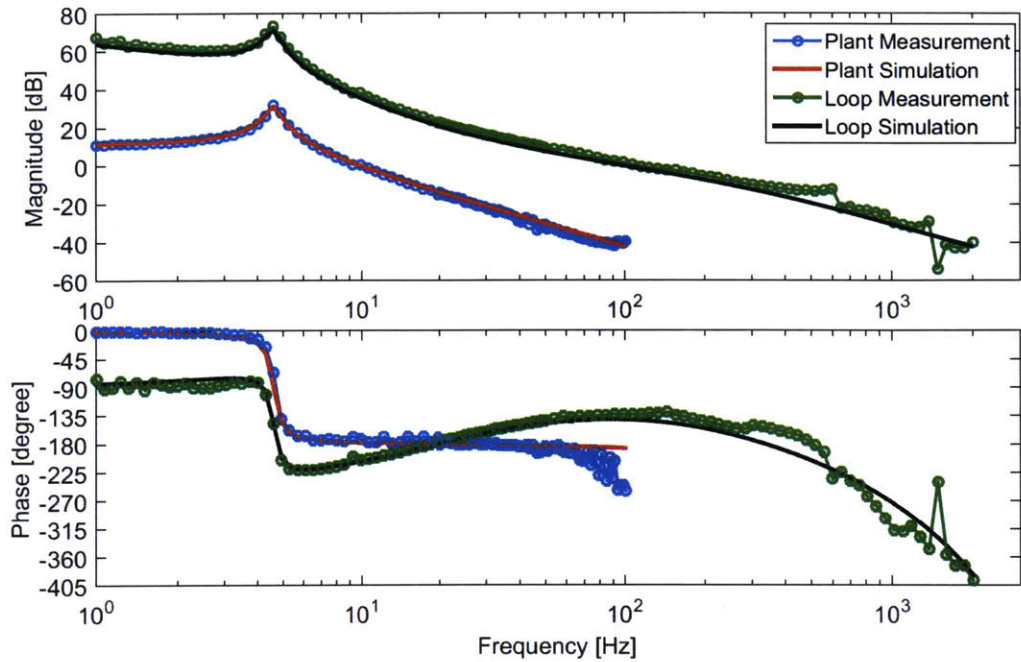


Figure 6-7: Measured and modeled frequency responses of plant and loop return ratio showing a crossover frequency of about 100 Hz and a phase margin of about 45° .

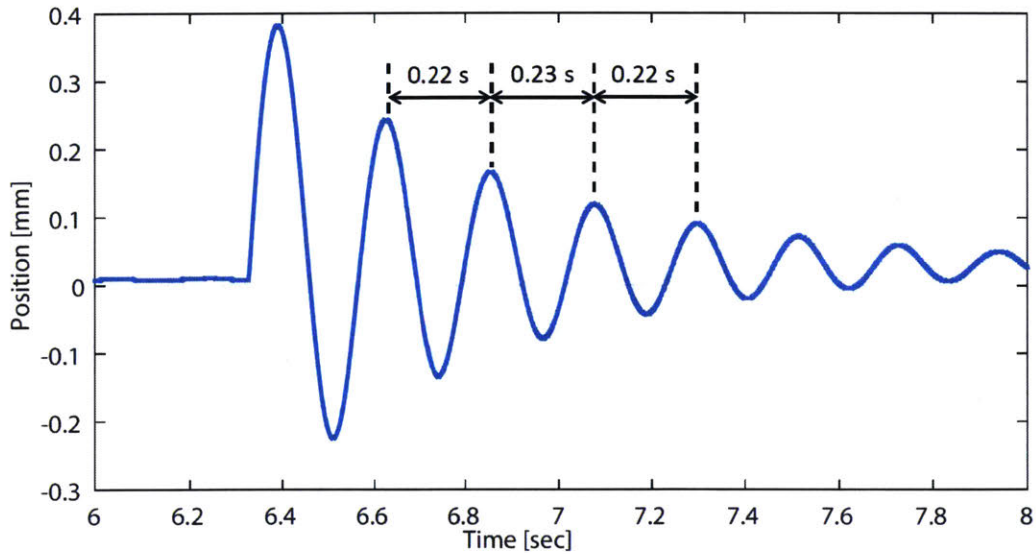


Figure 6-8: Measured time response of cogging resonance when perturbed about a stable equilibrium showing the frequency of about 4.5 Hz, consistent with the low frequency resonance observed in the measured frequency responses.

$$\phi_{max} = \sin^{-1} \left(\frac{\alpha - 1}{\alpha + 1} \right) \quad (6.8)$$

where ϕ_{max} indicates the maximum phase lead. We set $\alpha = 10$ to gain a phase lead of about 55° . The lead time constant determines the location of maximum phase lead with the relation of

$$w_{max} = \frac{1}{\sqrt{\alpha\tau}}, \quad (6.9)$$

and we choose it to coincide with our desired crossover frequency, $w_c = 2\pi f_c = 2\pi \times 100$, which gives $\tau = 5.03 \times 10^{-4}$. The loop gain is then calculated for the loop return ratio to have a unity gain at our crossover, resulting in $K = 39.73$. The last parameter to complete our controller design is the lag time constant, T_i . A rule of thumb for this value is to set the cutoff frequency, $w_{cut} = 1/T_i$ of a lag compensator one decade before the desired crossover so as to minimize a phase lag effect on the phase margin at crossover. Following this, we choose $T_i = 10/w_c = 15.9$ msec.

We implement the position controller in our real-time controller (National Instruments PXI-8110) with the deterministic loop rate of 10 kHz. To validate our controller design, we measure a loop return ratio, $L(s)$ using the DSA schematic shown in the right side of Figure 6-6, which gives magnitude ratio and phase difference of

$$\left| \frac{CH2}{CH1} \right| = | -PC | = | -L |, \quad \angle \frac{CH2}{CH1} = \angle(-PC) = \angle(-L). \quad (6.10)$$

Note that the ratio of CH1 to CH2 itself provides the loop transmission, $-L(s)$, so in order to obtain a desired loop return ratio, we need to flip the sign. Figure 6-7 shows the measured and fitted loop return ratio in a green line with data points and black solid line, respectively. As designed, the figure shows we have the crossover at 100 Hz with the phase margin of 45° . We also obtain a step response of our closed-loop system to a $20 \mu\text{m}$ position step input, and the measured response is shown in Figure 6-9. It shows the rise time, t_r (10%-90%) of about 1.7 msec, which implies a

-3dB bandwidth, f_{BW} of about 206 Hz following the relation of

$$f_{BW} = \frac{w_{BW}}{2\pi} \approx \frac{1}{2\pi} \frac{2.2}{t_r}. \quad (6.11)$$

This approximation value of -3dB bandwidth agrees well with a measured bandwidth of 194 Hz, showing the consistency between frequency and time domain responses. Also, with the phase margin, ϕ_{PM} of about 45° , we expect a percentage overshoot, PO of about 20.5 % in the step response based on the relations of

$$\zeta \approx \frac{\phi_{PM}}{100} \quad (6.12)$$

$$PO = 100 \times e^{\left(\frac{-\zeta\pi}{\sqrt{1-\zeta^2}}\right)}. \quad (6.13)$$

We have the percentage overshoot of about 30 % in the measured step response, and this is a bit higher than the expected overshoot of 20.5 % by (6.12). We speculate

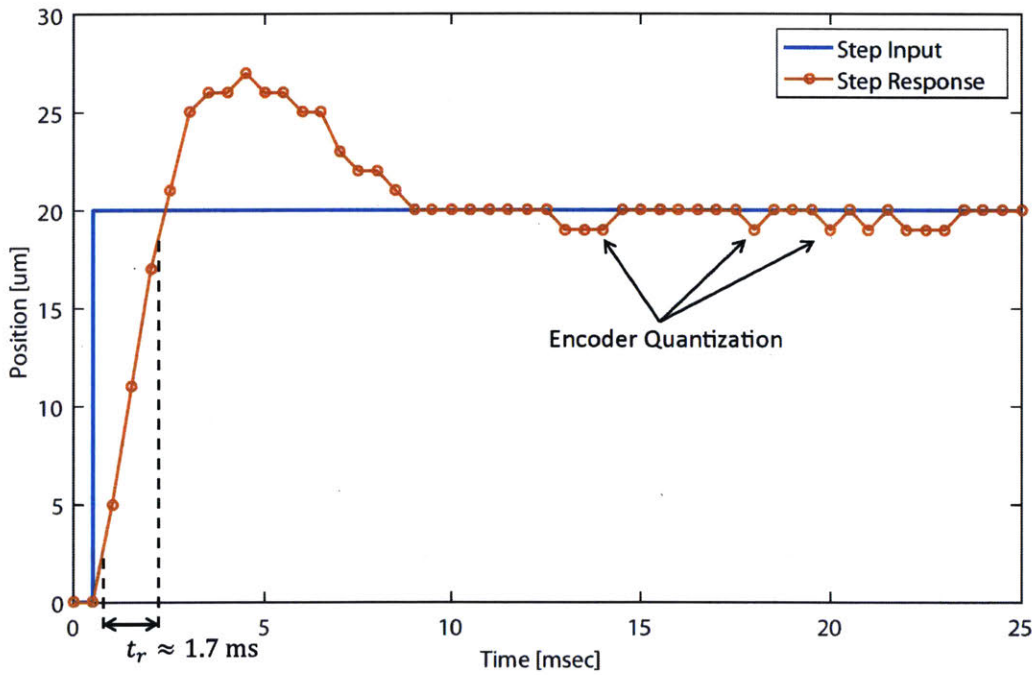


Figure 6-9: Measured step response of closed position control system to a step of 20 μm showing a rise time of about 1.7 msec and encoder quantization of 1 μm .

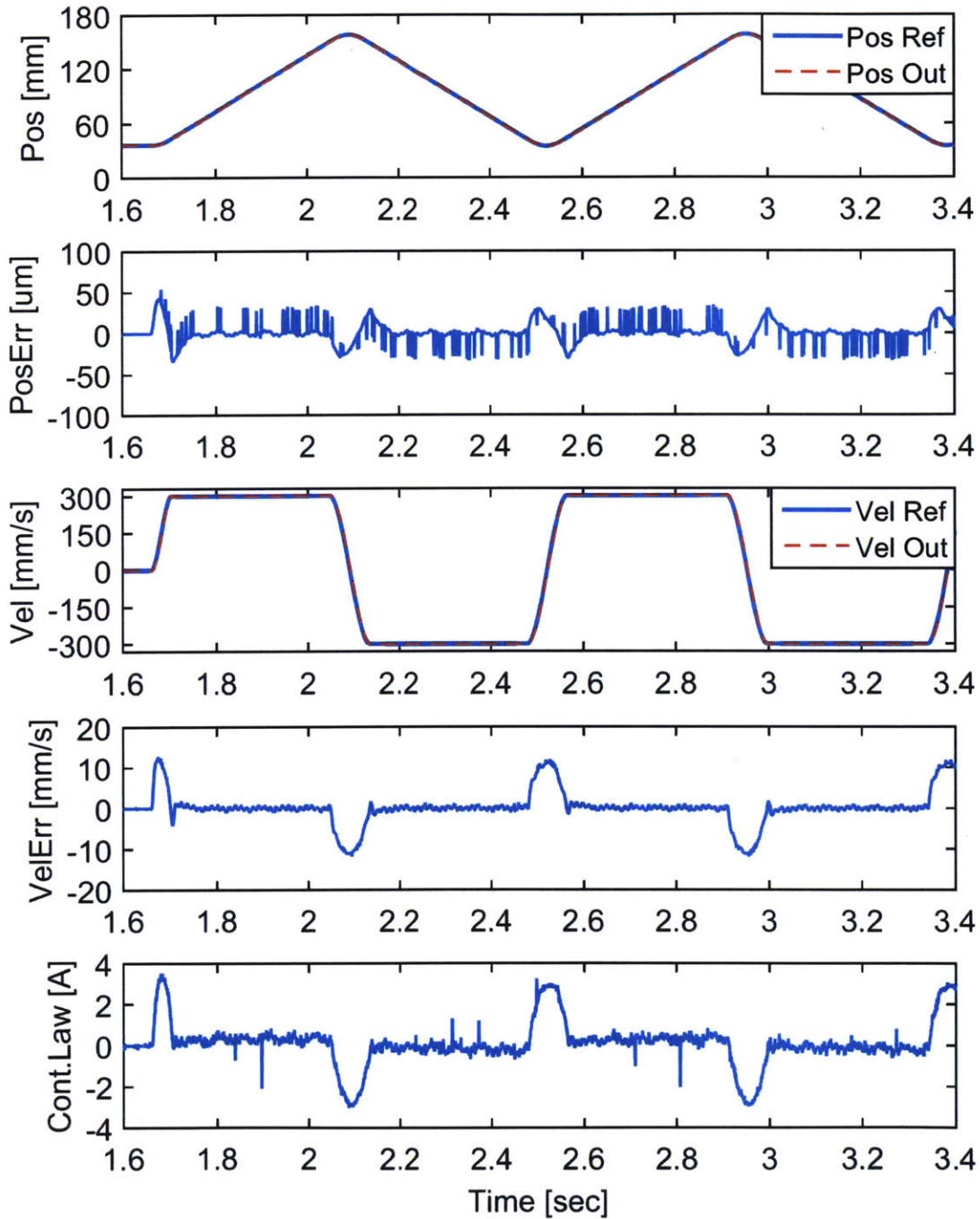


Figure 6-10: Measured tracking performance of closed position control system following a smooth trajectory with maximum acceleration of 10 m/s^2 and maximum velocity of 0.3 m/s .

that this difference is likely due to the effect of the lead zero.

We also test the tracking performance of the position controller with a position trajectory. A fourth order polynomial position trajectory is generated to have smooth velocity and acceleration curves, and commanded to the closed loop stage to follow. Figure 6-10 shows measured tracking performances in terms of position and velocity together with the required control effort in current, to a position trajectory with the maximum acceleration of 10 m/s^2 , maximum velocity of 0.3 m/s , and travel length of 120 mm . The overall position and velocity RMS errors are $12 \text{ }\mu\text{m}$ and 4 mm/s , respectively, while the RMS errors during a constant velocity region are $9.3 \text{ }\mu\text{m}$ and 0.5 mm/s , respectively.

6.2 Experimental Results

In this section, we present experimental results on the vibro-acoustic noise of the conventional linear motor. We begin to discuss the motor noise issue in a stationary status. Even without cycling the stage, we observe serious vibro-acoustic noise only by turning on the position controller. We find it stems from the encoder quantization together with a high loop gain, and discuss it with relevant experimental data in this section. We also discuss the motor noise in cyclic operations. Both vibrational and acoustic noise are measured and compared to find causes and understand mechanisms of the motor noise in this section, and a brief summary follows at the end.

6.2.1 Vibro-acoustic Noise in Stationary Position

Before operating our stage in a cyclic mode, we observe vibro-acoustic noise when the stage is commanded to a stationary position. We speculated that this problematic noise comes from impulse-like forces generated by peaky position errors due to the $1 \text{ }\mu\text{m}$ encoder quantization. In order to validate this reasoning, we use our measurement systems, discussed in Chapter 5, to measure both vibrational and acoustic noises of stationary stage. The accelerometers are mounted on the stage and the microphones are installed one meter away.

We first observe the noise measurements for the case with the encoder resolution, Δ of $1 \mu\text{m}$, which has the interpolation rate of $\times 20$ for the grating pitch of $20 \mu\text{m}$. Figure 6-11 shows the position error, when commanded to hold a stationary position, by the encoder quantization of $1 \mu\text{m}$, and resultant control effort generated by our high-gain position controller. As shown in the figure, control effort peaks are substantial because of significant quantization errors, and the cumulative amplitude spectrum (CAS) of control effort shows that it contains a broad spectrum frequency range, implying the possibility to excite all frequencies. In order to see if these impulse-like control efforts actually cause noise, we measure the motor vibro-acoustic noise for four different system conditions: i) only compressed air is turned on, ii) power electronics are also powered on, iii) position controller is turned on with sinewave commutation, and iv) controller is on with squarewave commutation. Figure 6-12 shows the CAS of accelerometer measurements for these four cases of system conditions both in Z and X directions.

When only the compressed air is turned on, there is essentially no vibration on the stage, as expected and shown with blue curves in Figure 6-12. We start to observe some vibration when powering up the amplifiers. This is due to the PWM switching containing/exciting all frequencies. Note that we do not need to worry about this switching noise if using linear drives. However, since those amplifiers are much more costly, we choose to work with PWM drives for our prototype experimental setup, and thus we choose our noise baseline to be the noise measured when powering up the amplifiers as shown with green solid lines in the figure.

More vibrational noises are observed when the position controller is turned on as shown in the figure with red and black curves. As expected from the significant control efforts by $1 \mu\text{m}$ quantization noise, we see increasing noise from the baseline, which comes from the stage eigen-modes excitation. This is more significant when the commutation waveform is a squarewave because it contains more high-frequency components and thus generates more force harmonics to excite stage dynamics. The most notable jump both in the measured CAS's of Z- and X-direction vibration data is located at about 630 Hz. This corresponds to a bending mode of our U-shaped stage.

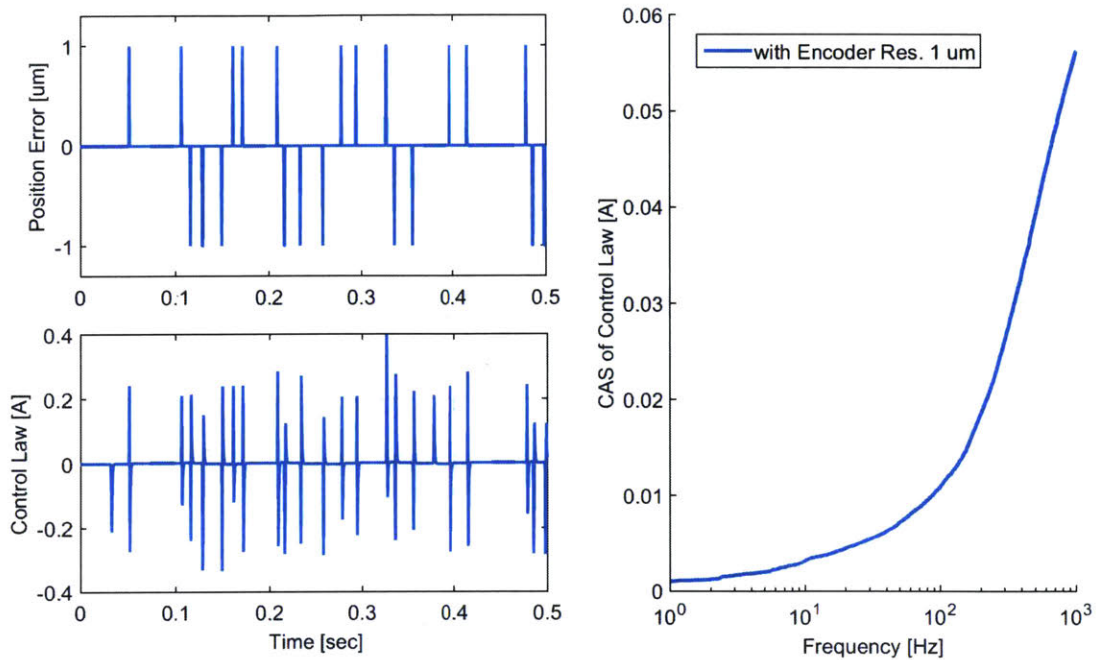


Figure 6-11: Encoder quantization and corresponding control effort with an interpolated resolution of $1 \mu\text{m}$ (left), and associated cumulative amplitude spectrum (CAS) (right).

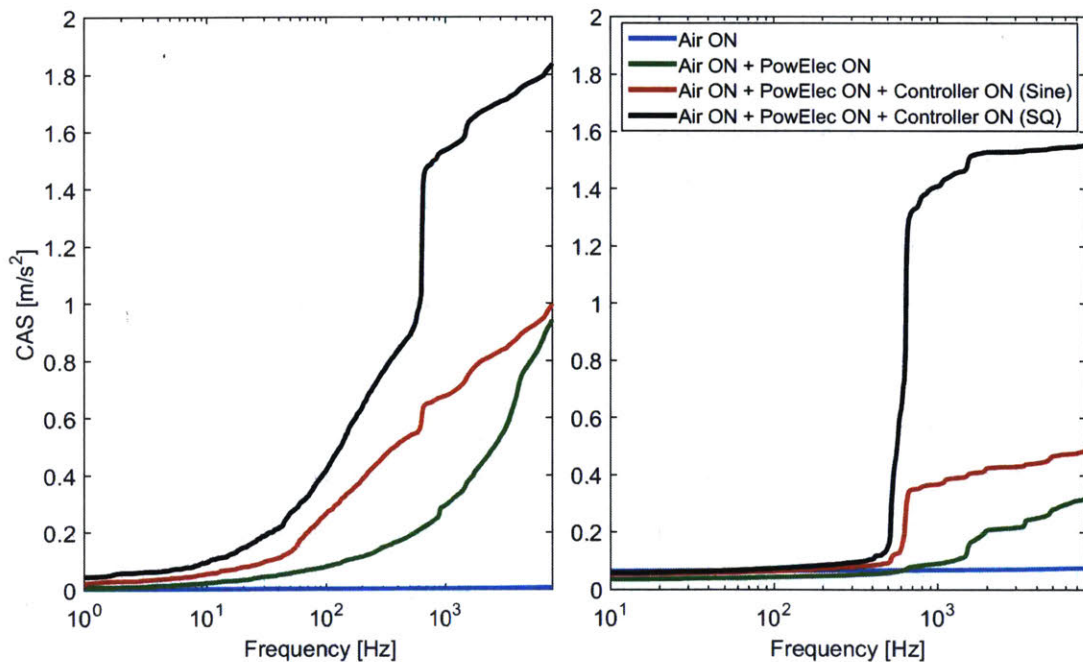


Figure 6-12: Cumulative amplitude spectrum (CAS) of accelerometer measurement data for four different conditions investigating motor stationary noise with the encoder resolution of $1 \mu\text{m}$. Z-direction (left) and X-direction (right).

Some of major stage dynamics are listed in Figure 6-13 with a simple mode-shape description for each corresponding eigen-frequency. We encounter these eigen-modes and eigen-frequencies throughout this chapter and after.

From these investigations, we understand that the coarse quantization error is the culprit of motor noises in stationary status, exciting stage dynamics to emit significant vibro-acoustic noises. In order to resolve this issue, we changed hardware to increase the interpolation ratio from $\times 20$ to $\times 200$ to have a ten times finer encoder resolution of $0.1 \mu\text{m}$. Figure 6-14 shows the quantization error and its associated control effort with $\Delta = 0.1 \mu\text{m}$, and compares them to those with $\Delta = 1 \mu\text{m}$. Due to much smaller position errors, the control effort peak is substantially reduced along with the associated spectral contents as shown in the CAS plot in Figure 6-14 with a red solid line. To see the effect of using $\Delta = 0.1 \mu\text{m}$ on the motor stationary noise, the vibrational noise is measured on the stage when the controller is turned on with squarewave commutation, and is compared with the case of $\Delta = 1 \mu\text{m}$ in Figure 6-15. In the CAS of both Z- and X-direction measurements, we can see that the stage vibration is significantly reduced with $\Delta = 0.1 \mu\text{m}$ to the extent that the CAS curve of controller-on case (purple line) is quite close to our noise baseline (green line) even when commutated with a squarewave. The stage dynamics once excited significantly with the coarse encoder resolution (black line) are now almost not excited when using the finer resolution. We observe the same results when measuring acoustic noise using our microphone system. Sound noise is measured in units of pascal for four different system conditions, and compared between the cases of coarse and fine resolution in Figure 6-16. Similarly to the vibrational noise measurements, the acoustic noise CAS with $\Delta = 1 \mu\text{m}$ shows significantly increasing noise level from the baseline (green line) when the controller is on, exciting stage eigen-modes, which is especially severe with squarewave commutation. However, when we change the encoder resolution to $\Delta = 0.1 \mu\text{m}$, not much of noise increase from the baseline is observed even when commutated by a squarewave. This is due to the fact that the quantization error and resultant control effort are so small that the stage dynamics are not that excited as before. A brief summary of our investigation on the motor stationary noise issue is


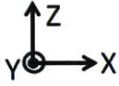





Eigen-Freq.	Eigen-Mode	Description
~4 Hz		Y-direction rigid body motion due to cogging force/stiffness 
~130 Hz		X-direction rigid body motion due to side air bearings
~360 Hz		Z-direction rigid body motion due to top air bearings
~500 Hz		Only side plates resonate.
~630 Hz		Side and top plates resonate together in X-Z plane.
~1100 Hz		Side and top plates resonate together in X-Z plane; high order mode.

Figure 6-13: Schematic of major stage eigen-modes with a brief description, experimentally obtained by a ping test.

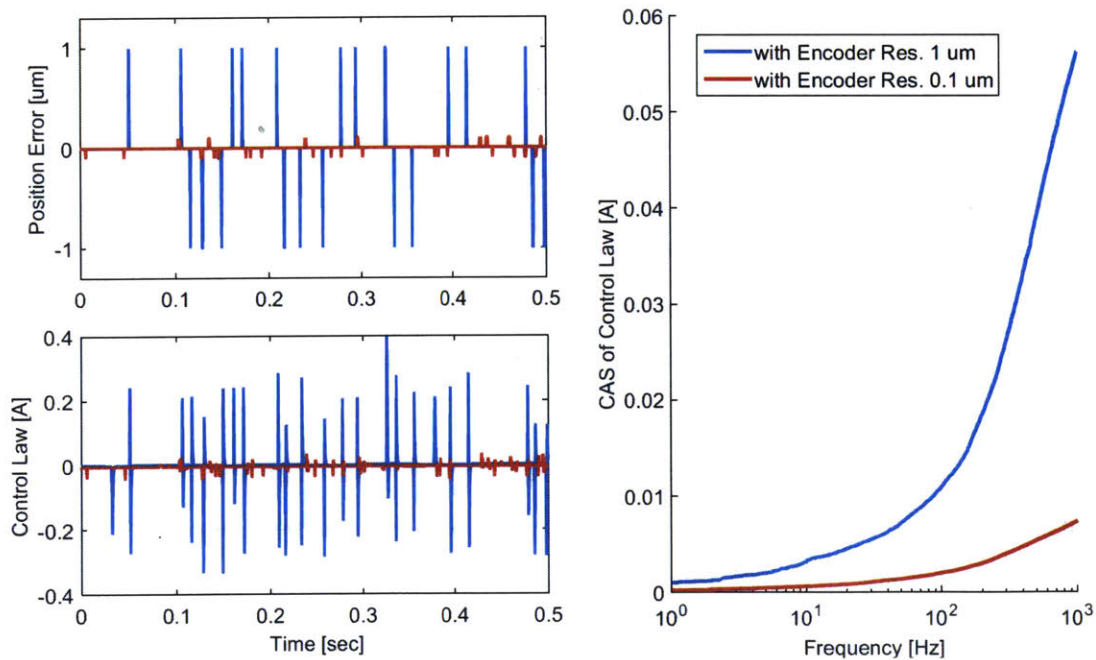


Figure 6-14: Encoder quantization and corresponding control effort with an interpolated resolution of 0.1 μm compared to the case with 1 μm resolution (left) and associated CAS (right).

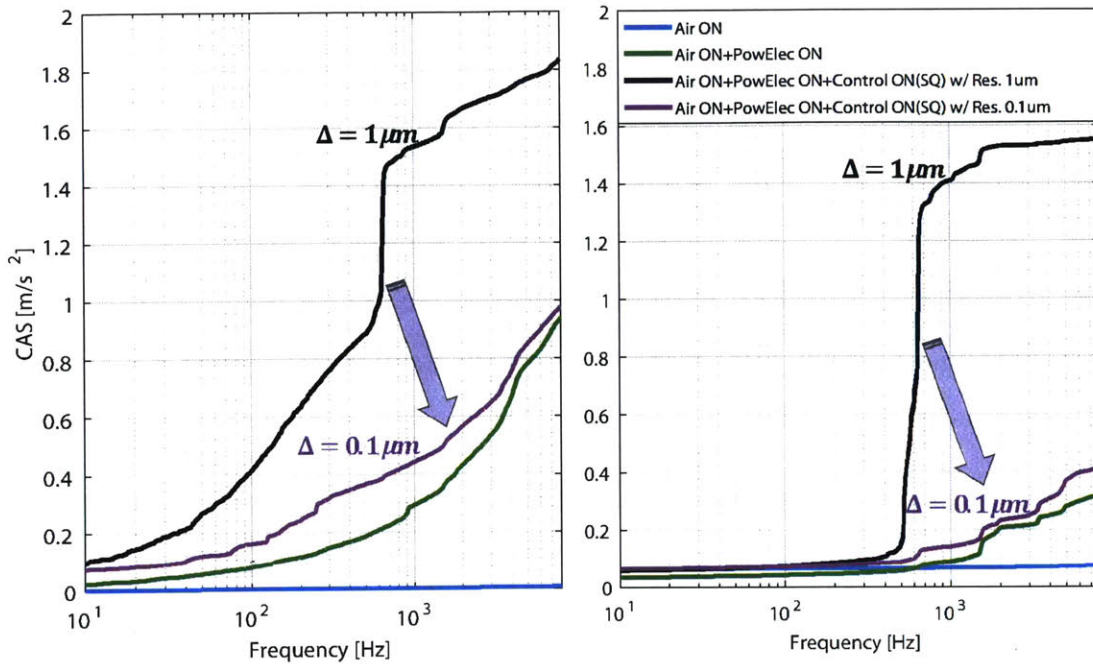


Figure 6-15: CAS of accelerometer measurement. Comparison between the encoder resolutions, $\Delta=0.1 \mu\text{m}$ and $\Delta=1 \mu\text{m}$, showing significant reduction of motor stationary noise with finer resolution. Z-direction data (left) and X-direction data (right).

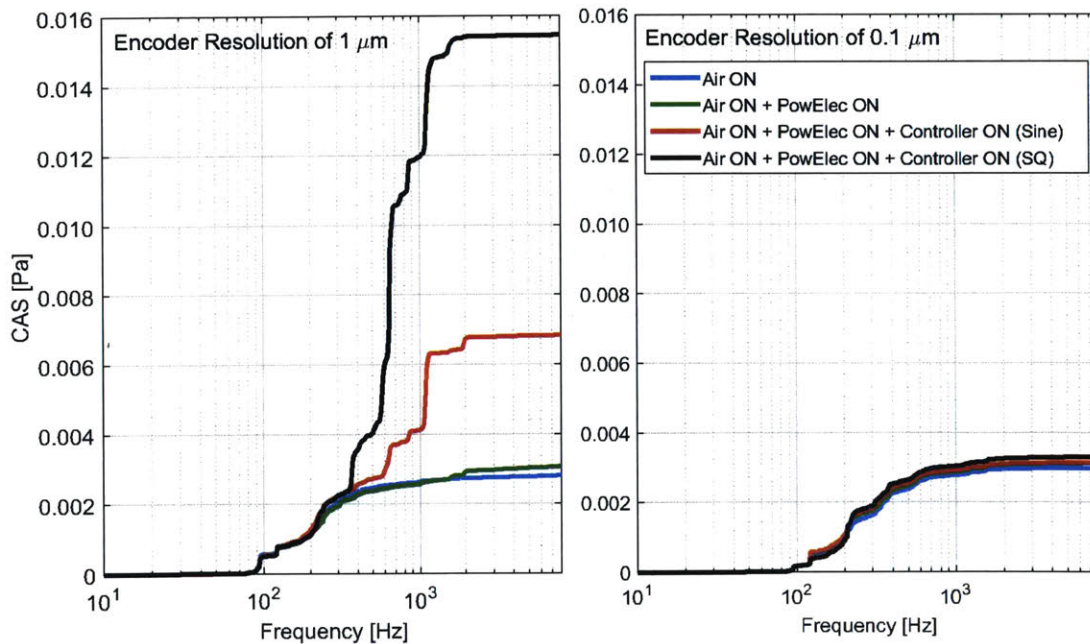


Figure 6-16: CAS of microphone measurement for four different conditions. Comparison between the encoder resolutions, $\Delta=0.1 \mu\text{m}$ (left) and $\Delta=1 \mu\text{m}$ (right), showing significant reduction of motor stationary noise.

listed as below.

- Motor noise is observed even in a stationary position when the position controller is turned on.
- Motor stationary noise comes from coarse quantization errors by the encoder resolution of $1 \mu\text{m}$.
- Coarse quantization error causes large control efforts and generates impulse-like forces to vibrate the stage, especially severe when stage dynamics are excited.
- Stage vibration by coarse quantization errors radiates acoustic noise that we hear.
- The motor stationary noise issue is largely resolved by upgrading the interpolation ratio to have ten times finer encoder resolution, $\Delta = 0.1 \mu\text{m}$.
- Finer resolution reduces the amplitude of quantization error and its resultant control effort, not causing serious stage vibration. From this point, we use the encoder resolution of $\Delta = 0.1 \mu\text{m}$ when operating the stage testbed and running experiments.
- Required RMS position error can be fulfilled even with the coarse encoder resolution, $\Delta = 1 \mu\text{m}$, as discussed in the previous section. However, the encoder quantization and its effects have to be also taken into account when choosing an encoder resolution for a high-precision system sensitive to noise.

6.2.2 Vibro-acoustic Noise during Cycle Operation

Here, we discuss the motor vibro-acoustic noise during cyclic operations. Note that the encoder resolution of $0.1 \mu\text{m}$ is used throughout this subsection and hereafter in order to minimize the quantization issue. Experiments are conducted with various conditions to better understand the causes and mechanism of the motor vibro-acoustic noise. Both vibrational and acoustic noises are measured in Z and X directions while the stage is cycled with either sinewave or squarewave commutation. Also, both

nonskewed and skewed magnet arrays are compared to study the effects of skewing magnets on the motor noise. In addition, the measurement data is separated into acceleration/deceleration and constant velocity regions to see if the motor noise behaves differently in each region. Note that we utilize two separate real-time controllers to independently implement the position control loop and the measurement loop, thereby keeping the control loop highly deterministic. The synchronization between these two controllers is achieved by a digital output signal, which turns on the measurement loop at the exact moment of stage cycling start. The position loop runs deterministically at 10 kHz in an National Instruments (NI) PXI-8110, and the measurement loop samples data at 50 kHz in an NI PXIe-8133.

We begin our investigation by comparing vibrational and sound noises while cycling the stage with a smooth trajectory with a maximum acceleration, A_{max} of 25 m/s² and maximum velocity, V_{max} of 1 m/s. Figures 6-17 and 6-18 show accelerometer and microphone data comparison during an acceleration region in both Z and X directions, respectively. We observe several eigen-frequencies excited, such as at 360 Hz, 500 Hz, 630 Hz, 1100 Hz, and etc., dominating the overall noise level in both accelerometer and microphone data. These stage dynamics are excited by the ample force harmonics of the conventional linear motor because, by design, its stator and rotor MMF's contain high spatial harmonics as discussed in Chapter 2. This also explains why we observe much larger noise level when the stage is commutated with a squarewave, exciting stage dynamics more severely.

From these observations, we can conclude that the sound noises we hear and microphones measure during an acceleration region come from the stage vibration, and this vibration is mostly caused by high force harmonics of the conventional motor, exciting the stage eigen-modes, as hypothesized in Chapter 1. One of the simplest approaches to reduce the vibro-acoustic noise using the same motor can be then to avoid a commutation waveform with high-frequency contents (e.g. squarewave) and use a smooth one (e.g. sinewave) to less excite the stage dynamics. However, a more fundamental solution is to change the motor magnetic design to have less force harmonics. This is why we develop our new fine-tooth motor as described in

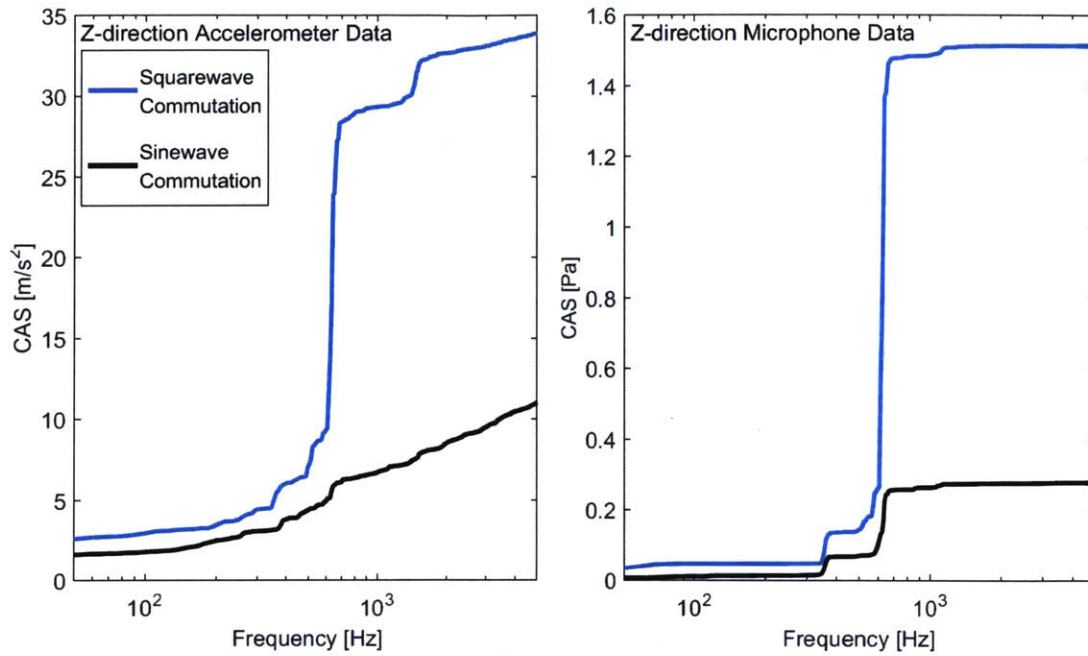


Figure 6-17: CAS comparison between squarewave and sinewave commutation cases: Z-direction accelerometer (left) and microphone measurement (right) at $A_{max} = 25$ m/s² and $V_{max} = 1$ m/s with non-skewed magnets.

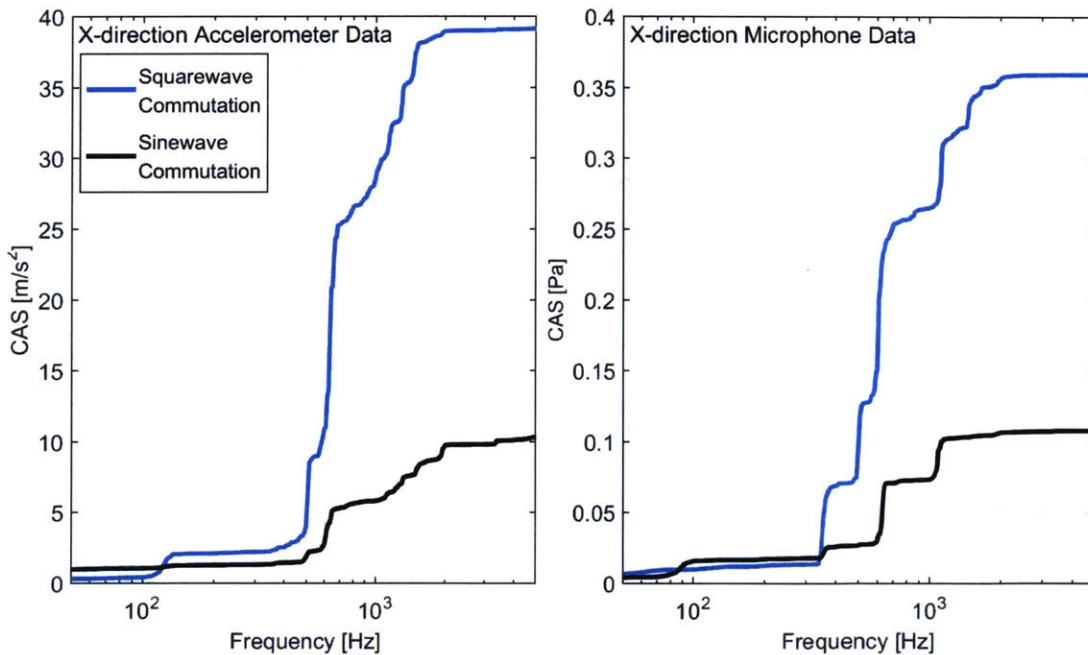


Figure 6-18: CAS comparison between squarewave and sinewave commutation cases: X-direction accelerometer (left) and microphone measurement (right) at $A_{max} = 25$ m/s² and $V_{max} = 1$ m/s with non-skewed magnets.

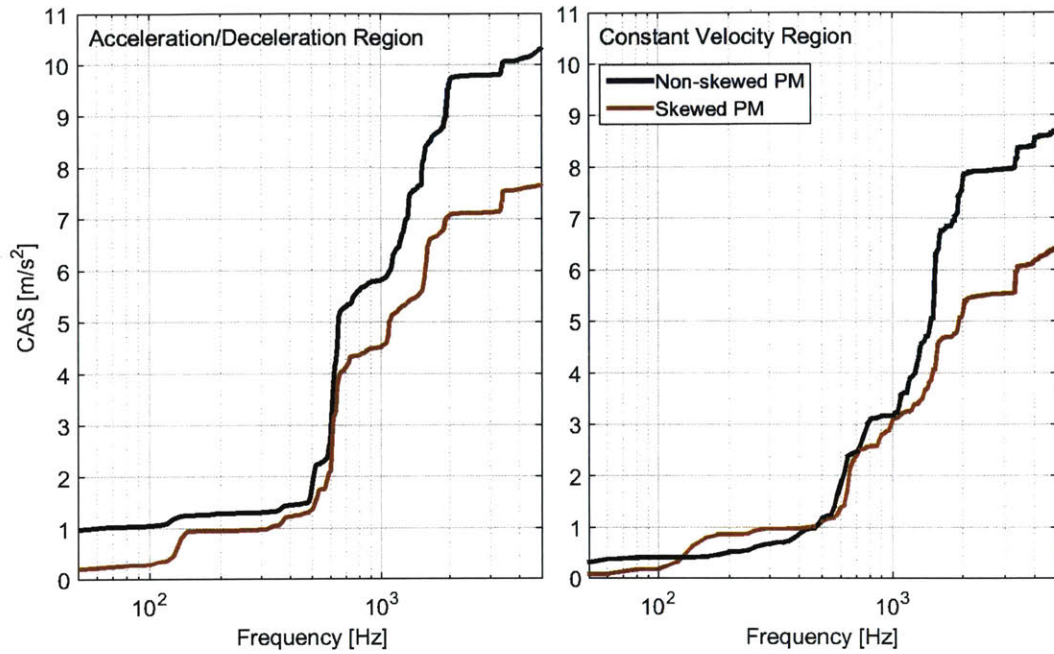


Figure 6-19: CAS of accelerometer measurements on stage side plate at $A_{max} = 25$ m/s² and $V_{max} = 1$ m/s with skewed and non-skewed magnets both during acceleration (left) and constant velocity (right), showing stage eigen-modes excitation for both cases. Eigen-modes associated with area of rapid change in CAS.

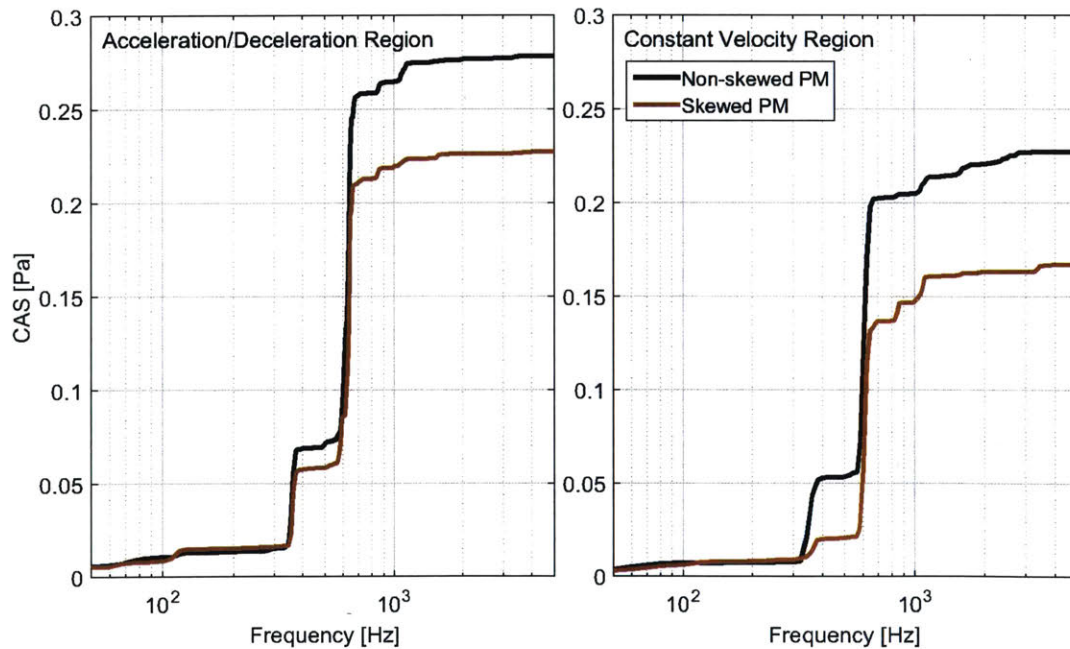


Figure 6-20: CAS of microphone measurements from above stage at $A_{max} = 25$ m/s² and $V_{max} = 1$ m/s with skewed and non-skewed magnets both during acceleration (left) and constant velocity (right) regions, showing stage eigen-modes excitation for both regions.

Chapter 3. Experimental results of this newly-designed motor and comparisons with the conventional 3-4 combination motor are discussed in Chapter 7.

We also investigate the motor vibro-acoustic noise in a constant velocity region together with the effect of skewing magnets. Figures 6-19 and 6-20 compare the vibrational and acoustic noises between acceleration and constant velocity regions. Note that sinewave commutation is used for these experiments. One might expect much less noise level in a constant velocity region since it nominally requires no acceleration and no thrust, thereby not much of force harmonics to excite the stage dynamics. However, what we observe from the measured data in the figures is different from the expectation that the vibro-acoustic noise in a constant velocity period contains similar level of stage dynamics to the cases in an acceleration region. This can be explained in terms of force disturbance, namely cogging force existing in the constant velocity regions. Even with skewed magnets, the cogging fundamental of the conventional motor cannot be eliminated, as discussed in Chapter 2, and magnetic forces have to be generated to overcome this cogging to achieve the commanded constant velocity. This generated force also contains higher harmonics due to the design of the conventional motor, thereby again exciting the stage eigen-modes even in a constant velocity region. Note that the measured vibro-acoustic noise level is a bit smaller with the skewed magnets. This is because skewing magnets acts as a low-pass filter to smoothen the rotor MMF, thereby generating less force harmonics.

As an additional effort to further investigate the motor noise in acceleration and constant velocity regions, we post-process our measurements to plot spectrograms. Figures 6-21 to 6-23 show measured spectrograms of a half cycle with the same acceleration of 25 m/s^2 and varying velocities of 0.4 m/s , 0.6 m/s , and 1.0 m/s , respectively. Velocity profiles commanded for the stage to follow are overlapped in white on the spectrograms to show each velocity region. The color map in the figures shows the sound pressure level (SPL) in dB with respect to a reference pressure, P_{ref} of $20 \mu\text{Pa}$. As expected from the CAS data previously shown in Figures 6-19 and 6-20, there is no clear distinction on the motor noise between acceleration/deceleration and constant velocity regions. This is because the stage eigen-modes (mainly at 630 Hz and

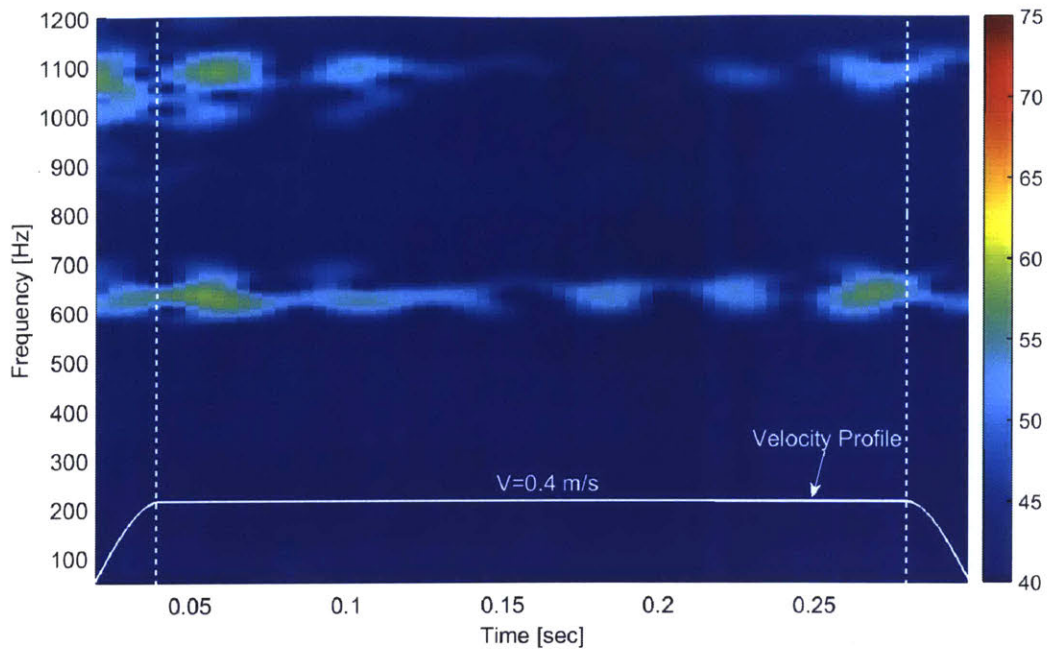


Figure 6-21: Spectrogram of microphone measurements during a half cycle of velocity profile with $A_{max} = 25 \text{ m/s}^2$ and $V_{max} = 0.4 \text{ m/s}$ with non-skewed magnets. Velocity profile commanded is overlapped in white to indicate acceleration/deceleration and constant velocity regions. The color-map shows sound pressure level (SPL) in dB re $P_{ref} = 20 \mu\text{Pa}$.

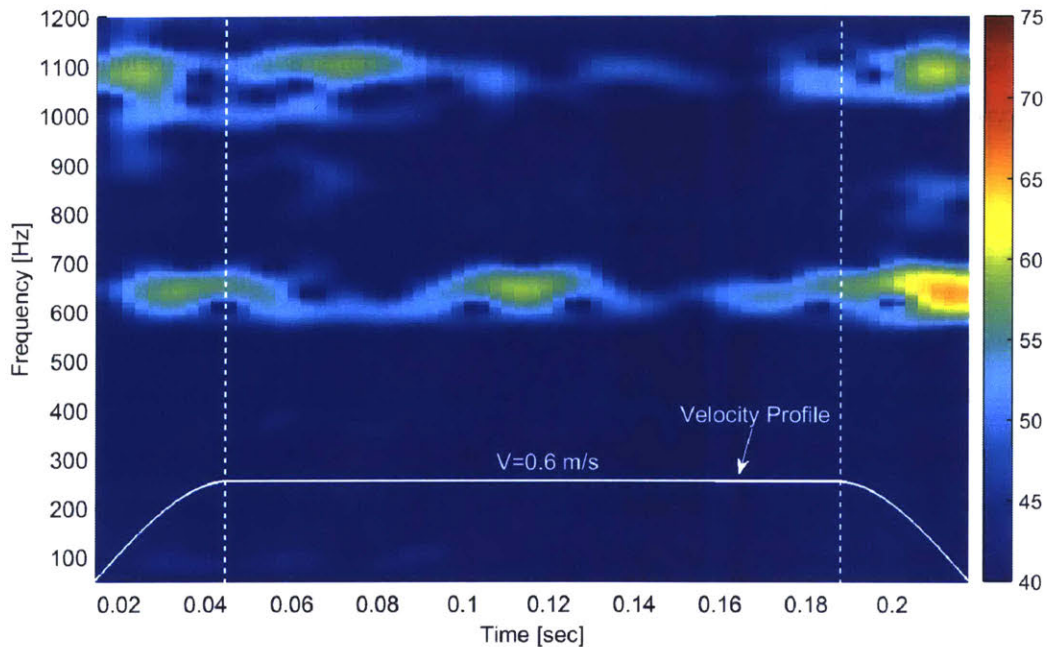


Figure 6-22: Spectrogram of microphone measurements during a half cycle of velocity profile with $A_{max} = 25 \text{ m/s}^2$ and $V_{max} = 0.6 \text{ m/s}$ with non-skewed magnets. Color-map shows SPL in dB re $P_{ref} = 20 \mu\text{Pa}$.

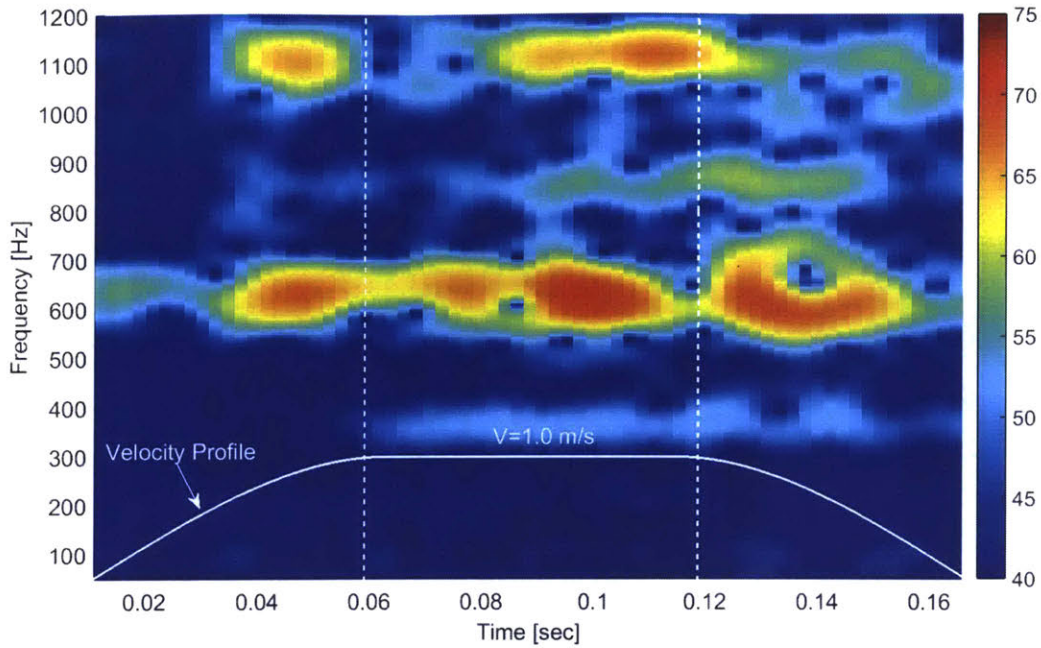


Figure 6-23: Spectrogram of microphone measurements during a half cycle of velocity profile with $A_{max} = 25 \text{ m/s}^2$ and $V_{max} = 1.0 \text{ m/s}$ with non-skewed magnets. Color-map shows SPL in dB re $P_{ref} = 20 \text{ } \mu\text{Pa}$.

1100 Hz) are excited by the generated magnet force 1) to achieve the required thrust during acceleration and 2) to overcome the cogging during a constant velocity region.

It might be expected to observe in the spectrograms a cogging-oriented and velocity-dependent noise components given by

$$f_{cogging} = \frac{v_c}{\lambda_{cogging}/n}, \quad (6.14)$$

where v_c , $\lambda_{cogging}$, and n are the constant velocity, fundamental cogging period, and cogging harmonic index, respectively. As discussed in Chapter 2, the conventional 3-4 combination motor (TL18 by Tecnotion) has a strong fourth harmonic component ($n = 4$) due to its 3-4 combination design. The cogging fundamental period is $\lambda_{cogging} = 16 \text{ mm}$, so the cogging-oriented noises are expected from the conventional motor at the frequencies of 100 Hz, 150 Hz, and 250 Hz for $v_c = 0.4 \text{ m/s}$, 0.6 m/s , and 1.0 m/s , respectively. However, we are not able to observe these noises from the spectrograms in Figures 6-21 to 6-23 because their amplitudes are so small that they

are dominated and disguised by the stage dynamics noise. We discuss in detail the issue of this cogging-oriented and velocity-dependent noise in Chapter 7 with our new fine-tooth motor.

6.2.3 Brief Summary

In this chapter, we discuss various aspects of the motor vibro-acoustic noises emitted from the conventional 3-4 combination linear motor. Some of important takeaways from this chapter are summarized as follows.

- Motor stationary noise is caused by coarse ($\Delta = 1 \mu\text{m}$) encoder quantization errors resulting in significant control effort peaks, and so exciting stage eigenmodes.
- Motor stationary noise is resolved by upgrading the interpolation ratio to have a finer encoder resolution, $\Delta = 0.1 \mu\text{m}$.
- Vibro-acoustic noise of the conventional 3-4 combination motor comes from the high motor force harmonics due to its magnetic design as discussed in Chapter 2. Noise mechanism is such a way that the high force harmonics vibrate the moving stage, and the stage vibration radiates the acoustic noise, as hypothesized in Chapter 1.
- We observe more noise when the linear motor is commutated with a squarewave function since it carries more high-frequency components and makes the stator MMF have more harmonics.
- Skewing magnets helps to reduce the overall motor noise level by smoothing the rotor (moving magnet tracks) MMF.
- Within the given magnetic design of the conventional 3-4 combination linear motor, the vibro-acoustic noise can be reduced by commutating with a smooth waveform (e.g. sinewave) and by skewing magnets. However, these are only

indirect and secondary methods, and cannot reduce the motor acoustic noise by a significant amount.

- A direct solution to the motor noise is to develop a new magnetic design where i) stator and rotor MMF's are smooth enough not to generate high force harmonics and ii) force disturbance (e.g. cogging) can be minimized so as not to vibrate the moving stage while operating in constant velocity regions. Such a motor design, which we call a fine-tooth motor, is introduced in Chapter 3, and experimentally validated in Chapter 7.

Chapter 7

Experiments with Fine-tooth Motor

This chapter presents studies of the vibro-acoustic noise of our new fine-tooth motor, and compares the results to those using the conventional motor described in Chapter 6. Advantages of low-noise and high shear stress achieved by the new fine-tooth motor design, discussed in Chapter 3, are experimentally validated in this chapter.

We discuss in the first section the control of the five-phase fine-tooth motor. The approaches towards the zero position definition, commutation algorithm, and position controller design are conceptually the same with the conventional 3-4 combination motor presented in Chapter 6. However, the practical methodologies to realize those tasks are different since the magnetic design of new motor is different from the conventional one in terms of the number of phases, winding patterns, and tooth pitch. We discuss these methodologies in detail in this chapter.

We then discuss the experimental results on the vibro-acoustic noise generated by our new motor in the next section. In order to compare the motor noise in acceleration periods to the results of the conventional motor, we present the results of our new motor to be compared with the previous data from Chapter 6. From this comparison, we observe a significant reduction on the motor noise during acceleration regions. The experimental data of the motor noise in constant velocity periods are also discussed in detail to show the effects of cogging force. We present the cogging-oriented motor noise data at different velocity levels both with non-skewed and skewed magnets, showing a significant cogging noise reduction by skewing magnets.

In addition to the motor noise reduction, our new fine-tooth motor shows higher force performance (e.g. higher shear stress) than the conventional 3-4 combination iron-core motor as discussed in Chapter 3. Experimental validation of this result is presented at end of this chapter, followed by a summary on the achievements of our new fine-tooth motor.

7.1 Control of Fine-tooth Motor

In this section, we discuss the commutation algorithm and position controller design to drive our new fine-tooth motor. For the commutation, the back EMF is used to define the zero reference position, and the five-phase commutation algorithm is implemented to generate the thrust in a desired direction. This section also presents the position controller design and its tracking performance.

7.1.1 Zero Electrical Position

In order to switch phase currents at the right moments to create a traveling stator MMF-wave, we need to know the position of the moving magnet track, thus requiring a defined zero reference position. As introduced in the previous chapter, we measure the back EMF from one of the armature coils to set the desired position for the zero reference. Our new motor armature is divided in four sections as shown in Figure 7-1. We use the phase A coils in Section#3 to measure the back EMF while moving the magnet track in the direction from Section#2 through Section#3. This is schematically illustrated in Figure 7-2, which is viewed from the cable-carrier side (top) of Figure 7-1. The phase A winding in Section#3 consists of 9 coils (coil A1 to A9) connected in series. This phase back EMF is measured while the four vertical magnets (PM#1 to #4) in the moving track pass all the 9 phase A coils. We follow the measurement steps discussed in Chapter 6, and the measured back EMF of the phase A winding with non-skewed magnets is plotted in Figure 7-3. Note that we use a reference mark in the encoder scale to set an initial zero position. We reset this initial location by the shift amount of the back EMF zero crossings so as to define our

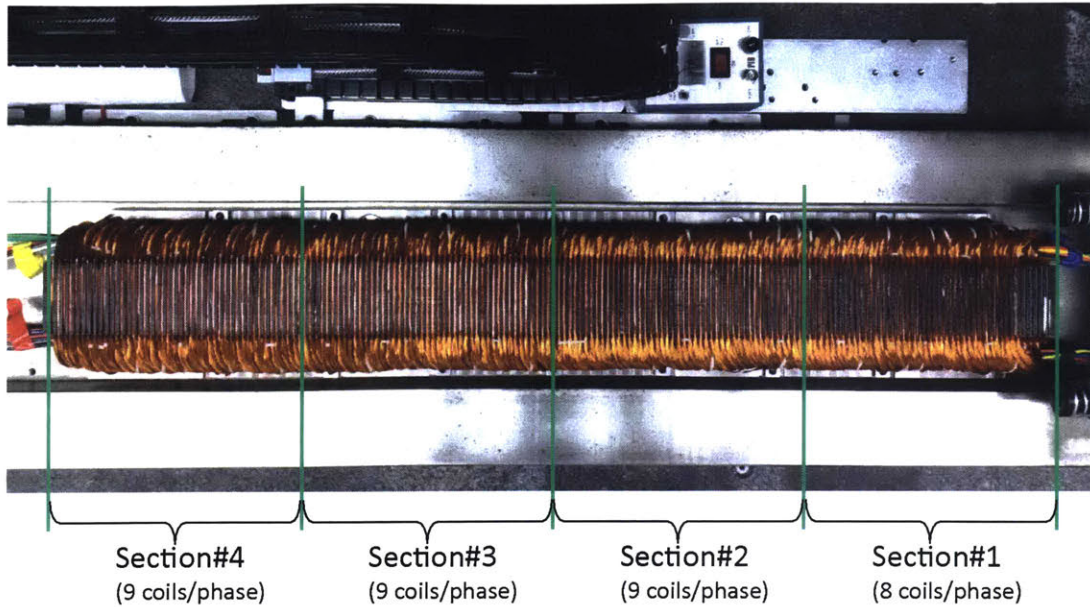


Figure 7-1: Picture of fine-tooth motor installed on the stage testbed, showing four winding sections.

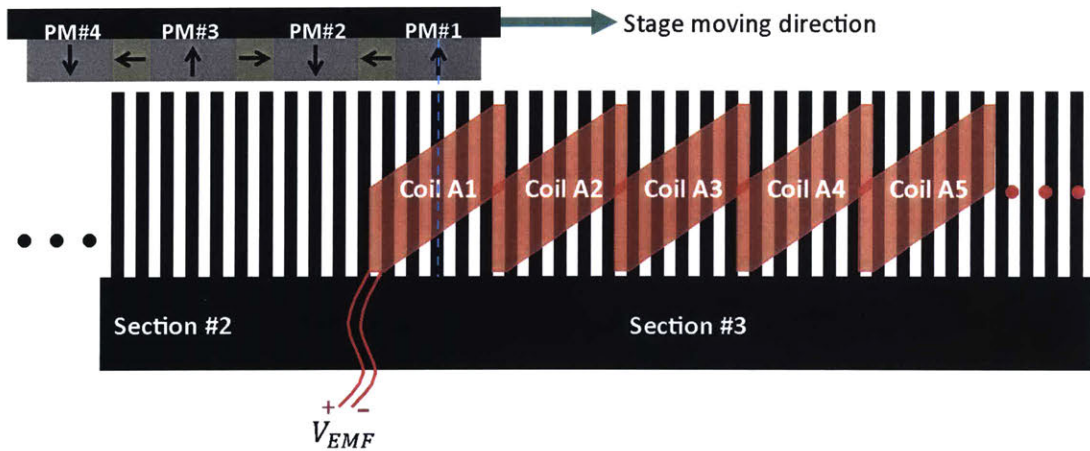


Figure 7-2: Schematic of fine-tooth linear motor lap winding configuration to measure the back EMF of the phase A coil in Section#3.

desired position to be the zero reference. In order to use this back EMF measurement to define the zero reference position, we need to first understand the measurement. To this end, we mark points of interest with circled numbers in Figure 7-3. We discuss these marks one by one below, following the notations shown in Figure 7-2.

- ① Magnet track is entering, so PM#1 starts engaging with Coil A1.

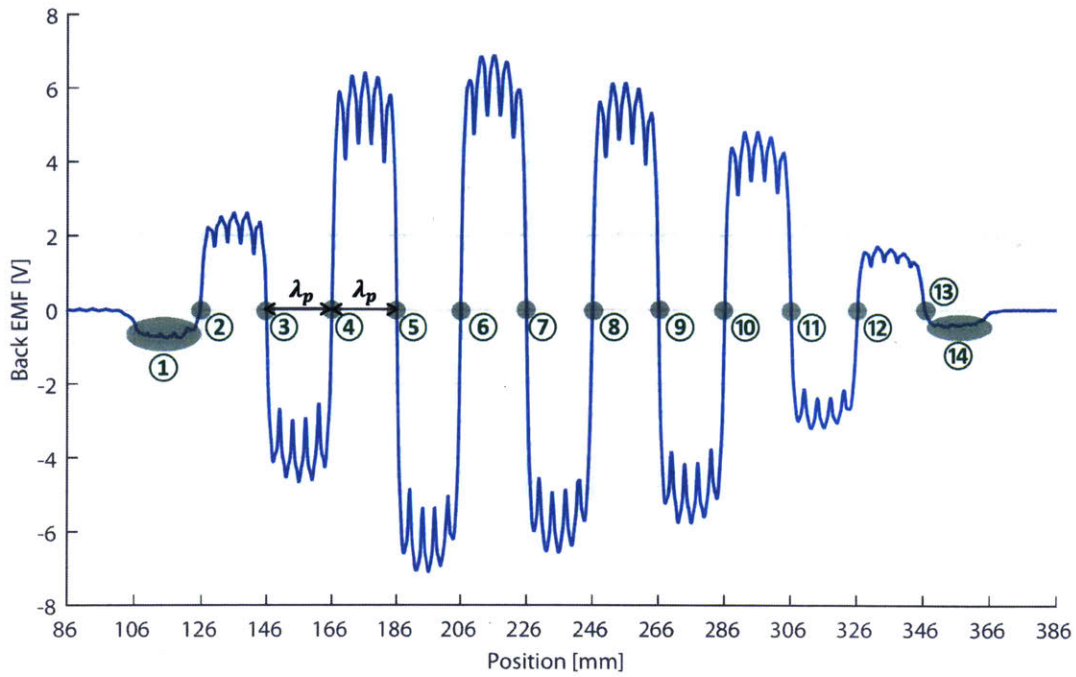


Figure 7-3: Measured back EMF of phase A coil in Section#3 of our new fine-tooth stator with non-skewed magnets, showing the zero-crossings with the interval of pole pitch, $\lambda_p = 20$ mm. Numbers in circles are discussed in text.

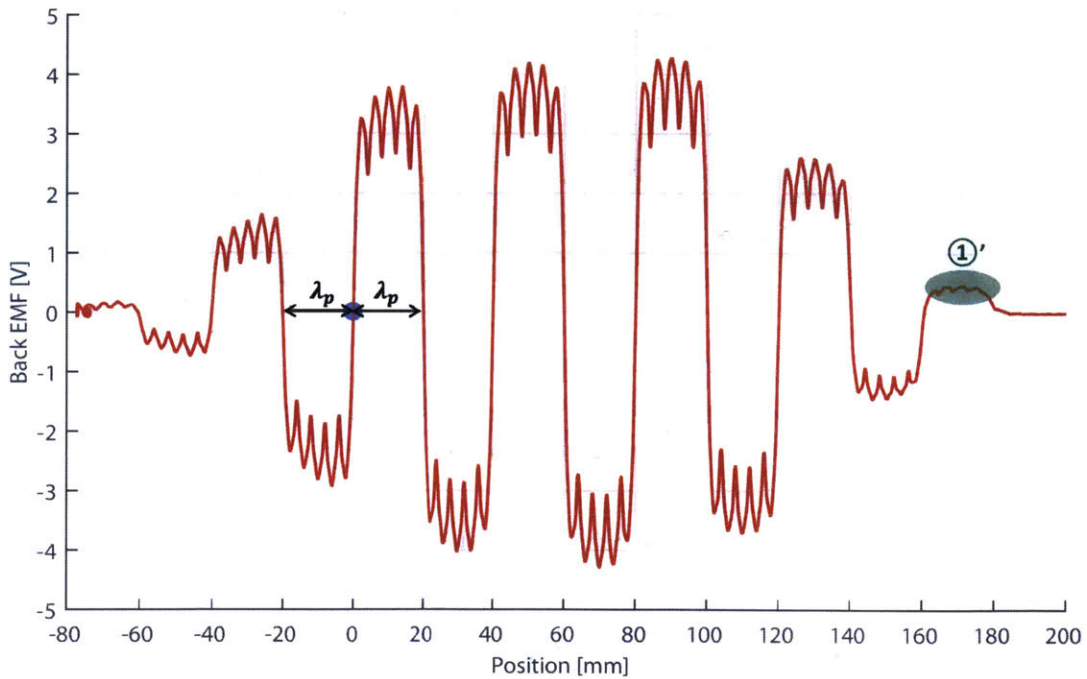


Figure 7-4: Measured back EMF of phase A coil in Section#2 after defining the desired zero reference position, which is illustrated by a blue dot.

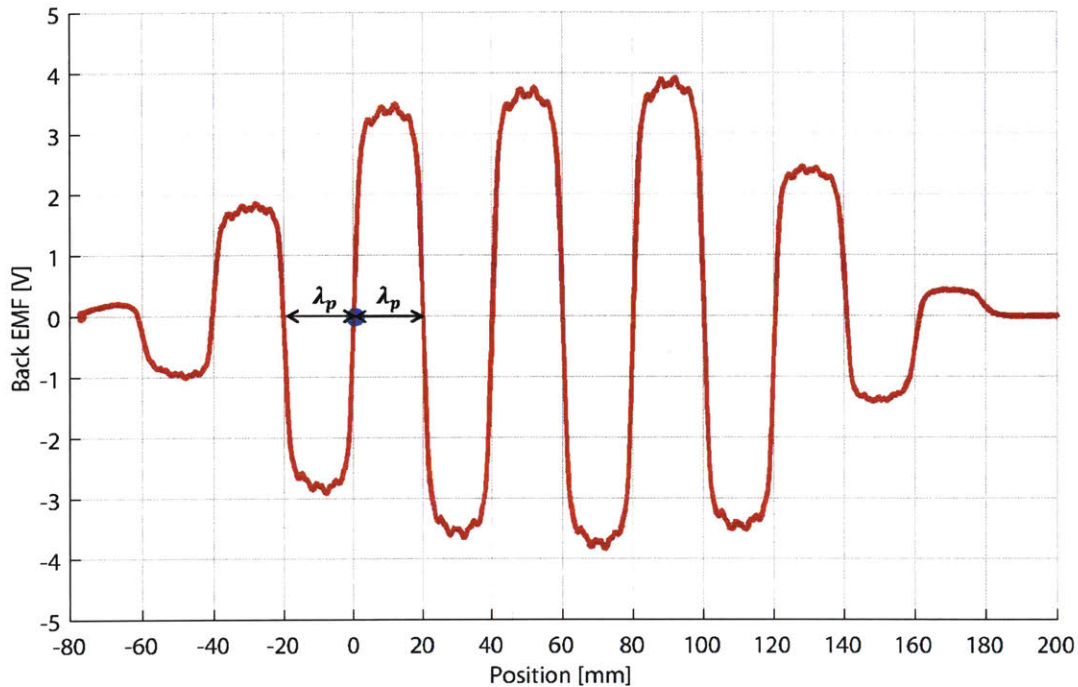


Figure 7-5: Measured back EMF of phase A coil in Section#2 with skewed magnets after defining the desired zero reference position, which is illustrated by a blue dot.

- ② PM#1 is aligned with Coil A1 as depicted in Figure 7-2.
- ③ PM#1 and #2 are aligned with Coil A1 and A2 simultaneously.
- ④ PM#1, #2, and #3 are aligned with Coil A1, A2, and A3.
- ⑤ ~ ⑩ All four magnets (PM#1 to #4) are aligned with four coils, A1-to-A4, A2-to-A5, ..., and A6-to-A9, respectively.
- ⑪ PM#2, #3, and #4 are aligned with Coil A7, A8, and A9.
- ⑫ PM#3 and #4 are aligned with Coil A8 and A9.
- ⑬ PM#4 is aligned with Coil A9.
- ⑭ Magnet track is exiting, so PM#4 gradually less engages with Coil A9.

We observe five *fingers* in every zero crossing interval in Figure 7-3, which are caused by the fine teeth engaged with non-skewed magnets. Unlike the lumped (or

shortest pitch) winding in the conventional 3-4 combination motor, we use the full-pitch winding which wraps five teeth. While a non-skewed magnet is passing each coil, it enters and exits a tooth five times, thereby yielding five local peaks resembling fingers. Note that these local peaks are not that notable with skewed magnets as can be seen in Figure 7-5.

The zero crossing distance is the same as the magnet pole pitch, $\lambda_p = 20$ mm as shown in the figure. Our desired zero position is where PM#4 is aligned with the first coil of the phase A in Section#2, as depicted in Figure 7-6. This location is 9 coils away from the zero crossing point of ⑤ in Figure 7-3. Using this, we calculate how much the initial zero position is shifted from the desired zero reference by the relation of

$$y_{\textcircled{5}} - 9 \times \lambda_c = 186 \text{ mm} - 9 \times 20 \text{ mm} = 6 \text{ mm} \quad (7.1)$$

where λ_c is the coil full-pitch distance, which is the same as the magnet pole pitch, λ_p . We reset the initial position to -6 mm so that the desired reference point is defined as zero. We measure the back EMF of phase A winding in Section#2 to confirm the zero reference, and Figure 7-4 shows the measurement. For this measurement, we move the magnet track in the opposite direction (from Section#3 through Section#2), and so the measured back EMF in Figure 7-4 is flipped. Specifically, the marked area of ①' is when the magnet track is entering the Coil A9 in Section#2. As depicted with a blue dot in the figure, we have our desired position correctly set to zero.

7.1.2 Commutation

Commutating a five-phase motor is different from a conventional three-phase motor. However, the principle is the same in that the phase currents have to be switched at the right moments to produce thrust in a desired direction. Figure 7-6 shows a magnetic configuration useful for discussion of our five-phase commutation algorithm. This configuration can be considered as a snapshot when the magnet track is located at the desired zero location, $y = 0$.

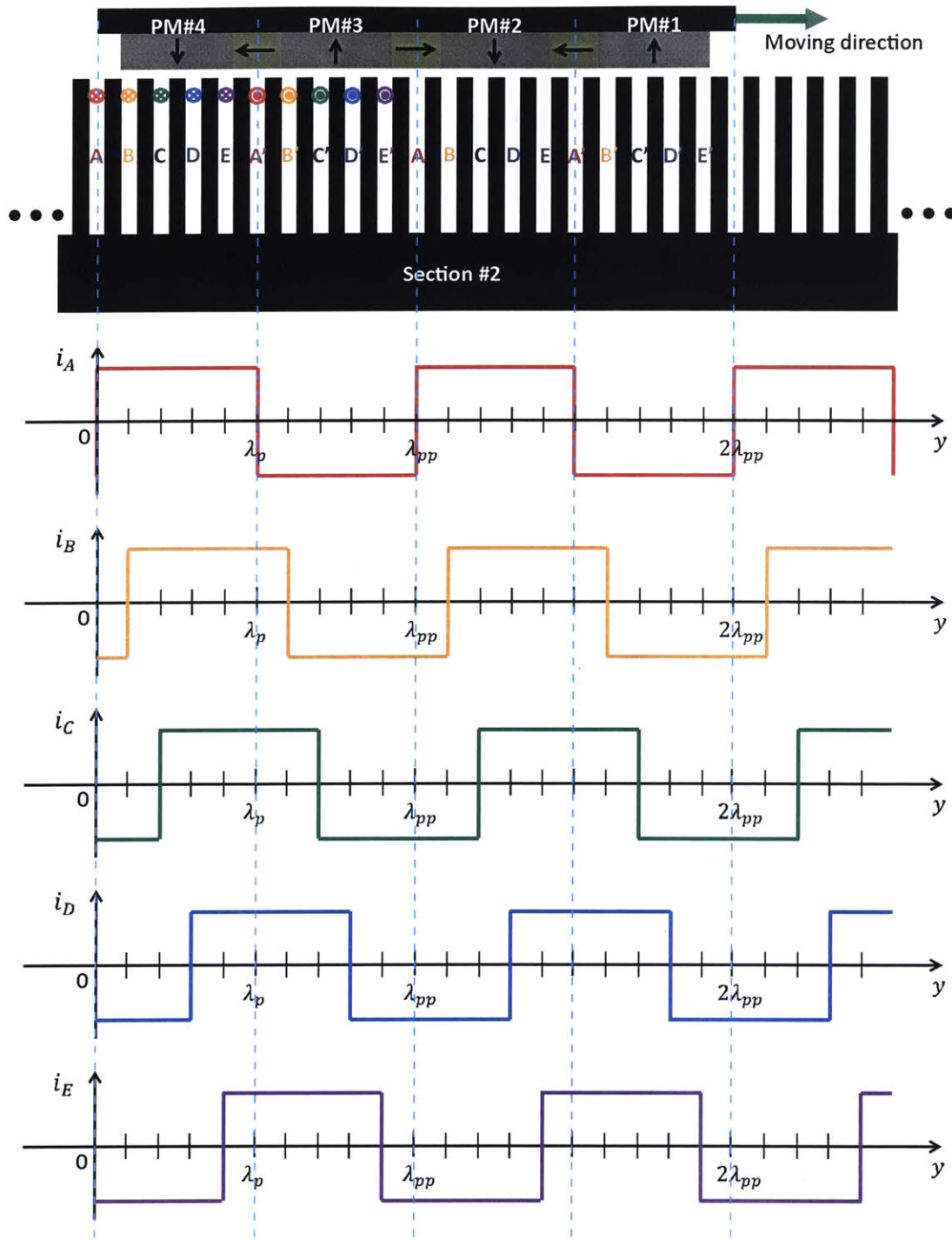


Figure 7-6: Squarewave commutation algorithm for a five-phase fine-tooth motor. Magnet track is shown at the desired zero reference position.

Parameters of A to E indicate the starting turns of the five-phase windings and A' to E' are the winding return paths. The winding directions illustrated in the figure are drawn to have rightward (+y) thrust generation on the magnet track. We can determine the force direction by the Lorentz force rule, where a magnetic force on a current-flowing conductor by a magnetic field, B is given as

$$F_{Lorentz} = lI \times B \quad (7.2)$$

where l and I are the conductor length and current vector, respectively. From (7.2), we see that the armature windings in Figure 7-6 would experience a force in leftward. Since the armature is the stationary part in our motor configuration, the opposite-direction (rightward) reaction force is exerted on the moving magnet track. At the particular moment of $y = 0$ as illustrated in the figure, the phase A current i_A instantaneously becomes zero and flips sign while the other phase currents should flow into-the-page (-) in order to generate the thrust rightward. When the magnet track is moved by the slot pitch $\lambda_s = \lambda_p/5$, the phase B current i_B should flip sign to maintain the thrust direction in +y as shown in Figure 7-6. This applies to all the other phase currents, and the plots in Figure 7-6 show this commutation algorithm for all five-phase currents in a squarewave form, which can be written as

$$\left\{ \begin{array}{l} i_A = I_p \text{square} \left(\frac{2\pi y}{\lambda_{pp}} \right) \\ i_B = I_p \text{square} \left(\frac{2\pi}{\lambda_{pp}} \left(y - \frac{\lambda_{pp}}{10} \right) \right) = I_p \text{square} \left(\frac{2\pi y}{\lambda_{pp}} - \frac{\pi}{5} \right) \\ i_C = I_p \text{square} \left(\frac{2\pi}{\lambda_{pp}} \left(y - \frac{2\lambda_{pp}}{10} \right) \right) = I_p \text{square} \left(\frac{2\pi y}{\lambda_{pp}} - \frac{2\pi}{5} \right) \\ i_D = I_p \text{square} \left(\frac{2\pi}{\lambda_{pp}} \left(y - \frac{3\lambda_{pp}}{10} \right) \right) = I_p \text{square} \left(\frac{2\pi y}{\lambda_{pp}} - \frac{3\pi}{5} \right) \\ i_E = I_p \text{square} \left(\frac{2\pi}{\lambda_{pp}} \left(y - \frac{4\lambda_{pp}}{10} \right) \right) = I_p \text{square} \left(\frac{2\pi y}{\lambda_{pp}} - \frac{4\pi}{5} \right) \end{array} \right. \quad (7.3)$$

where we define $\text{square}(\cdot) = \text{sgn}(\sin(\cdot))$. Since we have position sensors available, we can control the commutation waveforms in any desired shapes. We use both

squarewave and sinewave commutation to compare the motor noise. The sinewave commutation algorithm is given below in (7.4). The commutation algorithm is implemented in a real-time controller (National Instruments PXI-8110), and the five-phase currents are commanded to the power amplifiers. As discussed in Chapter 5, we have a total of 20 amplifiers to individually drive a total of 20 coils (5 phase coils per section \times 4 sections), so in order to implement the 5-phase commutation, the coil currents have to be assigned as $i_{1,6,11,16} = i_A$, $i_{2,7,12,17} = i_B$, $i_{3,8,13,18} = i_C$, $i_{4,9,14,19} = i_D$, and $i_{5,10,15,20} = i_E$.

$$\begin{cases} i_A = I_p \sin\left(\frac{2\pi y}{\lambda_{pp}}\right) \\ i_B = I_p \sin\left(\frac{2\pi}{\lambda_{pp}}\left(y - \frac{\lambda_{pp}}{10}\right)\right) = I_p \sin\left(\frac{2\pi y}{\lambda_{pp}} - \frac{\pi}{5}\right) \\ i_C = I_p \sin\left(\frac{2\pi}{\lambda_{pp}}\left(y - \frac{2\lambda_{pp}}{10}\right)\right) = I_p \sin\left(\frac{2\pi y}{\lambda_{pp}} - \frac{2\pi}{5}\right) \\ i_D = I_p \sin\left(\frac{2\pi}{\lambda_{pp}}\left(y - \frac{3\lambda_{pp}}{10}\right)\right) = I_p \sin\left(\frac{2\pi y}{\lambda_{pp}} - \frac{3\pi}{5}\right) \\ i_E = I_p \sin\left(\frac{2\pi}{\lambda_{pp}}\left(y - \frac{4\lambda_{pp}}{10}\right)\right) = I_p \sin\left(\frac{2\pi y}{\lambda_{pp}} - \frac{4\pi}{5}\right) \end{cases} \quad (7.4)$$

7.1.3 Position Control

We use the loop shaping technique to design a lead-lag compensator for the position control of our new fine-tooth motor. The same measuring schemes illustrated in Figure 6-6 are used to measure the frequency responses of plant and loop return ratio with the relations as in (6.5) and (6.10). The position loop we implement is schematically shown in Figure 7-7. The plant consists of the five-phase commutation algorithm, dynamics of power amplifiers with internal current controllers, and our fine-tooth motor. The encoder output is fed back to be subtracted from a reference position command, and a linear controller calculates necessary control effort, which is the current amplitude of commutation waveforms, to drive the motor to follow a given position trajectory. The position feedback loop is implemented in our real-time controller (PXI-8110) running deterministically at 10 kHz sample rate.

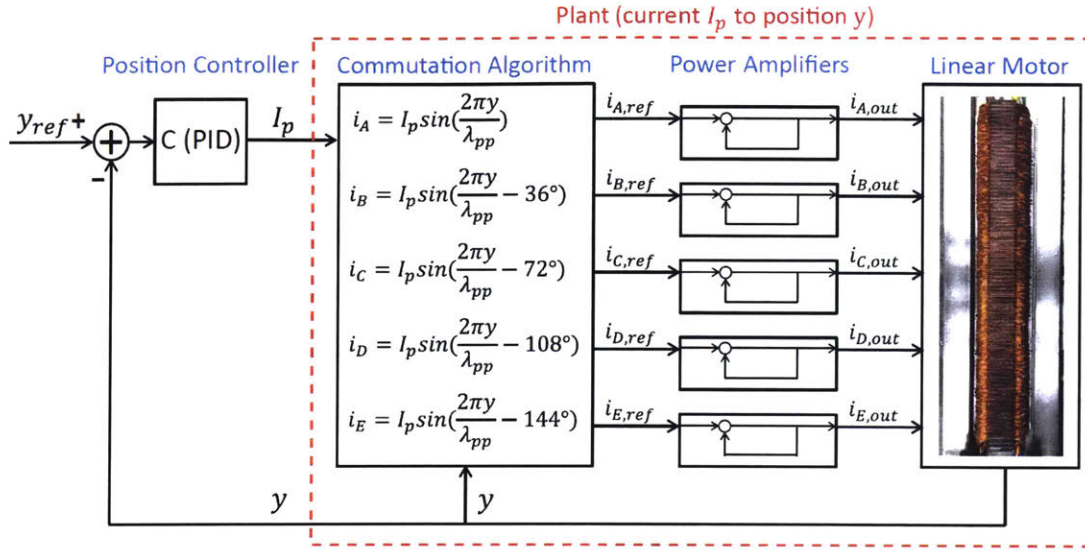


Figure 7-7: Schematic of position control loop with a plant of five-phase fine-tooth linear motor system and a PID (or lead-lag) controller.

We first measure the plant frequency response to see the plant characteristics, as shown in Figure 7-8 by the blue line with data points. There is a low-frequency resonance similar to the one observed in Figure 6-7 with the conventional motor. This low-frequency resonance is located at about 7.6 Hz. This is again due to the cogging stiffness since this plant response is measured with non-skewed magnets. In order to validate this, we perturb the stage about an equilibrium point and measure the time response as shown in Figure 7-9. The average oscillation period is about 132 msec, showing a frequency of about 7.6 Hz, consistent with what we observe from the frequency response. Note that this cogging resonance at 7.6 Hz is higher than the one at 4.5 Hz with the conventional motor. This indicates that the cogging stiffness is higher with our new motor when using non-skewed magnets.

The plant frequency response is fitted with a second order model written as

$$\begin{aligned}
 P_{model}(s) &= \frac{A}{s^2 + 2\zeta w_n s + w_n^2} e^{-\tau_d s} \\
 &\simeq \frac{6964}{s^2 + 2(0.03)(2\pi \times 7.6)s + (2\pi \times 7.6)^2} e^{-(300 \times 10^{-6})s}.
 \end{aligned} \tag{7.5}$$

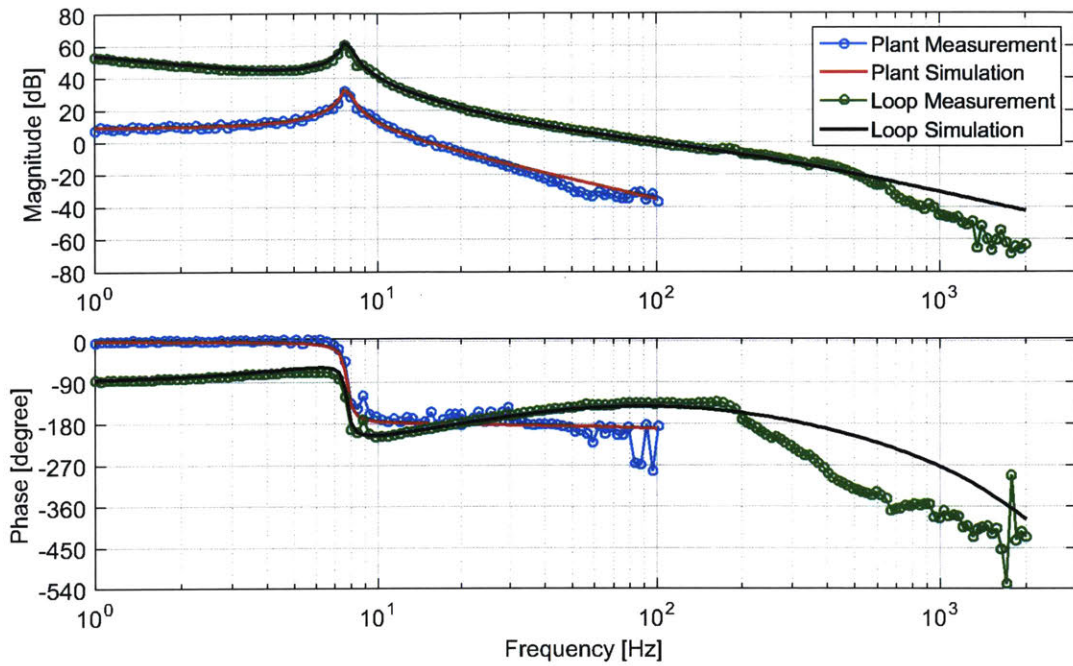


Figure 7-8: Measured and simulated frequency responses of plant and loop return ratio with the fine-tooth motor, showing a crossover frequency of about 100 Hz and a phase margin of about 45° .

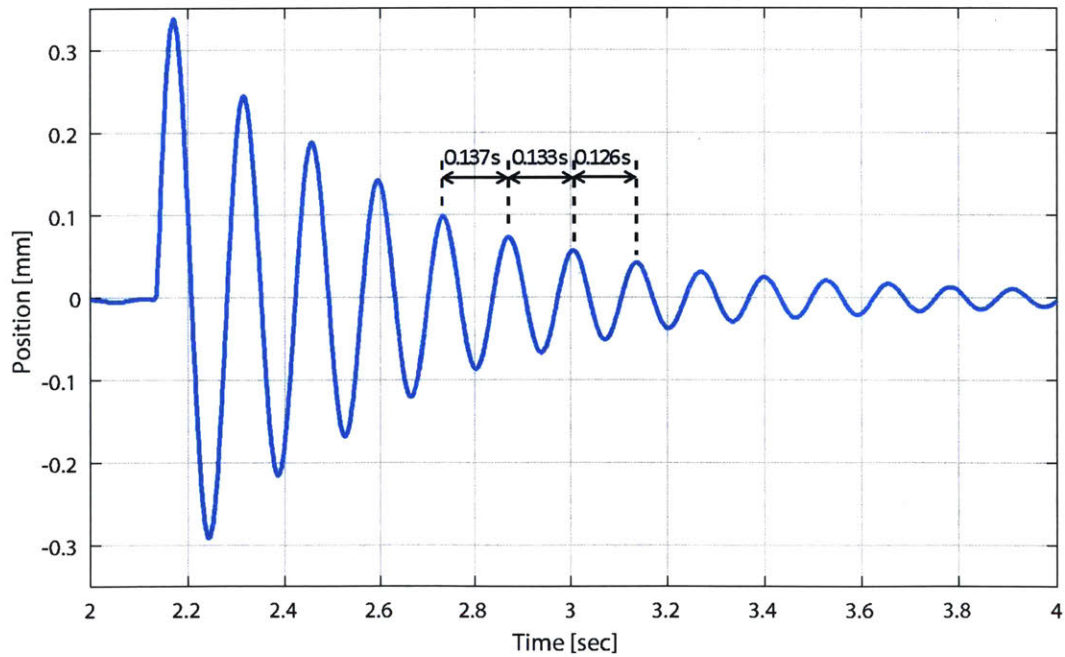


Figure 7-9: Measured time response of cogging resonance when perturbed about a stable equilibrium showing the frequency of about 7.6 Hz, consistent with the low frequency resonance observed in the measured frequency responses.

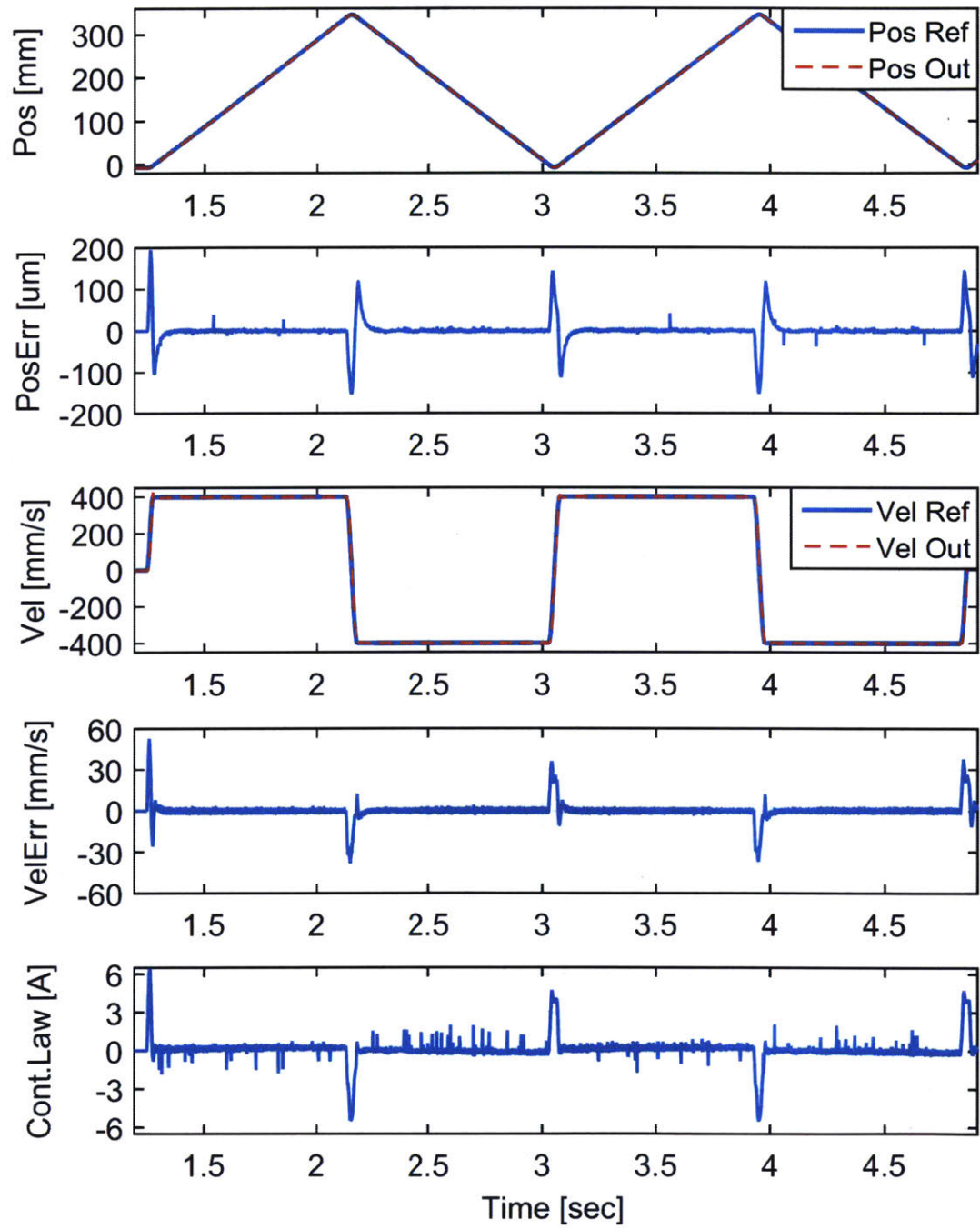


Figure 7-10: Measured tracking performance of closed position control system following a smooth trajectory with maximum acceleration of 25 m/s² and maximum velocity of 0.4 m/s.

This is plotted in Figure 7-8 with the red solid line, showing a reasonable agreement with the measured response. Based on the plant, we shape the loop return ratio to have a crossover at 100 Hz with a phase margin of 45° . We use the same controller form of (6.7) to add the phase lead of 55° at 100 Hz, so all the parameters defined in Chapter 6 are reused, except for the overall loop gain, K . The loop gain is calculated to be $K = 17.82$ to achieve the crossover at 100 Hz.

Figure 7-8 shows the measured loop return ratio with the green line with data points, and also the simulated one with the black solid line. We have the crossover at about 100 Hz with the phase margin of about 45° as designed. We conduct the tracking performance test by commanding a fourth order position trajectory with the maximum acceleration of 25 m/s^2 and maximum velocity of 0.4 m/s , traveling 350 mm back and forth. Figure 7-10 shows the overall tracking performance of our position closed-loop. Over a constant velocity region, the RMS velocity and position errors are 1.52 mm/s and $2.9 \text{ }\mu\text{m}$, respectively.

7.2 Experimental Results and Comparisons

In this section, we present extensive experimental results to show how our new fine-tooth motor outperforms the conventional 3-4 combination motor in terms of vibro-acoustic noise and force capability. We first discuss the experimental data of the vibro-acoustic noise during the acceleration and deceleration regions. In Chapter 6, significant vibro-acoustic noise is observed with the conventional motor because the generated force contains high harmonics, which excite the stage dynamics. Our fine-tooth motor, however, produces less force harmonics via its fine-tooth magnetic design. Therefore, we observe much less noise during not only acceleration regions, but also during constant velocity periods.

We also present the experimental results on the cogging-oriented and velocity-dependent noise in constant velocity regions. In this section, we compare the cogging-related noise of our new motor between the cases of non-skewed and skewed magnets, and show that our fine-tooth motor significantly reduce such noise by its magnetic

design of fine teeth. Noise measurements are compared in the form of spectrograms to show the noise difference between acceleration and constant velocity regions, and also to observe the effect of skewing magnets on the cogging noise.

In addition to the noise reduction, our new fine-tooth motor also shows higher force capability than the conventional 3-4 combination motor as discussed in Chapter 3. We present experimental validation of the force performance in this section, and conclude the chapter with a summary.

7.2.1 Vibro-acoustic Noise by Stage Dynamics

We observe in Chapter 6 that the conventional iron-core motor emits significant vibro-acoustic noise both in the acceleration and constant velocity regions, exciting the stage dynamics by high force harmonics. These experimental results are plotted in Figures 6-19 and 6-20 in terms of their associated cumulative amplitude spectra (CAS). Here, we present the vibro-acoustic noise of our new fine-tooth motor in the same manner in Figures 7-11 and 7-12 to compare the overall noise level to the conventional motor. The motor noise is measured while the stage is cycled following a fourth order position trajectory with a maximum acceleration of 25 m/s^2 and a maximum velocity of 1 m/s .

The vibrational noise during acceleration with the conventional motor (TL18 by Tecnotion) shows the average cumulated noise level of 9 m/s^2 while it is about 0.9 m/s^2 with our new fine-tooth motor. This is a significant noise reduction, namely ten to one. The acoustic noise during acceleration also shows a significant noise reduction in average from 0.253 Pa ($\approx 82 \text{ dB}$) to 0.0156 Pa ($\approx 58 \text{ dB}$), showing about 16 to 1 reduction. These significant overall noise reductions are also observed during constant velocity regions for both vibrational and acoustic noises. This is because our fine-tooth motor contains, by design, less force harmonics so that the stage dynamics are not significantly excited in either the acceleration or constant velocity region. Specifically, the major stage eigen-frequencies of 360 Hz , 500 Hz , and 630 Hz dominate the overall noise level when the stage testbed is driven by the conventional motor. However, when our new fine-tooth motor is used, these eigen-

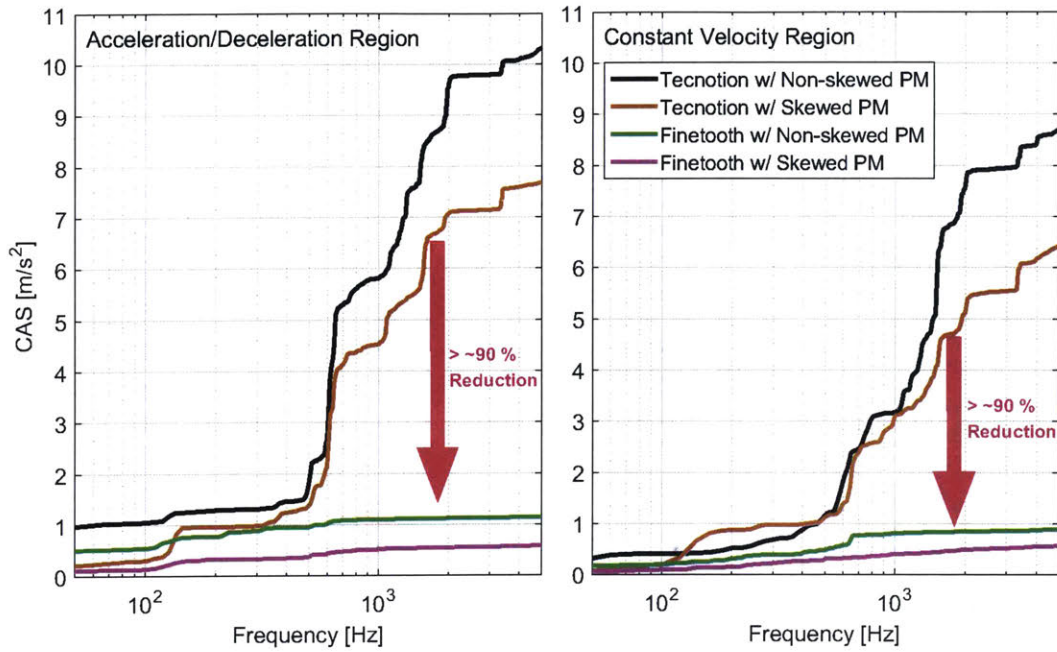


Figure 7-11: CAS comparison of accelerometer measurements between Tecnotion motor and new fine-tooth motor, showing more than average of 90 % noise level reduction. Vibrational noises are measured for a stage cycle at $A_{max} = 25 \text{ m/s}^2$ and $V_{max} = 1 \text{ m/s}$ both during acceleration (left) and constant velocity (right) regions.

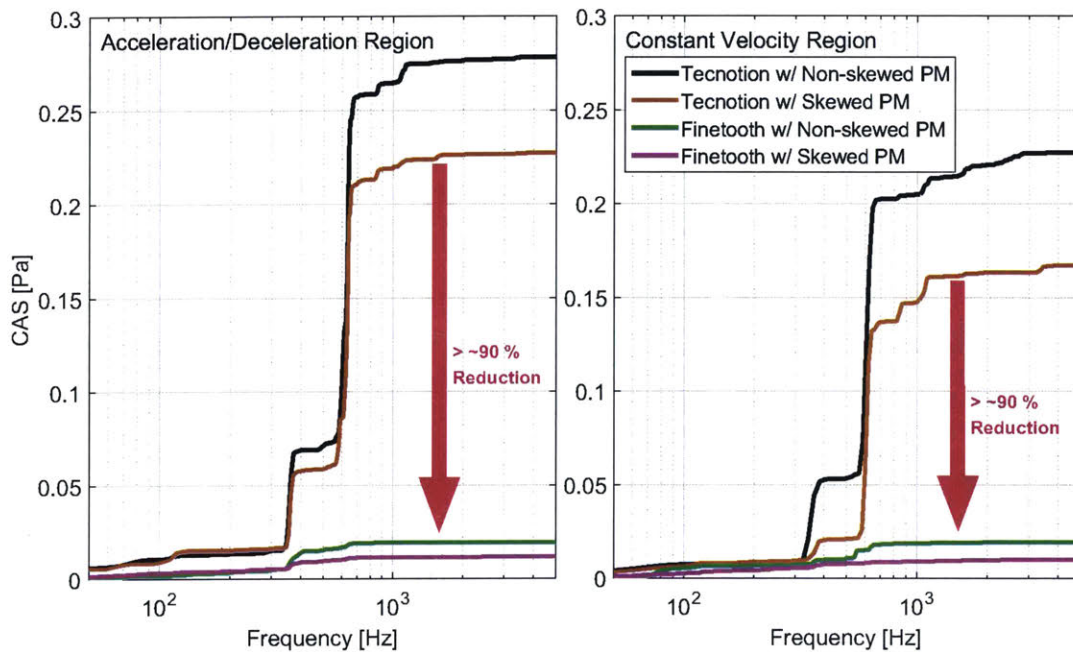


Figure 7-12: CAS comparison of microphone measurements between Tecnotion motor and new fine-tooth motor, showing more than average of 90 % noise level reduction. Acoustic noises are measured at $A_{max} = 25 \text{ m/s}^2$ and $V_{max} = 1 \text{ m/s}$ both during acceleration (left) and constant velocity (right) regions.

Case \ Output	CA of Vibration Noise (Ratio) [m/s^2]		CA of Acoustic Noise (Ratio) [Pa, dB]	
	Acc./Decel. Region	Const. Vel. Region	Acc./Decel. Region	Const. Vel. Region
Tecnotion w/ Non-skewed PM	10.31 (1)	8.71 (0.84)	0.278 \approx 83dB (1)	0.228 \approx 81dB (0.82)
Tecnotion w/ Skewed PM	7.67 (0.74)	6.41 (0.62)	0.227 \approx 81dB (0.82)	0.167 \approx 78dB (0.60)
Finetooth w/ Non-skewed PM	1.14 (0.11)	0.89 (0.09)	0.019 \approx 60dB (0.07)	0.019 \approx 60dB (0.07)
Finetooth w/ Skewed PM	0.58 (0.06)	0.56 (0.05)	0.012 \approx 55dB (0.04)	0.010 \approx 54dB (0.04)

Figure 7-13: Overall noise level comparison for both vibrational and acoustic noises in all four motor cases experimented at $A_{max} = 25 \text{ m/s}^2$ and $V_{max} = 1 \text{ m/s}$. Ratio is presented for each noise with a reference level (1) of Tecnotion with non-skewed PM during an acceleration region.

modes are less excited as can be seen by the smaller jumps at those frequencies from the CAS's in Figures 7-11 and 7-12. We also observe that the overall noise level is smaller with skewed magnets. This is because skewing magnets i) helps reduce the cogging and ii) serves as a low-pass-filter for the rotor MMF to have less harmonics.

In Figure 7-13, we show a table of the cumulated noise levels during both acceleration and constant velocity regions for each of all four cases of motor types. Note that the cumulative amplitude (CA) of vibrational noise has units of [m/s^2], and the acoustic noise is in [Pa] and [dB]. The decibel value in blue indicates the sound pressure level (SPL) calculated with respect to a reference pressure, $P_{ref} = 20 \mu\text{Pa}$. For instance, if we compare the acoustic noise level between the conventional motor (by Tecnotion) and our fine-tooth motor both with non-skewed PM, the sound pressure level is decreased from 83 dB to 60 dB. Qualitatively speaking, this is the noise difference between a truck passing by and a quiet office, i.e., a large reduction. The table also shows ratio values within parentheses. For both vibrational and acoustic noises, the case of Tecnotion with non-skewed PM during an acceleration region is used as the reference. For example, the fine-tooth motor with skewed magnets has the vibrational noise reduction of 94 % compared to the Tecnotion motor with non-skewed magnets (\therefore ratio of 1 to 0.06).

We summarize our observations from the experimental results as below.

- Our fine-tooth motor shows a significant vibro-acoustic noise reduction of 90 % in average compared to the conventional 3-4 combination motor.
- The stage dynamics are significantly less excited with our new motor because the fine-tooth motor design produces smoother stator and rotor MMF's, thereby generating much less force harmonics.
- Overall noise level is smaller with skewed magnets because i) skewing reduces the cogging and ii) skewing can serve as low-pass-filtering the rotor MMF so that it contains less harmonics.
- Unlike the case with the conventional motor, our fine-tooth motor shows a clear distinction of the vibro-acoustic noise between acceleration and constant velocity regions. We discuss these details in Section 7.2.2 below.

7.2.2 Vibro-acoustic Noise by Cogging Force

We discuss the vibro-acoustic noise of our fine-tooth motor by the cogging force in this subsection. The experimental data are obtained while cycling the stage at various speeds with both the non-skewed and skewed magnets. With non-skewed magnets, the cogging-related noise is observed to be dominant during constant velocity regions. The cogging, however, can be eliminated by skewing magnets, and so we observe that the cogging-related noise becomes significantly reduced with skewed magnets.

Specifically, the stage is cycled following velocity profiles with a maximum acceleration of 45 m/s^2 and different velocities from 1.6 m/s to 2.4 m/s for the cogging-related noise experiments. Thus the cogging noise frequencies will scale with this speed. According to the relationship written in (7.6), we expect the cogging-oriented noise at 400 Hz to 600 Hz , respectively. Note that (7.6) is the same as (6.14), but n is chosen to be 1 since the fundamental is the major cogging component in our fine-tooth motor. Also, the cogging period, λ_{cogging} is shorter since we have a fine tooth pitch, λ_t in our new motor design.

$$f_{cogging} = \frac{v_c}{\lambda_{cogging}} = \frac{v_c}{\lambda_t} \quad (7.6)$$

We present the experimental results with the non-skewed magnets first where the cogging noise, $f_{cogging}$ is expected to be dominantly observed. We then show the test results with the skewed magnets to discuss the effect of skewing magnets on the vibro-acoustic noise over constant velocity periods. Spectrograms are used for the noise comparison. We can observe in the spectrograms the noise behavior difference between acceleration and constant velocity regions.

Noise with Non-skewed Magnets

We first discuss the cogging-oriented and velocity-dependent vibro-acoustic noise with the non-skewed magnets. Cogging can be considered as a force disturbance which the moving stage experiences. This is the major force component during constant velocity regions, since the motor coil current is low in these regions. Since the cogging is a periodic and fluctuating force, it vibrates the stage at a certain frequency which scales with the stage velocity, as given in (7.6). Figure 7-14 shows the measured cogging (red line) and the simulated cogging by FEM (blue line) in both the normal (Z) and tangential (Y) directions. Their spatial spectra are compared in Figure 7-15. The cogging curves agree well with each other. However, we see from both figures that the actual measurement has smaller amplitude than the calculated one. We speculate that this discrepancy may come from two reasons. One is that there might be some misalignment in the actual hardware assembly such that the motor air gap distance and the skew angle are different from their nominal values of 550 μm and 0° (for non-skewed magnets), respectively. Another possible reason is the magnetic end effects in the cross-scan direction (X). The finite element simulation model is in 2D so that the end effects in the scan direction (Y) are considered, but are not considered in the cross-scan direction. This also might cause the cogging amplitude difference. Except for this discrepancy, the measured cogging behaves as expected from the simulation. The fundamental cogging period is the tooth pitch, $\lambda_t = 4 \text{ mm}$ and the fundamental

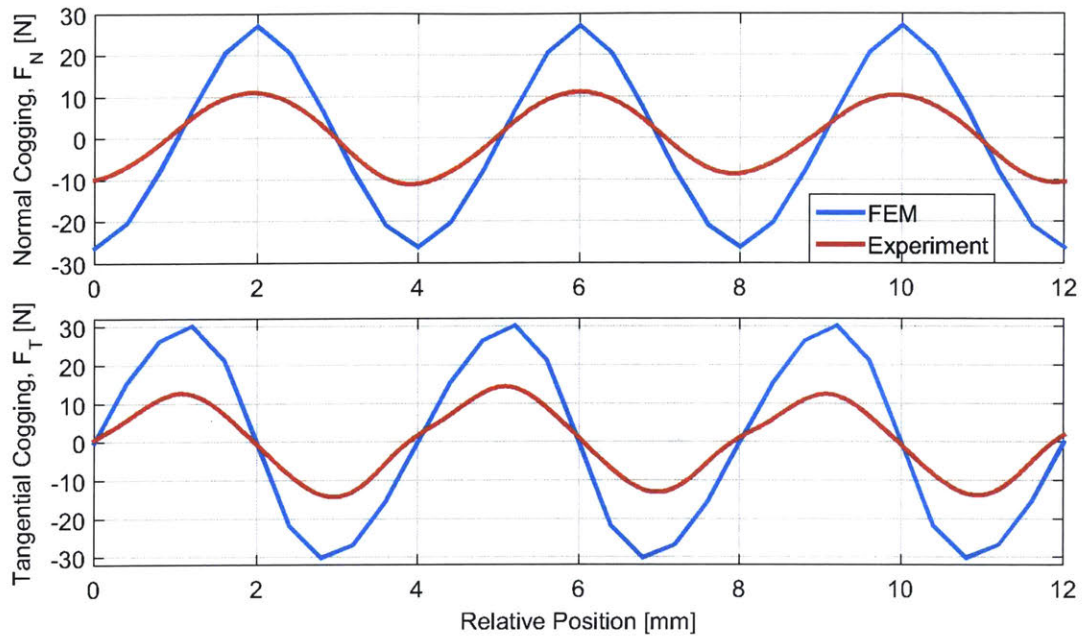


Figure 7-14: Cogging force comparison between FEM simulation and experiment, both with non-skewed magnets. Cogging fundamental period of a tooth pitch, $\lambda_t = w_t + w_s = 4$ mm.

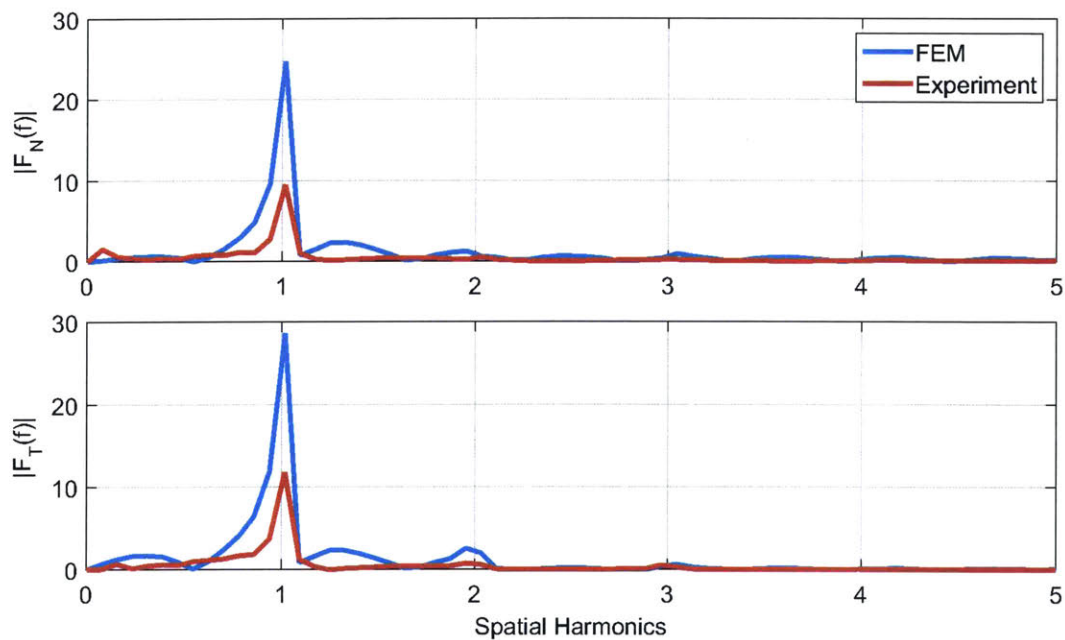


Figure 7-15: Spatial spectrum comparison of cogging force between FEM simulation and experiment, both with non-skewed magnets. Major component is the fundamental, as expected.

is the sole and major component without any notable harmonics, in both Z and Y directions, as illustrated in the spatial spectrum in Figure 7-15.

In order to observe the vibro-acoustic noise caused by this cogging force, we measure both vibrational and acoustic noises while cycling the stage at the same acceleration of $A_{max} = 45 \text{ m/s}^2$ with three different levels of velocity at $V_{max} = 1.6 \text{ m/s}$, 2.0 m/s , and 2.4 m/s . The measured data are post-processed to obtain spectrograms where we can see the time-varying spectrum of frequencies. Figures 7-16 to 7-21 show the spectrogram comparisons of both Z- and X-direction vibro-acoustic noises for the constant velocities of 1.6 m/s , 2.0 m/s , and 2.4 m/s , respectively. For all figures, the spectrogram of accelerometer data is on the left side while microphone data is on the right side. All the spectrograms are during a half cycle of acceleration, constant velocity, and deceleration. The corresponding velocity profile is depicted in white at the bottom of the figure for each spectrogram. Since we cycle the stage with the fixed travel range of 350 mm , time and travel lengths for the constant velocity region become shorter for the higher velocity. The color map in the spectrograms is logarithmic, showing the power spectra of vibrational and acoustic noises in the units of $(\text{m/s}^2)^2$ and dB , respectively. Note that the decibel unit indicates the sound pressure level (SLP) with respect to a reference pressure of $20 \mu\text{Pa}$.

Unlike the motor noise data of the conventional 3-4 combination motor shown in Chapter 6, we observe a clear distinction between acceleration and constant velocity regions as shown in the all figures of spectrograms. For example, from the Z-direction vibro-acoustic noise measurements in Figure 7-16, we observe the stage dynamics excitations at around 360 Hz , 500 Hz , and 630 Hz during acceleration and deceleration regions while the cogging-oriented noise at 400 Hz dominates the noise over the constant velocity period without much of the stage eigen-modes excited. In fact, when we perform the cycle experiments, we clearly hear almost a pure tone of cogging frequency acoustic noise during a constant velocity period. We also see the resemblance between spectrograms of accelerometer and microphone data, validating the noise mechanism of the stage vibration radiating the acoustic noise. The distinction between acceleration and constant velocity regions holds for all cases of

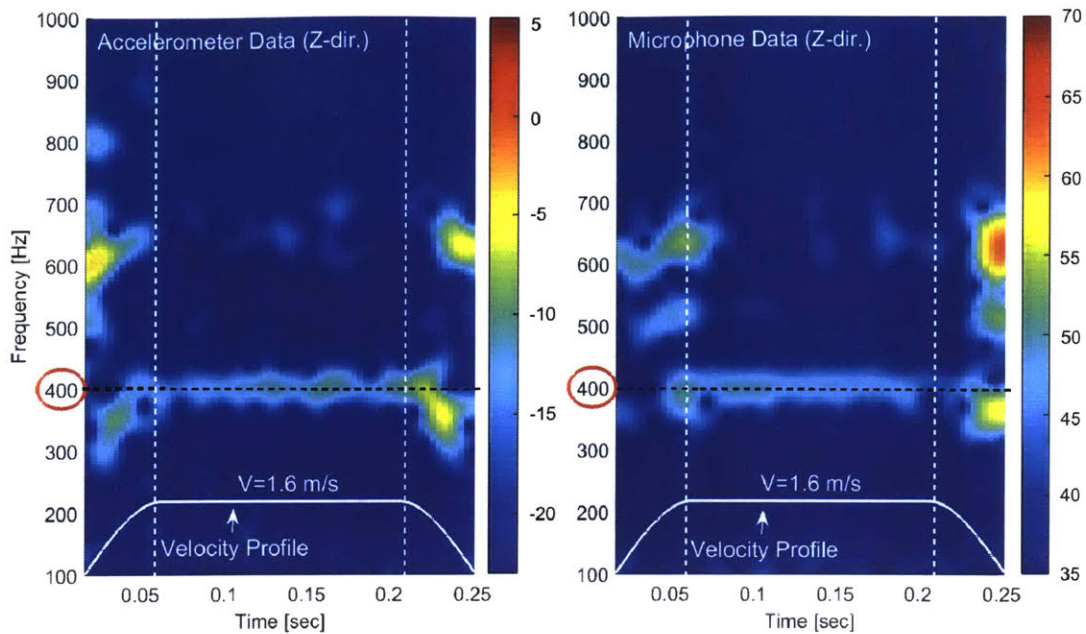


Figure 7-16: Spectrogram comparison of vibrational (left) and acoustic (right) noises of our new fine-tooth motor in Z-direction during a half cycle with $A_{max} = 45 \text{ m/s}^2$ and $V_{max} = 1.6 \text{ m/s}$, showing clear distinction between acceleration and constant velocity regions. Note cogging-driven noise at 400 Hz.

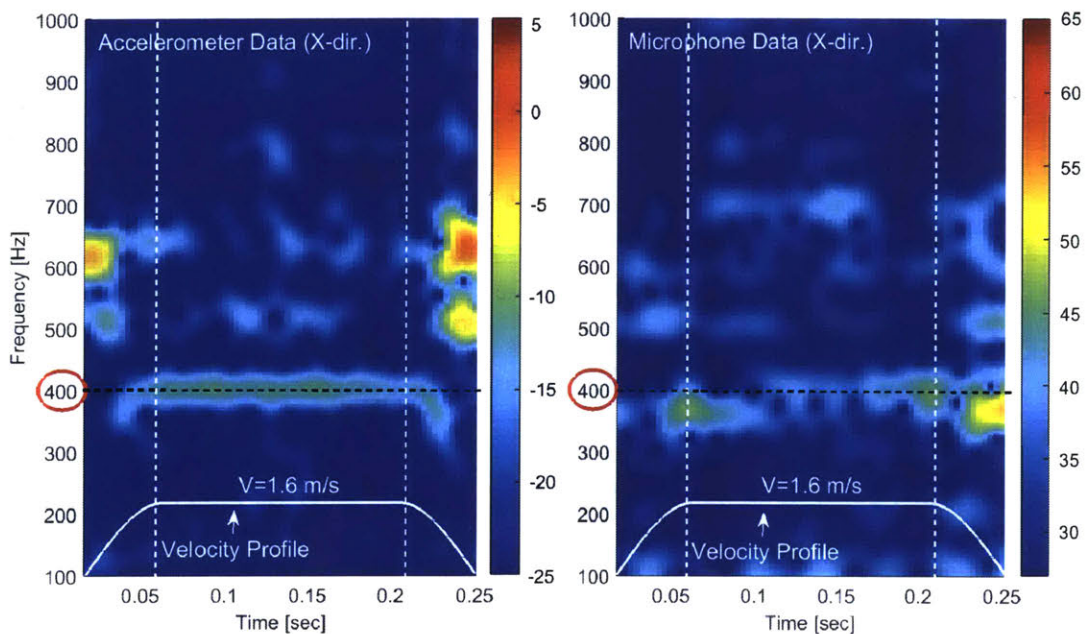


Figure 7-17: Spectrogram comparison of vibrational (left) and acoustic (right) noises of our new fine-tooth motor in X-direction during a half cycle with $A_{max} = 45 \text{ m/s}^2$ and $V_{max} = 1.6 \text{ m/s}$, showing clear distinction between acceleration and constant velocity regions. Note cogging-driven noise at 400 Hz.

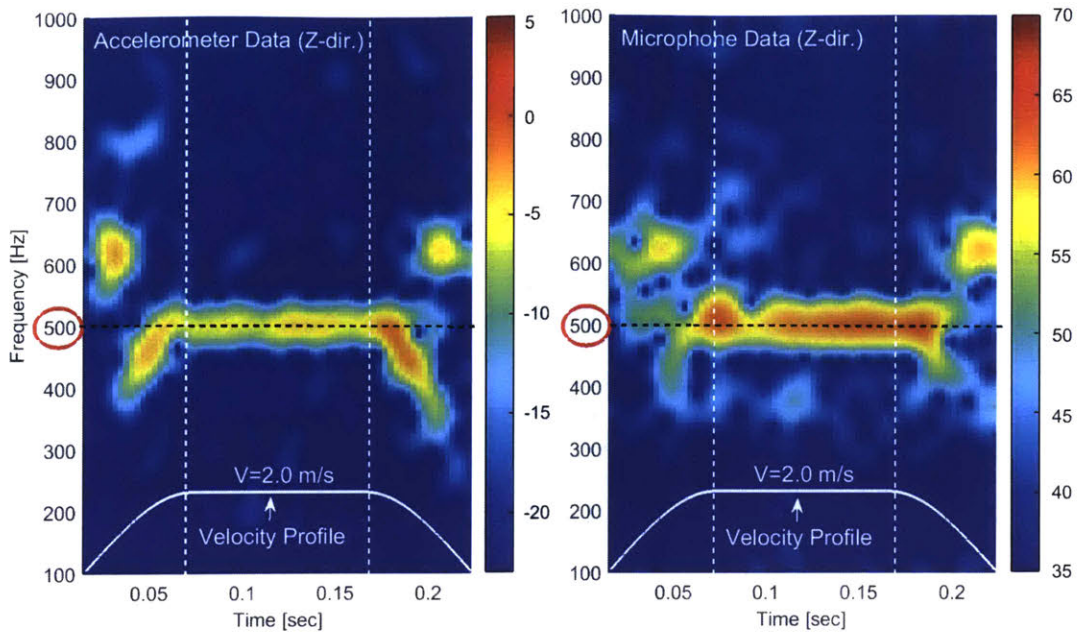


Figure 7-18: Spectrogram comparison of vibrational (left) and acoustic (right) noises of our new fine-tooth motor in Z-direction during a half cycle with $A_{max} = 45 \text{ m/s}^2$ and $V_{max} = 2.0 \text{ m/s}$, showing clear distinction between acceleration and constant velocity regions. Note cogging-driven noise at 500 Hz.

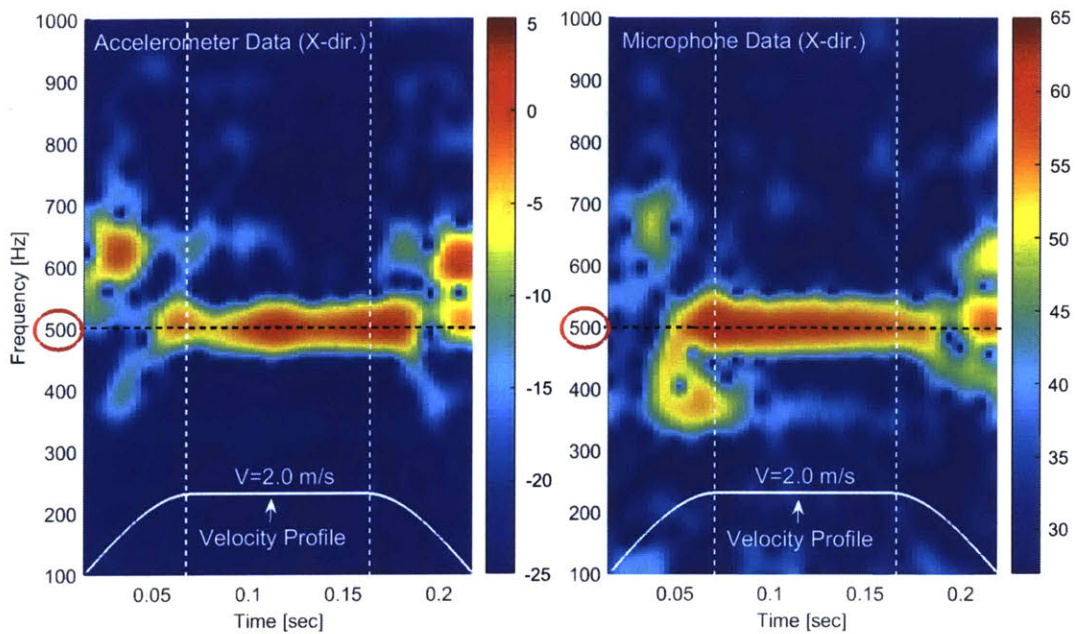


Figure 7-19: Spectrogram comparison of vibrational (left) and acoustic (right) noises of our new fine-tooth motor in X-direction during a half cycle with $A_{max} = 45 \text{ m/s}^2$ and $V_{max} = 2.0 \text{ m/s}$, showing clear distinction between acceleration and constant velocity regions. Note cogging-driven noise at 500 Hz.

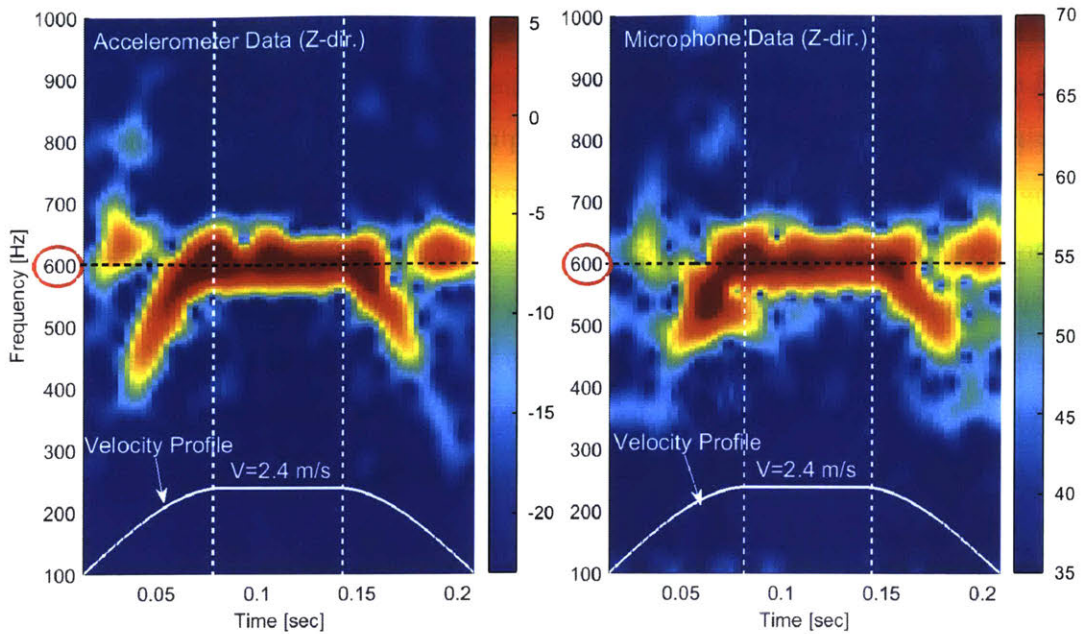


Figure 7-20: Spectrogram comparison of vibrational (left) and acoustic (right) noises of our new fine-tooth motor in Z-direction during a half cycle with $A_{max} = 45 \text{ m/s}^2$ and $V_{max} = 2.4 \text{ m/s}$, showing clear distinction between acceleration and constant velocity regions. Note cogging-driven noise at 600 Hz.

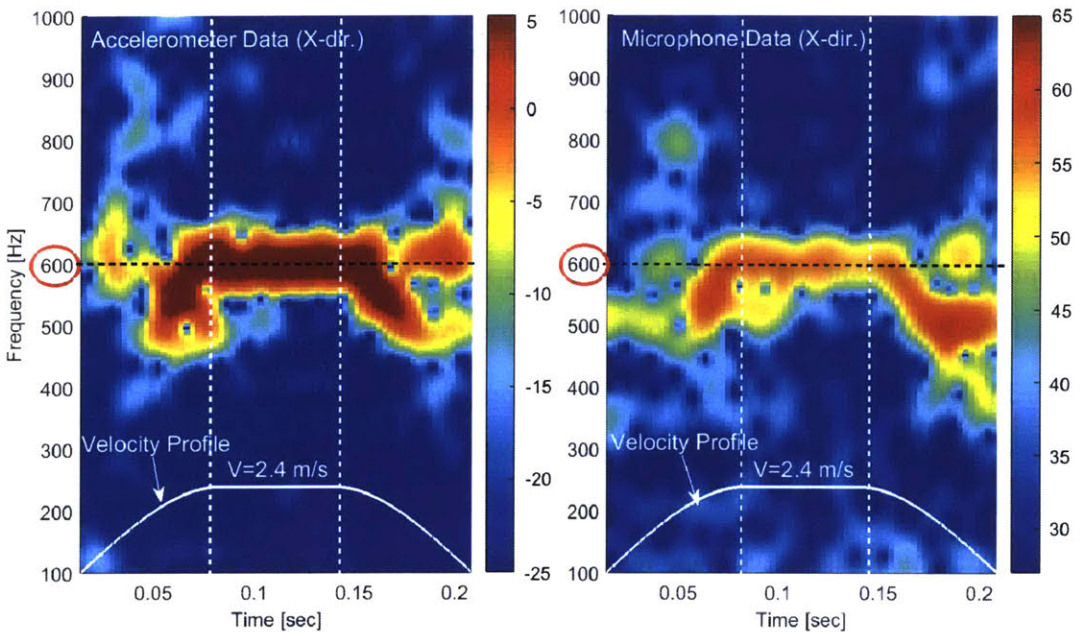


Figure 7-21: Spectrogram comparison of vibrational (left) and acoustic (right) noises of our new fine-tooth motor in X-direction during a half cycle with $A_{max} = 45 \text{ m/s}^2$ and $V_{max} = 2.4 \text{ m/s}$, showing clear distinction between acceleration and constant velocity regions. Note cogging-driven noise at 600 Hz.

velocities as shown in the figures. As expected by (7.6), the experimental results also show the velocity dependency of the cogging noise in that the noises over constant velocity regions are located at varying frequencies of 400 Hz, 500 Hz, and 600 Hz for the velocities of 1.6 m/s, 2.0 m/s, and 2.4 m/s, respectively. Note that we also notice the intensity difference of the cogging-oriented noises depending on the velocity level. For example, the cogging noise at 600 Hz for 2.4 m/s in Figure 7-20 shows higher amplitude (~ 70 dB) than the noise at 400 Hz for 1.6 m/s in Figure 7-16 (~ 50 dB). This is because the noise amplitude is amplified when its frequency becomes closer to an eigen-frequency, which is the bending-mode frequency of 630 Hz in our case.

The experimental data validate that the cogging force vibrates the stage at a certain frequency depending on the stage velocity, and this is the dominant motor noise source during a constant velocity region. Conversely, it is the stage dynamics excitation that dominates the motor noise during acceleration. The velocity dependency of this cogging-oriented noise is also observed from the spectrograms at various velocities. In order to show these aspects at a quick glance, we present another experimental data set. For this test, we command the stage to follow a trajectory with an increasing constant velocity level at each cycle, namely from 1.6 m/s to 2.2 m/s by 0.2 m/s while measuring the vibro-acoustic noise along the cycles. The spectrogram obtained from this measurement with non-skewed magnets is shown in Figure 7-22 with the velocity profile overlapped in white. The bright regions in the figure illustrate the constant velocity regions. This spectrogram is from the microphone data, and the color map shows the sound pressure level in dB.

In the spectrogram, we observe the cogging-oriented noise dominating the constant velocity regions (brighter portions) at increasing frequencies of 400 Hz, 450 Hz, 500 Hz, and 550 Hz for 1.6 m/s, 1.8 m/s, 2.0 m/s, and 2.2 m/s, respectively. When we hear this noise in person, it sounds as if the stage plays a musical scale with increasing pitch. Note that we observe again that the cogging noise intensity increases when the cogging noise frequency becomes closer to the eigen-frequency of 630 Hz, as discussed earlier. During acceleration and deceleration regions (darker portions), on the other hand, the stage dynamics noise is dominant at 360 Hz, 500 Hz, and 630

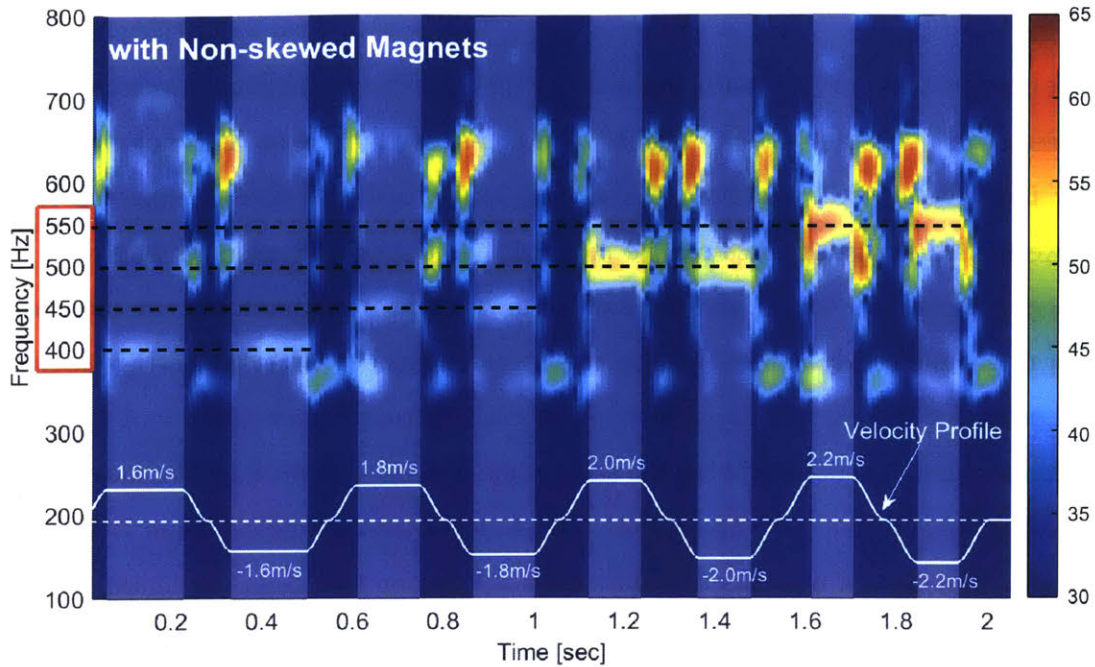


Figure 7-22: Spectrogram of acoustic noise of new fine-tooth motor with non-skewed magnets during an increasing-velocity cycles with $A_{max} = 45 \text{ m/s}^2$ and $V_{max} = 1.6 \text{ m/s}$ to 2.2 m/s , showing cogging-oriented and velocity-dependent noise during constant velocity regions. Note varying frequency cogging-driven noise at 400, 500, and 550 Hz.

Hz. The cogging noise is not observed during these acceleration regions because i) the travel length for an acceleration region is short and ii) velocity changes over such a region so the temporal frequency of cogging force is distributed over a wide range, not concentrated on one frequency. Another interesting observation found during acceleration and deceleration regions is the zero-noise points. At every half cycle, the velocity flips its sign as shown from the velocity profile in white in Figure 7-22. At those points of sign-flipping, the velocity and acceleration instantaneously become zero, meaning the momentary stop of the moving stage. We observe no noise at those points, which supports our hypothesis that the motor acoustic noise comes from the moving part vibrated by magnetic force fluctuations.

Noise with Skewed Magnets

We observe that our fine-tooth motor shows the cogging-oriented and velocity-dependent noise during constant velocity regions with non-skewed magnets. This noise is caused by the cogging force vibrating the moving stage, and therefore is expected to be lowered if the cogging force can be reduced. We use skewed magnets to reduce the cogging force. Due to the advantage of having the fine tooth pitch, we can reduce the cogging significantly without compromising the thrust by slightly skewing magnets. In order for the skewed magnets to span the full tooth pitch of $\lambda_t = 4$ mm with 52mm-long magnets, we choose the skew angle of $\text{atan}(4/52) \approx 4.4^\circ$. We measure the cogging force of our new motor with the skewed magnets and compare it with the case of non-skewed magnets in Figure 7-23. As can be seen from the figure, skewing significantly reduces the cogging in both the normal and tangential directions. Specifically, the peak-to-peak amplitudes are reduced from 22.26 N (normal) and 28.62 N (tangential) to 2.22 N and 2.99 N, respectively. This is about a 10-to-1 reduction in both directions. In theory, the cogging can be completely eliminated if we skew magnets to span one full tooth pitch. However, the actual cogging measurement shows a bit of residual force. This might be due to any possible misalignment in the hardware assembly and also to the magnetic end effects in the cross-scan X-direction.

The cogging reduction with the skewed magnets leads to associated noise reduction. In order to observe this and compare the results with those using non-skewed magnets, we measure both the vibrational and acoustic noises while the stage testbed is cycled with the same trajectories at $A_{max} = 45 \text{ m/s}^2$ with $V_{max} = 1.6 \text{ m/s}$, 2.0 m/s , and 2.4 m/s . Spectrograms of the vibro-acoustic noises are compared between the non-skewed and skewed magnets at these three velocity levels. Figures 7-24 to 7-29 show these comparisons with the non-skewed PM cases in the left side and the skewed PM cases in the right side for all figures. The corresponding velocity profile is again overlapped in white to show the constant velocity region for each case.

In Figures 7-24 and 7-25 with the non-skewed magnets, we observe the cogging noises in both accelerometer and microphone data at the expected frequency of 400

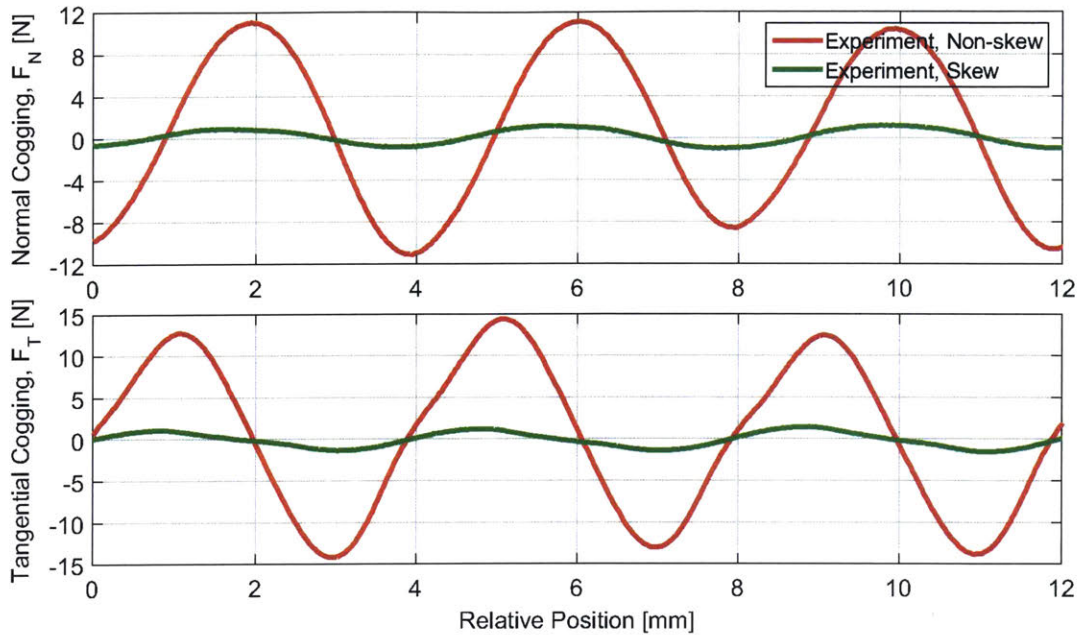


Figure 7-23: Fine-tooth motor cogging force measurement comparison between non-skewed and skewed magnets, showing significant reduction in cogging with skewing. Cogging fundamental period equals a tooth pitch, $\lambda_t = w_t + w_s = 4$ mm.

Hz during the constant velocity region. However, when the skewed magnets are used, these cogging noises are almost completely eliminated as shown in the right side of figures, thereby leaving almost no significant noise during the constant velocity region. In fact, when the stage is cycled with the skewed magnets, we hear less noise in constant velocity regions. In the acceleration and deceleration regions, however, we observe the noises from the stage dynamics excitations. From the figures, we see that the same stage eigen-modes are excited either with the non-skewed or the skewed magnets. We speculate that even this noise during acceleration can be greatly reduced if we configure our fine-tooth motor in a double-sided configuration, thereby canceling out the normal forces. We propose a future study on this subject, which is discussed in Chapter 8.

For the higher velocity of 2.4 m/s, we observe some cogging-noise even with the skewed magnets as shown in Figures 7-28 and 7-29. This is due to the facts that i) there is a cogging residual even after skewing the magnets as shown with our cogging

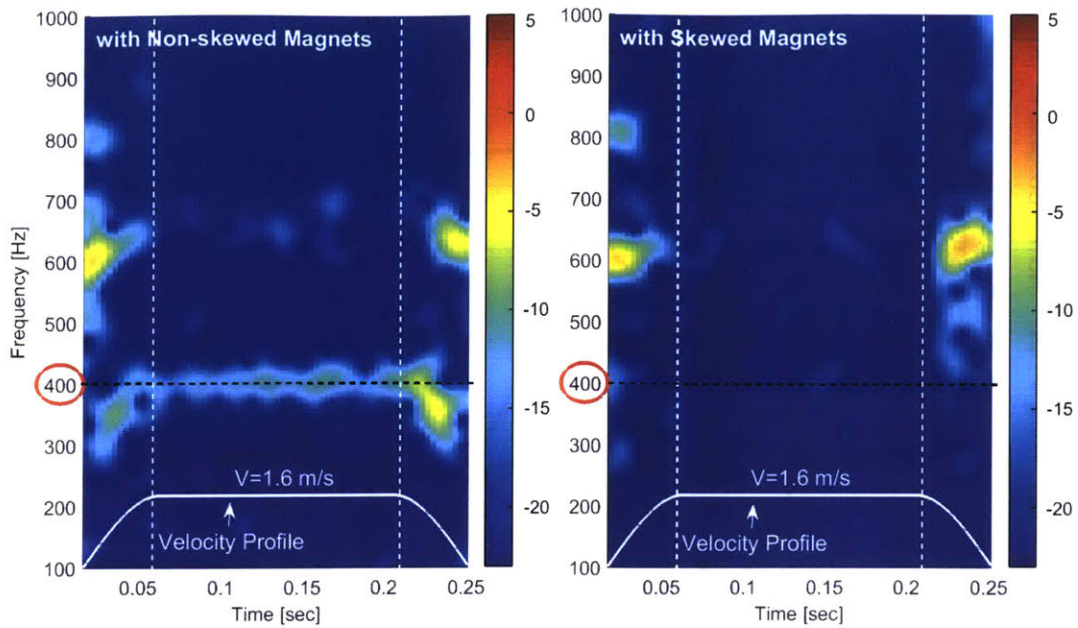


Figure 7-24: Spectrogram comparison of vibrational noises of our new fine-tooth motor between non-skewed (left) and skewed (right) magnets during a half cycle with $A_{max} = 45 \text{ m/s}^2$ and $V_{max} = 1.6 \text{ m/s}$, showing significant reduction of 400 Hz cogging-related noise during constant velocity region.

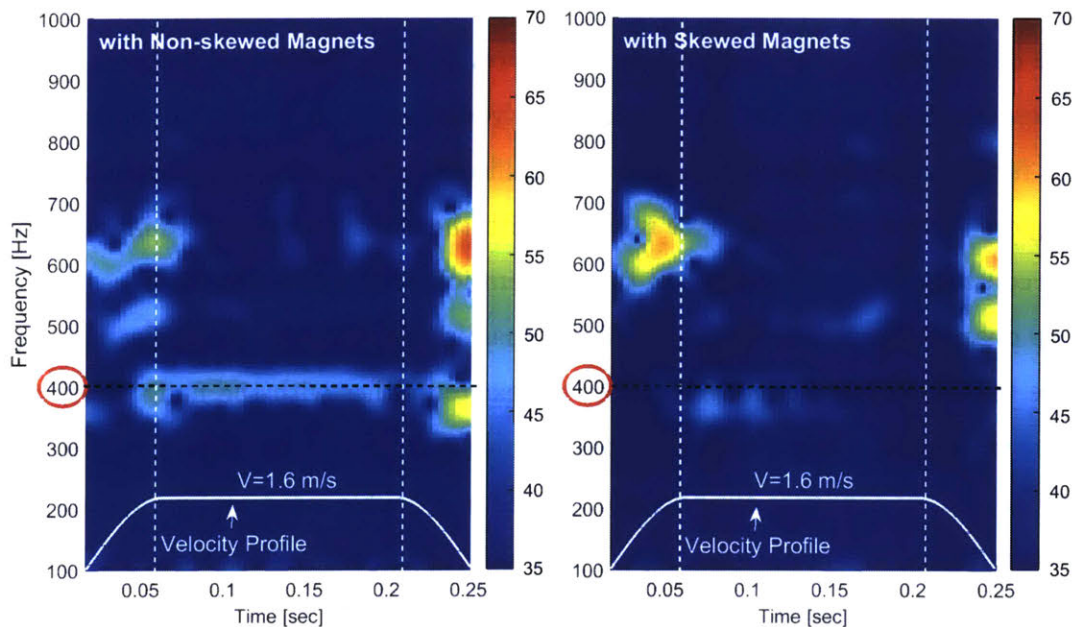


Figure 7-25: Spectrogram comparison of acoustic noises of our new fine-tooth motor between non-skewed (left) and skewed (right) magnets during a half cycle with $A_{max} = 45 \text{ m/s}^2$ and $V_{max} = 1.6 \text{ m/s}$, showing significant reduction of 400 Hz cogging-related noise during constant velocity region.

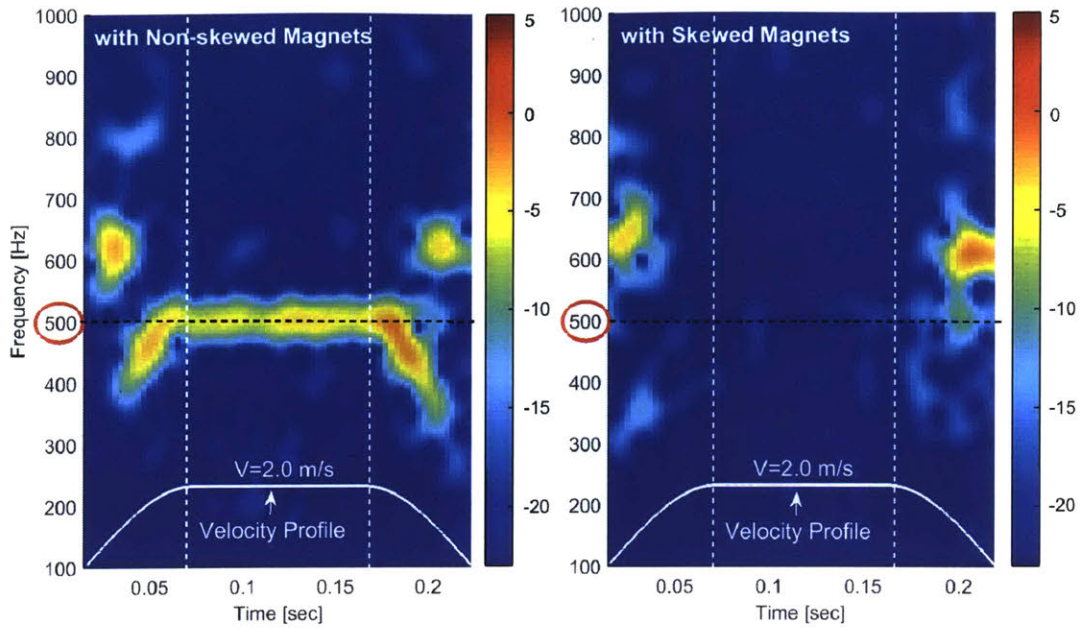


Figure 7-26: Spectrogram comparison of vibrational noises of our new fine-tooth motor between non-skewed (left) and skewed (right) magnets during a half cycle with $A_{max} = 45 \text{ m/s}^2$ and $V_{max} = 2.0 \text{ m/s}$, showing significant reduction of 500 Hz cogging-related noise during constant velocity region.

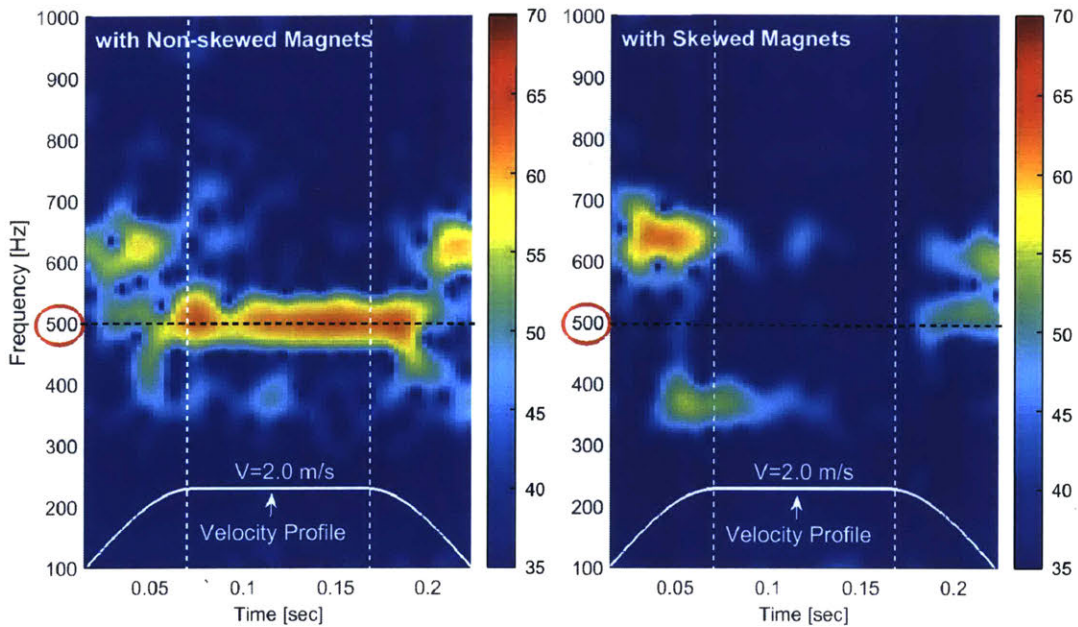


Figure 7-27: Spectrogram comparison of acoustic noises of our new fine-tooth motor between non-skewed (left) and skewed (right) magnets during a half cycle with $A_{max} = 45 \text{ m/s}^2$ and $V_{max} = 2.0 \text{ m/s}$, showing significant reduction of 500 Hz cogging-related noise during constant velocity region.

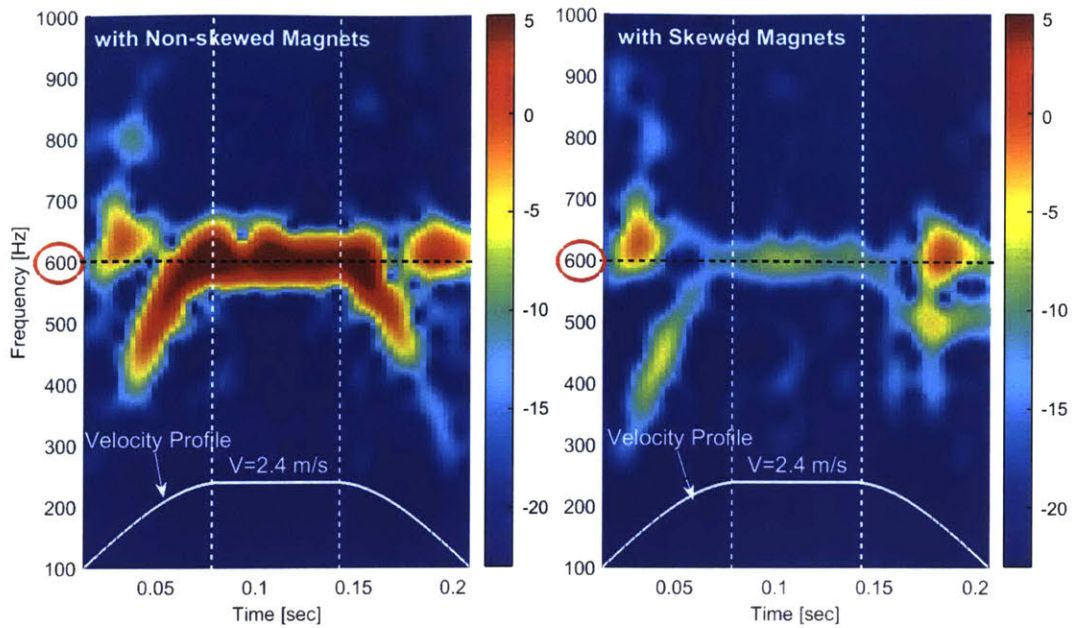


Figure 7-28: Spectrogram comparison of vibrational noises of our new fine-tooth motor between non-skewed (left) and skewed (right) magnets during a half cycle with $A_{max} = 45 \text{ m/s}^2$ and $V_{max} = 2.4 \text{ m/s}$, showing significant reduction of 600 Hz cogging-related noise during constant velocity region.

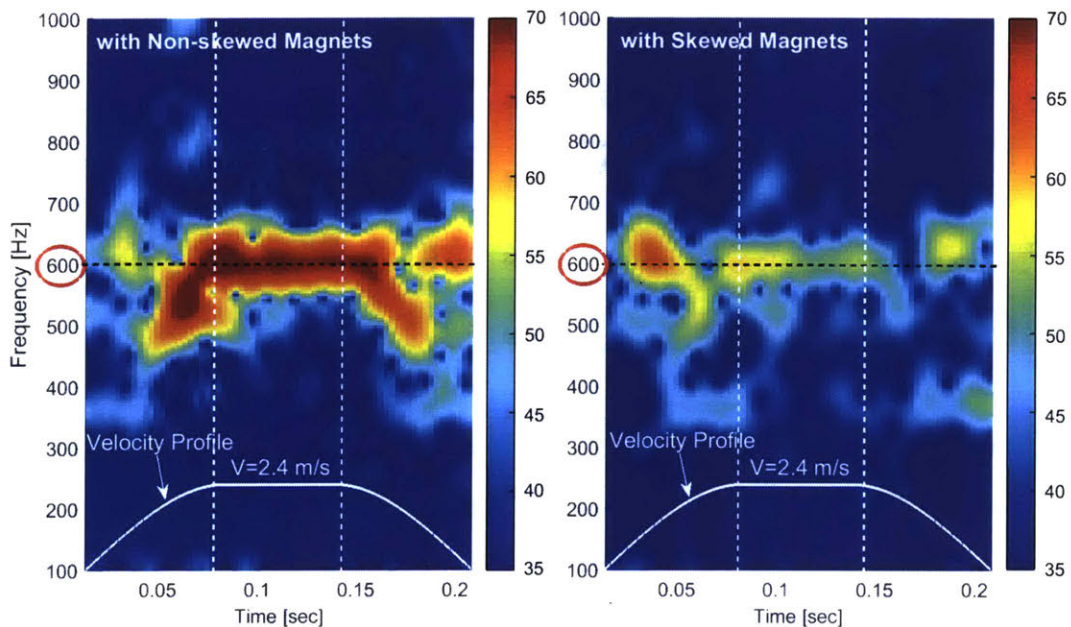


Figure 7-29: Spectrogram comparison of acoustic noises of our new fine-tooth motor between non-skewed (left) and skewed (right) magnets during a half cycle with $A_{max} = 45 \text{ m/s}^2$ and $V_{max} = 2.4 \text{ m/s}$, showing significant reduction of 600 Hz cogging-related noise during constant velocity region.

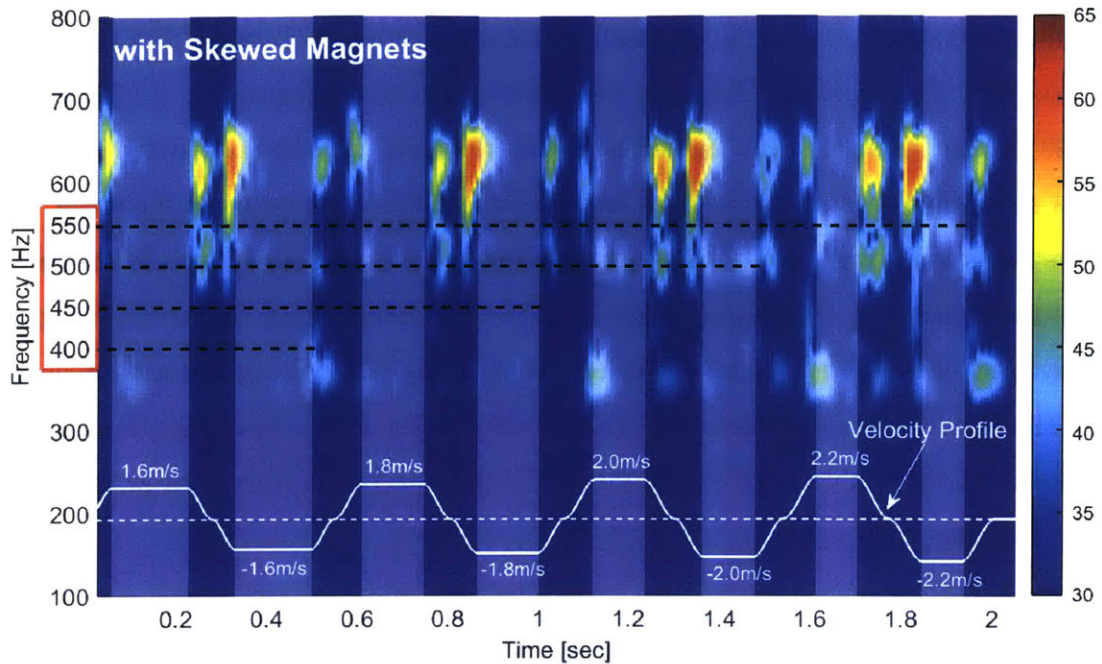


Figure 7-30: Spectrogram of acoustic noise of new fine-tooth motor with skewed magnets during an increasing-velocity cycles with $A_{max} = 45 \text{ m/s}^2$ and $V_{max} = 1.6 \text{ m/s}$ to 2.2 m/s , showing that cogging-oriented noises during constant velocity regions are significantly reduced.

measurement in Figure 7-23 and ii) the cogging noise frequency is close to a stage eigen-frequency so that its intensity is amplified. Even though the cogging noise is not completely eliminated, the reduction is still significant. In fact, Figure 7-29 shows the SPL drop of almost 20 dB by skewing magnets, which is equivalent to a 10-to-1 reduction of the noise pressure in [Pa]. When we hear it in person, we notice this noise reduction very clearly.

We also present the experimental data of stage cycles with increasing velocity with the skewed magnets. As before, the constant velocity level is increased by 0.2 m/s at each cycle from 1.6 m/s to 2.2 m/s while measuring the motor vibro-acoustic noise. We obtain the spectrogram from the microphone data, and it is shown in Figure 7-30. While there is still motor noise associated with stage dynamics during acceleration and deceleration regions (darker portions), we see that the cogging noise during constant velocity regions (brighter portions) is significantly reduced. For 1.6

m/s and 1.8 m/s, the cogging noises at 400 Hz and 450 Hz are almost completely eliminated such that it is not noticeable within the chosen SPL range. For the higher velocities of 2.0 m/s and 2.2 m/s, we observe a bit of cogging noise at 500 Hz and 550 Hz, but these are at a smaller level than the case with the non-skewed magnets. As mentioned earlier, we can hear an increasing pitch when we cycle the stage with the non-skewed magnets to follow such a velocity-increasing trajectory. With skewed magnets, however, the cogging noise is sufficiently reduced that we cannot recognize any pitch changes in the noise. We believe that the residual cogging noise together with the noise during acceleration can be reduced even farther by configuring our new motors in the double-sided configuration. We plan to pursue this work in the future as discussed in Chapter 8.

7.2.3 Force Performance of New Fine-tooth Motor

In addition to the significant noise reduction, our new fine-tooth motor also shows the higher force performance than the conventional 3-4 combination iron-core motor, as discussed and simulated in Chapter 3. In this subsection, we experimentally validate this by showing that the actual force performance of our new motor agrees with the expected one from the simulation. In Chapter 3, we present the expected force performance of our new fine-tooth motor in terms of shear stress (N/mm²). Here we compare the experimental data of both the conventional and our new motors to the simulated shear stress data.

In the motor design phase in Chapter 3, the power dissipation is estimated with calculated coil resistances by the wire gauge (or cross-section area) and expected coil length. The estimated coil resistance of a fundamental unit is $R_{T_{ec},unit,cal} = 2.58 \Omega$ for the conventional motor and $R_{FT,unit,cal} = 7.02 \Omega$ for our fine-tooth motor. Note that the fundamental unit indicates a basic magnetic configuration required to generate the thrust, which are a 3-coil-4-magnet combination length for the conventional motor and one pole-pair length for our new motor. In this subsection, we use the measured values of the winding resistances to calculate the power dissipation, and plot the shear stress performance for both simulation and experimental results. The measured resistance

values for a fundamental unit are $R_{T_{ec,unit,meas}} = 2.64 \Omega$ and $R_{FT,unit,meas} = 9.10 \Omega$. The measured winding resistance of the fine-tooth motor is about 30 % larger than the calculation while it is only 2 % different for the conventional motor. This is due to the end-turn length, which is calculated as an arc in our estimate. The conventional motor has lumped (or shortest pitch) windings, so the actual end-turn length is well predicted with the arc assumption. However, with the fine-tooth motor, the end-turn has to be longer to cope with the coil overlapping caused by the double-layered full-pitch windings over the narrow slots. In fact, we deliberately made the coils even longer for our motor prototype to facilitate the manufacturing process and reduce the turn-around time. For commercial-level motor constructions, we believe there is room for reducing the end-turn length.

Using the measured resistance values, we obtain the shear stress performance for both the simulated data and the experimental data, and it is shown in Figure 7-31. The blue and black curves are simulated results, and the purple stars and red aster-

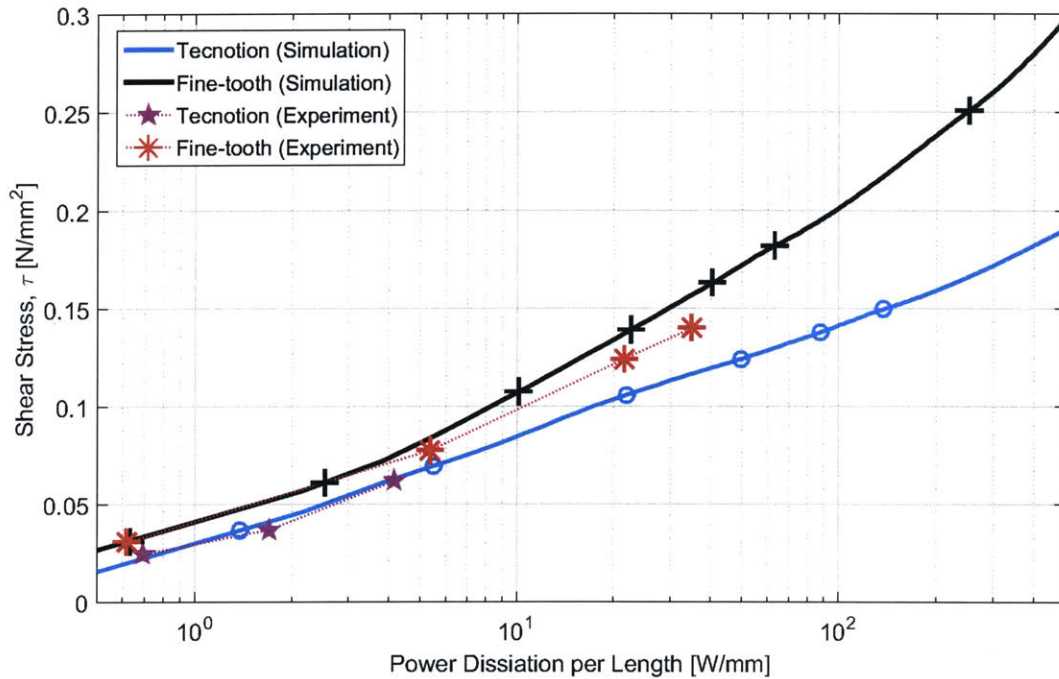


Figure 7-31: Motor force performance comparison between conventional and new motors. Several experimental data are overlapped with simulation results, showing reasonable agreement.

			Conventional Motor			Fine-tooth Motor		
M_{stage} [kg]			11.5			11.5		
M_{PM} [kg]			0.365			0.470		
a_p [m/s ²]	I_p [A]	τ [N/mm ²]	10	3.54	0.025	10	1.65	0.031
			15	5.56	0.037			
			25	8.68	0.062	25	4.85	0.078
						40	9.74	0.124
						45	12.40	0.140
A [mm ²]			92×52			74×52		
R_{unit} [Ω]			2.64			9.10		
λ_{unit} [mm]			48			40		

Figure 7-32: Table of parameters required to obtain shear stress data points over unit power both for conventional and new motors.

isks are experimental data points for the conventional and new motors, respectively. The experimental data points of the shear stress, τ versus the unit length power dissipation, p_λ are obtained by

$$\tau = \frac{F_{thrust}}{A} = \frac{(M_{stage} + M_{PM})a_p}{A} \quad [\text{N/mm}^2] \quad (7.7)$$

$$p_\lambda = \frac{P_{diss}}{\lambda_u} = \frac{I_p^2 R_{unit}}{\lambda_u} \quad [\text{W/mm}]$$

where M_{stage} , M_{PM} , a_p , A , P_{diss} , I_p , and λ_u are the stage structure mass, moving magnets mass, peak acceleration, thrust-generating area, instantaneous power dissipation, peak current, and fundamental unit length, respectively. Note that the thrust force is calculated with the total moving mass multiplied by the peak acceleration, which is achieved at the peak current. This peak current value is then used to calculate the unit length power dissipation. Experimentally obtained values of these parameters for both the conventional and new motors are compared in Figure 7-32. Note that skewed magnets are used for both motor types.

The experimental data points are calculated using these values in the table and are plotted with the purple stars for the conventional motor and the red asterisks for our new fine-tooth motor in Figure 7-31. Note that the data points of the conventional motor are limited to relatively low power because this motor emitted too much vibro-acoustic noise even at a relatively low power level. We were thus unwilling to run at higher power levels. The data points for our new motor, on the other hand, are limited by the thermal and travel length limits. The experimental results of the conventional motor agree well with the finite element analysis while there is discrepancy with our fine-tooth motor as the power level increases. We speculate that this is likely due to the saturation limit difference between the finite element tool and the actual material. Despite this discrepancy, however, we can see that our motor behaves closely to the simulation results, showing higher force performance than the conventional motor. Given that the material saturation and the leakage issues can be mitigated by using cobalt-iron (e.g. Hyperco50) for the stator material rather than silicon-iron (M-19) as discussed in Chapter 3, we can expect more force potential, especially for a higher power range.

7.2.4 Thermal Performance of New Fine-tooth Motor

In this subsection, we present the thermal performance of our new fine-tooth motor in terms of a thermal resistance and thermal time constant. These values help us to understand the thermal limits of our new fine-tooth motor at a given power level with a given cooling system. We measure the temperature of the winding coils while cycling the stage at the peak acceleration of 25 m/s^2 and a steady-state velocity of 0.4 m/s with a travel of 350 mm . Figure 7-33 shows the measured temperature (orange line with data points) over time together with a fitted curve (black line) using a first order thermal model. The ordinate of the plot is the measured temperature increase in units of degrees Celsius from an initial temperature of 25°C .

Figure 7-34 shows the simplified first order thermal model we use to fit the measured temperature response in Figure 7-33. We can obtain the first order differential equation as

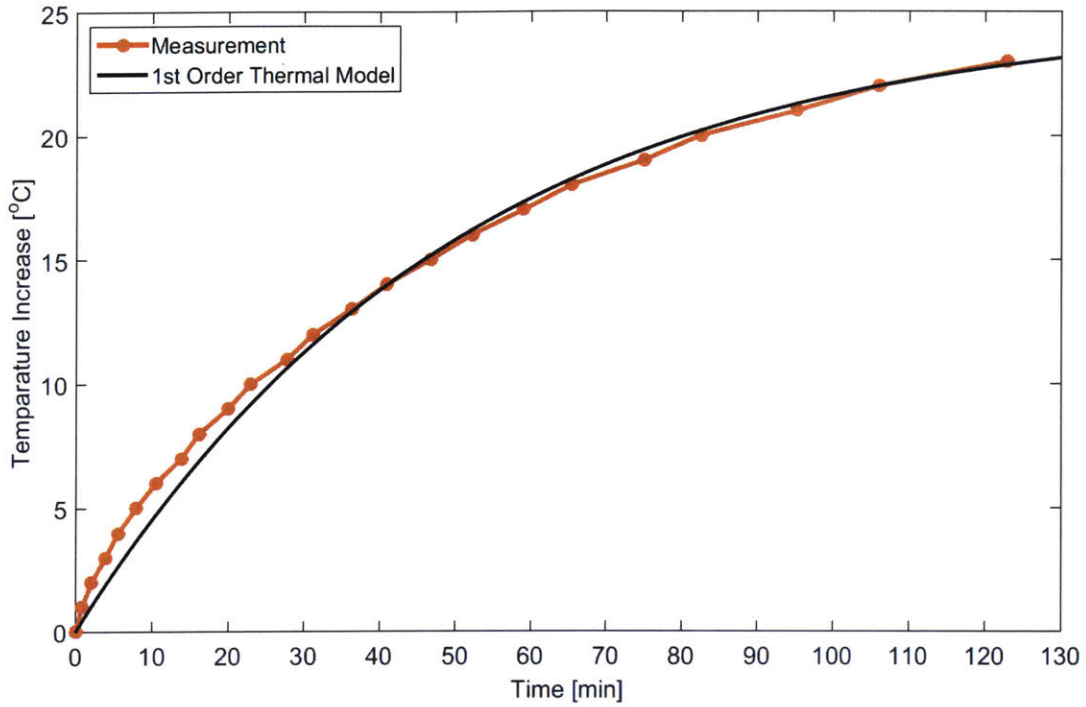


Figure 7-33: Temperature response to a power input to show the thermal performance of our new fine-tooth motor. The orange curve with data points shows the temperature measurements and the black line is a fitted curve with a first order thermal model. Note that the ordinate shows the motor coil temperature increase relative to an initial temperature of 25°C.

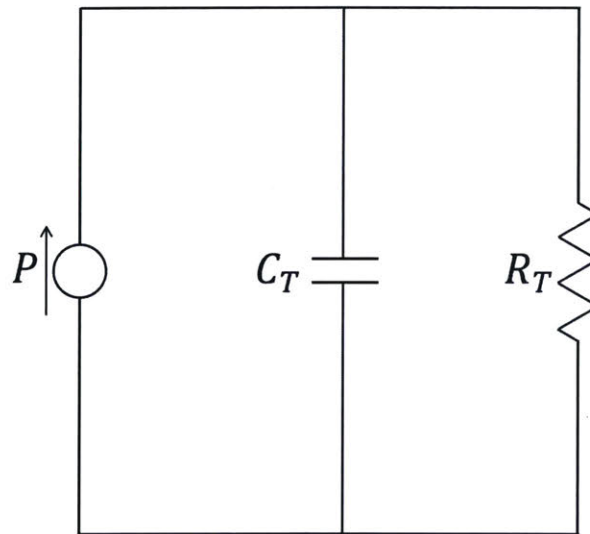


Figure 7-34: Simplified first order thermal model of RC circuit for the motor, where P , C_T , and R_T are the power source, thermal capacitance, and thermal resistance.

$$R_T C_T \frac{dT}{dt} + T = P R_T, \quad (7.8)$$

where R_T , C_T , T , t , and P are the thermal resistance of the motor, thermal capacitance, temperature increase, time, and power input, respectively. From (7.8), we can calculate the temperature temporal response to a power step input as

$$T(t) = P_{RMS} R_T \left(1 - e^{-\frac{1}{R_T C_T} t}\right) = P_{RMS} R_T \left(1 - e^{-t/\tau}\right), \quad (7.9)$$

where P_{RMS} and τ are the RMS (root mean square) power input to the motor and thermal time constant, respectively. When the stage is cycled by our new fine-tooth motor at the peak acceleration of 25 m/s² and a maximum velocity of 0.4 m/s, with the travel length of 350 mm, 1) the RMS current density in wire is calculated to be $J_{RMS} = 3.2$ A/mm² and 2) the RMS power is calculated to be $P_{RMS} = 111.88$ W for the whole stator. With this power input value, we obtain the thermal performance values of

$$\begin{cases} R_T = 0.2235 \text{ K/W} \\ C_T = 13426 \text{ J/K} \\ \tau = R_T C_T = 3000 \text{ sec} = 50 \text{ min} \end{cases} \quad (7.10)$$

by fitting the measured temperature curve. The fitted curve in Figure 7-33 is obtained with the values in (7.10).

From the measured thermal performance, we can predict our motor's force performance in terms of the stage acceleration [m/s²] in the single-sided stage configuration and the shear stress density [N/mm² or psi]. Figure 7-33 shows the temperature increase of about 25°C by the RMS power input of 111.88 W where we have the single-sided stage acceleration of $A_{stage} = 25$ m/s² and the shear stress density of $\tau_{shear} = 0.078$ N/mm² (as shown in Figure 7-32) with the RMS current density in

wire of $J_{RMS} = 3.2 \text{ A/mm}^2$. If we assume a temperature increase of 100°C , which is approximately the motor upper operating temperature, the RMS power will be four times larger and current will be two times larger so that we would have

$$\begin{cases} P_{RMS} = 111.88 \times 4 = 447.52 \text{ W} \\ J_{RMS} = 3.2 \times 2 = 6.4 \text{ A/mm}^2 \\ A_{stage} = 25 \times 2 = 50 \text{ m/s}^2 \simeq 5 \text{ G} \\ \tau_{shear} = 0.078 \times 2 = 0.156 \text{ N/mm}^2 \simeq 22.626 \text{ psi} \end{cases} \quad (7.11)$$

as the performance limit of our new motor for continuous operation when air-cooled. Note that the RMS current density of $J_{RMS} = 6.4 \text{ A/mm}^2$ is within a rule-of-thumb current density range of 6 to 10 A/mm^2 used for air-cooled machines. Note also that the acceleration here is for the single-sided configuration with two magnet pole pairs as shown in Figures 3-43 and 7-6. When we configure the stage in the double-sided manner with the longer magnet tracks (five magnet pole pairs as shown in Figure 3-43), we could have the stage acceleration up to about $250 \text{ m/s}^2 \simeq 25 \text{ G}$ with our new fine-tooth motors when air-cooled.

Assuming we apply an input power increased by 100 times, which gives 11.188 kW ($\simeq 111.88 \times 100$) to our motor, we would have the motor performance of

$$\begin{cases} P_{RMS} = 111.88 \times 100 = 11.188 \text{ kW} \\ J_{RMS} = 3.2 \times 10 = 32 \text{ A/mm}^2 \\ A_{stage} = 25 \times 10 = 250 \text{ m/s}^2 \simeq 25 \text{ G} \\ \tau_{shear} = 0.078 \times 10 = 0.78 \text{ N/mm}^2 \simeq 113.13 \text{ psi.} \end{cases} \quad (7.12)$$

Such high power dissipation could only be sustained with a carefully designed water cooling system. Note that the RMS current density in this case is 32 A/mm^2 , which is lower than the current density limit of 50 A/mm^2 for a heavily-water-cooled system as discussed in Chapter 3. At such a high exciting current level, the stator material will be saturated so that the stage acceleration and the shear stress density will

not increase linearly as approximated in (7.12). However, we can see the high force potential of our motor from these predicted values, and thus convince ourselves that the high shear of 0.28 N/mm^2 ($\simeq 40.6 \text{ psi}$) as predicted by FEM at 50 A/mm^2 in Figure 3-32 can be possibly achieved if a sufficient water cooling system is designed. The use of cobalt iron as the stator laminations can also be of significant help to achieve the predicted high shear.

7.2.5 Brief Summary

We discuss the investigation and resolution of the motor vibro-acoustic noise issues with the extensive experimental results using both the conventional 3-4 combination motor and our new fine-tooth motor in this chapter. Our hypotheses on the root causes of motor noise and its mechanism discussed in Chapter 1 are experimentally validated throughout this chapter (along with the previous chapter). This chapter particularly presents that both the overall noise level and the cogging-oriented noise are significantly reduced by the magnetic design of our new fine-tooth motor. Here we summarize our observations on the motor noise issues from the comprehensive experimental results.

- Acoustic noise of linear iron-core motors is caused by the mechanical vibration of the moving stage, which is excited by the magnetic force fluctuations. In other words, high force harmonics mechanically vibrate the moving stage, and this vibration radiates the acoustic noise.
- Forces exerted on the moving stage consist of i) magnetic force generated by energizing phase currents to achieve necessary accelerations and to overcome any force disturbance (e.g. cogging) and ii) magnetic force disturbance, mostly cogging caused by the magnetic interaction between iron-core teeth and permanent magnets.
 - Generated force contains various spatial harmonics depending on the motor magnetic design. These spatial force harmonics can be transferred to

temporal harmonics through a stage velocity. Magnetically generated force is in general dominant during acceleration and deceleration periods.

- Force disturbance can be represented by the cogging force when the stage cycles without any friction or load. This cogging force may also contain spatial harmonics depending on the geometric relation of magnetic components, which can also be transmitted to temporal harmonics by a stage velocity. Cogging force generally dominates during constant velocity regions.
- The conventional 3-4 combination iron-core motor contains high force harmonics caused by its coarse-tooth design. These force harmonics are generated throughout a whole cycle i) to achieve a required acceleration during acceleration regions, and ii) to overcome the cogging force during constant velocity periods.
 - Stage dynamics are excited for both regions due to these high harmonics in the magnetically generated force.
 - Even with skewed magnets, a significant amount of cogging still remains to be overcome by magnetic forces, thereby also exciting stage eigen-modes.
 - Vibro-acoustic noise from the stage dynamics excitation dominates the noise over a whole stage cycle period so that the motor noise caused by cogging is not noticeable during constant velocity regions.
- Our fine-tooth motor generates less force harmonics due to its fine-tooth design. This is why the stage eigen-modes are less excited and so the overall noise level is significantly reduced.
 - With the non-skewed magnets, the clear distinction on the motor noise is observed: the stage dynamics noise for acceleration regions and the cogging-oriented noise for constant velocity regions. The cogging noise also shows the velocity dependency so that we can hear the stage playing

a musical scale at several different noise pitches as changing the stage velocity.

- With the skewed magnets, the cogging is significantly reduced due to its fine-tooth design. Therefore, the cogging-oriented noise is also significantly reduced during constant velocity regions. This noise reduction is well noticed by direct hearing in that we do not hear much of noise pitch changes when the stage is cycled at different velocities.
- The linear stage testbed with our fine-tooth motor shows significant vibro-acoustic reduction compared to the conventional iron-core motor. We believe the motor vibro-acoustic noises can be reduced further in both the acceleration and constant velocity regions by the double-sided configuration.
- Our new fine-tooth motor also shows higher force capability, namely higher shear stress per unit power, than the conventional iron-core motor. Our new motor has greater potential for high-power and high-current-density applications, e.g. a lithography scanner.

Chapter 8

Conclusions and Suggestions for Future Work

8.1 Conclusions

This thesis describes the design, construction, and test of a new fine-tooth linear iron-core permanent magnet motor to simultaneously achieve high shear stress density and low vibro-acoustic noise. We present in this thesis studies of the vibro-acoustic noise issue of linear iron-core permanent magnet motors. It is hypothesized and experimentally validated that such motor noise is caused by high force harmonics vibrating the moving stage, and is especially severe when the stage eigen-modes are excited. Such stage vibration can be transmitted through the system structure and can radiate as acoustic noise, thereby disturbing precision machines.

The observed overall acoustic noise level in Pascals is reduced by 93 % from the conventional 3-4 combination linear motor to our new fine-tooth motor during the acceleration period with non-skewed magnets. In terms of the sound pressure level (SPL), this is a significant noise reduction from 83 dB to 60 dB. This is the same as the noise difference we feel between a big truck passing by and a quiet office. The cogging-driven and velocity-dependent noise, which is dominant in constant velocity regions, is also significantly reduced in our new motor design. The fine-tooth motor design with its small tooth pitch reduces the cogging force by a factor of 10-to-1 when

using skewed magnets. The fine-tooth motor cogging-driven acoustic noise is reduced by 90 % in Pascals while simultaneously increasing the thrust performance relative to a conventional motor.

We also present in this thesis the force performance of our new fine-tooth motor both in simulations and experiments. We compare the force performance between the conventional linear iron-core motor and our new motor in the aspects of the shear stress density [N/mm^2] and acceleration [m/s^2]. In order to have a fair comparison between two different motors, the force performance is compared versus the power dissipation per motor fundamental unit and the RMS (root mean square) current density in the coil wire. The motor fundamental unit means the minimal motor magnetic configuration to produce force, which consists of 3 iron-core teeth and 4 magnets for the conventional motor and one pole pair for our new fine-tooth motor. Our new motor shows the predicted shear stress improvements of 28 % at the prototype practical power level of 500 W per motor unit and 84 % at a high RMS current density in the wire of 50 A/ mm^2 relative to a conventional motor. Especially in a two-sided configuration, this new fine-tooth motor may enable unprecedented high stage acceleration in precision machines.

We list the primary contributions of this thesis together with what we learned in the process as follows:

1. Designed a new linear iron-core permanent magnet motor to achieve high shear stress density and low acoustic noise.
 - (a) The new fine-tooth linear motor has the design features of fine teeth, narrow and deep slots, five phases, and moving Halbach magnet array. These create smoother stator and rotor MMFs to reduce high frequency force harmonics while simultaneously providing high shear stress density.
 - The multiple fine teeth creates a stator MMF close to the ideal sinusoidal waveform, and the Halbach magnet array reduces the high frequency harmonic content of the rotor MMF, as discussed in Section 3.1.

- The simulated force ripple of our new fine-tooth motor shows a significant peak-to-peak reduction with the ratio of 9-to-1 and 5-to-1 in the normal and tangential directions, respectively. Moreover, the force ripple of our new fine-tooth motor mainly contains the fundamental component while there are significant higher frequency force harmonics expected with the conventional 3-4 combination motor, as presented in Section 3.4.
- Motor force ripple reduction both in the harmonic content and amplitude leads to significant operational noise reduction. With our new fine-tooth motor, the overall acoustic noise level in Pascals is reduced by 93 % during the acceleration period with non-skewed magnets, as compared to the conventional motor. The cogging-driven and velocity-dependent noise, which is dominant in constant velocity regions, is also significantly reduced in our new motor design by 90 % in Pascals, as experimentally shown in Sections 7.2.
- Our new fine-tooth motor is designed to also provide higher shear stress than the conventional 3-4 combination motor. Our new motor shows predicted shear stress improvements of 28 % (from 0.090 N/mm² to 0.115 N/mm²) at the prototype practical power level of 10 W/mm and 84 % (from 0.167 N/mm² to 0.308 N/mm²) at an anticipated ultimate RMS (root mean square) current density limit with water cooling in the coil wires of 50 A/mm², as shown in Section 3.4.
- By using a high number of phases (even higher than five phases), we might be able to achieve 1) a smoother stator MMF, which is even closer to the ideal fundamental waveform and 2) higher shear stress density. However, we chose a five-phase motor because 1) it becomes more difficult to wind coils with increasing end-turn overlapping for a higher number of phases and 2) the shear stress per power decreases with higher number of phases than 5, as discussed in Section 3.3.
- By using thin iron-core teeth (even thinner than our design of 2 mm),

a smoother stator MMF can be achieved. However, we chose a tooth width of 2 mm because 1) the manufacturing of thinner teeth can be difficult and time-consuming, 2) it would require a thinner wire for the same number of turns, thereby increasing the inductance and thus requiring higher-rating power amplifiers, and 3) the tooth width of 2 mm shows the highest stage acceleration prediction among the design variants, as analyzed in Section 3.3.

(b) Our fine-tooth motor has the magnetic configuration of moving short magnets with stationary long armature.

- Various conceptual designs are considered for four different motor magnetic configurations, depending on which part is moving or stationary and which is long or short, as presented in Section 4.2.
- We chose the magnetic configuration of moving short magnets and stationary long armature to have 1) higher acceleration by reducing the moving mass and 2) the minimal number of umbilical cables attached to the moving stage.

2. Constructed an operational prototype of the new fine-tooth motor.

(a) Double-layered full-pitch concentrated five-phase windings are used in the stator armature.

- The stator laminations are made of silicon iron with a total number of 180 slots where a total number of 175 coils (since the first 5 and last 5 slots are only half-filled) are wound, as shown in Section 3.5.
- We used silicon iron for the stator material to reduce the prototyping cost and lead time, as discussed in Section 3.4. We expect however a shear stress increase of about 30 % by using cobalt iron (e.g. Hyperco50) due to its high saturation limit. We also decided to use thinner wires (23 AWG with 126 turns per slot) so as to facilitate the winding process with relatively easier end-turn bending and pack-

ing. The completed stator armature with all the winding, wiring, and cabling is shown in Section 3.5.

(b) Both skewed and non-skewed Halbach magnet tracks are fabricated and tested.

- It can be challenging to assemble a Halbach magnet array since the horizontal magnets between the vertical magnets tend to flip themselves to be aligned with the vertical magnets. A practical assembly process for a Halbach magnet array is illustrated in Section 3.5. This assembly was accomplished by Fred Sommerhalter.

3. Experimentally demonstrated the noise and force performance of our new fine-tooth motor.

(a) The vibro-acoustic noise in both acceleration and constant velocity regions is significantly reduced, as compared to a conventional 3-4 combination linear iron-core motor.

- The conventional motor emits significant acoustic noise in both acceleration and constant velocity regions. Specifically, the total noise in 5 kHz bandwidth is measured to be 0.278 Pa (≈ 83 dB) and 0.228 Pa (≈ 81 dB) in the acceleration and constant velocity regions, respectively. Such significant noise with the conventional motor comes from the stage dynamics excitation as discussed in Section 6.2.
- Our new motor shows a significant noise reduction in both regions. We have 93 % acoustic noise reduction in Pascals in the acceleration region and 91 % reduction in the constant velocity region, as shown in Section 7.2. This significant noise reduction stems from the fact that our new fine-tooth motor design generates less high frequency force harmonics, thereby less exciting the stage dynamics, as discussed in Chapters 3 and 7.
- Our new motor also shows a significant reduction of the cogging-driven noise. With our fine-tooth motor design, the cogging force amplitude,

and thus the cogging-related noise, are reduced by about 90 % by simply using skewed magnets with a small skew angle of 4° , as shown in Section 7.2.

- (b) The force performance of shear stress density versus power per unit is experimentally validated to prove the high force capability of our new motor, as discussed in Section 7.2.
 - (c) The thermal performance of our new fine-tooth motor is experimentally obtained by measuring the temperature of the stator coils for more than two hours while cycling the stage at the peak acceleration of 25 m/s^2 and a steady-state velocity of 0.4 m/s with a travel of 350 mm . From the measured thermal performance, our new fine-tooth motor is expected to provide a shear stress density of 0.156 N/mm^2 ($\simeq 22.626 \text{ psi}$) and an acceleration of about 25 G for a double-sided motor configuration at the RMS current density in the coil wires of 6.4 A/mm^2 when air-cooled. We also predict a shear stress density of 0.780 N/mm^2 ($\simeq 113.13 \text{ psi}$) at the 32 A/mm^2 when water cooled. The details on the thermal performance of our new motor are presented in Section 7.2.
4. Designed and constructed an experimental linear stage testbed to test both the conventional and our new motors.
- (a) The experimental testrig is equipped with essential functions to facilitate noise investigation, including air bearings, force dynamometer, position sensors, and low-vibration cable carrier, as presented in Chapter 5.
 - (b) The stage testbed has a flexible design which can accommodate both the single- and double-sided motor configurations with either the conventional motor or our new fine-tooth motor.
 - Various conceptual designs of the experimental linear stage testbed are considered in Section 4.2 for each of four magnetic configurations of 1) moving short magnet and stationary long coil, 2) stationary long

- magnet and moving short coil, 3) moving long magnet and stationary short coil, and 4) stationary short magnet and moving long coil.
- The configuration of moving short magnet and stationary long coil is selected to have higher stage acceleration and lower number of umbilical cables. We chose the modular design of up-and-down structural configuration for relatively easier disassembly and reassembly process, as discussed in Chapters 4 and 5.
- (c) Both the conventional motor and our new motor are commutated and position controlled for the stage testbed to be operated for noise investigation.
- A three-phase commutation and linear position controller are implemented for the conventional 3-4 combination motor. We achieve a position loop crossover frequency of 100 Hz with a phase margin of 45° , and the RMS position error during a constant velocity region of $9.3 \mu\text{m}$, as discussed in Section 6.1.
 - We implement a five-phase commutation for our new fine-tooth motor. The position controller is designed to have a loop crossover frequency of 100 Hz with a phase margin of 45° . We accomplish the RMS position error of $2.9 \mu\text{m}$ during a constant velocity period, as presented in Section 7.1.
5. Experimentally proved that the vibro-acoustic noise of linear iron-core permanent magnet motors is caused by high frequency force harmonics vibrating the stage and thus radiating the acoustic noise.
- (a) The hypothesis on the noise mechanism discussed in Section 1.3 is experimentally proved in Chapters 6 and 7 by measuring and comparing the vibrational and acoustic noise data of both the conventional 3-4 combination motor and our new fine-tooth motor.
6. Developed the hybrid layer model for our fine-tooth linear iron-core permanent magnet motor. This modeling method is adapted from the rotary motor model

invented by Dr. Matthew Angle at MIT [3].

- (a) Our hybrid layer model 1) uses a network of nonlinear reluctances in the stator iron-core and for the fringing fields and 2) solves Maxwell's equations in the magnet track for magnet array patterns including the conventional pattern of N-S-N-S and the Halbach array, as discussed in Section 3.2.
- (b) We assume the periodicity of the magnetic fields for the hybrid layer model, and thus observe a bit of discrepancy at the ends of magnet tracks, compared to the finite element method, as presented in Section 3.2. The effect of the ends is observed to be not significant in both the simulated air-gap magnet flux density and cogging force. We thus speculate that the end-effects would not significantly affect the motor noise either, especially when using multiple magnet pole pairs. We believe however it can be a relevant future work to investigate the effect of magnet track ends to the motor noise generation.
- (c) We use our hybrid layer model in conjunction with the finite element (FEA) model to design our new fine-tooth motor. At present, the hybrid layer model shows convergence issues when the stator material is highly saturated, as discussed in Sections 3.2 and 3.3, thus only the FEA model is used at high current density. We speculate that this issue comes from the fact that the current flux-tube model does not contain any leakage paths between teeth. A possible approach to upgrade the hybrid layer model is discussed in Section 8.2 below as a suggestion for future work.

8.2 Suggestions for Future Work

In this section, we discuss suggestions for future work.

8.2.1 Control Algorithms for Further Noise Reduction

This thesis mainly focuses on the magnetic design of the new motor to resolve the motor noise issue. As presented in Chapter 7, the vibro-acoustic noise is significantly reduced in both the acceleration and constant velocity regions by the fine-tooth design itself and by the usage of skewed magnets. However, there is still residual noise 1) in the acceleration region at high acceleration levels due to the force ripple and 2) in the constant velocity region at high velocity levels due to the residual cogging force. We believe that this residual noise can be reduced further by a proper control algorithm to directly control the normal and/or shear force of the motor. We can first map the residual forces fluctuation during cyclic operation, and then control it out on the fly.

8.2.2 Hybrid Layer Model Upgrade

We discuss in Chapter 3 the limitation of our hybrid layer model in that it does not converge when the core material is highly saturated. We speculate that this is because the equivalent magnetic circuit we use in the flux-tube model of the stator armature does not contain any flux leakage paths, as shown in Figure 3-6. The current hybrid layer model should thus be upgraded to include the leakage paths in the slots, as proposed in Figure 8-1. The fundamental schematic of reluctance network is the same as the one we use in Figure 3-6, but the leakage reluctances \mathcal{R}_L 's are added as shown in red in the figure.

We believe this augmented flux-tube model may enhance the performance of the hybrid layer model by providing correct paths to the magnetic flux when the material is highly saturated, thereby helping the model to converge even at higher excitation currents. The added leakage reluctances might add more mathematical complexity to the flux-tube model, and might even require an internal iteration loop within the flux-tube model itself. However, the hybrid layer model with such enhanced computational performance will be of great help to reduce motor design time.

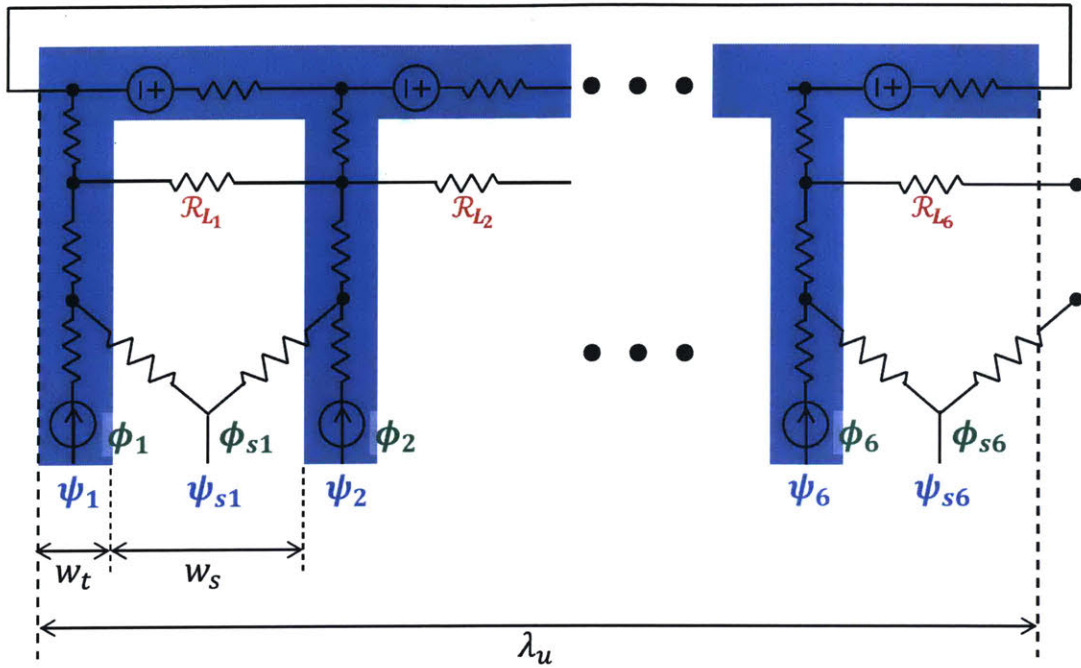


Figure 8-1: Network of nonlinear reluctances including the leakage paths between teeth to upgrade the hybrid layer model.

8.2.3 Double-sided Stage Configurations

In the scope of this thesis, the single-sided stage configuration is used for both the conventional and our new motors for noise investigation and performance experiments. In the single-sided configuration, a significant motor noise reduction is achieved by the magnetic design of our new fine-tooth motor, as discussed in Chapter 7. In addition, we believe that the motor noise can be reduced further when we map out the residual force fluctuation by a normal- and shear-direction force control, as discussed in the previous subsection.

In the sense of canceling the residual force fluctuation in the normal direction, we can also implement a double-sided stage configuration where identical stator and magnet track are used in a mirrored fashion. The proposed double-sided stage configuration is shown in Figure 8-2 together with a picture of the existing single-sided stage. By symmetrically configuring the identical motors in the lower and upper po-

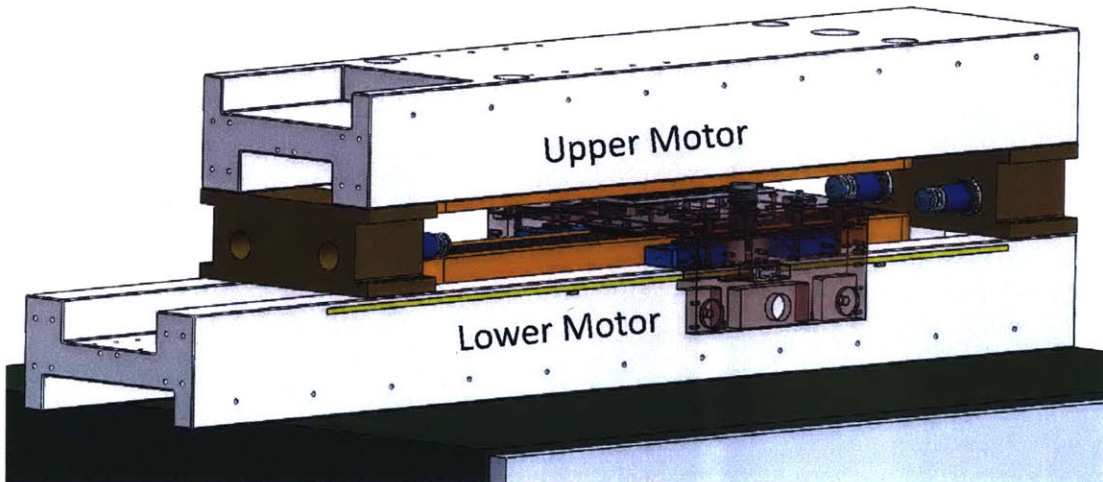
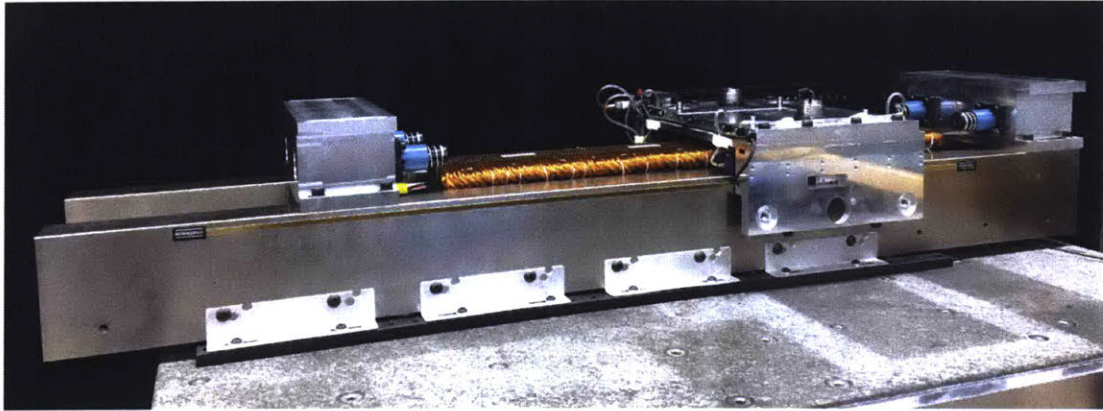


Figure 8-2: CAD design of the double-sided motor configuration (lower) augmented from the existing experimental testbed with the single-sided motor configuration (upper).

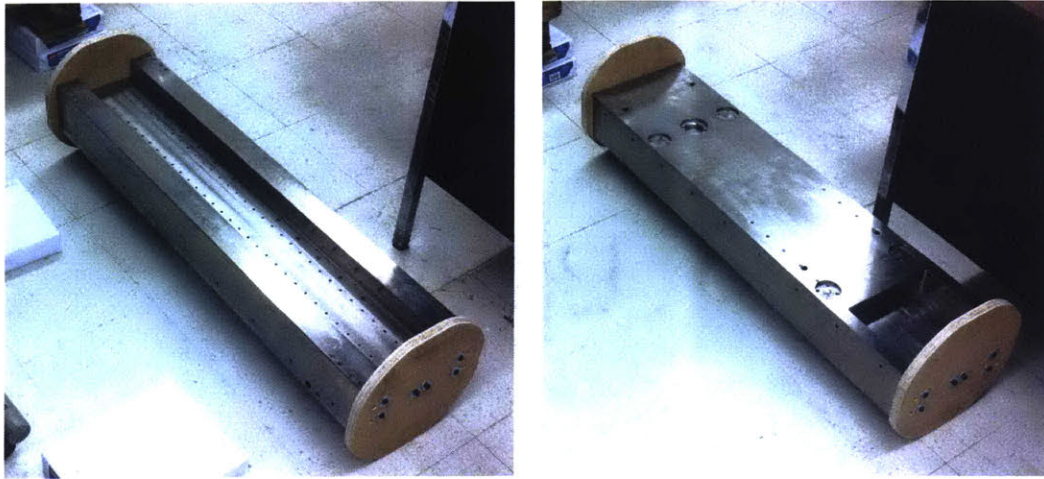


Figure 8-3: Proposed method of flipping the 1040-mm (41-in) base guide bar using two rotating wheels at the ends.

sitions as shown in the figure, we can cancel out the normal forces and thus expect further noise reduction. Moreover, we can simultaneously achieve almost twice the acceleration, since the added magnet track (~ 0.47 kg for our fine-tooth motor) in the upper portion is relatively lighter than the stage structure (~ 11 kg).

We have a shorter guide bar (1040 mm) in our possession, which has the same shape and cross-section as the larger one (1295 mm) used in the existing single-sided stage testbed, as presented in Chapter 5. This structure can be used as a base for the upper motor as depicted in Figure 8-2. Note that we encountered one interesting and practical question in the design phase of the double-sided stage, which is how to flip a 184-kg chunk of steel. Lifting of such a heavy structure can be handled with an engine hoist, but flipping is not a trivial task. We propose to use two rotating plywood wheels at the ends as shown in Figure 8-3. The rotating wheels have four flat portions so that we can rotate the bar by 90° and keep it from rolling at each position. We can install a motor onto the guide bar in the position of left-side photo in the figure, flip it as shown in the right-side picture, and lift it by an engine hoist to position over the existing single-sided stage setup. The space between the lower and upper base structures are defined by the spacers as presented in Chapters 4 and 5, and as shown in Figure 8-2. In order to properly cancel the normal force in this

double-sided configuration, it is critical to have correct alignment between the lower and upper motors. We suggest to measure the back EMFs from the same phase coils of both motors for the purpose of longitudinal alignment.

8.2.4 Liquid Cooling

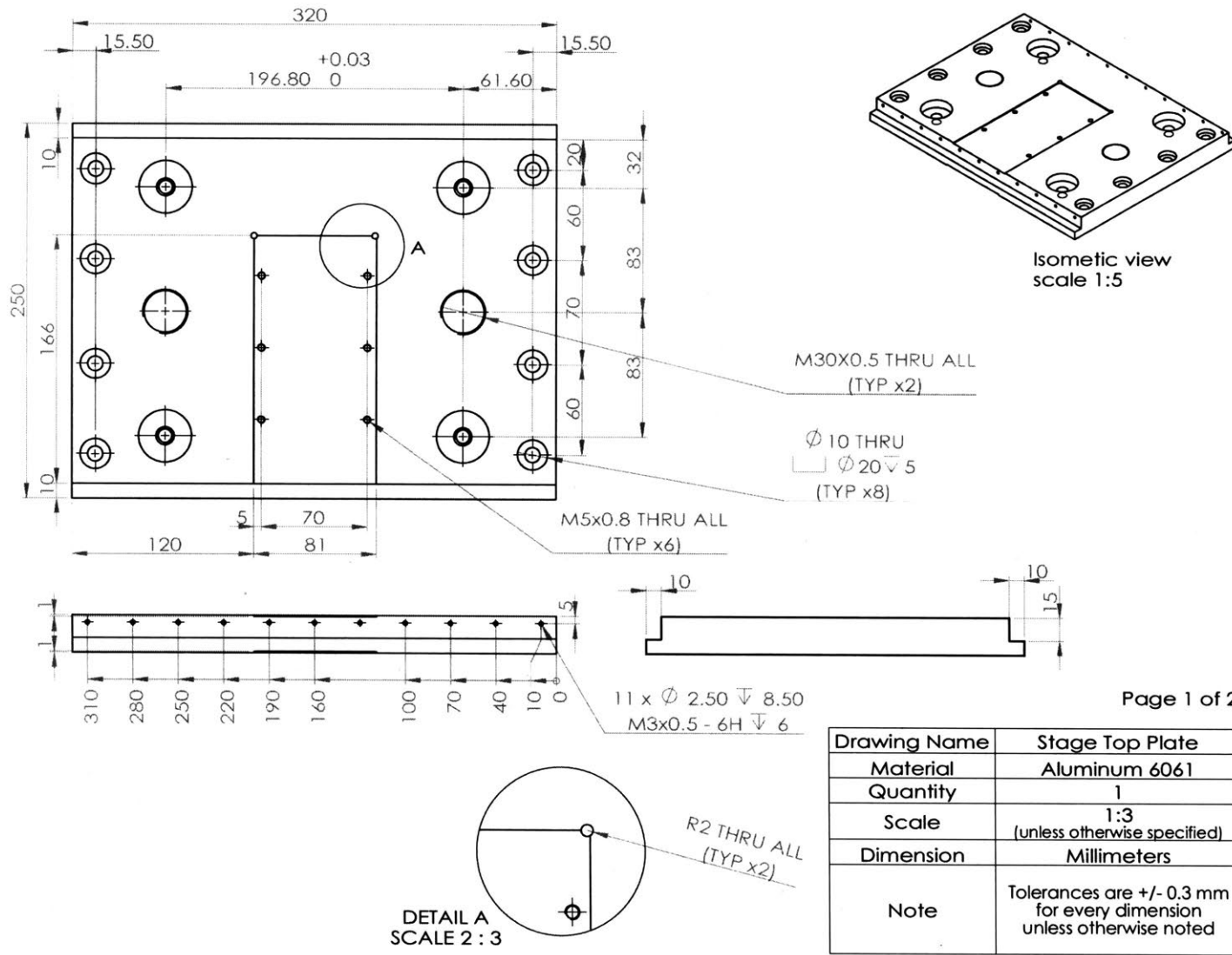
In the scope of this thesis, both the conventional motor and our new fine-tooth motor were driven with a small temporal duty cycle for the noise experiments and motor performance demonstration. The motor driving power level was also not too high, either. Thus, we relied on the motor thermal mass to absorb power spikes, and air cooling to dissipate the average power, and did not use liquid cooling. However, it is critical to have a proper cooling mechanism for industrial high-power continuous operations, such as in photo-lithography machines. For our new motor with such narrow slots, we propose to implement the liquid cooling on the end-turns for a large conduction surface contact directly with the coils. The design and implementation of such a liquid cooling system can be a relevant future work.

In summary, while there are many promising future studies, this thesis clearly shows a new direction for motion control. Our new fine-tooth motor widens the performance envelope of acceleration in precision positioning systems, while simultaneously achieving low vibration and acoustic noise output. This new motor thus establishes a new level of capability as will like be required in future generations of high performance precision manufacturing equipment, such as in semiconductor lithography machines.

Appendix A

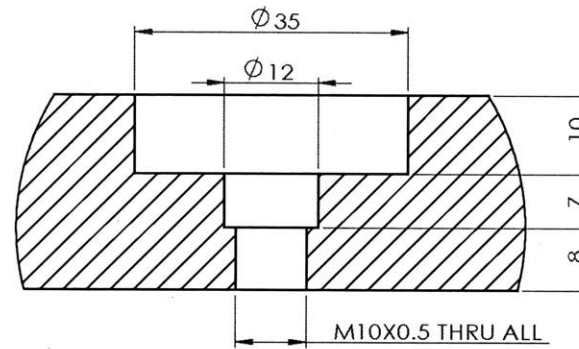
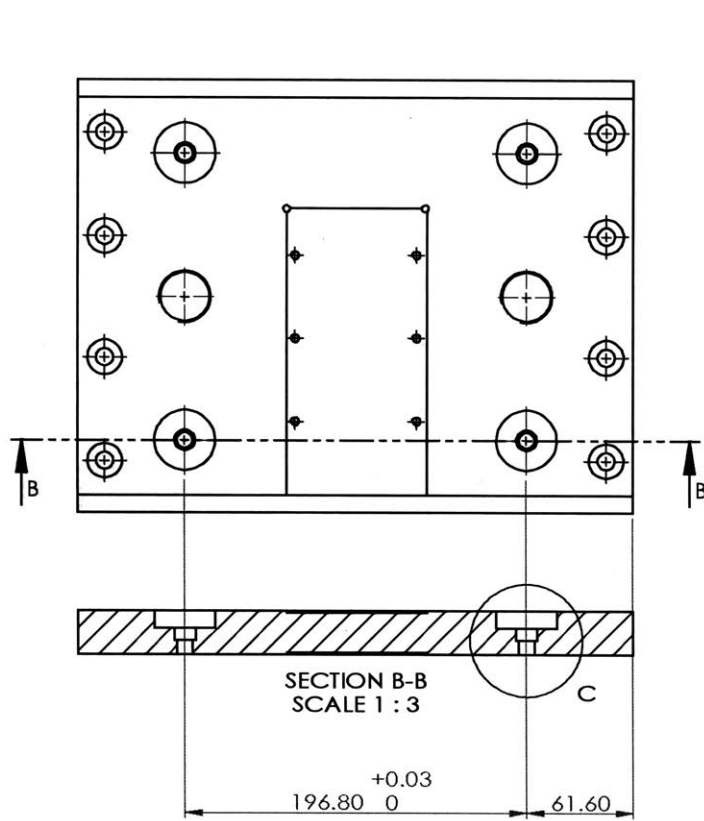
Drawings of Testbed Components

In this appendix, we present the drawings of the hardware components we use for our experimental linear stage testbed and our new fine-tooth motor. Figures from A-1 to A-14 show the drawings of the parts used in the experimental testrig, such as the moving stage structure, holding magnets, and spacers. Figures from A-15 to A-26 show the drawings of the components for our new fine-tooth motor including the stator armature laminations, mounting plates, and magnet plates.



Drawing Name	Stage Top Plate
Material	Aluminum 6061
Quantity	1
Scale	1:3 (unless otherwise specified)
Dimension	Millimeters
Note	Tolerances are +/- 0.3 mm for every dimension unless otherwise noted

Figure A-1: Drawing of the stage top plate. Page 1 of 2.



DETAIL C
SCALE 3 : 2

Note: Repeat the Detail C
for all 4 locations.

Page 2 of 2

Drawing Name	Stage Top Plate
Material	Aluminum 6061
Quantity	1
Scale	1:3 (unless otherwise specified)
Dimension	Millimeters
Note	Tolerances are +/- 0.3 mm for every dimension unless otherwise noted

Figure A-2: Drawing of the stage top plate. Page 2 of 2.

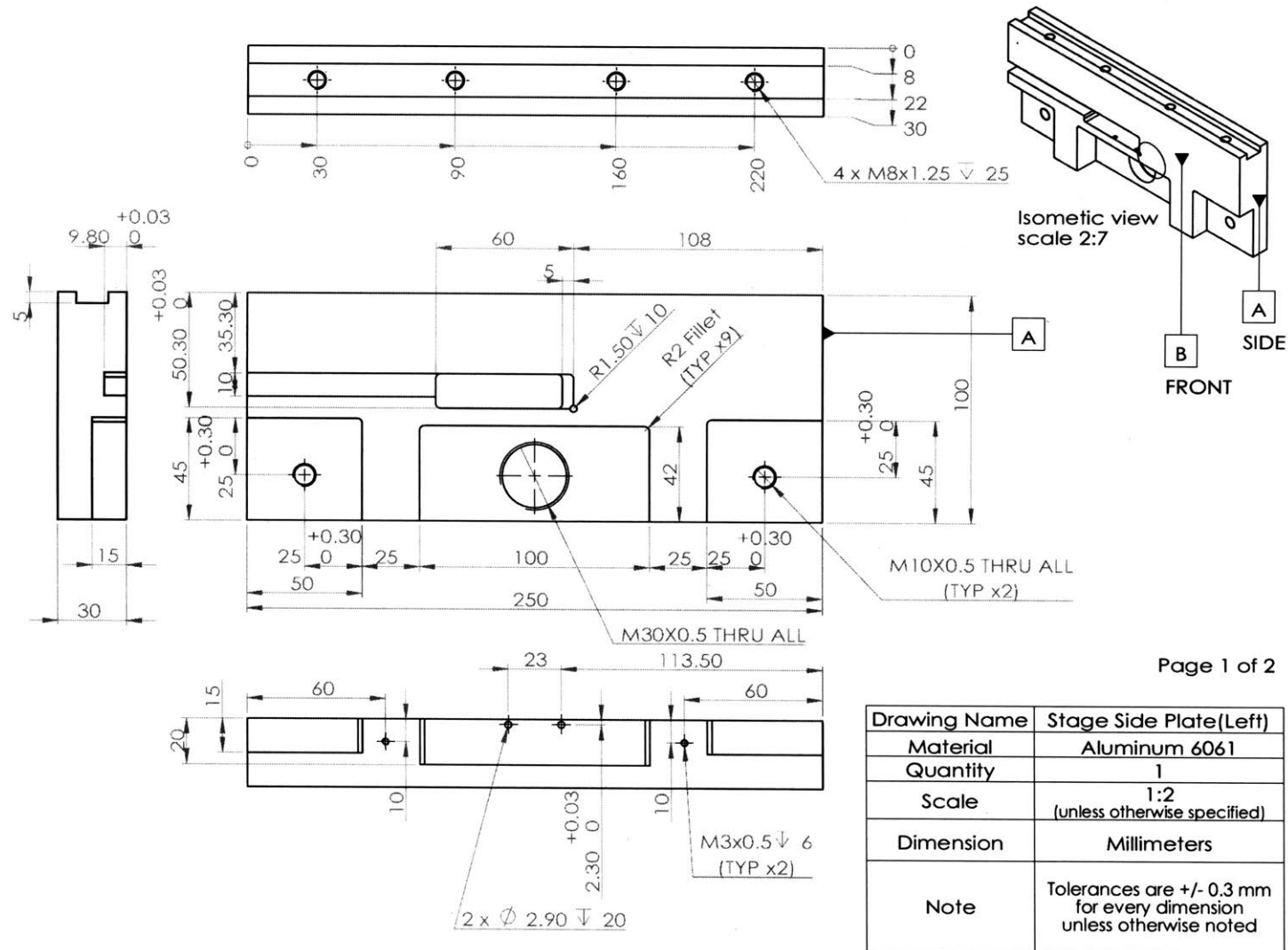
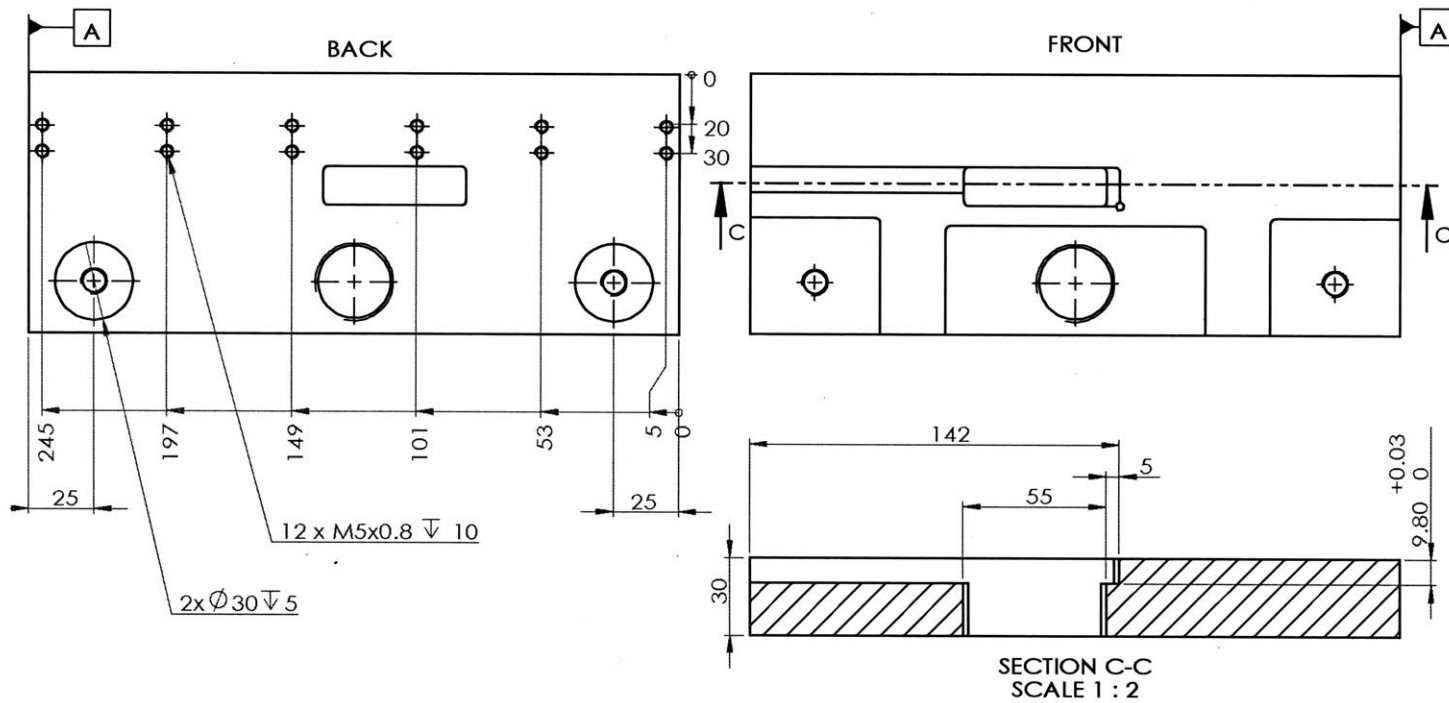


Figure A-3: Drawing of the stage left-side plate. Page 1 of 2.



Page 2 of 2

Drawing Name	Stage Side Plate (Left)
Material	Aluminum 6061
Quantity	1
Scale	1:2 (unless otherwise specified)
Dimension	Millimeters
Note	Tolerances are +/- 0.3 mm for every dimension unless otherwise noted

Figure A-4: Drawing of the stage left-side plate. Page 2 of 2.

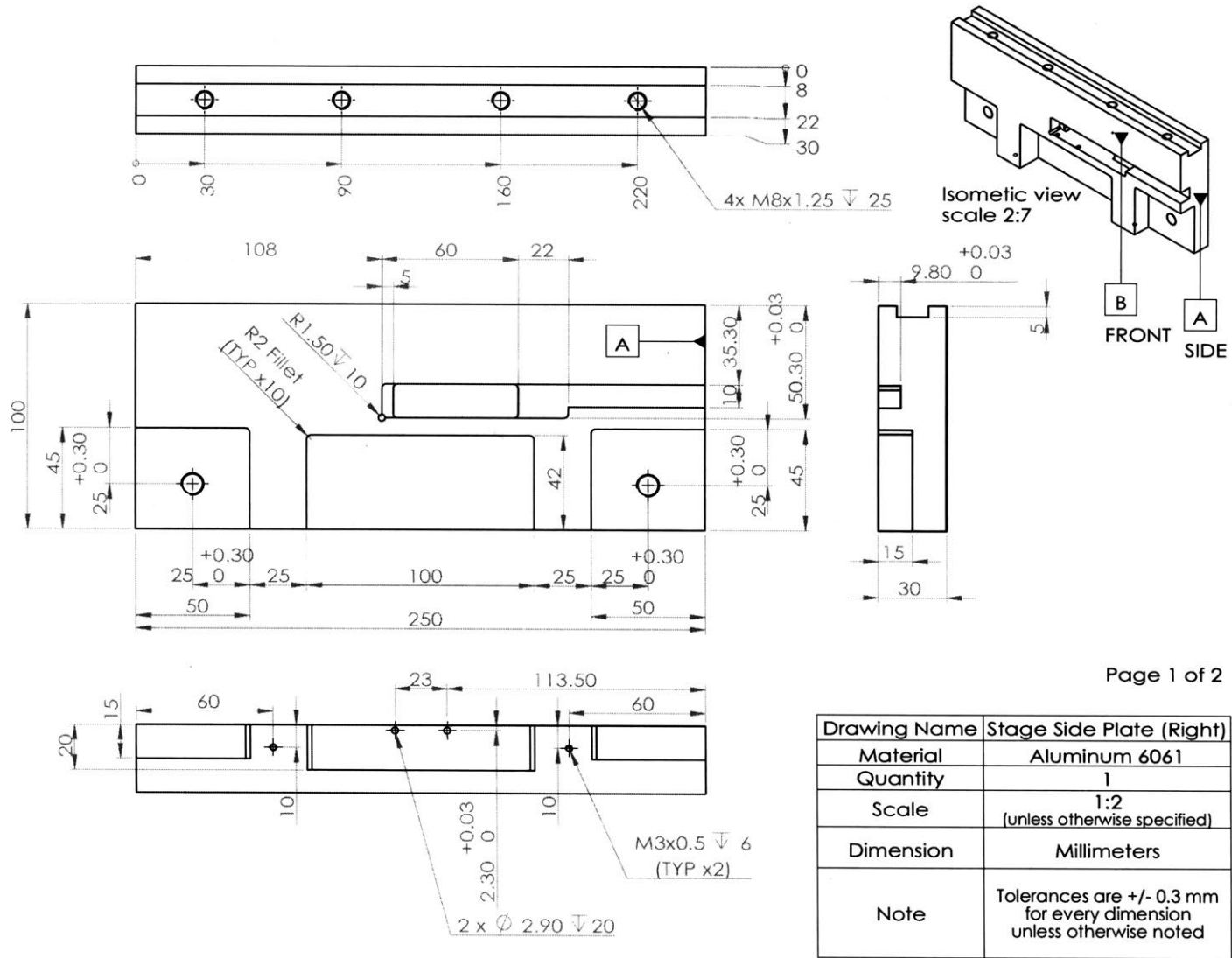
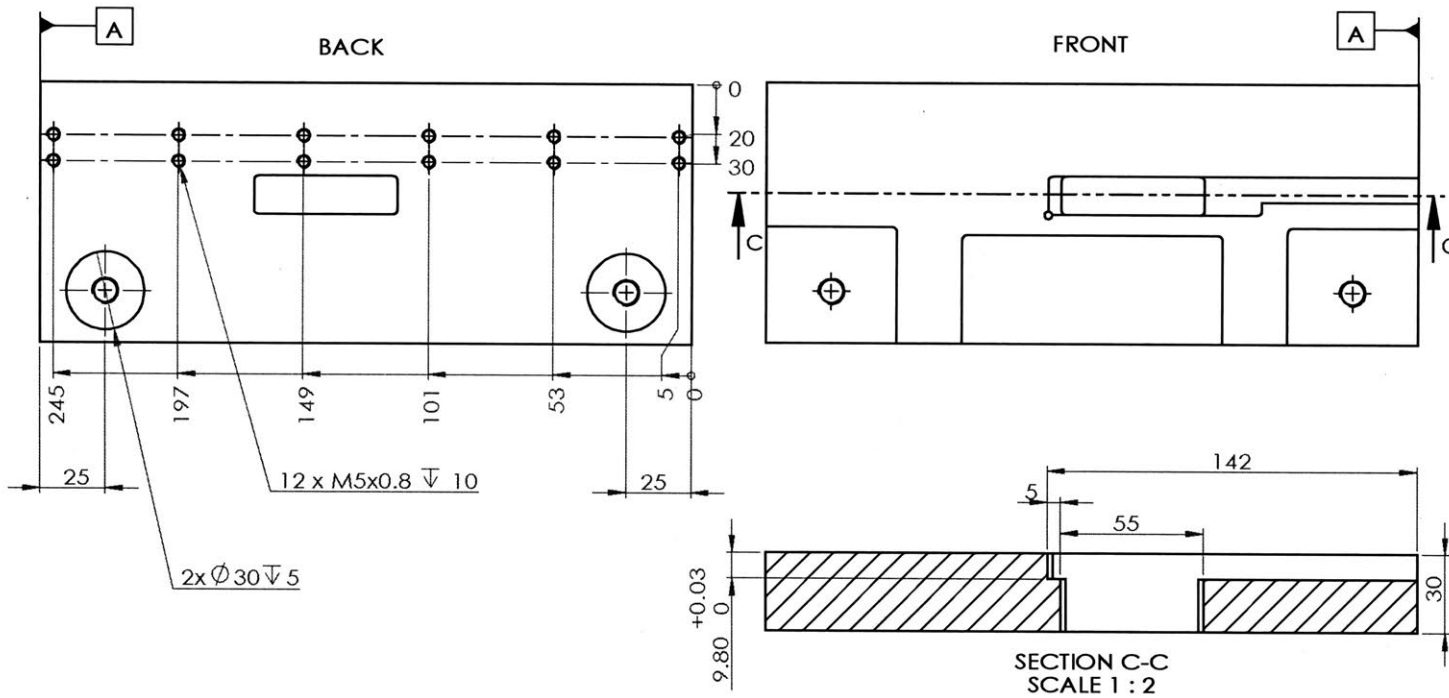


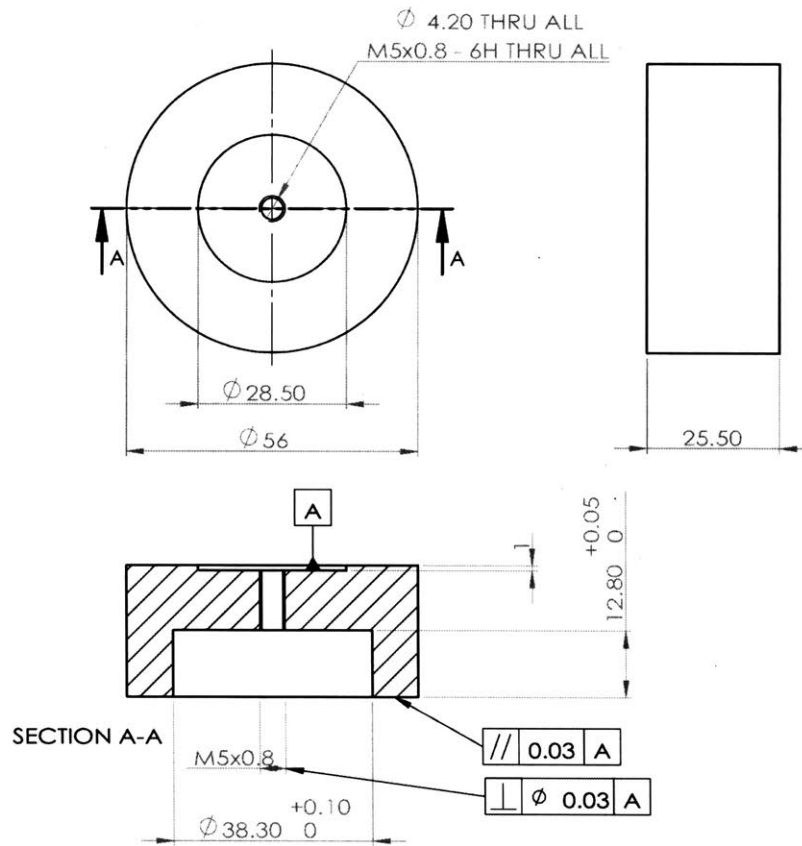
Figure A-5: Drawing of the stage right-side plate. Page 1 of 2.



Page 2 of 2

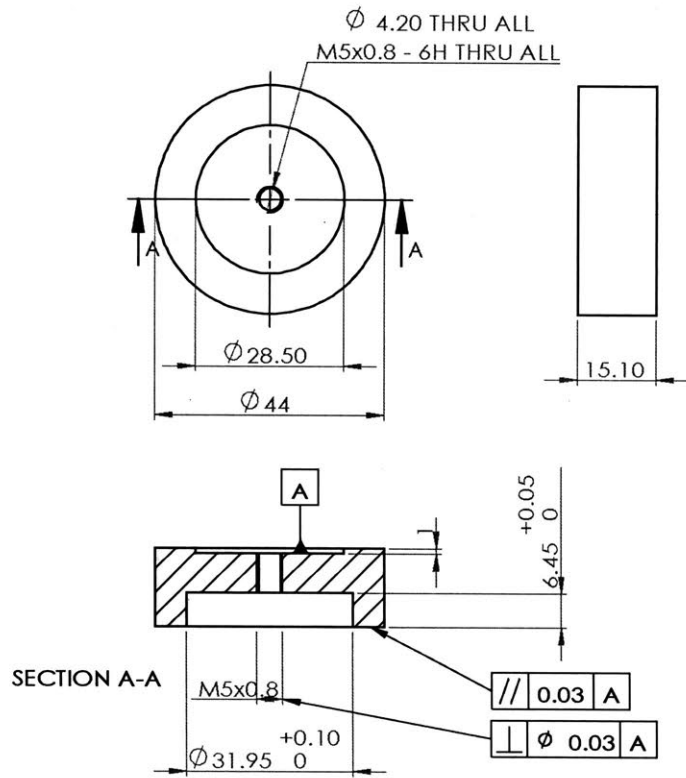
Drawing Name	Stage Side Plate(Right)
Material	Aluminum 6061
Quantity	1
Scale	1:2 (unless otherwise specified)
Dimension	Millimeters
Note	Tolerances are +/- 0.3 mm for every dimension unless otherwise noted

Figure A-6: Drawing of the stage right-side plate. Page 2 of 2.



Drawing Name	Holding Magnet Housing Type1
Material	1018 Steel
Quantity	2
Scale	1:1 (unless otherwise specified)
Dimension	Millimeters
Note	Tolerances are +/- 0.3 mm for every dimension unless otherwise noted

Figure A-7: Drawing of the top holding magnet for preloading top air bearings.



Drawing Name	Holding Magnet Housing Type2
Material	1018 Steel
Quantity	1
Scale	1:1 (unless otherwise specified)
Dimension	Millimeters
Note	Tolerances are +/- 0.3 mm for every dimension unless otherwise noted

Figure A-8: Drawing of the side holding magnet for preloading side air bearings.

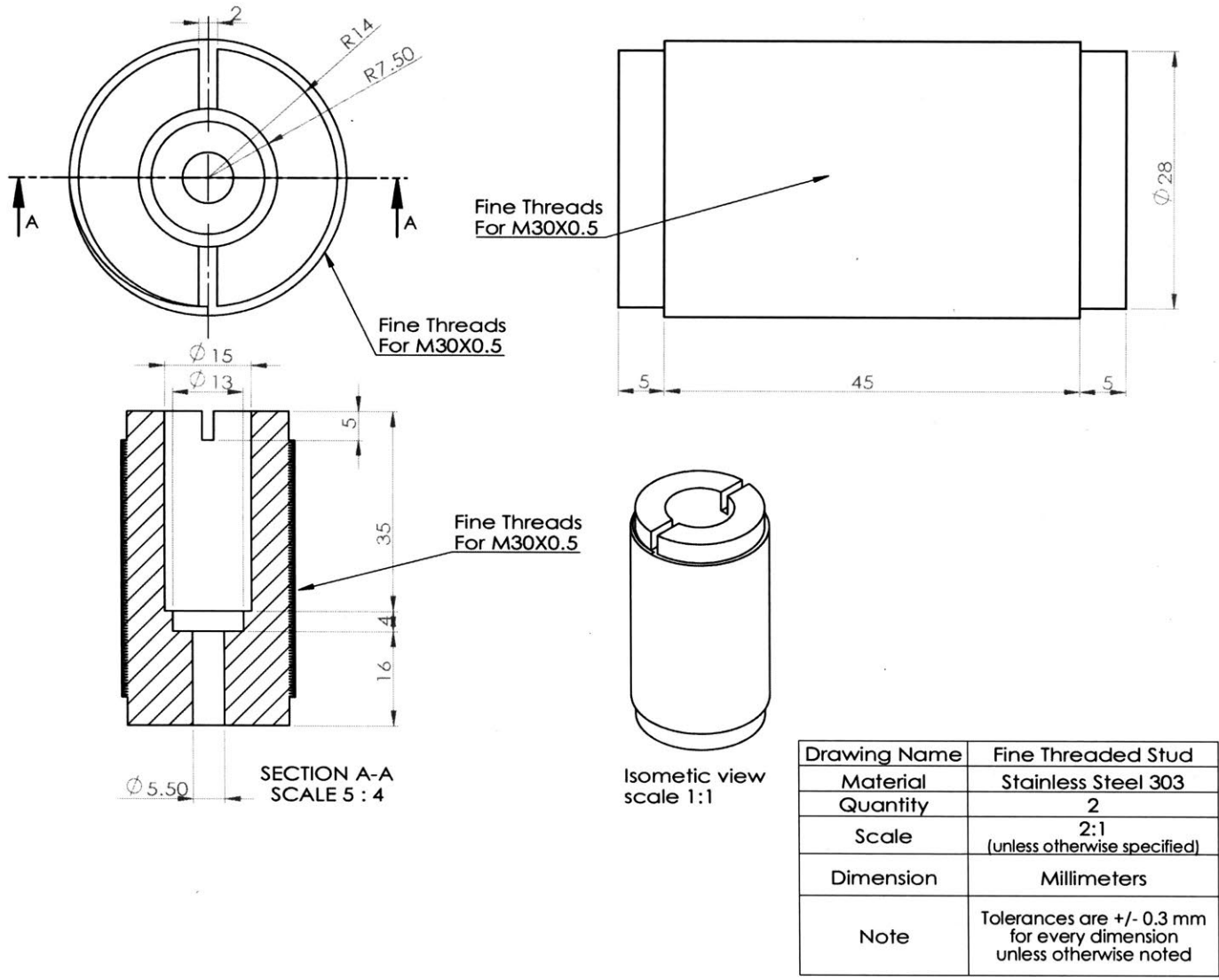
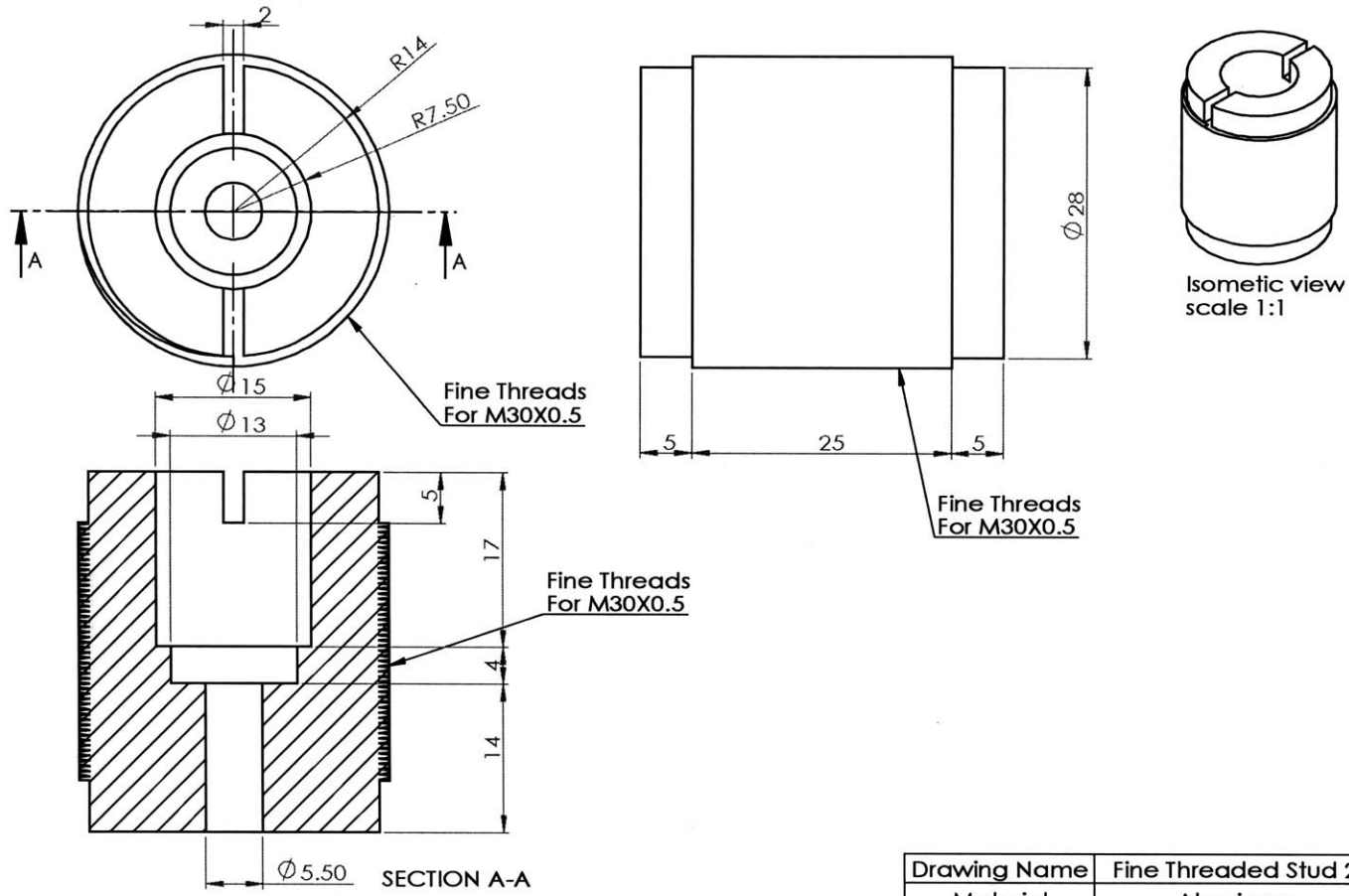


Figure A-9: Drawing of the threaded stud for the top holding magnet to control the preloading force in the normal (Z) direction.



Drawing Name	Fine Threaded Stud 2
Material	Aluminum
Quantity	1
Scale	2:1 (unless otherwise specified)
Dimension	Millimeters
Note	Tolerances are +/- 0.3 mm for every dimension unless otherwise noted

Figure A-10: Drawing of the threaded stud for the side holding magnet to control the preloading force in the cross-scan (X) direction.

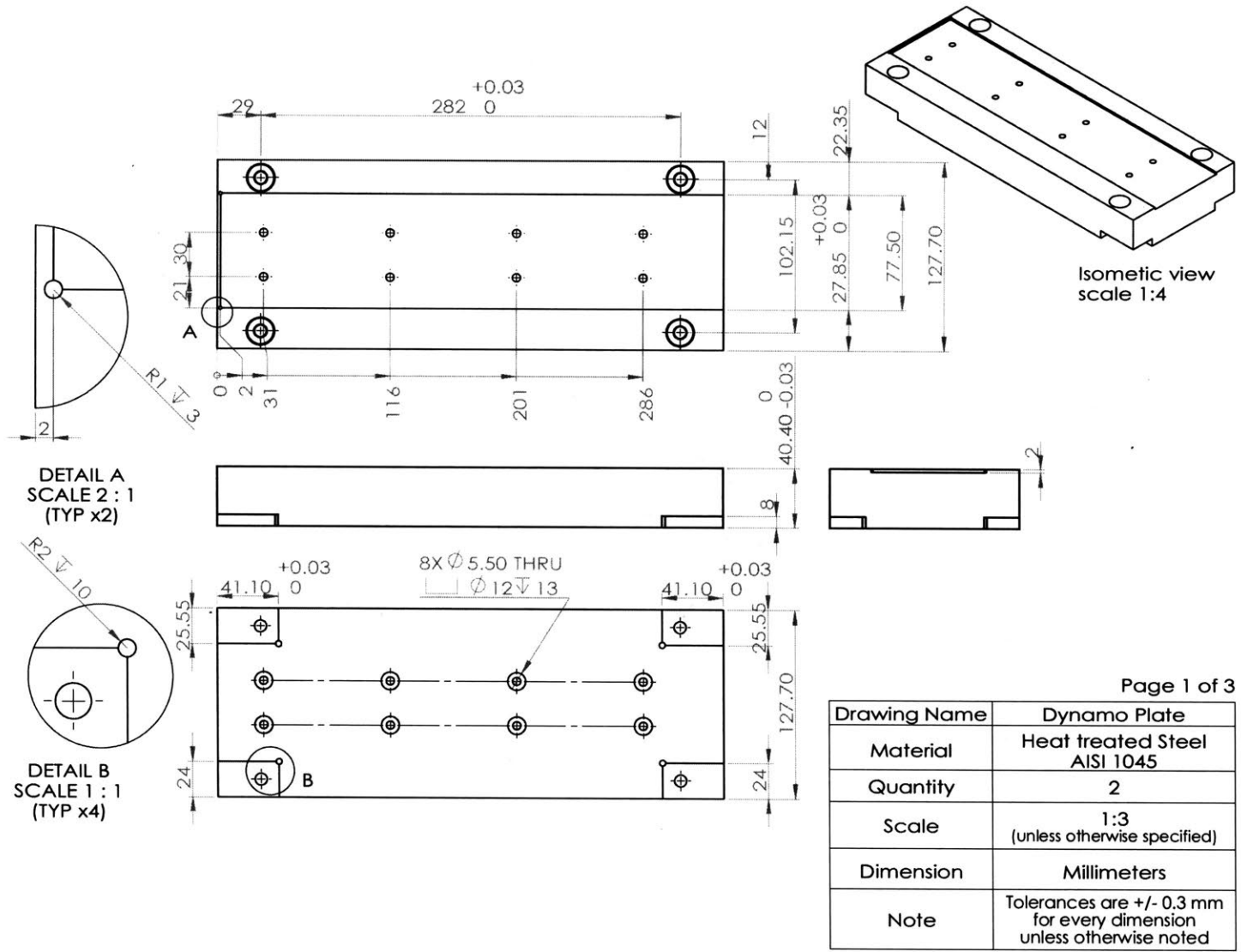


Figure A-11: Drawing of the mounting plate for the conventional motor (TL18 by Tecnotion), also serving as the dynamometer upper plate. Page 1 of 3.

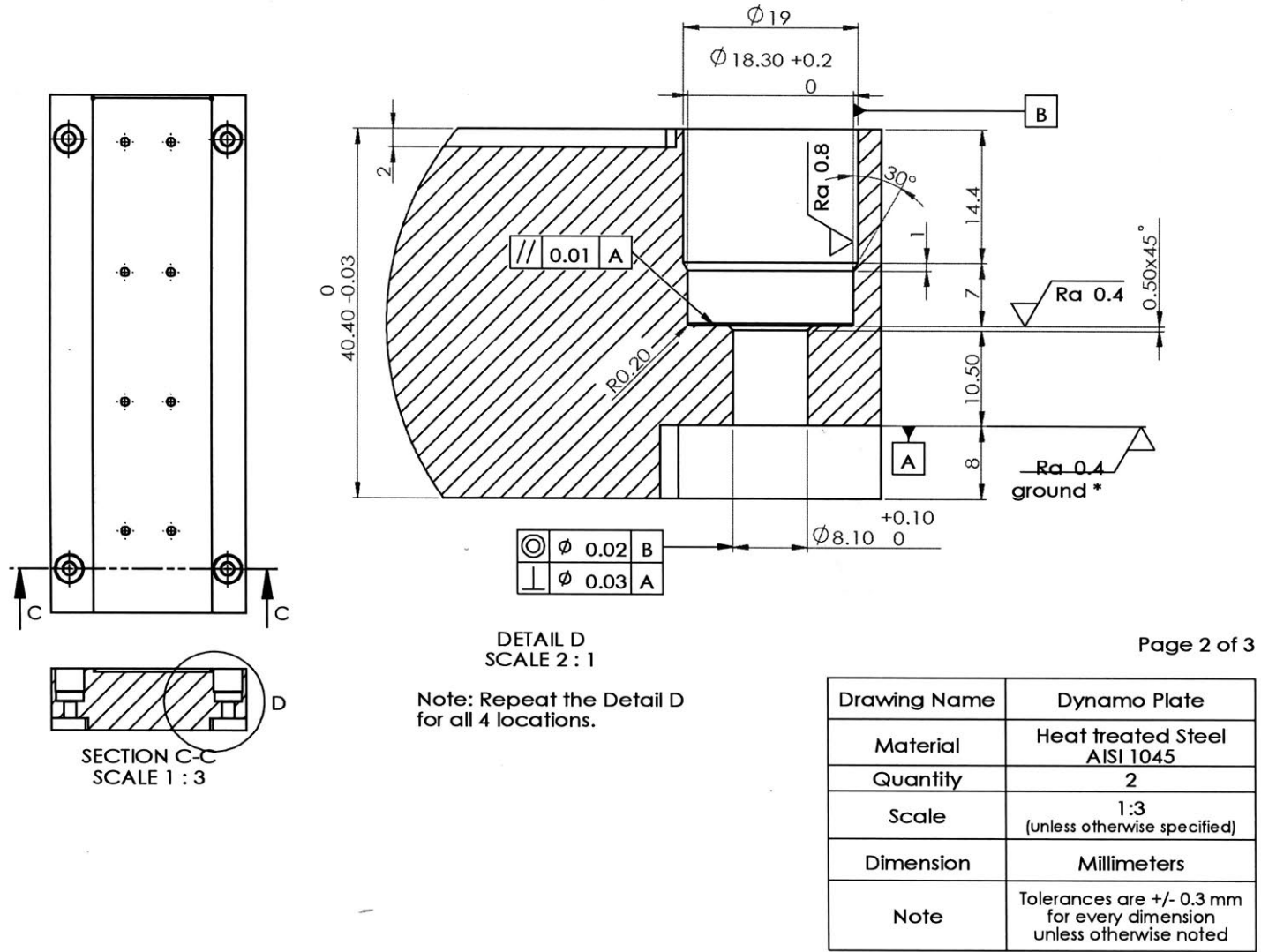


Figure A-12: Drawing of the mounting plate for the conventional motor (TL18 by Tecnotion), also serving as the dynamometer upper plate. Page 2 of 3.

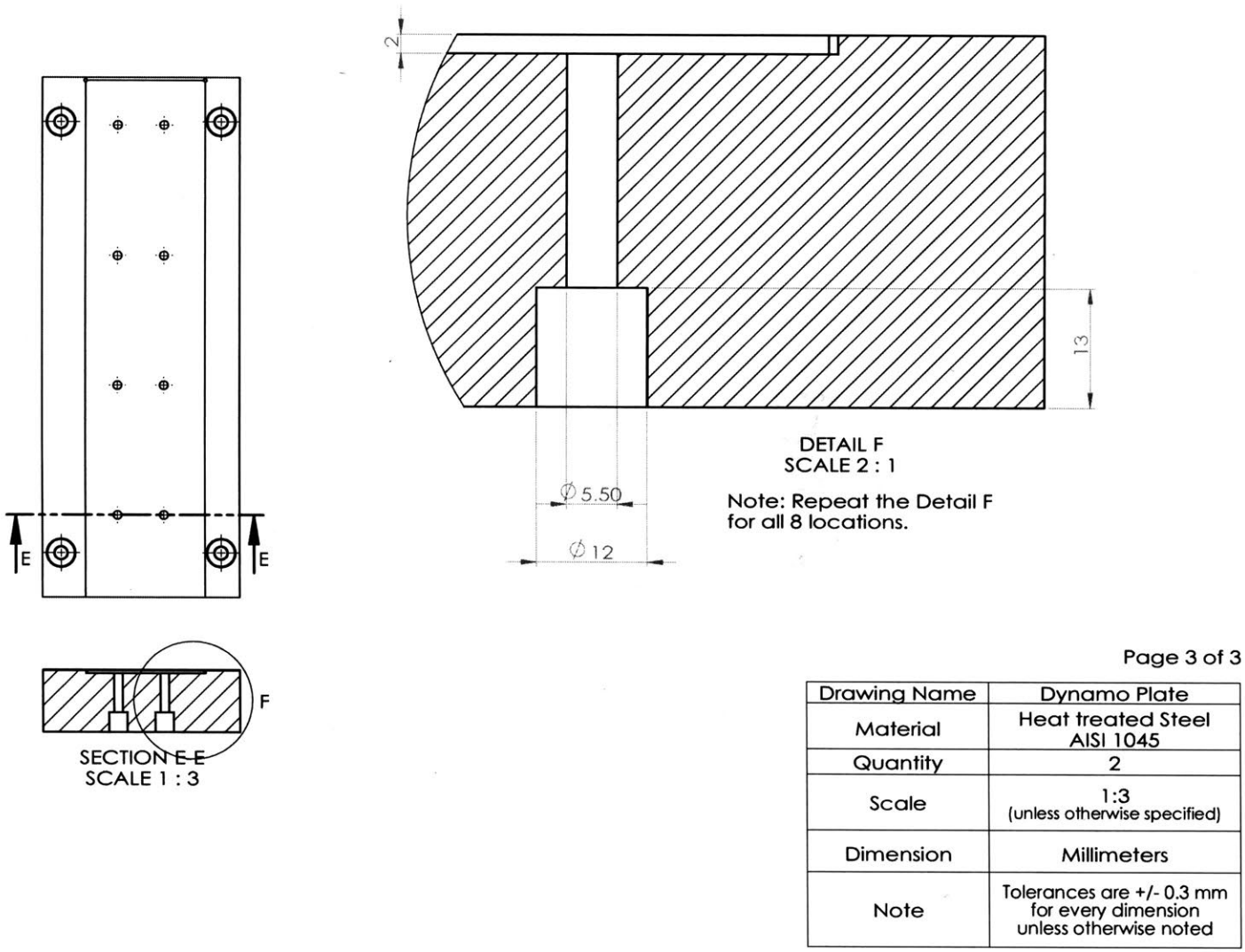
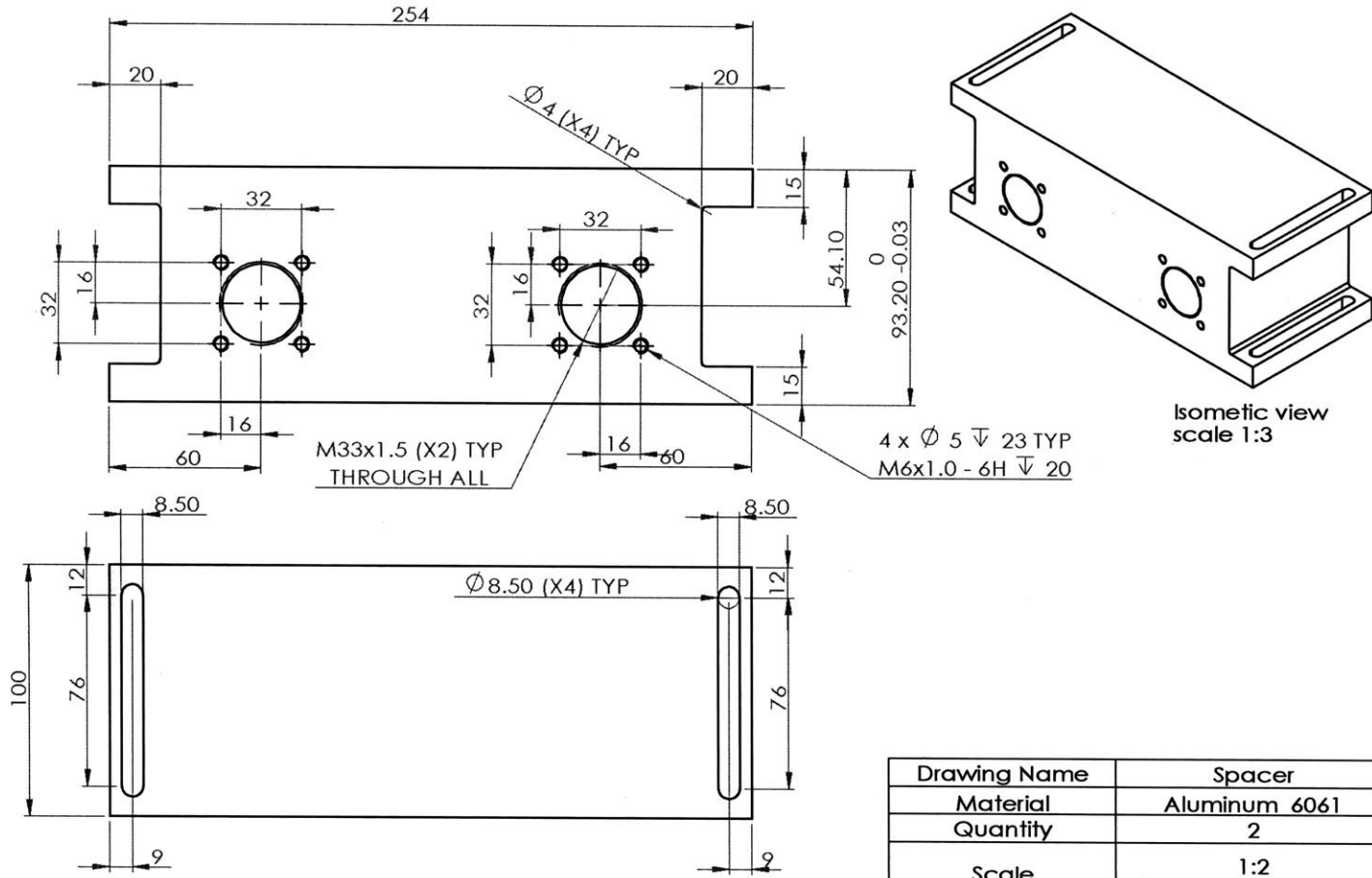
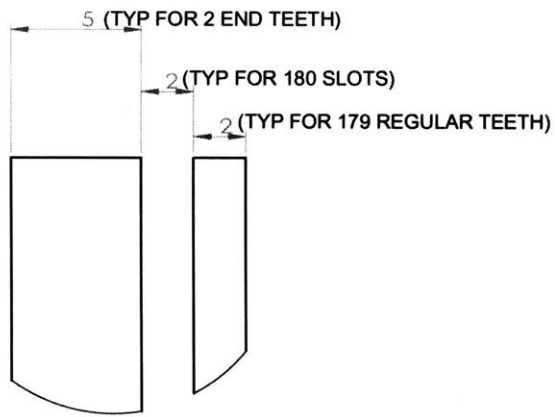
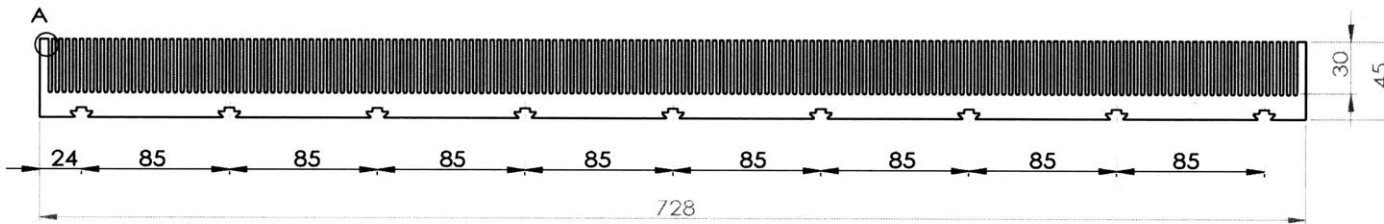


Figure A-13: Drawing of the mounting plate for the conventional motor (TL18 by Tecnotion), also serving as the dynamometer upper plate. Page 3 of 3.



Drawing Name	Spacer
Material	Aluminum 6061
Quantity	2
Scale	1:2 (unless otherwise specified)
Dimension	Millimeters
Note	Tolerances are +/- 0.3 mm for every dimension unless otherwise noted

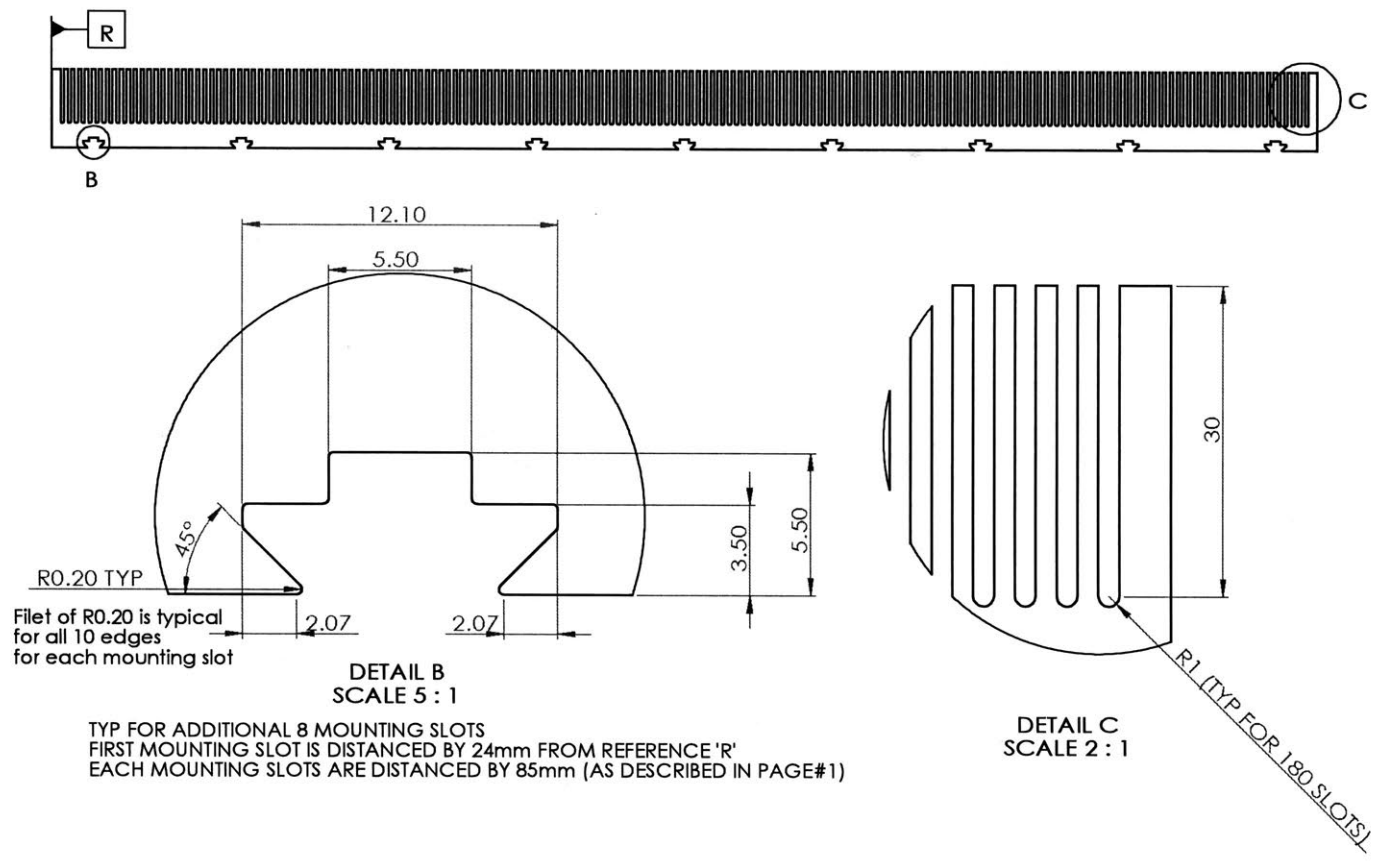
Figure A-14: Drawing of the spacer, providing correct space for the double-sided stage configuration. The spacer also serves as the mounting plate for the shock absorbers.



DETAIL A
SCALE 5 : 1

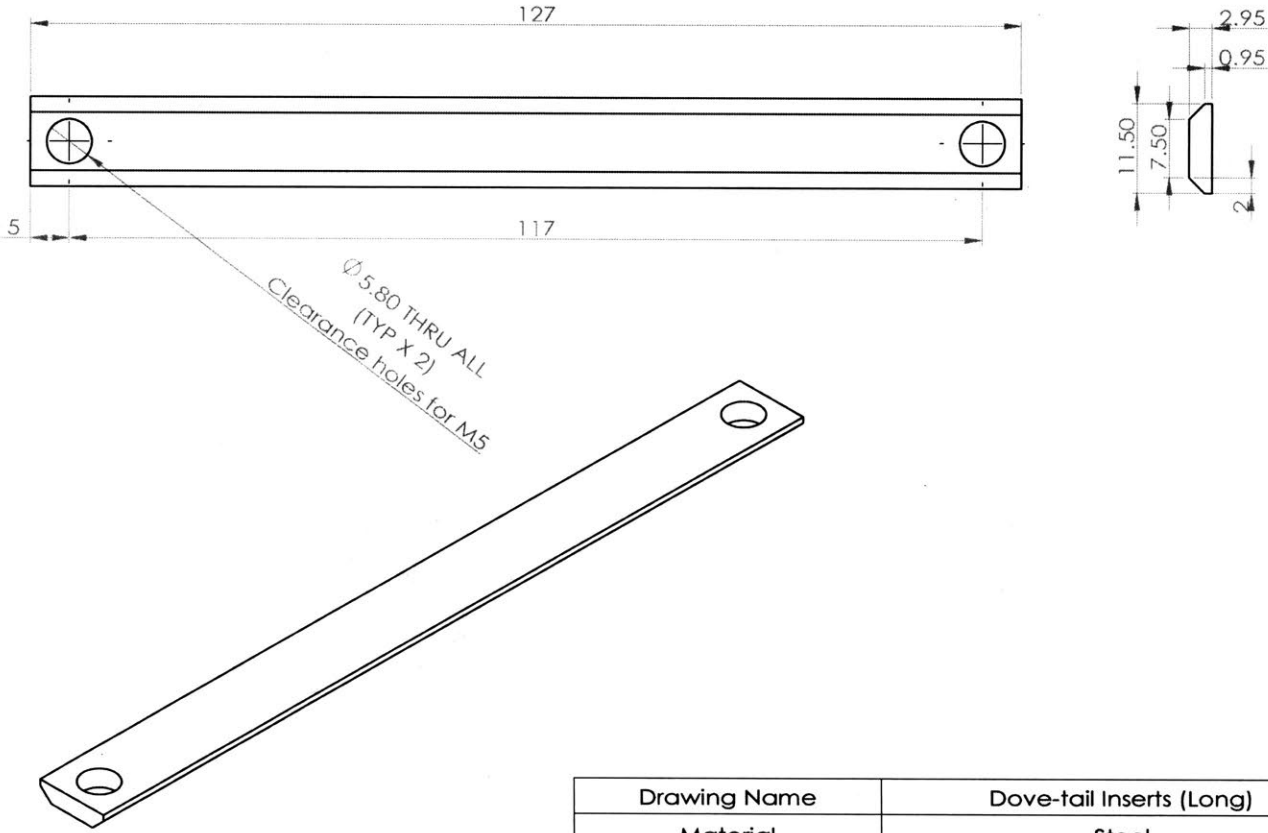
Drawing Name	Lamination
Material	M19
Quantity	2 Stators
Scale	1:3 (unless otherwise specified)
Dimension	Millimeters (Tolerance: +/-0.05mm)
Note on Lamination	- Lamination Thickness: 350 micrometers - Number of slot: 180
Stack Width	52 mm +/- 1 Lamination

Figure A-15: Drawing of the stator laminations of our new fine-tooth motor. Page 1 of 2.



PAGE 2/2

Figure A-16: Drawing of the stator laminations of our new fine-tooth motor. Page 2 of 2.



Drawing Name	Dove-tail Inserts (Long)
Material	Steel
Quantity	14
Scale	3:2 (unless otherwise specified)
Dimension	Millimeters (Tolerance: -0.05mm)

Figure A-17: Drawing of the dove-tail insert used to mount our new fine-tooth motor stator.

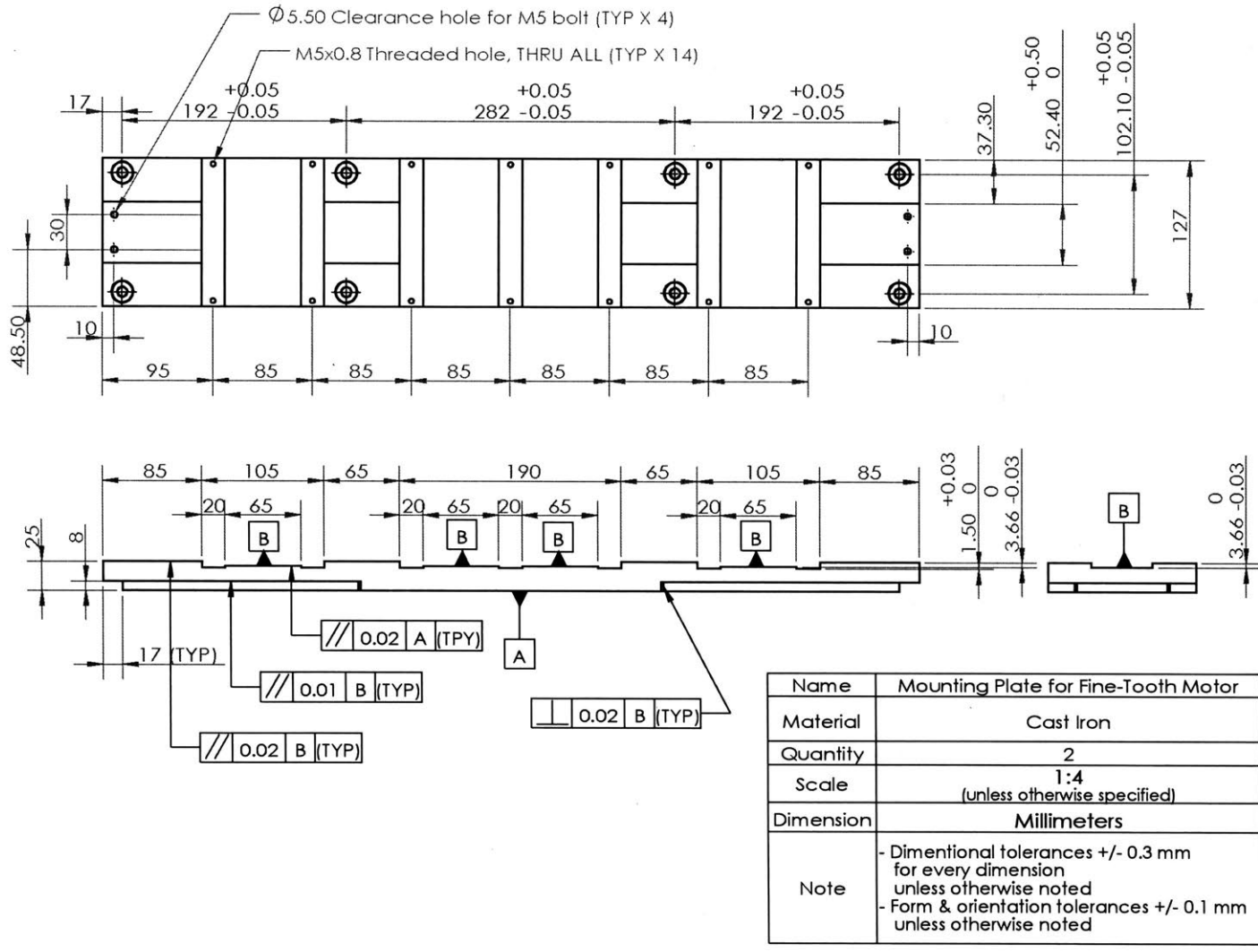
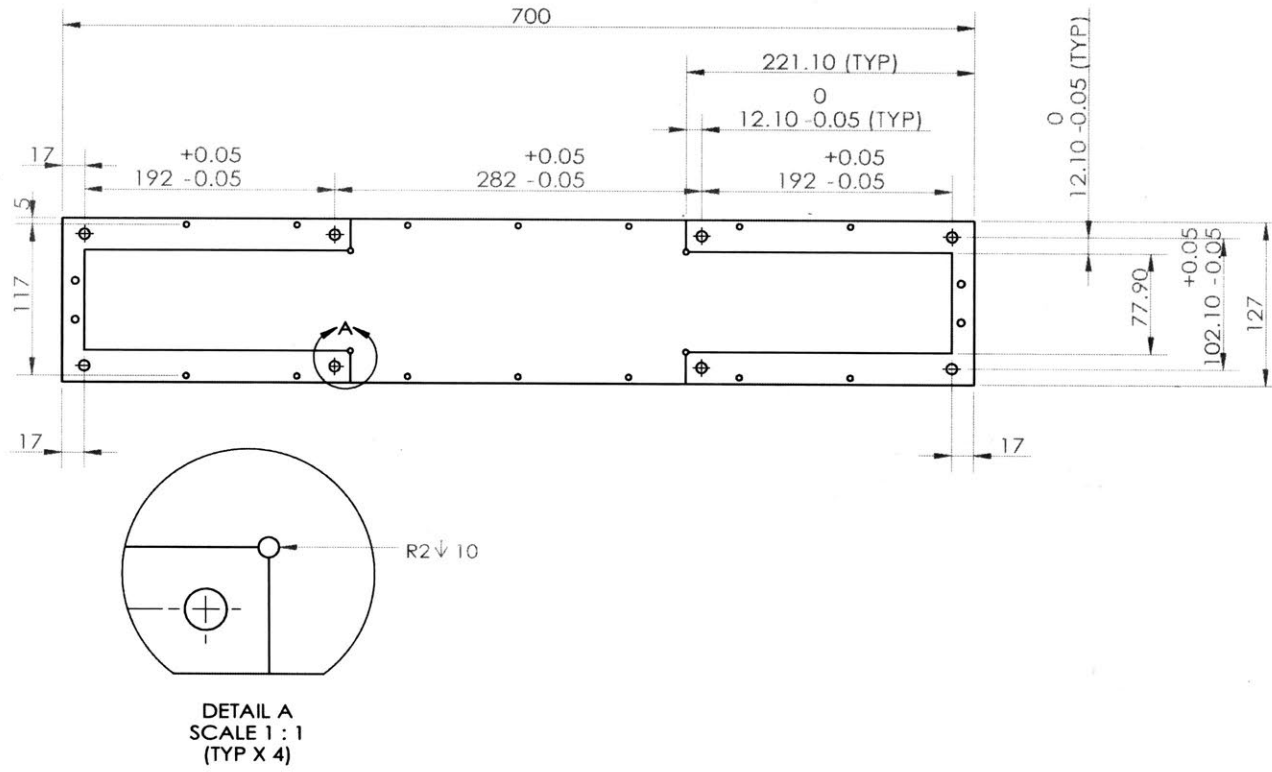


Figure A-18: Drawing of the mounting plate for our new fine-tooth motor, also serving as the dynamometer upper plate. Page 1 of 4.



Page 2 of 4

Figure A-19: Drawing of the mounting plate for our new fine-tooth motor, also serving as the dynamometer upper plate. Page 2 of 4.

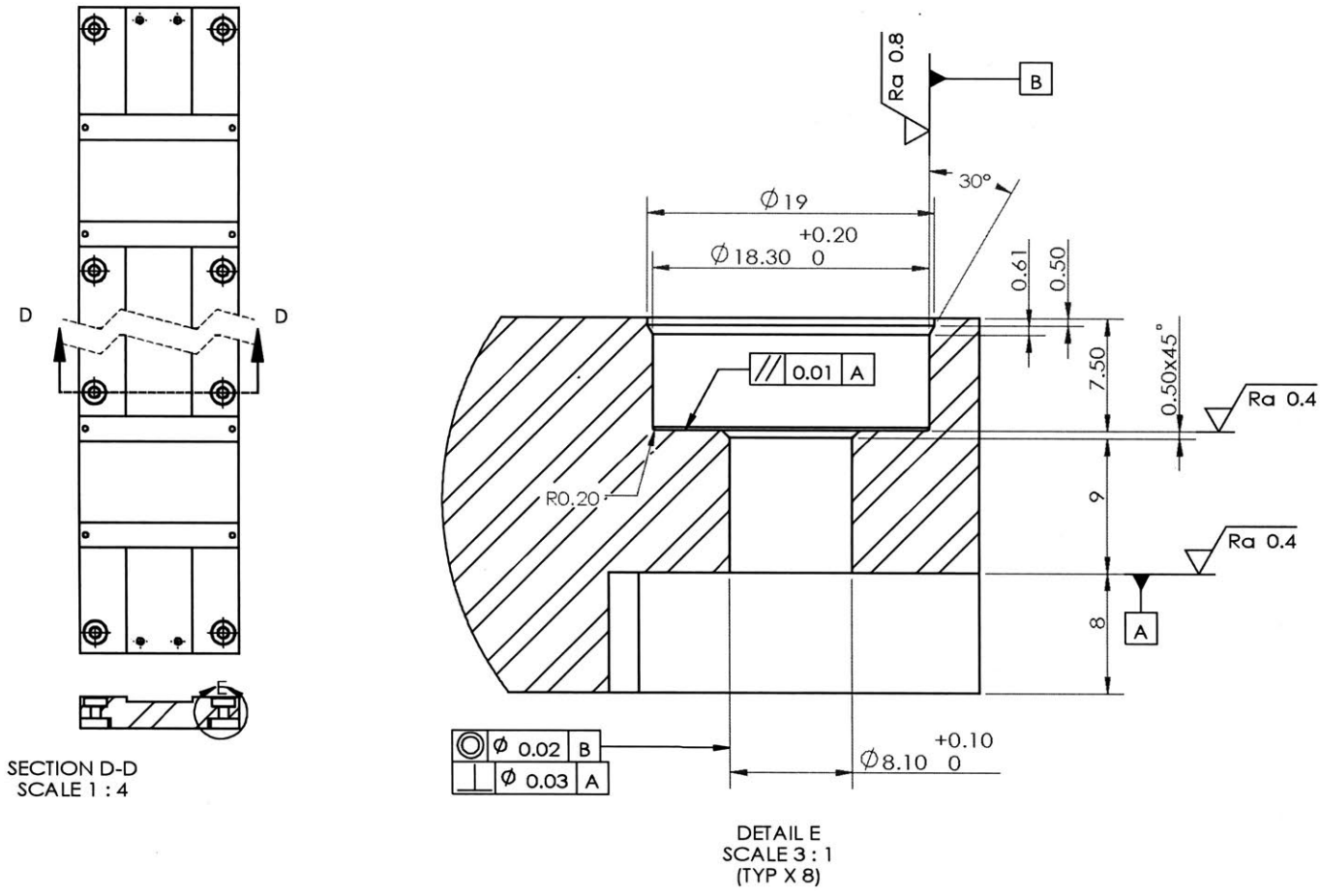
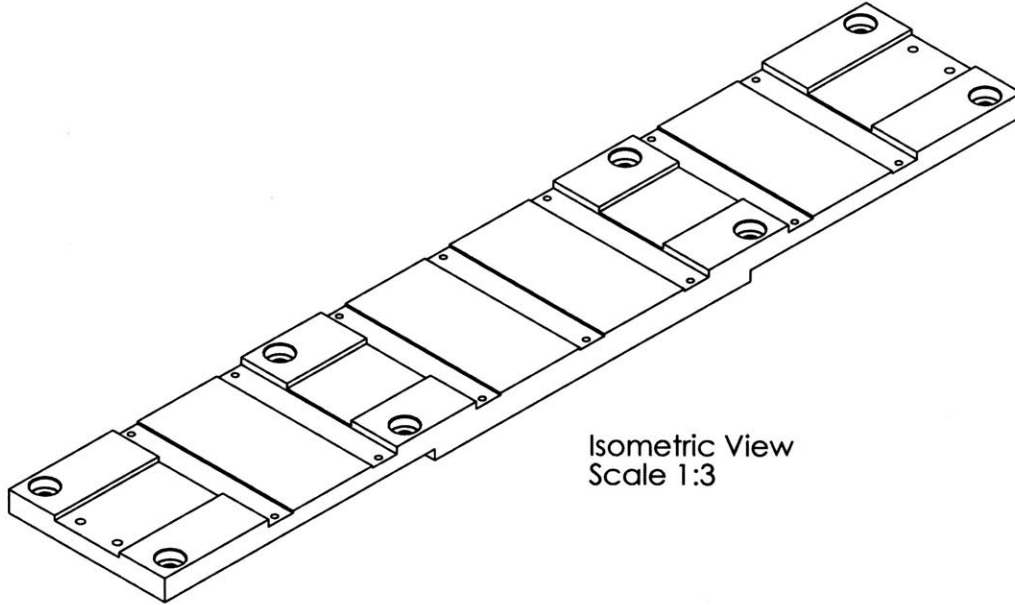
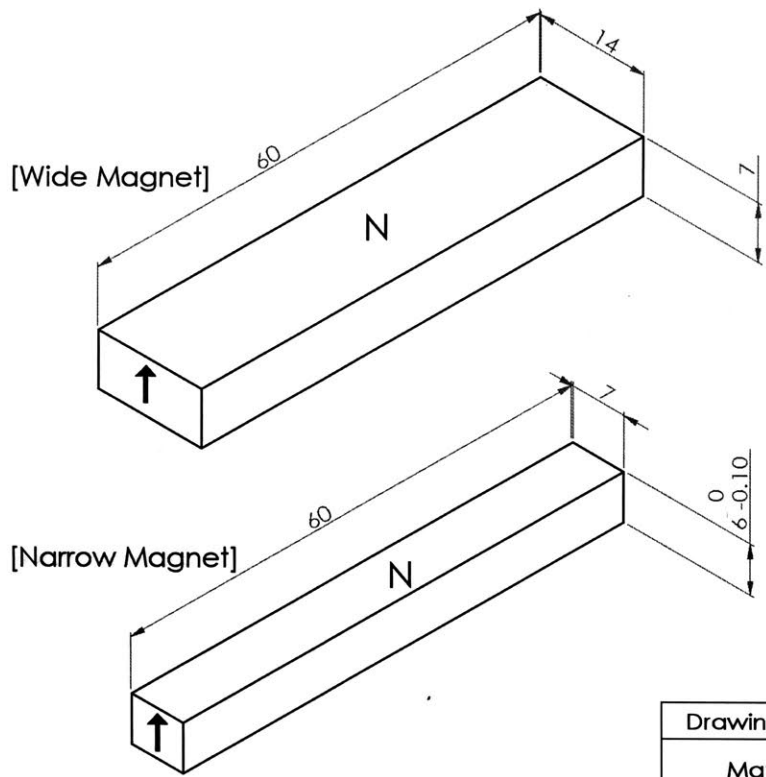


Figure A-20: Drawing of the mounting plate for our new fine-tooth motor, also serving as the dynamometer upper plate. Page 3 of 4.



Isometric View
Scale 1:3

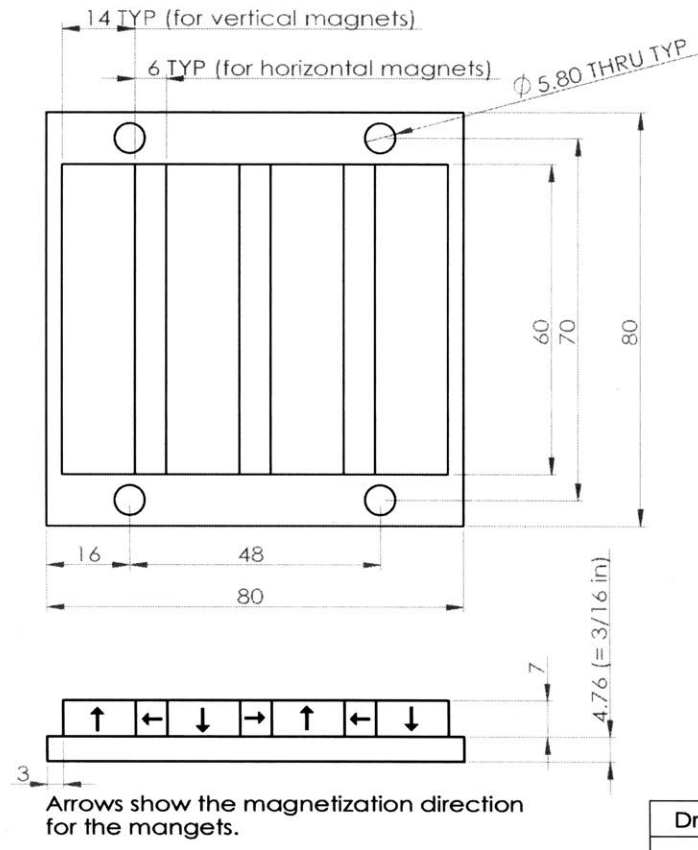
Figure A-21: Drawing of the mounting plate for our new fine-tooth motor, also serving as the dynamometer upper plate. Page 4 of 4.



[Arrow and 'N' (for North) indicate the direction of magnetization]

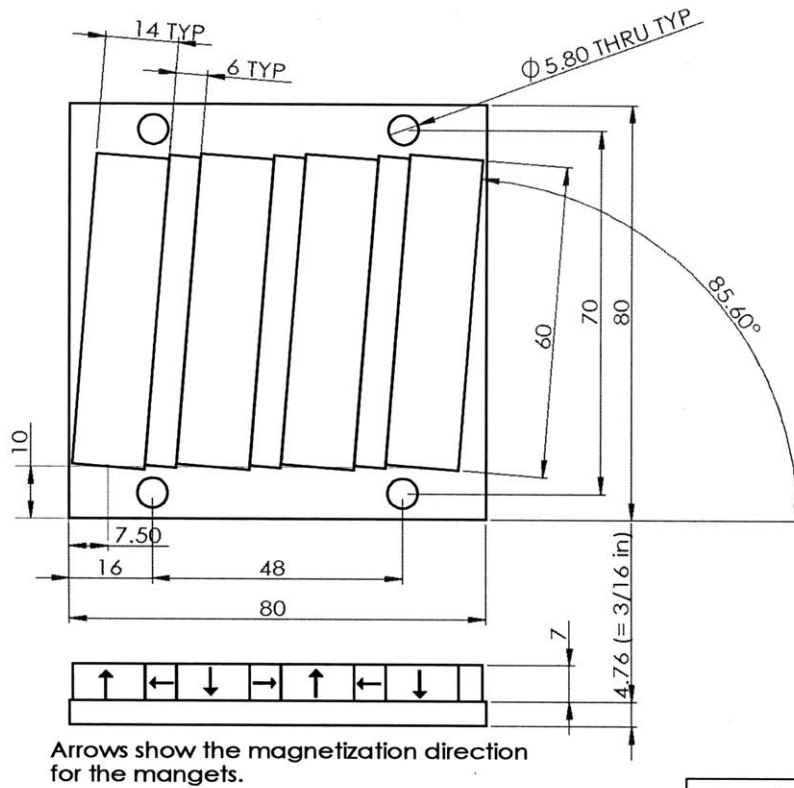
Drawing Name	Magnets
Material	N42 Neodymium Magnet with Nickel Plated
Quantity	65 for Wide Magnet 75 for Narrow Magnet
Scale	2:1 (unless otherwise specified)
Dimension	Millimeters (Tolerance: +/-0.05mm unless otherwise specified)

Figure A-22: Drawing of the vertical (wide) and horizontal (narrow) magnets used in the magnet tracks of our new fine-tooth motor.



Drawing Name	Magnet Plate (Short & Nonskewed)
Material	- PM: N42 Grade Neodymium Magnets - Back Iron: 1018 Steel
Quantity	2 Magnet Plates
Scale	1:1 (unless otherwise specified)
Dimension	Millimeters (Tolerance: +/-0.1mm)
Magnet Array	- Halbach Array

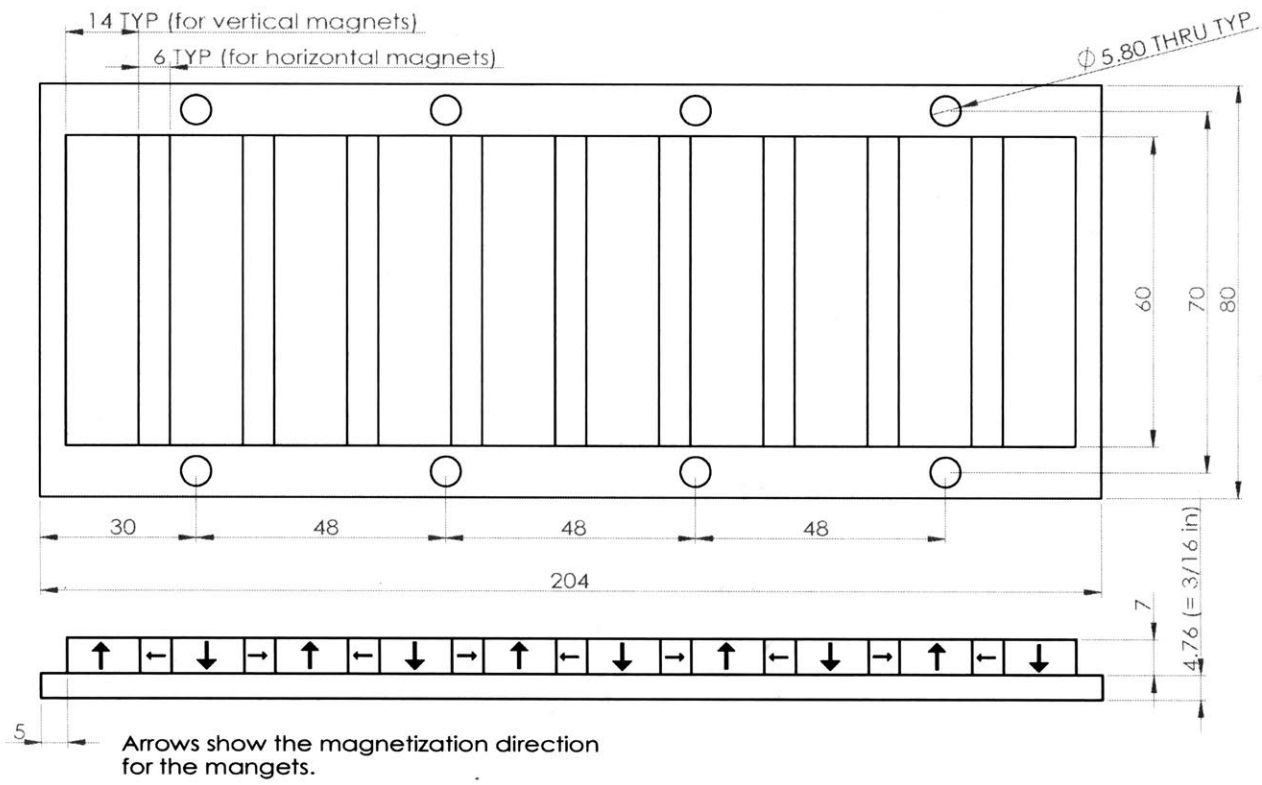
Figure A-23: Drawing of the non-skewed magnet track of our new fine-tooth motor. Short version used in the single-sided motor configuration.



Arrows show the magnetization direction for the magnets.

Drawing Name	Magnet Plate (Short & Skewed)
Material	- PM: N42 Grade Neodymium Magnets - Back Iron: 1018 Steel
Quantity	2 Magnet Plates
Scale	1:1 (unless otherwise specified)
Dimension	Millimeters (Tolerance: +/-0.1mm)
Magnet Array	- Halbach Array - Magnet size is the same as nonskewed plate

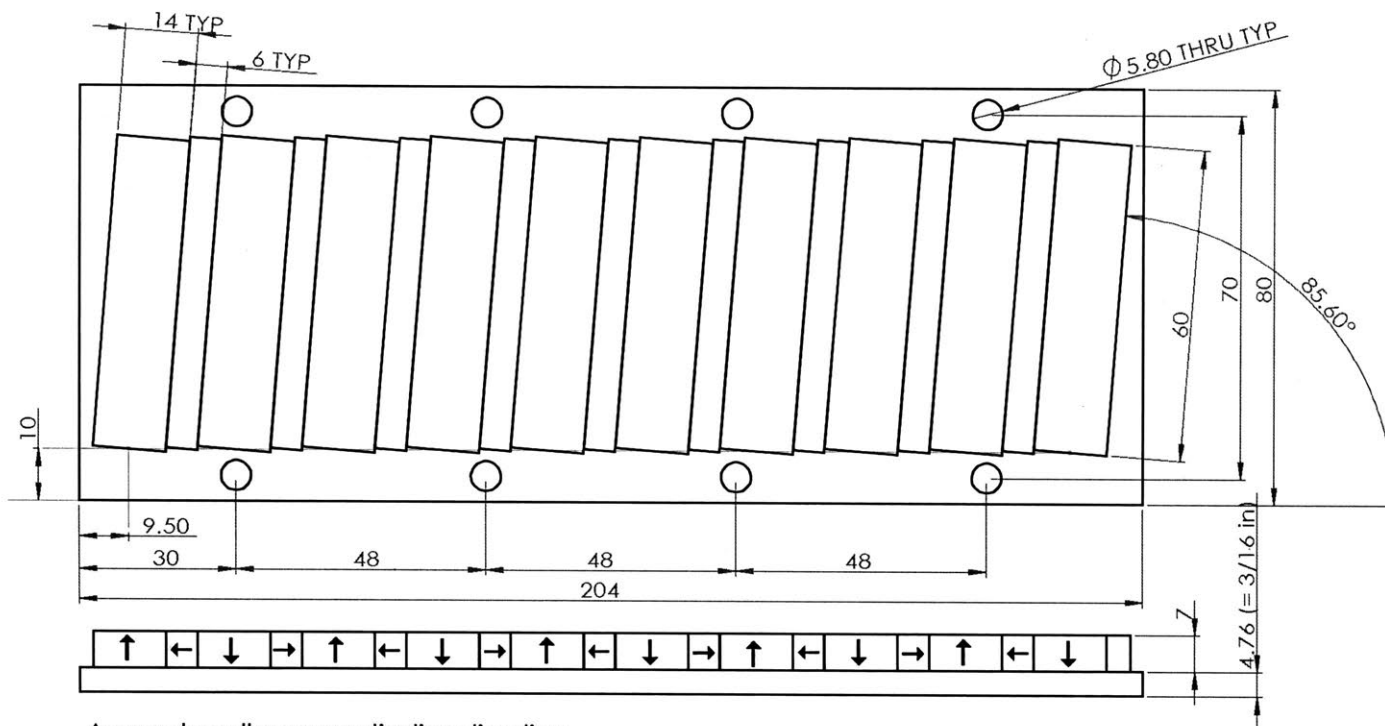
Figure A-24: Drawing of the skewed magnet track of our new fine-tooth motor. Short version used in the single-sided motor configuration.



Arrows show the magnetization direction for the magnets.

Drawing Name	Magnet Plate (Long & Nonskewed)
Material	- PM: N42 Grade Neodymium Magnets - Back Iron: 1018 Steel
Quantity	2 Magnet Plates
Scale	1:1 (unless otherwise specified)
Dimension	Millimeters (Tolerance: +/-0.1mm)
Magnet Array	- Halbach Array

Figure A-25: Drawing of the non-skewed magnet track of our new fine-tooth motor. Long version to be used in the double-sided motor configuration.



Arrows show the magnetization direction for the magnets.

Drawing Name	Magnet Plate (Long & Skewed)
Material	- PM: N42 Grade Neodymium Magnets - Back Iron: 1018 Steel
Quantity	2 Magnet Plates
Scale	1:1 (unless otherwise specified)
Dimension	Millimeters (Tolerance: +/-0.1mm)
Magnet Array	- Halbach Array - Magnet size is the same as nonskewed plate

Figure A-26: Drawing of the skewed magnet track of our new fine-tooth motor. Long version to be used in the double-sided motor configuration.

Appendix B

List of Vendors and Manufacturers

In this appendix, we provide a list of vendors and manufacturers we worked with for the work discussed in this thesis. The list is in the alphabetical order.

- **ACE Controls Inc.**

- 23435 Industrial Park Dr., Farmington, MI 48335, USA (800-521-3320)
- Website: <http://www.acecontrols.com>
<http://www.pearse-bertram.com> (Distributor in Massachusetts)
- Contact: Joshua Lambert (JLambert@pearse-bertram.com)

- **Advanced Motion Controls**

- 3805 Calle Tecate, Camarillo, CA 93012, USA (805-389-1935)
- Website: <http://www.a-m-c.com>
- Contact: Eric Covella (ecovella@a-m-c.com)

- **EIS**

- 2825 Southampton Road, Philadelphia, PA 19154, USA (215-673-7220)
- EIS-Philadelphia Electrical Market (Motor Insulation and Sleeving)
- Website: <http://eis-inc.com>

- **Fred Sommerhalter**
 - Motor Builder
 - Contact: fsommerh@optonline.net

- **Kistler USA**
 - 75 John Glenn Drive, Amherst, NY 14228-2171, USA (716-691-5100)
 - Website: <https://www.kistler.com/us/en>
 - Contact: Spence Wende (spence.wende@kistler.com), sales.us@kistler.com

- **K&J Magnetics, Inc.**
 - 18 Appletree Ln., Pipersville, PA 18947, USA (215-766-8055)
 - Website: <http://www.kjmagnetics.com>
 - Contact: contactus@kjmagnetics.com

- **McMaster-Carr**
 - 200 New Canton Way, Robbinsville, NJ 08691-2343, USA (609-689-3000)
 - Website: <https://www.mcmaster.com>
 - Contact: nj.sales@mcmaster.com

- **MWS Wire Industries**
 - 31200 Cedar Valley Dr., Westlake Village, CA 91362, USA (818-991-8553)
 - Website: <http://www.mwswire.com/>

- **National Instruments**
 - 11500 Mopac Expwy Austin, TX 78759-3504, USA (512-683-0100)
 - Website: <http://www.ni.com>
 - Contact: NI Support Group (support@ni.com)

- **New Way Air Bearings**

- 50 McDonald Blvd. Aston, PA 19014, USA (610-494-6700)
- Website: <http://www.newwayairbearings.com>
- Contact: Drew Devitt (CTO, ddevitt@newwayairbearings.com),
Tim Claffey (tclaffey@newwayairbearings.com)

- **Ningbo Yunsheng Magnet Devices Technology Co., LTD.**

- Anju North Road, Xiaogang, Beilun, Ningbo, Zhejiang, China
(Zip Code 315801, US Phone 650-827-7928)
- Contact: Julia Zhou (juliazhou@yunshengusa.com)
George Zhang (george.zhang@yunshengusa.com)

- **PCB Piezotronics**

- 3425 Walden Avenue, Depew, NY 14043-2495, USA (800-828-8840)
- Website: <http://www.pcb.com>
- Contact: info@pcb.com

- **Polaris Laser Laminations, LLC.**

- 2725 Norton Creek Drive, West Chicago, IL 60185, USA (630-444-0760)
- Website: <http://polarislaserlaminations.com>
- Contact: Lynn Girard (lgirard@polarislaserlaminations.com)

- **Renishaw**

- 5277 Trillium Blvd, Hoffman Estates, IL 60192, USA (631-321-0418)
- Website: <http://www.renishaw.com>
- Contact: Charlie Falco (charlie.falco@renishaw.com)
Tim Goggin (Tim.Goggin@renishaw.com)

- **Tecnotion**

- Twentepoort West 15, 7609 RD Almelo, Netherlands (+31-546-536-300)
- Website: <http://www.tecnotion.com>
- Contact: Erwin Hofste (Erwin.Hofste@Tecnotion.com)

- **Tsubaki KabelSchlepp**

- 301 E. Marquardt Dr., Wheeling, IL 60090, USA (847-459-9500)
- Website: <http://www.ustsubaki.com>
<http://www.motionindustries.com> (Distributor in MA)
- Contact: Mark Tanguay (Mark.Tanguay@motion-ind.com)

Bibliography

- [1] G. Moore, "Cramming more components onto integrated circuits," *Electronics Magazine*, vol. 38, no. 8, pp. 33–35, 1995.
- [2] H. Butler, "Position control in lithographic equipment," *IEEE Control Systems Magazine*, vol. 31, no. 5, pp. 28–47, 2011.
- [3] M. G. Angle, "Modeling, design, and optimization of permanent magnet synchronous machines," PhD Dissertation, Massachusetts Institute of Technology, Department of Electrical Engineering and Computer Science, 2016.
- [4] D. E. Cameron, J. H. Lang, and S. D. Umans, "The origin and reduction of acoustic noise in doubly salient variable-reluctance motors," *Industry Applications, IEEE Transactions on*, vol. 28, no. 6, pp. 1250–1255, 1992.
- [5] D. E. Cameron, "Origin and reduction of acoustic noise in variable-reluctance motors," Master's thesis, Massachusetts Institute of Technology, Department of Electrical Engineering, 1990.
- [6] C.-Y. Wu and C. Pollock, "Analysis and reduction of vibration and acoustic noise in the switched reluctance drive," *Industry Applications, IEEE Transactions on*, vol. 31, no. 1, pp. 91–98, 1995.
- [7] C. Pollock and C.-Y. Wu, "Acoustic noise cancellation techniques for switched reluctance drives," *Industry Applications, IEEE Transactions on*, vol. 33, no. 2, pp. 477–484, 1997.
- [8] R. S. Colby, F. M. Mottier, and T. J. Miller, "Vibration modes and acoustic noise in a four-phase switched reluctance motor," *Industry Applications, IEEE Transactions on*, vol. 32, no. 6, pp. 1357–1364, 1996.
- [9] R. Islam and I. Husain, "Analytical model for predicting noise and vibration in permanent-magnet synchronous motors," *Industry Applications, IEEE Transactions on*, vol. 46, no. 6, pp. 2346–2354, 2010.
- [10] Y. Asano, Y. Honda, H. Murakami, Y. Takeda, and S. Morimoto, "Novel noise improvement technique for a pmsm with concentrated winding," in *Power Conversion Conference, 2002. PCC-Osaka 2002. Proceedings of the*, vol. 2. IEEE, 2002, pp. 460–465.

- [11] B. Cassoret, R. Corton, D. Roger, and J.-F. Brudny, "Magnetic noise reduction of induction machines," *Power Electronics, IEEE Transactions on*, vol. 18, no. 2, pp. 570–579, 2003.
- [12] J. Le Besnerais, V. Lanfranchi, M. Hecquet, P. Brochet, and G. Friedrich, "Prediction of audible magnetic noise radiated by adjustable-speed drive induction machines," *Industry Applications, IEEE Transactions on*, vol. 46, no. 4, pp. 1367–1373, 2010.
- [13] L. T.-P. Timár-P and P. Tímár, *Noise and vibration of electrical machines*. North Holland, 1989, vol. 34.
- [14] P. Vijayraghavan and R. Krishnan, "Noise in electric machines: a review," in *Industry Applications Conference, 1998. Thirty-Third IAS Annual Meeting. The 1998 IEEE*, vol. 1. IEEE, 1998, pp. 251–258.
- [15] R. Girgis and S. Vermas, "Method for accurate determination of resonant frequencies and vibration behaviour of stators of electrical machines," in *IEE Proceedings B-Electric Power Applications*, vol. 128, no. 1. IET, 1981, p. 1.
- [16] S. Verma, K. Williams, and R. Singal, "Vibrations of long and short laminated stators of electrical machines part i: Theory, experimental models, procedure and set-up," *Journal of sound and vibration*, vol. 129, no. 1, pp. 1–13, 1989.
- [17] K. Williams, R. Singal, and S. Verma, "Vibrations of long and short laminated stators of electrical machines part ii: Results for long stators," *Journal of sound and vibration*, vol. 129, no. 1, pp. 15–29, 1989.
- [18] R. Singal, S. Verma, and K. Williams, "Vibrations of long and short laminated stators of electrical machines part iii: Results for short stators and validity of simplified frequency equation," *Journal of sound and vibration*, vol. 129, no. 1, pp. 31–44, 1989.
- [19] Z. Zhu, Y. Liu, and D. Howe, "Minimizing the influence of cogging torque on vibration of pm brushless machines by direct torque control," *IEEE transactions on magnetics*, vol. 42, no. 10, pp. 3512–3514, 2006.
- [20] S.-M. Hwang, J.-B. Eom, G.-B. Hwang, W.-B. Jeong, and Y.-H. Jung, "Cogging torque and acoustic noise reduction in permanent magnet motors by teeth pairing," *IEEE Transactions on Magnetics*, vol. 36, no. 5, pp. 3144–3146, 2000.
- [21] T. M. Jahns and W. L. Soong, "Pulsating torque minimization techniques for permanent magnet ac motor drives-a review," *IEEE transactions on industrial electronics*, vol. 43, no. 2, pp. 321–330, 1996.
- [22] N. Bianchi and S. Bolognani, "Design techniques for reducing the cogging torque in surface-mounted pm motors," *IEEE Transactions on Industry Applications*, vol. 38, no. 5, pp. 1259–1265, 2002.

- [23] E. Favre, L. Cardoletti, and M. Jufer, "Permanent-magnet synchronous motors: A comprehensive approach to cogging torque suppression," *IEEE Transactions on Industry Applications*, vol. 29, no. 6, pp. 1141–1149, 1993.
- [24] T. Li and G. Slemon, "Reduction of cogging torque in permanent magnet motors," *IEEE Transactions on Magnetics*, vol. 24, no. 6, pp. 2901–2903, 1988.
- [25] T. Ishikawa and G. R. Slemon, "A method of reducing ripple torque in permanent magnet motors without skewing," *IEEE Transactions on Magnetics*, vol. 29, no. 2, pp. 2028–2031, 1993.
- [26] N. Bianchi, S. Bolognani, and A. Cappello, "Reduction of cogging force in pm linear motors by pole-shifting," *IEE Proceedings-Electric Power Applications*, vol. 152, no. 3, pp. 703–709, 2005.
- [27] N. Ekreem, A. Olabi, T. Prescott, A. Rafferty, and M. Hashmi, "An overview of magnetostriction, its use and methods to measure these properties," *Journal of Materials Processing Technology*, vol. 191, no. 1, pp. 96–101, 2007.
- [28] A. Moses and S. Pegler, "The effects of flexible bonding of laminations in a transformer core," *Journal of sound and vibration*, vol. 29, no. 1, pp. 103–112, 1973.
- [29] A. Moses, "Measurement of magnetostriction and vibration with regard to transformer noise," *IEEE Transactions on Magnetics*, vol. 10, no. 2, pp. 154–156, 1974.
- [30] T. Hilgert, L. Vandeveld, and J. Melkebeek, "Comparison of magnetostriction models for use in calculations of vibrations in magnetic cores," *IEEE Transactions on Magnetics*, vol. 44, no. 6, pp. 874–877, 2008.
- [31] B. Weiser, H. Pftzner, and J. Anger, "Relevance of magnetostriction and forces for the generation of audible noise of transformer cores," *IEEE Transactions on Magnetics*, vol. 36, no. 5, pp. 3759–3777, 2000.
- [32] K. Delaere, W. Heylen, R. Belmans, and K. Hameyer, "Comparison of induction machine stator vibration spectra induced by reluctance forces and magnetostriction," *IEEE Transactions on Magnetics*, vol. 38, no. 2, pp. 969–972, 2002.
- [33] T. G. Hilgert, L. Vandeveld, and J. A. Melkebeek, "Numerical analysis of the contribution of magnetic forces and magnetostriction to the vibrations in induction machines," *IET Science, Measurement & Technology*, vol. 1, no. 1, pp. 21–24, 2007.
- [34] A. M. Trzynadlowski, F. Blaabjerg, J. K. Pedersen, R. L. Kirlin, and S. Legowski, "Random pulse width modulation techniques for converter-fed drive systems-a review," *IEEE Transactions on Industry Applications*, vol. 30, no. 5, pp. 1166–1175, 1994.

- [35] F. Blaabjerg, J. K. Pedersen, P. Kjær, L. Andersen, and P. Nielsen, "Investigation and reduction of acoustical noise from switched reluctance drives in current and voltage control," in *Proceedings of International Conference on Electrical Machines, Icem'94, Paris, 1994*, 1994.
- [36] H. Stemmler and T. Eilinger, "Spectral analysis of the sinusoidal pwm with variable switching frequency for noise reduction in inverter-fed induction motors," in *Power Electronics Specialists Conference, PESC'94 Record., 25th Annual IEEE. IEEE*, 1994, pp. 269–277.
- [37] R. J. Belmans, L. D'Hondt, A. J. Vandenput, and W. Geysen, "Analysis of the audible noise of three-phase squirrel-cage induction motors supplied by inverters," *IEEE transactions on industry applications*, no. 5, pp. 842–847, 1987.
- [38] R. J. Belmans, D. Verdyck, W. Geysen, and R. D. Findlay, "Electro-mechanical analysis of the audible noise of an inverter-fed squirrel-cage induction motor," *IEEE Transactions on Industry Applications*, vol. 27, no. 3, pp. 539–544, 1991.
- [39] R. Krishnan and P. Vijayraghavan, "State of the art: acoustic noise in switched reluctance motor drives," in *Industrial Electronics Society, 1998. IECON'98. Proceedings of the 24th Annual Conference of the IEEE*, vol. 2. IEEE, 1998, pp. 929–934.
- [40] N. N. Farve, "Design of a low-mass high-torque brushless motor for application in quadruped robotics," Master's thesis, Massachusetts Institute of Technology, Department of Electrical Engineering and Computer Science, 1990.
- [41] A. Banerjee, J. H. Lang, and J. L. Kirtley, "Fine grain commutation: Integrated design of permanent-magnet synchronous machine drives with highest torque density," in *Electrical Machines (ICEM), 2012 XXth International Conference on*. IEEE, 2012, pp. 671–677.
- [42] J. J. Cathey, D. A. Topmiller, and S. A. Nasar, "A tubular self-synchronous motor for artificial heart pump drive," *IEEE transactions on biomedical engineering*, no. 3, pp. 315–319, 1986.
- [43] J. Eastham, R. Akmese, and H. Lai, "Optimum design of brushless tubular linear machines," *IEEE Transactions on Magnetics*, vol. 26, no. 5, pp. 2547–2549, 1990.
- [44] K. J. Meessen, J. J. Paulides, and E. A. Lomonova, "Modeling and experimental verification of a tubular actuator for 20-g acceleration in a pick-and-place application," *IEEE Transactions on Industry Applications*, vol. 46, no. 5, pp. 1891–1898, 2010.
- [45] W.-J. Kim, M. Berhan, D. Trumper, and J. Lang, "Analysis and implementation of a tubular motor with halbach magnet array," in *Industry Applications Conference, 1996. Thirty-First IAS Annual Meeting, IAS'96., Conference Record of the 1996 IEEE*, vol. 1. IEEE, 1996, pp. 471–478.

- [46] D. De Groot and C. Heuvelman, "Tubular linear induction motor for use as a servo actuator," in *IEE Proceedings B-Electric Power Applications*, vol. 137, no. 4. IET, 1990, pp. 273–280.
- [47] A. Musolino, R. Rizzo, and E. Tripodi, "The double-sided tubular linear induction motor and its possible use in the electromagnetic aircraft launch system," *IEEE Transactions on Plasma Science*, vol. 41, no. 5, pp. 1193–1200, 2013.
- [48] K. Sato, M. Katori, and A. Shimokohbe, "Ultrahigh-acceleration moving-permanent-magnet linear synchronous motor with a long working range," *IEEE/ASME Transactions on Mechatronics*, vol. 18, no. 1, pp. 307–315, 2013.
- [49] K. Sato, "Thrust ripple reduction in ultrahigh-acceleration moving-permanent-magnet linear synchronous motor," *IEEE Transactions on Magnetics*, vol. 48, no. 12, pp. 4866–4873, 2012.
- [50] K. Sato, "High-precision and high-speed positioning of 100g linear synchronous motor," *Precision Engineering*, vol. 39, pp. 31–37, 2015.
- [51] W. Monkhorst, "Dynamic error budgeting: A design approach," Ph.D. dissertation, TU Delft, Delft University of Technology, 2004.
- [52] L. Jabben, *Mechatronic design of a magnetically suspended rotating platform*. TU Delft, Delft University of Technology, 2007.
- [53] D. Meeker, *User's Manual of Finite Element Method Magnetics*, 2010.
- [54] A. E. Fitzgerald, C. Kingsley, S. D. Umans, and B. James, Eds., *Electric machinery*. McGraw-Hill New York, 2003, vol. 5.
- [55] D. Meeker, *User's Manual of Finite Element Method Magnetics: OctaveFEMM*, 2013.
- [56] S. Seok, A. Wang, M. Y. M. Chuah, D. J. Hyun, J. Lee, D. M. Otten, J. H. Lang, and S. Kim, "Design principles for energy-efficient legged locomotion and implementation on the mit cheetah robot," *IEEE/ASME Transactions on Mechatronics*, vol. 20, no. 3, pp. 1117–1129, 2015.
- [57] S. Seok, A. Wang, M. Y. Chuah, D. Otten, J. Lang, and S. Kim, "Design principles for highly efficient quadrupeds and implementation on the mit cheetah robot," in *Robotics and Automation (ICRA), 2013 IEEE International Conference on*. IEEE, 2013, pp. 3307–3312.
- [58] H.-W. Park, S. Park, and S. Kim, "Variable-speed quadrupedal bounding using impulse planning: Untethered high-speed 3d running of mit cheetah 2," in *2015 IEEE International Conference on Robotics and Automation (ICRA)*. IEEE, 2015, pp. 5163–5170.

- [59] K. Halbach, "Design of permanent multipole magnets with oriented rare earth cobalt material," *Nuclear instruments and methods*, vol. 169, no. 1, pp. 1–10, 1980.
- [60] K. Halbach, "Perturbation effects in segmented rare earth cobalt multipole magnets," *Nuclear Instruments and Methods in Physics Research*, vol. 198, no. 2, pp. 213–215, 1982.
- [61] K. Halbach, "Application of permanent magnets in accelerators and electron storage rings," *Journal of Applied Physics*, vol. 57, no. 8, pp. 3605–3608, 1985.
- [62] D. L. Trumper, M. E. Williams, and T. H. Nguyen, "Magnet arrays for synchronous machines," in *Industry Applications Society Annual Meeting, 1993., Conference Record of the 1993 IEEE*. IEEE, 1993, pp. 9–18.
- [63] J. Ofori-Tenkorang, "Permanent-magnet synchronous motors and associated power electronics for direct-drive vehicle propulsion," PhD Dissertation, Massachusetts Institute of Technology, Department of Electrical Engineering and Computer Science, 1997.
- [64] J. R. Melcher, *Continuum electromechanics*. MIT press Cambridge, 1981, vol. 2.
- [65] H. A. Haus and J. R. Melcher, *Electromagnetic fields and energy*. Prentice Hall, 1989.
- [66] D. L. Trumper, W.-j. Kim, and M. E. Williams, "Design and analysis framework for linear permanent-magnet machines," *IEEE Transactions on Industry Applications*, vol. 32, no. 2, pp. 371–379, 1996.
- [67] V. Ostovic, *Dynamics of saturated electric machines*. Springer Science & Business Media, 2012.
- [68] M. Zahn, *Electromagnetic Field Theory: a problem solving approach*. John Wiley & Sons, 1979.
- [69] I. MacKenzie, "Design and control methods for high-accuracy variable reluctance actuators," PhD Dissertation, Massachusetts Institute of Technology, Department of Mechanical Engineering, 2015.
- [70] X. Lu, "Electromagnetically-driven ultra-fast tool servos for diamond turning," PhD Dissertation, Massachusetts Institute of Technology, Department of Mechanical Engineering, 2005.
- [71] D. J. Kluk, "An advanced fast steering mirror for optical communication," Master's thesis, Massachusetts Institute of Technology, Department of Mechanical Engineering, 2007.
- [72] D. R. Nohavec, "Magnetic bearing design for interferometric mirror-scanning mechanisms," Master's thesis, Massachusetts Institute of Technology, Department of Mechanical Engineering, 1997.